Combustion and Decomposition of Hydrazinium Nitroformate (HNF) and HNF Propellants

Jeroen Louwers

Combustion and Decomposition of Hydrazinium Nitroformate (HNF) and HNF Propellants

Combustion and Decomposition of Hydrazinium Nitroformate (HNF) and HNF Propellants

PROEFSCHRIFT

ter verkrijging van de graad van doctor
aan de Technische Universiteit Delft,
op gezag van de Rector Magnificus prof. ir. K.F. Wakker,
in het openbaar te verdedigen ten overstaan van een commissie,
door het College voor Promoties aangewezen,
op 2 juni 2000 te 16:00 uur

door Jeroen LOUWERS
natuurkundig ingenieur
geboren te Waalre

Dit proefschrift is goedgekeurd door de promotor:
Prof. Dr. D.J.E.M. Roekaerts

Samenstelling promotiecomissie:

Rector Magnificicus	Voorzitter
Prof. Dr. D.J.E.M. Roekaerts	Technische Universiteit Delft, promotor
Prof. Dr. Dipl.-Ing. K. Hanjalić	Technische Universiteit Delft
Prof. Dr. Ir. H.E.A. van den Akker	Technische Universiteit Delft
Prof. Dr. Ir. Th.H. van der Meer	Technische Universiteit Twente
Prof. Dr. Ir. H.J. Pasman	TNO Defensie Onderzoek, Delft
Dr. Ir. G.M.H.J.L. Gadiot	TNO Prins Maurits Laboratorium, Rijswijk
Ir. H.F.R. Schöyer	Europese Ruimtevaart Organisatie ESA, Noordwijk

ISBN: 90-9013556-1

This work was financially supported by The Dutch Technology Foundation STW under contract number DTN66.4108.

Cover: HNF crystals (*by Leander Teepe - TNO Prins Maurits Laboratory*). Compared to conventional solid propellants, propellants based on HNF are characterized by an increased performance and have cleaner exhaust gases.

"I might construct a rocket, in the form
Of a huge locust, driven by impulses
Of villainous saltpeter from the rear,
Upwards by leaps and bounds"

Cyrano in Cyrano de Bergerac, act III

Samenvatting

Verbranding en Ontleding van Hydrazinium Nitroformaat (HNF) en HNF stuwstoffen

Ontdekking van de ruimte, intercontinentale telecommunicatie, navigatie en lange termijn weersvoorspelling zijn slecht enkele voorbeelden van wat mogelijk is geworden dankzij de komst van betrouwbare raketten. Momenteel worden de kosten van lanceringen steeds belangrijker. Vermindering van de lanceerkosten van satellieten is uiterst belangrijk voor aanbieders van lanceringen om competitief te blijven. Eén van de mogelijkheden om kosten te verminderen is overstappen op stuwstoffen met hogere prestaties. Raketten voorzien van stuwstoffen met betere prestaties kunnen zwaardere (of meer) satellieten lanceren, voor dezelfde kosten.

Hydrazinium nitroformaat (HNF, $N_2H_5{\cdot}C(NO_2)_3$) is een oxydator met een zeer hoge energie inhoud. Dit maakt HNF een mogelijke kandidaat om de huidige generatie van oxydatoren in vaste stuwstoffen te vervangen. HNF-stuwstoffen hebben tot 7% hogere prestaties dan huidige stuwstoffen. In tegenstelling tot de huidige generatie van stuwstoffen, bevatten HNF-stuwstoffen geen chloor. Daardoor zijn de uitlaatgassen schoner en minder milieubelastend.

De werkzaamheden die beschreven zijn in dit proefschrift hebben als doelstelling meer inzicht te verkrijgen in de ontleding en verbranding van HNF en HNF-stuwstoffen. De oxydator is een belangrijk ingrediënt in de vaste stuwstof. Typisch bestaat de stuwstof voor meer dan 60% uit oxydator. Daarom kunnen de verbrandingseigenschappen sterk veranderen, wanneer de oxydator wordt vervangen. In dit werk wordt de verbranding van puur HNF en HNF-stuwstoffen beschreven. In het bijzonder dat van stuwstoffen met een energetisch glycidyl azide polymeer (GAP) als binder.

Diverse experimentele technieken zijn gebruikt in deze studie. De HNF vlamstructuur en ontledingsgassen zijn bestudeerd met behulp van absorptie van ultra-violet en zichtbaar licht. Een laser geïnduceerde fluorescentie techniek is gebruikt om vlamstructuren zichtbaar te maken. Als versimpeling van heterogene stuwstoffen, is ook de verbranding van alternerende laagjes binder en oxydator, zogenaamde "sandwiches", onderzocht. Verder is gebruik gemaakt van micro-thermokoppel technieken en een ultrasone pulse-echo techniek voor bepaling van afbrandsnelheden. Diverse modellen voor de verbranding van HNF en HNF-stuwstoffen zijn ontwikkeld. Eén groep van modellen maakt gebruikt van globale kinetische reacties. De andere benadering gaat uit van gedetailleerde kinetiek.

Dit werk toont aan dat de ontleding van HNF begint door een proton overdracht. De verbranding van HNF wordt gekenmerkt door een zeer kleine vlamzone. Hoewel de chemische samenstelling van HNF sterk lijkt op die van nitramine en double-base stuwstoffen, heeft de vlamstructuur geen duidelijke twee-traps structuur. Het merendeel van de energie is afkomstig van reacties van NO_2 met andere ontledingsprodukten. In een tweede zone ontleed NO naar O_2 en N_2 via trage, energetische neutrale, reacties. Het effect van HNF-deeltjesgroote op de verbranding van HNF/GAP-stuwstoffen is klein. Dit kan worden verklaard door de hoge energie afgifte van de kleine HNF vlam dicht bij het verbrandingsoppervlak. De verbranding van HNF/GAP-stuwstoffen vindt plaats op een manier waarin binder en HNF onafhankelijk van elkaar verbranden.

Summary

Combustion and Decomposition of Hydrazinium Nitroformate (HNF) and HNF Propellants

Space exploration, intercontinental telecommunication, navigation and long term weather forecasting are some examples of what has become possible with the development of reliable rockets. After this technical step forwards, launch economics are now becoming more and more important. Reducing the launch costs of satellites is of prime importance for launch operators to remain in business for the future. One of the ways to reduce costs, is by improving the performance of the propellant. Rockets containing propellants with improved performance can launch heavier (or more) satellites with the same hardware cost.

Hydrazinium nitroformate (HNF, $N_2H_5{\cdot}C(NO_2)_3$) is an oxidizer with a very high energetic content. This makes HNF an attractive candidate to replace oxidizers that are currently in use for solid rocket propellants. HNF-propellants potentially have up to 7% performance gain compared to the existing solid propellants. Unlike the current generation of propellants, HNF-propellants do not contain chlorine and have cleaner, more environmental benign, exhaust gases.

The work described in this thesis focuses on obtaining a better understanding of the decomposition and combustion of HNF and HNF-propellants. The oxidizer is an important ingredient in the solid propellant. Typically the oxidizer accounts for more than 60% of the total propellant weight. Therefore the burning rate characteristics can change dramatically when one type of oxidizer is replaced by another one. The combustion of both pure HNF and that of HNF-propellants is addressed. In particular that of propellants with an energetic glycidyl azide polymer (GAP) binder.

Several experimental techniques have been employed in this study. The HNF flame structure and decomposition gases were studied by ultra-violet and visible absorption. Planar laser-induced fluorescence was used to image flame structures. As a simplification of propellants, the combustion of alternating stacks of oxidizer and binder, so called "sandwiches", was studied. Also embedded micro-thermocouples and ultrasound techniques have been employed. The combustion of HNF and HNF-propellants was modeled. Several models are presented in this thesis. One group of models uses simplified global reactions. The other approach is that of detailed kinetics. Both types of models are applied to HNF and HNF-propellants.

This works shows that the decomposition of HNF is initiated by a proton transfer step. HNF combustion takes place in a small zone. Even at ambient pressure most heat release occurs within the first millimeter of the flame. Although the chemical composition of HNF is very similar to that of nitramines and double-base propellants, the flame structure of HNF does not have a clear two-stage combustion zone. Most energy is released by reaction of NO_2 with other decomposition products. In a second stage the NO decomposes to O_2 and N_2 via slow, energetically neutral, reactions. The effect of particle size on the burn rate of HNF/GAP-propellants was found to be small. This is explained by the high energy release of the short hot HNF flame close to the surface. Combustion of HNF/GAP-propellants is found to occur in a sequential way in which the binder and HNF combust independently.

Contents

1 Introduction **1**
- 1.1 Background . . . 1
- 1.2 Objectives . . . 6
- 1.3 Thesis outline . . . 6

2 Hydrazinium nitroformate **9**
- 2.1 Introduction . . . 9
- 2.2 Properties . . . 9
- 2.3 Decomposition . . . 15
  - 2.3.1 Previous work . . . 15
  - 2.3.2 Experimental study of the decomposition of HNF . . . 17
  - 2.3.3 HNF decomposition mechanism . . . 22
- 2.4 Quantum chemical calculations . . . 23
  - 2.4.1 Semi-empirical calculations . . . 23
  - 2.4.2 Ab initio calculations . . . 25
- 2.5 Conclusions . . . 26

3 Experimental approach **29**
- 3.1 Introduction . . . 29
- 3.2 Pressed samples . . . 29
- 3.3 Propellant manufacturing . . . 36
  - 3.3.1 Sandwiches . . . 36
  - 3.3.2 Propellants . . . 37
- 3.4 Diagnostic techniques . . . 38
  - 3.4.1 Laser induced fluorescence . . . 38
  - 3.4.2 UV-Vis absorption . . . 41
  - 3.4.3 Micro-thermocouples . . . 41
- 3.5 Experimental facility . . . 42
- 3.6 Strand burner . . . 44
- 3.7 Conclusions . . . 46

4 HNF combustion **47**
- 4.1 Introduction . . . 47
- 4.2 Background . . . 47
- 4.3 Neat HNF combustion . . . 52
  - 4.3.1 Burn rate . . . 52

4.3.2 Micro-thermocouple measurements 53
4.4 Flame structure 56
4.4.1 Emission spectroscopy 56
4.4.2 Absorption spectroscopy 57
4.4.3 PLIF experiments 60
4.4.4 Temperature profile 65
4.5 Radiation enhanced combustion 66
4.6 Mixtures containing HNF 67
4.7 Conclusions 73

5 HNF sandwiches and propellants **75**
5.1 Introduction 75
5.2 Binders 75
5.2.1 Glycidyl azide polymer 75
5.2.2 Hydroxyl terminated polybutadiene 81
5.3 HNFsandwiches 82
5.3.1 Emission imaging 82
5.3.2 PLIF experiments 85
5.4 HNF propellants 90
5.4.1 Burn rate 91
5.4.2 Emission imaging 96
5.4.3 PLIF experiments 97
5.5 Conclusions 98

6 Modeling **99**
6.1 Introduction 99
6.2 Simplified model for HNF combustion 99
6.2.1 Model 100
6.2.2 Results 103
6.2.3 Conclusions 109
6.3 PREMIX modeling 112
6.3.1 Description of the model 112
6.3.2 HNF chemistry 116
6.3.3 Solution 117
6.3.4 PREMIX program 118
6.3.5 Results 118
6.3.6 Conclusions 122
6.4 BDP propellant model 126
6.4.1 Model input 126
6.4.2 Results 127
6.5 BIGMIX: 2D computational fluid dynamics model 132
6.5.1 BIGMIX modifications 132
6.5.2 Model input 132
6.5.3 Implementation 133
6.5.4 Results 134
6.6 BDP vs BIGMIX 136

6.7 Conclusions 141

7 Ultrasound **143**
7.1 Introduction 143
7.2 Ultrasound 144
7.2.1 Propagation 144
7.2.2 Reflection 145
7.2.3 Attenuation 145
7.2.4 Pulse-echo technique 145
7.2.5 Ultrasound properties of HNF 146
7.3 HNF combustion model 147
7.3.1 Condensed phase 148
7.3.2 Gas phase 149
7.3.3 Solution 150
7.3.4 Input data 150
7.3.5 Model validation 150
7.4 Experiments 153
7.4.1 Description of the experimental setup 153
7.4.2 Ultrasound data reduction 156
7.5 Results 157
7.5.1 Model results 157
7.5.2 Experimental results 157
7.6 Conclusions 163

8 Combustion modification **167**
8.1 Introduction 167
8.2 Time-averaged combustion 167
8.3 Pressure exponent reduction 169
8.4 Initial experiments 170
8.5 Conclusions 171

9 Conclusions **173**

Bibliography **177**

A Solution of the PREMIX equations **191**

B Flame chemistry **195**
B.1 HNF flame chemistry 195
B.2 GRI-mech flame chemistry 201

C Glossary **209**
C.1 Glossary of terms 209
C.2 Symbols 210
C.3 Acronyms 213

D Publications **215**

Acknowledgments **217**

Stellingen **219**

Curriculum vitae **220**

Index **221**

Chapter 1

Introduction

1.1 Background

Ever since the existence of mankind, people explored their surroundings. The reason for this exploration has changed with time. In the prehistoric times the need for food and changing climates urged families to move. In the late middle ages most parts of the world had been explored in a search for new spices, vegetables and plants unknown in the western world. More recently the explorers left the earth, culminating in the first landing on the moon in 1969. In that period space exploration was driven by nationalism. It has become an international effort now, illustrated by the construction of the international space station.

Nowadays manned space missions are outnumbered by commercial satellite launches. Satellites play an important role in e.g. communication, navigation and environmental monitoring. With the advent of commercial launch operators, competition has emerged. Launch cost reductions are essential to compete in this fast growing market. There are several ways of reducing the cost of the launch of a satellite. One of the simplest solutions to reduce the launch costs is propellant performance improvement [54]. Propellants with high performance lead to smaller systems for a specific payload mass, or increased payload mass for the same launcher size. The performance of a rocket propellant is expressed by its specific impulse[1]. The specific impulse I_s is a measure of the amount of propellant mass flow ($\dot{m}$) for a given constant thrust F [147]:

$$I_s = F/\dot{m}\,. \tag{1.1}$$

A higher specific impulse leads to less propellant mass for a given thrust envelope. This reduction in the weight of the rocket further reduces the needed thrust, thereby even further reducing the rockets weight. This mechanism explains that a few percent increase of specific impulse can lead to significant increases of the payload mass.

It can be shown that $I_s \propto \sqrt{(T_f/M)}$, where T_f is the flame temperature of the mixture, and M the molecular weight of the formed gaseous products. So, a high performance propellant combination is characterized by a high flame temperature and low molecular weight combustion products.

[1] Throughout this thesis an elementary background in solid propellants is assumed. Readers that are unfamiliar with some of the terms that are used, may consult the glossary in Appendix C on page 209. This Appendix also contains a nomenclature and a list of symbols.

Rocket motors

Rocket motors are classified according to the physical mechanism supplying the energy release. Examples are nuclear propulsion and electrical propulsion, which are the minority of propulsive devices. The high thrust needed for lifting large rockets is nowadays exclusively obtained from chemical propulsion. The energy of chemical propulsive devices originates from oxidation reactions and decomposition of highly energetic components. Chemical propulsive devices can be further classified according to the aggregation state of the propellants. Liquid rocket motors combust liquid propellants. A typical example of a liquid propellant combination is liquid oxygen and liquid hydrogen, used e.g. in the first stage of the Ariane 5, and in the Space Shuttle's main engines. Hybrid rockets motors have propellants that are in a different aggregation state , e.g. solid polyethylene (fuel) and liquid nitrogen tetroxide (oxidizer).

Solid rocket motors consist of monolithic propellant grain that contains both the oxidizer and the fuel. The operating principle is very simple. The simplest solid rocket motor, is that of a fireworks rocket. Because of their simplicity, solid rockets are very reliable, easy to handle, and can be launched at any moment without delay. These characteristics make solid rocket motors also very attractive for military missiles. Figure 1.1 shows a typical solid rocket motor with its most important components.

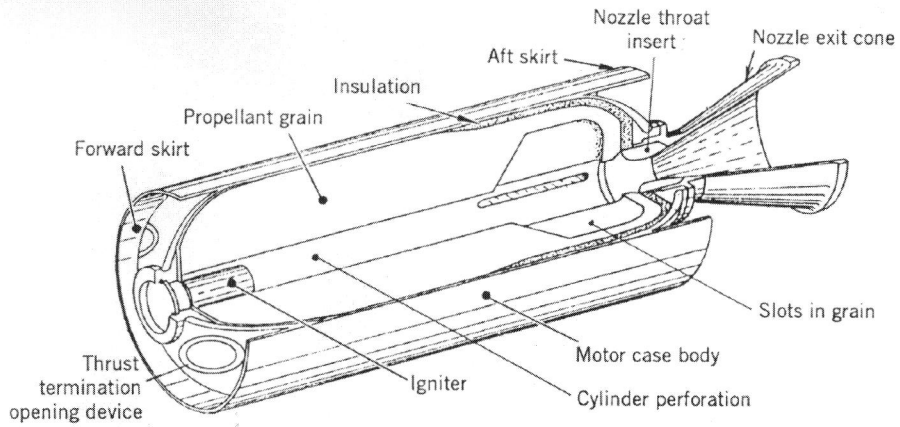

Figure 1.1: *Typical solid propellant rocket motor showing the most important components (from Ref. [147]).*

The oxidizer and fuel of a solid rocket motor can be intimately mixed resulting in an almost homogeneous propellant. A typical example is the family of double base propellants, consisting of nitrocellulose in which nitroglycerine is dissolved. Today, double base propellants have almost completely been replaced by composite propellants that have a higher performance, better mechanical properties and longer shelf life. Composite propellants are a heterogeneous mixture of oxidizer and fuel, see Fig. 1.2. Usually the oxidizer is ammonium perchlorate (NH_4ClO_4, AP). Typical fuels are the family of polybutadienes ($\sim CH_{1.5}$, PB), such as hydroxyl terminated polybutadiene, HTPB. The fuel forms a matrix

that holds the oxidizer crystals together, and is therefore called binder. Often a metallic fuel, e.g. aluminum (Al), is added to increase the combustion temperature and thereby the specific impulse. Best known example of the AP/PB/Al propellant combination are the two boosters of the Space Shuttle, each containing 250 tons of solid propellant. Typically, a composite propellant contains 12-14% binder, 18% aluminum and the remaining is AP. Composite propellants are manufactured by vacuum mixing of the binder pre-polymer and the other ingredients. This highly viscous liquid mixture is then casted in the rocket motor casing or liner. The mixture is then cured. For curing several methods are used, depending on the selected pre-polymer. Examples of curing agents are multifunctional isocyanates and epoxides.

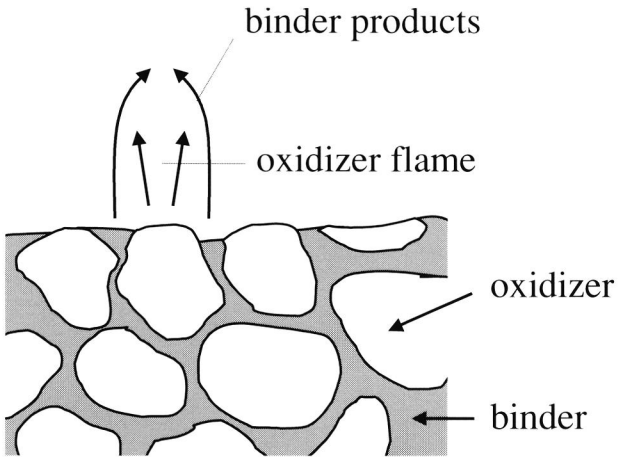

Figure 1.2: *Schematic of the combustion of a composite propellant.*

High performance solid rocket propellants

Because the performance has a large impact on the payload mass, there is a continuous effort to search for new solid propellants with improved performance. Replacement of the oxidizer by more energetic oxidizers yields the highest performance gain. Several oxidizers have been identified as candidate oxidizers to replace AP in the future propellants [1]. The most promising are ammonium dinitramide ($NH_4N(NO_2)_2$, ADN) and hydrazinium nitroformate ($N_2H_5C(NO_2)_3$, HNF). ADN research is concentrated in the United States and Sweden [22, 60, 75, 119, 159]. The main center of HNF research is located in the Netherlands [49, 134, 135, 136], with the European Space Agency (ESA) and Netherlands Agency for Aerospace Programmes (NIVR) as main sponsors. Besides replacing the oxidizer, further performance gain can be obtained by replacing the binder by a more energetic compound. Typical examples are binders containing energetic azide groups (like glycidyl azide polymer GAP and poly 3,3-bis-azidomethyl-oxetane BAMO [89]). Other energetic binders containing large amounts of oxygen in the form of nitrates are also being investigated. Typical examples are polyNIMMO (poly (3-NitratoMethyl-3-Methyl Oxetane), and polyGLYN (poly Glycidyl Nitrate) [1, 24].

Some typical performance graphs of HNF/GAP-propellants in comparison with conventional AP/HTPB-propellants are shown in Fig. 1.3 (calculations with NASA SP-273 code [53]) . These performance curves show that HNF has improved performance as compared to the conventional AP/HTPB propellants. The theoretical performance gain is about 7%. The compositions of Fig. 1.3 are not optimized for performance and are illustrative only. HNF propellants have the highest theoretical performance of all known solid propellants. Figure 1.3 shows that the performance of an aluminized AP-HTPB propellant is exceeded by a non-aluminized HNF/GAP propellant.

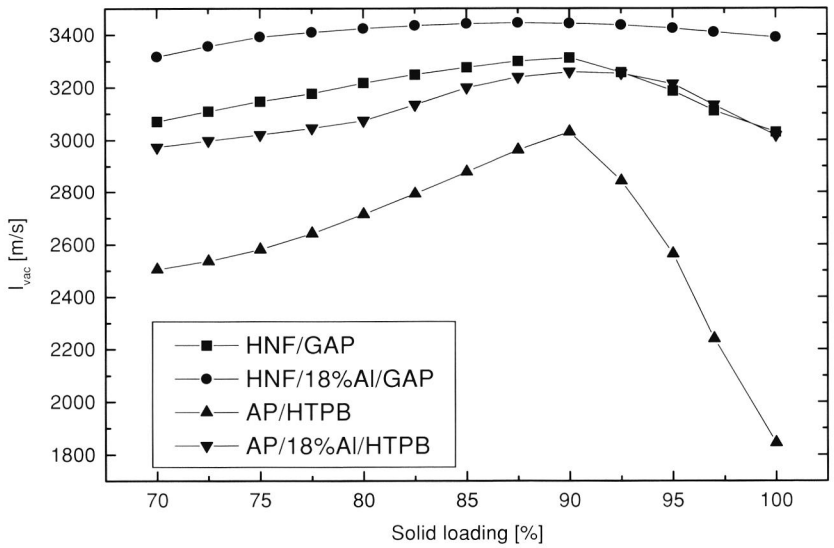

Figure 1.3: *Vacuum specific impulse of some typical HNF propellants in comparison with AP propellants (combustion pressure 10 MPa, expansion ratio 100, equilibrium flow).*

Ammonium perchlorate propellants generate about 20% hydrochloric acid (HCl) as a combustion product. Although the total acid deposition of space launches is small in comparison with the world's total acid release [12], the public opinion requires search for new propellants that are more environmentally acceptable [72]. Chlorine scavenged propellants have been developed to almost completely reduce the acid emission, but always with the penalty of a performance loss [39]. Because HNF does not contain chlorine, HCl is not formed during combustion. Their clean exhaust gases and their performance, make HNF-propellants a very attractive candidate to replace the current family of AP-propellants in the future.

An application related to that of composite propellants, is the use of propellants containing about 40% HNF as high-performance gas generators for ducted ramjet rockets [101].

Except for use in solid composite propellants, HNF is also a very attractive monopropellant when dissolved in e.g. water [13]. The performance of HNF-solutions can match (or even outperform) that of the toxic hydrazine. This makes HNF a promising candidate to replace hydrazine in many applications such as attitude control systems for satellites and emergency power units.

Combustion of composite propellants

The combustion of composite propellants is governed by numerous physical and chemical processes (see Fig. 1.4). The oxidizer and binder products are heated from their initial ambient temperature to the temperature at the surface of the propellant. The energy from this heating comes from several sources such as heat conduction from the gas phase, radiation from the gas phase and exothermic processes in the condensed phase. During heating the components may exhibit a phase change (melting or vaporization). Also crystal structure changes and formation of cracks and pores due to thermal stresses have been observed. Thermophysical properties such as conductivity and heat capacity change continuously because of the extreme changes in physical state of the components.

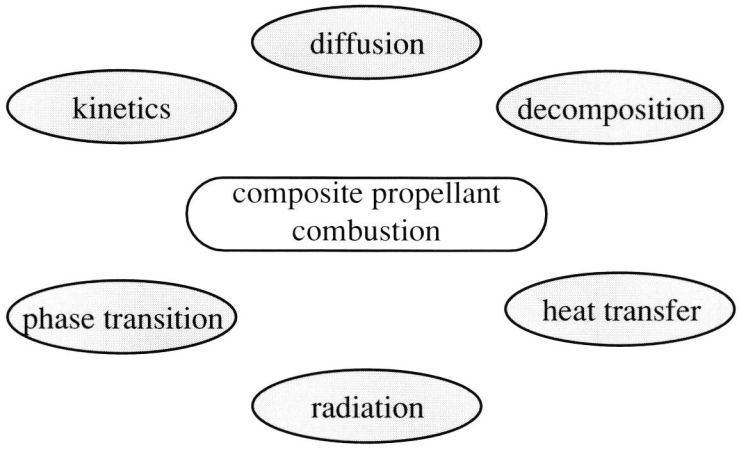

Figure 1.4: *Processes of composite propellant combustion.*

At, or close to, the propellant surface several scenarios are possible. Both the oxidizer and binder decompose and combust in the gas phase, or vaporization takes place before decomposition, or exothermic reactions take place at the propellant surface e.g. in a melt layer. For real propellants none of these examples describes accurately what takes place, but in general it is a complex system in which all of these processes participate. The contribution of each of these processes is generally dependent on the conditions, such as pressure and initial temperature. In the gas phase the binder and oxidizer products mix and react. Dependent on the particle size, the oxidizer products may decompose exothermically before reacting with the binder products, essentially yielding a diffusion flame of oxidizer and binder decomposition products. In the other limit of small oxidizer particle size, mixing occurs before the reaction takes place. In this case the gas phase may be considered premixed. For these two limiting cases the dependence on pressure is

different, which explains the difference in regression rate as function of pressure for different particle sizes, as observed in AP propellants.

HNF programs

In the late 80's HNF research was picked up again by TNO. A desk study for new storable propellants had shown that HNF-propellants have a very high performance [116]. In a contract funded by ESA and NIVR, HNF propellants were formulated and motor firings were carried out. This work lead to the 'proof of concept of HNF/Al/GAP solid propellants' [117], and confirmed the higher performance of these propellants by experiments. Because of the promising results a larger program (GSTP-1) was started, sponsored by the European Space Agency. The objective of this work was further development of HNF propellants with energetic binders [153]. Several European institutes and industries participated in this program (from Norway, United Kingdom and The Netherlands). After the GSTP-1 program the GSTP-2 phase 1 program was started. This program focused on the origin of thermal decomposition and the improvement of HNF stability and morphology. Follow-up programs will address propellant technology with the improved HNF from GSTP-2 phase 1. The work in this thesis contributes to the other HNF-programs by addressing more fundamental aspects of the combustion of HNF.

1.2 Objectives

The goal of this work is to obtain a more fundamental understanding of the decomposition and combustion behavior of HNF and HNF-propellants. This knowledge is necessary for tailoring of propellant properties for actual applications, and for understanding the effect of varying parameters on the combustion properties.

The objectives defined at the beginning of this study are:

- Obtaining insight into the decomposition of HNF and HNF-based propellants and the structure of the flame zone. The HNF (propellant) flame structure will be determined by PLIF (planar laser-induced fluorescence) and other visualization experiments.
- Combustion modeling of HNF and HNF-propellants. Models are used for interpretation of experimental data, and to improve the understanding of the combustion mechanisms.
- Search for suitable catalysts. To tailor the combustion behavior of HNF propellants, the effects of potential catalysts will be investigated.

1.3 Thesis outline

The outline of this thesis is as follows: The properties of HNF are discussed in Chapter 2. This includes thermophysical properties, production aspects, decomposition and quantum chemical modeling. The products formed during decomposition are studied by absorption measurements. Chapter 3 addresses the experimental approach of this study. Experimental facilities and techniques and methods of sample preparation are described in detail in this

Chapter. The combustion of HNF and HNF with additives is the topic of Chapter 4. In this Chapter experimental results of the regression rate, flame structure and temperature profile are described. The combustion of HNF sandwiches and propellants is presented in Chapter 5. This includes the study of the binder-oxidizer diffusion flame structure, effect of HNF particle size, solid loading etc. In Chapter 6 several models are presented. The first model is a very simple model for the combustion of neat HNF. It explains the pressure dependency of the burn rate, effect of an external laser heat flux, and temperature sensitivity. Because of the simplicity of the model, it is an excellent tool to obtain a better insight in the combustion of HNF. The second model is an expansion of the simple HNF model. The global reaction steps are replaced by a chemical mechanism, that was developed for nitramine combustion. The results of this model can be compared with experimental determined species profiles. The third model in Chapter 6 is a simplified model for the combustion of HNF-GAP propellants. The model is based on the BDP-model and predicts the effects of pressure, particle size, and solid loading on the regression rate. The last model calculates the flame structure above a HNF-GAP sandwich by solving transport equations for mass, momentum, energy and species mass fractions. In Chapter 7 the results of a study of the (unsteady) combustion of HNF with ultrasound are presented. To process the experimental data an unsteady combustion model is needed. This model is also presented, and the results are compared to data from existing laser-recoil experiments. The combustion mechanisms of HNF and HNF-propellants are reviewed in Chapter 8. The goal of this Chapter is to find ways to reduce the pressure exponent of HNF-propellants. Chapter 9 gives the conclusions of this work.

Chapter 2

Hydrazinium nitroformate

2.1 Introduction

Hydrazinium nitroformate (HNF) is the hydrazine (N_2H_4) salt of nitroform ($HC(NO_2)_3$). In the sixties, HNF and HNF-based propellants were studied as part of a large scale research program on advanced propellants. In the early seventies HNF research was suddenly stopped. There seem to be two major reasons for this termination [118]. HNF appeared to be incompatible with the usual hydrocarbon binders, because the HNF attacks the double bonds of the unsaturated binder [106]. Another reason for the end of HNF research is the hazardous synthesis method of nitroform, one of the two main ingredients for HNF production. Later on it has been found that it is possible to manufacture stable HTPB/HNF propellants [101]. This observation supersedes the earlier finding of incompatibility with double bonds. Also, a safer production method for nitroform has been developed by Rockwell, which does not require the dangerous distillation of nitroform anymore. In the late 80's, interest in HNF was renewed, mainly because of the need for high performance propellants to reduce launch costs. Furthermore, the increasing global concern of the chlorine emission of ammonium perchlorate (AP) based solid propellants, makes this chlorine-free oxidizer a very attractive candidate to replace AP.

In this Chapter the physical properties of HNF will be discussed first (section 2.2). The decomposition of HNF is discussed in section 2.3. This sections contains a literature review in section 2.3.1, followed by a description of experiments of the decomposition of HNF at combustionlike conditions in section 2.3.2. Semi-empirical and ab initio calculations of HNF are presented in section 2.4.

2.2 Properties

HNF is an orange-yellow solid with chemical formula $N_2H_5{\cdot}C(NO_2)_3$ (see Fig. 2.1). HNF is made by a precipitation reaction between hydrazine (N_2H_4) and nitroform ($HC(NO_2)_3$):

$$N_2H_{4\,(l)} \;+\; HC(NO_2)_{3\,(l)} \;\longrightarrow\; N_2H_5^+{\cdot}C(NO_2)_{3\,(s)}^- \;+\; 84\ \text{kJ/mole}\,. \tag{2.1}$$

As this reaction is exothermic, the process vessel must be thoroughly cooled. After reaction, the HNF crystals are re-crystallized, to improve the purity of the raw HNF, and to control the particle size. The process of manufacturing HNF is described in several

patents [105, 148, 167]. Currently Aerospace Propulsion Products (APP) (Bergen op Zoom, The Netherlands) is the sole commercial supplier of HNF. APP produces HNF on a pilot scale with a maximum capacity of 300 kg per year (Fig. 2.2). Purity is an important factor for the stability of HNF. Friction and impact sensitivity, melting point, and thermal stability are very sensitive to the purity of the HNF [135].

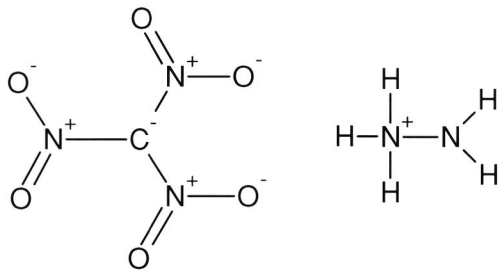

Figure 2.1: *Molecular structure of HNF.*

HNF particles tend to crystallize in needle-shaped crystals, with large length over diameter ratio's (L/D). Needle shaped HNF is not desirable for propellant production because the rheology of these crystals prevents the manufacturing of propellants with high solid loadings needed to obtain a high performance. Cubic, or spherical crystals would be ideal for both sensitivity and casting properties. By recrystallization, the L/D ratio has been reduced to $4 \ldots 5 : 1$, see Fig. 2.3. The different manufacturing processes also allow to steer the mean particle size. At this moment it is possible to manufacture HNF crystals with particle size varying between 5 and 2000 μm. L/D ratio's of 1:1 have been obtained in the past by ultrasound recrystallization [3]. APP is currently able to reduce L/D to $\sim 2 : 1$ by crystallization with ultrasound, and further improvements to the production method are still under development [154].

Three different HNF grades are currently available [160]: HNF produced by evaporation, E-grade; HNF produced by cool crystallization, C-grade; and HNF from a solvent/non-solvent process, S-grade. In general, the evaporation process yields the most stable HNF, but the particle size distribution is broad. By the cool crystallization the largest particles are produced. The crystals shown in Fig. 2.3 were obtained from cool crystallization. The crystals from the S-process are the smallest that are produced at this moment. S-grade material has an equivalent spherical diameter of $\sim 50\mu$m. In this work the HNF grades will be denoted by their production method (E, C or S), followed by an identification number, e.g. S-16.

The most important properties of HNF are summarized in Table 2.1. The properties of HNF are very sensitive to its purity. The standard analysis to determine HNF purity are titration of the acid content (giving HNF content based on acid content) and titration of hydrazine content (giving HNF content based on hydrazine content). Contaminated HNF showed values for the impact sensitivity < 1 Nm, which is too sensitive for use as a propellant ingredient. Purification by recrystallization of the product gives an improvement, and impact sensitivity values of $2 \ldots 5$ Nm have been obtained. Also the vacuum thermal stability (VTS) of HNF and HNF-propellants is strongly affected by the purity of the HNF and the method of production. For example: the S-grade HNF has a higher gas evolution

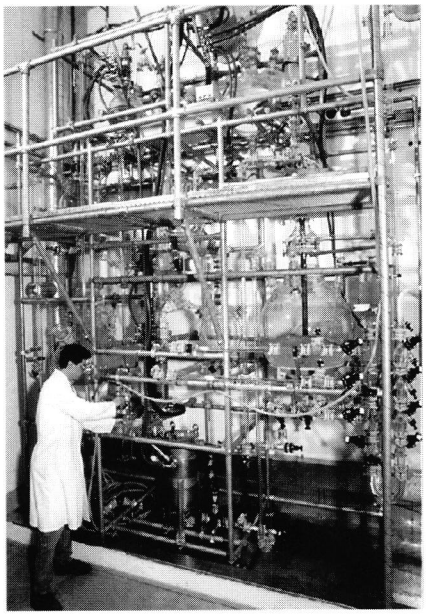

Figure 2.2: *HNF pilot scale reactor production facility at APP. The large glass reactor seen at the right is the main reaction vessel. The remaining of the setup is used for nitroform extraction, and washing and recrystallization of the obtained HNF material.*

than the two other grades due to solvents in the final material.

Thermophysical properties

The heat of formation reported in Ref. [130] is $\Delta H_f^0 = -72$ kJ/mole. Recent measurements by Kon'kova and Matyushin show $\Delta H_f^0 = -76.86 \pm 1.13$ kJ/mole obtained from the measured energy of combustion of $\Delta H_c = -1031.23 \pm 1.13$ kJ/mole [73]. The heat of solution of HNF in water is $\Delta H_{sol} = 50.04 \pm 0.08$ kJ/mole [73].

The thermal properties of HNF as function of temperature were measured by Hanson-Parr and Parr [57]. Pressed samples of HNF were heated and the response of HNF to a heat pulse was measured. From this response the thermal diffusivity, α_c, specific heat capacity c_c, and the thermal conductivity λ_c were determined. The thermal diffusivity was found to be nearly temperature independent in the range $20 - 110$°C. The linear fits of the obtained results are (temperature T in °C):

$$\begin{aligned} \alpha_c(T) &= 1.62 \cdot 10^{-3} + 1.2 \cdot 10^{-6} \cdot T \quad \text{cm}^2/\text{s} \\ c_c(T) &= 0.83 + 0.0014 \cdot T \quad \text{J/gK} \\ \lambda_c(T) &= 2.50 \cdot 10^{-3} + 6.8 \cdot 10^{-6} \cdot T \quad \text{W/cmK} \end{aligned}$$

The heat capacity as function of temperature was also determined from differential scanning calorimetry (DSC) measurements at TNO/PML, see Fig. 2.4. At 20°C c_c=1.16 kJ/kgK,

Figure 2.3: *Re-crystallized HNF with length over diameter ratio's* $4 \ldots 5$*, mean diameter about* $500\,\mu m$*.*

which is above the value of 0.86kJ/kgK obtained by Hanson-Parr and Parr. In the measurements of Hanson-Parr and Parr all three properties are determined from a single experiment and form a complete consistent data-set, but makes an unambiguous determination of the individual properties more difficult.

The heat of vaporization, H_{evap} of HNF was estimated by Trouton's rule, which relates boiling temperature T_b and H_{evap}, according to

$$\frac{H_{evap}}{T_b} = x \,, \tag{2.2}$$

where $x = 96-134\,\mathrm{J/(moleK)}$ for nitroaromatic compounds [21]. Assuming that an average value of $x = 115\,\mathrm{J/(moleK)}$ is valid for HNF as well, it is found that $H_{evap} = 350\,\mathrm{J/g}$. The melting heat of HNF, H_m, is assumed to be equal to that of the nitramines HMX and RDX, which were shown to be equal per mass unit [11], $H_m = 161\ \mathrm{J/g}$.

The heat of sublimation is defined as $H_{subl} = H_m + H_{evap}$. The Clausius-Clapeyron relations relates the heat of sublimation to the vapor pressure, p_s, according to:

$$\log p_s = A - H_{subl}/(RT) \,, \tag{2.3}$$

where A is a constant. Existing data available at TNO of the vapor pressure of HNF in the temperature range $34.4 - 67.7°\mathrm{C}$, yields $H_{subl} = 530\ \mathrm{J/g}$, which compares well with the sum of the melting and evaporation heat $H_m + H_{evap} = 511\ \mathrm{J/g}$.

The UV-Vis and IR absorption spectra of HNF are shown in Fig.'s 2.5 and 2.6 respectively. The UV-spectrum of hydrazine and nitroform are also shown. Both species have an absorbance in the UV. This was 'discovered' recently, although the spectra of both species have been described in literature [63, 141]. It is currently under investigation to use the UV-absorption spectrum of dissolved HNF to determine the purity of the HNF in terms of hydrazine and nitroform content [137].

Molecular formula		$N_2H_5C(NO_2)_3$	
Molecular weight	M	183.08	g/mole
Density	ρ_c	1860 ± 10	kg/m^3
Melting point	T_m	124	°C
Vacuum thermal stability (60°C, 48h)		0.1-1.8	ml/g
Thermal diffusivity	α_c	$\sim 1 \cdot 10^{-8}$	m^2/s
Heat of combustion	ΔH_c	-1066	kJ/mole
Heat of formation	ΔH_f	-72	kJ/mole
Heat of solution in water	ΔH_{sol}	50.04 ± 0.08	kJ/mole
Adiabatic flame temperature	T_f	2766	K
Oxygen balance		+13	%
TNT equivalent (theoretical)		$130 - 150$	%
Impact sensitivity		$2 - 5$	Nm
Friction sensitivity		$18 - 36$	N
Electro Static Discharge (50/50 no fire)		$0.72 - 4.5$	J
Lethal dosis	ld_{50}	128	mg/kg body weight

Table 2.1: *Overview of properties of HNF (from Ref.'s [73, 160]).*

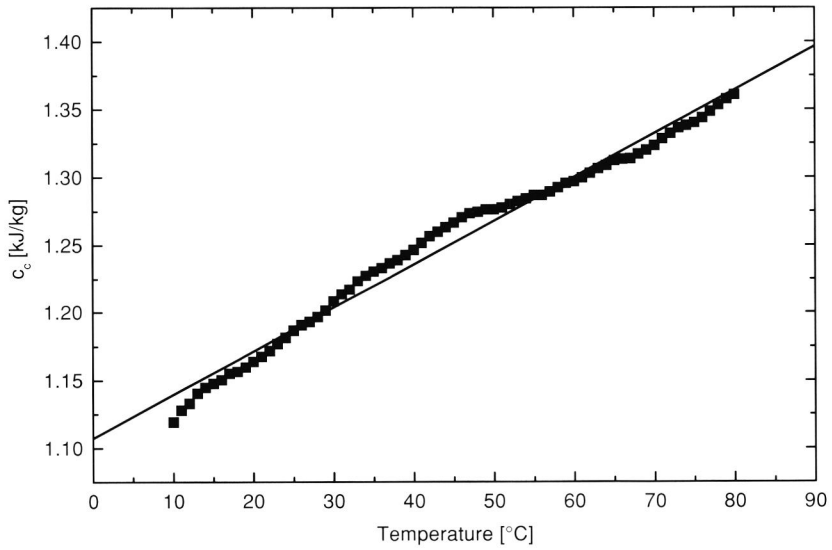

Figure 2.4: *Heat capacity of HNF as determined from DSC measurements (pressed HNF S13, heating rate 10°C/min, sample mass 8.955 mg).*

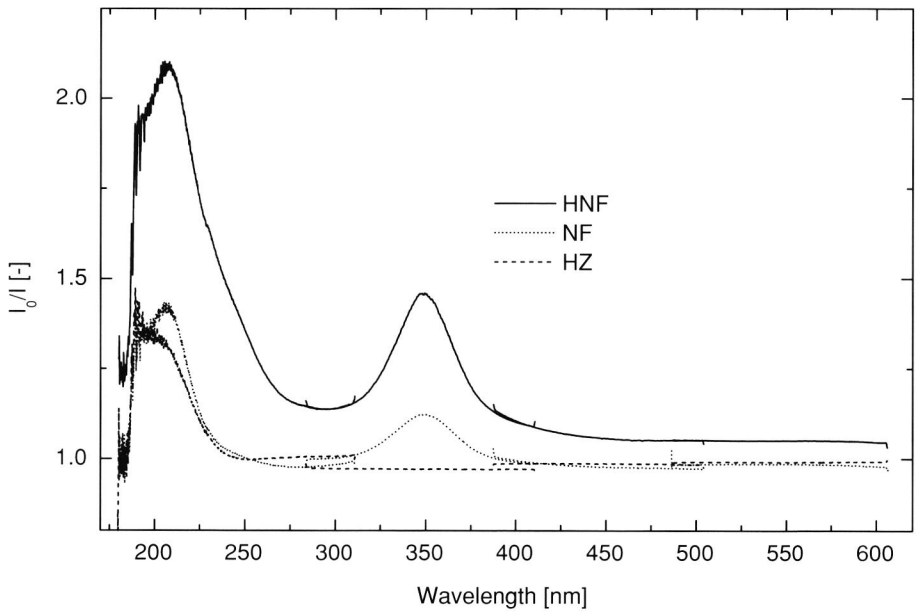

Figure 2.5: *UV/Vis absorption spectrum of HNF, hydrazine (HZ) and nitroform (NF) dissolved in water [65].*

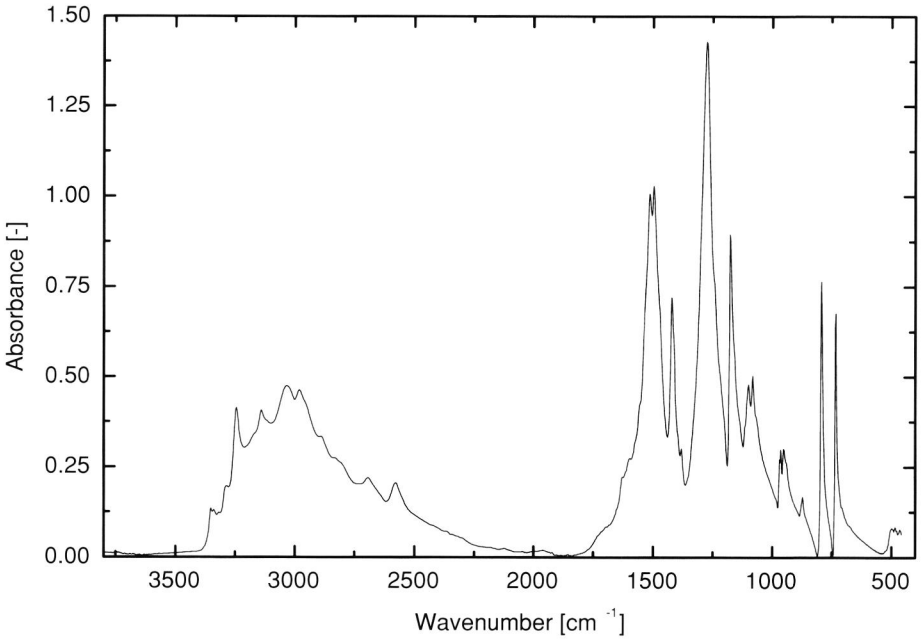

Figure 2.6: *IR absorption spectrum of HNF.*

2.3 Decomposition

In this section the decomposition of HNF is addressed. In section 2.3.1 the findings of other workers are summarized. The work described in section 2.3.2 was carried out during a visit to the Naval Air Warfare Center (NAWC) China Lake, in cooperation with T.P. Parr and D.M. Hanson-Parr. For this study HNF was obtained from the Air Force Philips Laboratory. This section ends with a proposed decomposition mechanism for HNF, based on the experimental findings.

HNF's stability, reactivity and curing were summarized by Van der Heijden [58]. Within the GSTP-2 program a large effort was undertaken to determine the process behind the thermal decomposition of HNF at storage temperatures (below $\sim$ 100°C). This work led to more insight of the decomposition mechanism of HNF [169]. Due to the restricted character of this work, these results are not published in this thesis.

2.3.1 Previous work

Differential scanning calorimetry (DSC) experiments of HNF first show a melting stage, starting at 130°C, followed by an exothermic peak at around 135°C, see Fig. 2.7. Compared to ADN the maximum heat flow at the exotherm is about an order of magnitude larger [170]. Because the melting and decomposition merge, it is impossible to accurately determine the melting heat from this type of experiments.

Koroban et al. studied the decomposition of HNF in the temperature range of 70 to 100°C [74]. In the first part of the decomposition, formation of ammonium nitroformate, (ANF, $NH_4C(NO_2)_3$), H_2O, N_2O and N_2 was observed. In this stage of the decomposition no CO_2 formation was observed. The amount of CO_2 was found to increase with increasing HNF conversion. Two competing decomposition reactions were identified: First the spontaneous cleavage of nitro groups in the nitroform anion. These reactions have a very high activation energy, $E_a \sim 167$ kJ/mole. The other reaction is that between nitroform and hydrazine.

To simulate the decomposition behavior of HNF under combustion-like conditions, temperature-jump (T-jump) experiments were carried out by Williams and Brill [163]. In these experiments a small sample is rapidly heated on a platinum heating ribbon. Species detection was carried out by a Fourier Transform Infra-Red (FT-IR) apparatus. It was verified that the heating ribbon did not catalyze the HNF decomposition, and that the amount of N_2H_4 formed was not changed when a silver heating filament was used. The time to the first exothermic reactions is dependent on the heating rate. This time-to-exotherm can be used to determine the activation energy.

The T-jump studies show a strong dependence of temperature on the species formed during decomposition. It was found that decomposition can roughly be divided into three temperature regions:

1. *Decomposition below* 123° *C:*
   Below the melting temperature of HNF, only preheating, and very slow decomposition occurs.

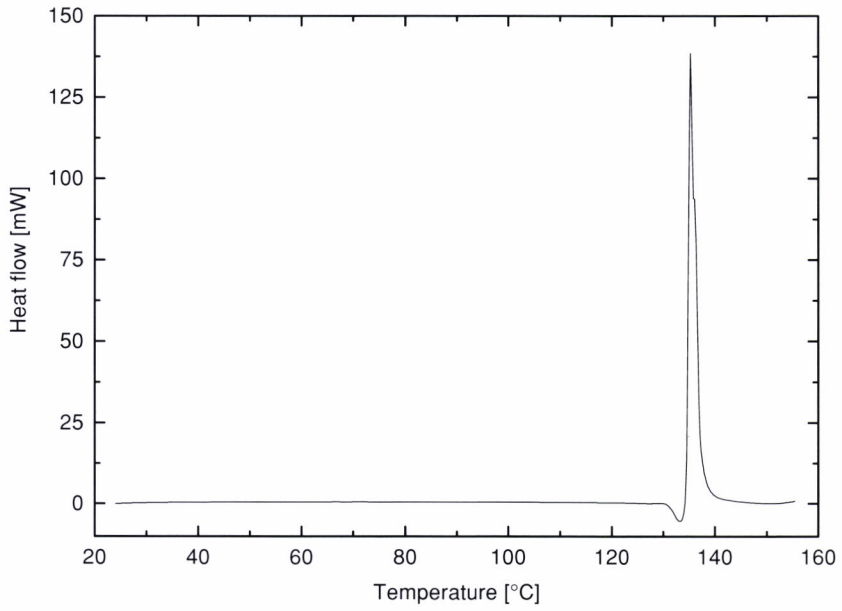

Figure 2.7: *DSC plot of HNF E-8 (heating rate 10°C/min, sample mass 2.727 mg).*

2. *Decomposition at* $123 \ldots 260°C$*:*
Ammonium nitroformate aerosol, $HC(NO_2)_3$, N_2H_4, N_2O, H_2O, and CO were detected in the gaseous phase. HNF aerosol was not detected, so the evaporation of HNF followed by decomposition in the gas phase was found to be negligible. The following reaction scheme was proposed:

$$2\,HNF_{(s)} \longrightarrow 2\,ANF + N_2 + H_2 + 126\,kJ/mole\,, \tag{2.4}$$

$$HNF_{(l)} \longrightarrow HC(NO_2)_{3\,(g)} + N_2H_4 - 37\,kJ/mole\,, \tag{2.5}$$

$$2\,ANF_{(l)} \longrightarrow N_2O + 2\,CO + 4\,H_2O + 5/2\,O_2 + 3\,N_2 + 360\,kJ/mole\,. \tag{2.6}$$

Taken together, the reactions above yield 305 kJ/(mole of HNF).

3. *Decomposition above* $260°C$*:*
Above 260°C, the formation of CO_2 is observed for the first time. The amount of CO_2 increases with increasing temperature, hence the exothermicity increases with temperature. Above 350°C, the amounts of ANF, N_2O, and CO reduce. At 400°C the reaction can be described by

$$HNF \longrightarrow 2\,NO + CO_2 + 2\,H_2O + 3/2\,N_2 + 1/2H_2 + 623\,kJ/mole\,. \tag{2.7}$$

This reaction is the most strongly exothermic of all reactions above. The products of this reaction are not in thermodynamic equilibrium concentrations that exist at

the theoretical adiabatic flame temperature. Further reaction at higher temperature is expected.

The time-to-exotherm during a T-jump experiment, can be related to the melt layer decomposition activation energy, E_m. It was found that $E_m = 105\,\mathrm{kJ/mole}$. This value should be compared with the activation energy of condensed phase decomposition $E_c = 167\,\mathrm{kJ/mole}$ found by Koroban et al. [74]. The trend $E_c > E_m$ is also found for other energetic materials, such as HMX and RDX [163].

The above reaction pathways are different from those proposed by Von Elbe et al. [42]. By simple analytical techniques, they determined that NO_2 was released during HNF monopropellant combustion. This NO_2 reacts with the hydrazine component of HNF, liberating nitroform, according to

$$2\,NO_2 + N_2H_4{\cdot}HC(NO_2)_3 \longrightarrow N_2O + NH_4NO_3 + HC(NO_2)_3\,. \tag{2.8}$$

Because the free nitroform is unstable well below 120°C, this reaction is immediately followed by

$$HC(NO_2)_3 \longrightarrow x\,NO_2 + \text{intermediate products}\,. \tag{2.9}$$

where x is presumably > 1, but cannot exceed 3. It was concluded that at elevated temperatures, confinement of HNF in a closed container constitutes a severe explosion hazard, because a run-away increase of the NO_2 concentration, terminating in an explosion may be expected. Effective venting of the container to remove trace amounts of NO_2 would mitigate this hazard.

The difference between the results of Williams and Von Elbe is remarkable. During combustion Von Elbe found that NO_2 plays an important role, whereas Williams found no evidence of NO_2 in T-jump experiments at combustion-like temperatures and temperature gradients. These differences may be explained by the fact that NO_2 is very unstable and might not be detected above the platinum filament, because it is already reduced to NO by e.g. the released hydrazine.

As a side note, the acid:base relation between nitroform and hydrazine suggests that ions may play a role in the chemical decomposition of the material. It was found by Von Elbe et al., that the chemical reaction zone is electrically conductive and hence contains mobile ions [42]. The total number of mobile ions that form a conductive path between the electrodes is essentially independent of the thickness of the foam zone, i.e. the pressure.

2.3.2 Experimental study of the decomposition of HNF

Except for the T-jump experiments, the experimental work of the previous section focuses on the longterm stability of HNF. To simulate more combustion-like conditions, the decomposition of HNF has been studied in "hot cell" and "hot plate" experiments [102]. In the hot-cell experiments the HNF is heated in a quartz cell. The cell is submerged in a heated aluminum block. By passing a beam of light through holes in the block it is possible to measure the UV-absorption. The hot cell experiments were carried out with either a preheated or a slowly heated cell. In the decomposition experiments, small amounts of HNF (about 50 mg) were dropped into the cell or onto the plate.

The setup for the absorption experiments is sketched in Fig. 2.8. A 150 W UV-enhanced Xe-arc lamp (Oriel) generates ultra-violet and visible light (Xe). The light is focused above

the plate or in the hot cell by lenses L3 and L4. The beam passes through the decomposition gasses, and is then focused onto the slit of spectrometer S (Spex 1681-C) (through lenses L1 and L2) The dispersed spectrum is measured by an optical multi-channel analyzer O (OMA, Princeton Appl. Res. 1461 with 1420-UV detector). The absorption spectrum $A(\lambda)$, is determined from the measured reference spectrum (just before the experiment) $I_0(\lambda)$, and the spectrum measured during combustion $I(\lambda)$, according to

$$A(\lambda) = \log\left(\frac{I_0(\lambda)}{I(\lambda)}\right) . \tag{2.10}$$

Characteristic dips in $A(\lambda)$ are associated with absorption by specific species at wavelength λ. The results from earlier work, suggest the formation of NO, NO_2, N_2O, CO, CO_2, H_2O, hydrazine, nitroform, ANF. Not all of these species have characteristic absorption spectra in the UV/Vis range, e.g. CO, CO_2 and H_2O.

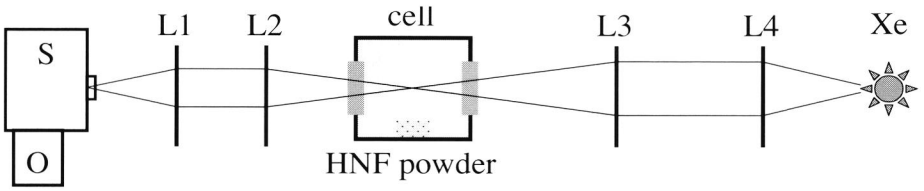

Figure 2.8: *Schematic of the setup used for the absorption experiments.*

In all the decomposition experiments a distinct absorption peak at 280 nm is visible, see Fig. 2.9. This peak is probably associated with an NO_2 or aldehyde group formed during decomposition. This peak was observed at temperatures as low as 110°C, after HNF was heated for up to an hour without melting. At higher temperatures, it appears to be an initial product, since it disappears after the HNF has been consumed (in the closed cell).

Absorption due to the presence of hydrazine could not be demonstrated. This may be explained by the fact that large absorption peaks from other products are present in the hydrazine peak region (230-240 nm) that possibly drown small hydrazine absorption peaks. Ammonium nitrate has an absorption peak around 300 nm. No peak was detected in this region. As the absorption coefficient of ammonium nitrate (AN) is very small, this does not imply that no AN is present.

Around 200 nm N_2O is identified. Figure 2.10 shows a comparison between absorption of hot N_2O and HNF in a 130°C cell. Below 200 nm the oxygen from the atmosphere absorbs strongly, which makes it impossible to perform measurements below 200 nm.

It was found that HONO is formed starting at temperatures as low as 160°C. HONO appears to be a "first" gaseous product. NO_2 seems to be a product of the HONO decomposition (see Fig. 2.11). During the test first the HONO shows up, then the NO_2 starts to appear and grows with time. Another explanation is that the NO_2 is formed from further HNF decomposition. Absorption was measured at two different positions in the cell. At the bottom (close to the HNF), the HONO was prominent. In the top of the cell, 45 mm above the HNF, the HONO signal is weak. This indicates that HONO has almost decomposed completely after 45 mm. NO is not a "first" gaseous product. It is only detected if a particle ignited (Fig. 2.12), whereas HONO formed without ignition.

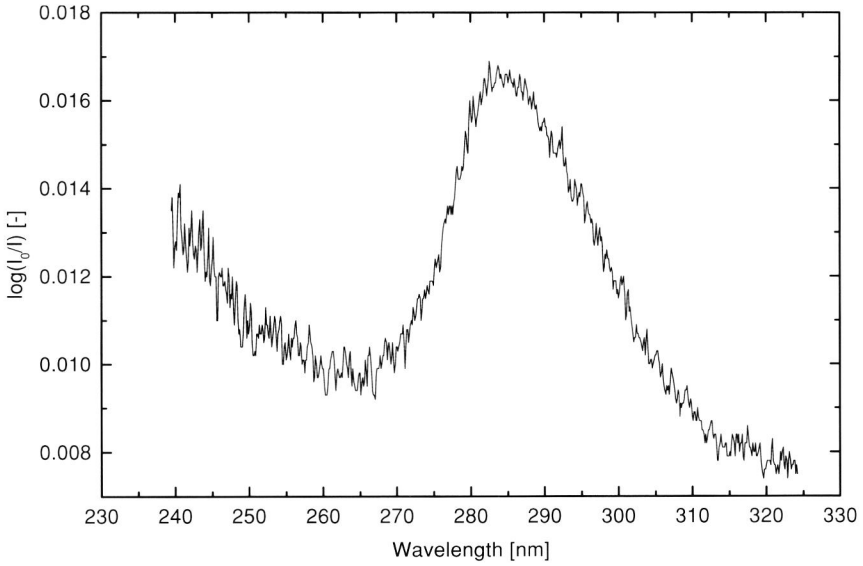

Figure 2.9: *Typical absorption peak around 280 nm measured during the decomposition experiments.*

Yellow condensate was formed on the sapphire windows of the window bomb during combustion experiments at low pressure and is also observed before ignition of the sample. Some of this condensate was washed off with distilled water for further analysis. The absorption spectrum of this solution was measured, and compared with that of a solution of HNF in water. The absorption spectra were found to be similar (ratio of the 350 nm peak to the one around 228 nm is the same), see Fig. 2.13. This indicates that (part of) the HNF vaporizes, or leaves the surface as particulates. This is a different result than that obtained by Williams and Brill, who did not observe HNF in the gas phase [10]. The 350 nm peak was only observed in the hot cell tests, not in the hot plate experiments.

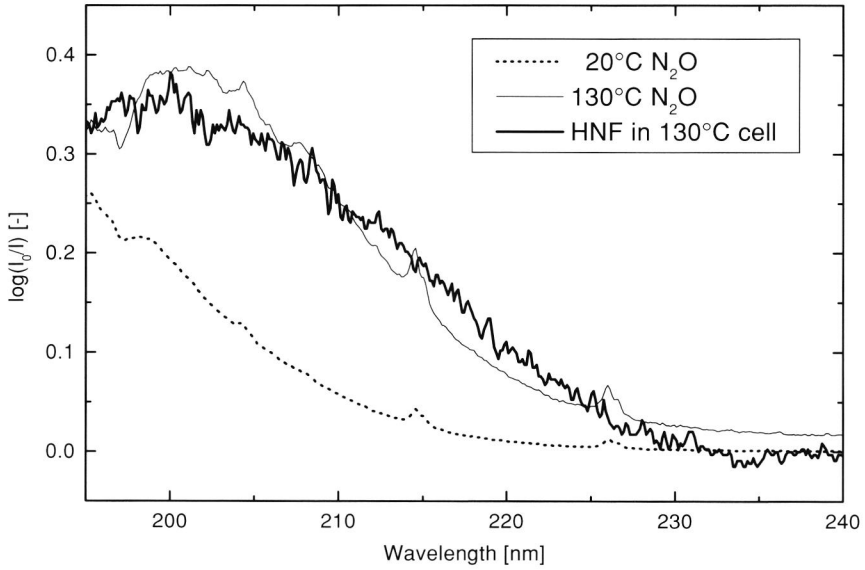

Figure 2.10: *Comparison between N_2O at room temperature and at 130°C and 130°C HNF decomposition gases. The tail of N_2O extends towards higher wavelengths, with higher temperatures.*

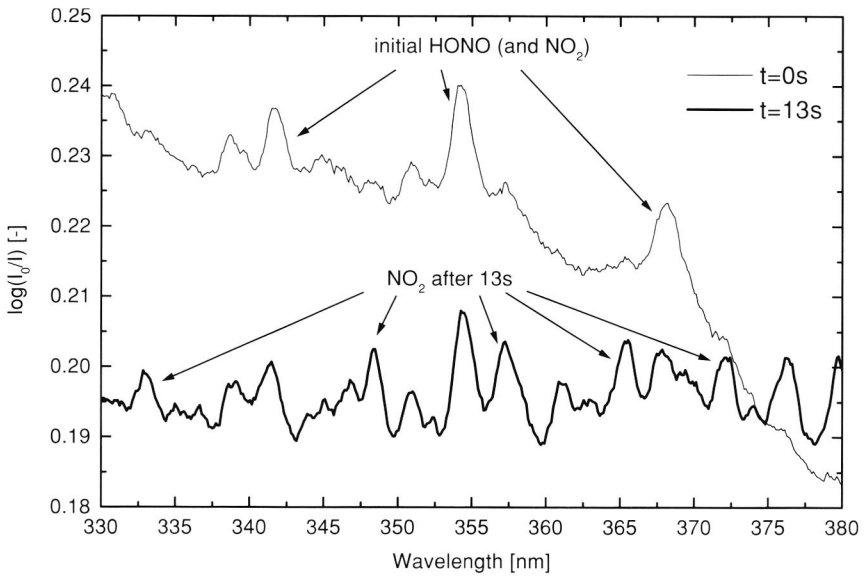

Figure 2.11: *Absorption spectrum of HNF dropped into the hot cell at 248°C (beam height 12 mm above the surface).*

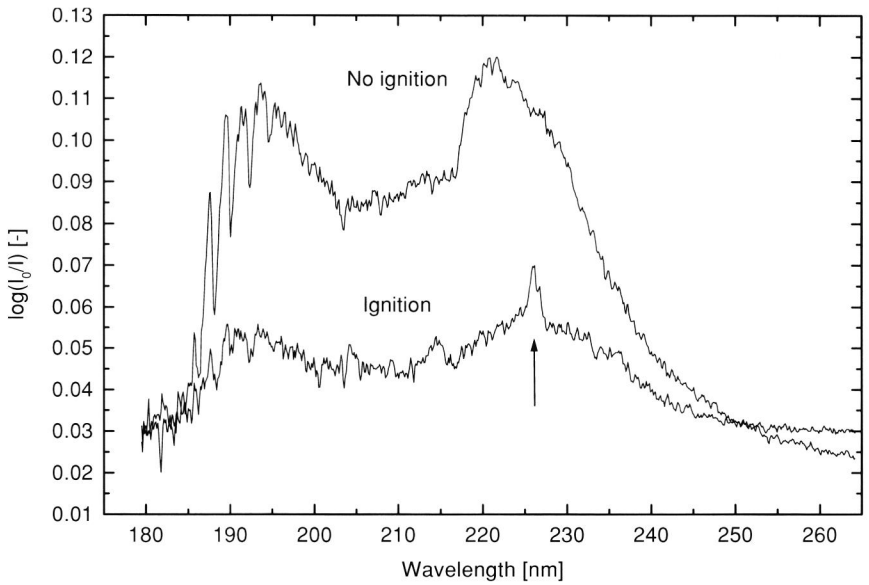

Figure 2.12: *Absorption spectra of HNF dropped onto a hot plate at 291°C. NO peaks are only observed in case of ignition.*

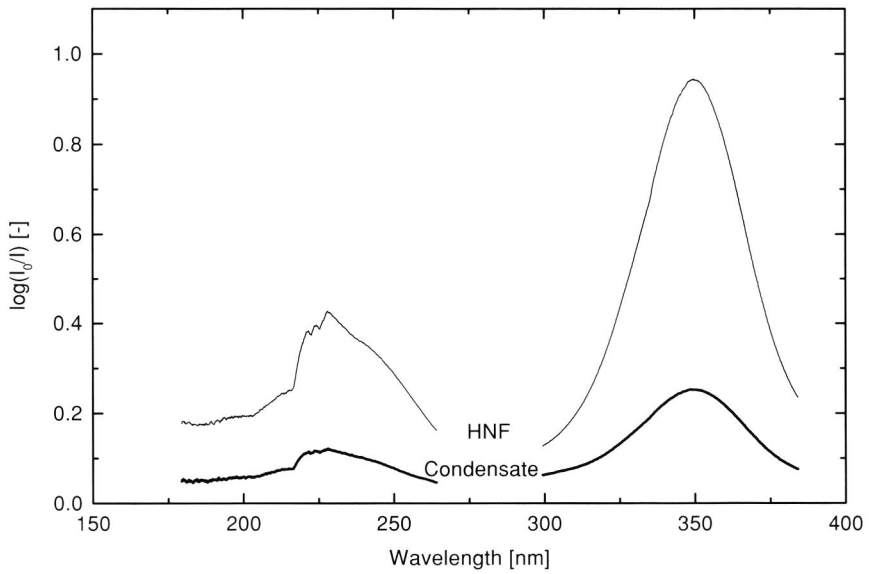

Figure 2.13: *Comparison of absorption spectra of HNF dissolved in water, and window condensate dissolved in water.*

2.3.3 HNF decomposition mechanism

The decomposition experiments that were presented in the previous section may be used to determine the most probable step for initial HNF decomposition. This is important information, e.g. for stabilization of HNF decomposition, but also for combustion modeling.

It was observed by Williams and Brill, that hydrazine (N_2H_4) is formed during HNF decomposition [10]. However, because of its reactivity, it was only detected at the onset of decomposition. Hydrazine is rapidly expended by exothermic decomposition (above 811 K), or by reaction with NO_2 [132]. It was discussed in the previous section that already at low temperatures HONO and N_2O were detected. NO_2 was only formed after HONO detection.

The mechanism presented in Fig. 2.14 is proposed for the decomposition of HNF. The initial step for HNF is assumed to be a hydrogen subtraction (intramolecular hydrogen atom transfer) from the hydrazine moiety.

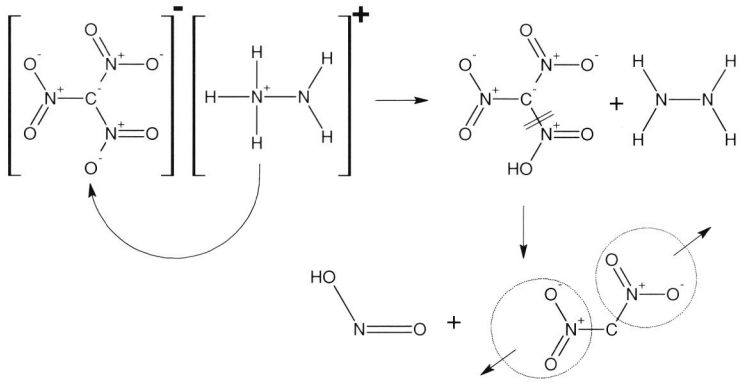

Figure 2.14: *Proton transfer decomposition of HNF. After the proton transfer N_2H_4 and HONO are released. Further decomposition might occur according to the steps shown.*

Several observations support this mechanism:

- In aromatic nitro compounds (e.g. nitrobenzene) a similar mechanism was also found to be the first step [115]. More recently similar mechanisms were also found in shock-initiation of nitroarenes [30]. The importance of intramolecular transfer of hydrogen in nitramine decomposition was also suggested by Ermolin and Zarko [44].

- Rate determining C-NO_2 homolysis is known in the gas phase of nitroaromatic compounds, but it has never been observed in condensed phase experiments [30]. N-NO_2 bond scission is known to be an important step for nitramine combustion [44]. However, the C-NO_2 bond is stronger than the N-NO_2 bond, which makes direct C-NO_2 bond scission unlikely. Also during the decomposition of nitroalkenes HONO has been observed. Unimolecular or bimolecular hydrogen transfer mechanisms were identified to yield this HONO [151].

- Semi-empirical molecular orbital calculations using the MOPAC program have been carried out (see section 2.4). These calculations show that the activation energy for the H-transfer from the hydrazine has an activation energy of 84 kJ/mole. This value is in excellent agreement with the value of 75-86kJ/mole, which was needed to obtain good agreement between experimental and modeling results [96, 99]. H-transfer to the C-atom of the nitroform was found to have an activation energy of 98 kJ/mole. The scission of a C-NO_2 bond in HNF was calculated to have an activation energy of 283 kJ/mole. So, at low to moderate temperatures, the H-transfer to the NO_2 groups seems most likely to occur.

Subsequent decomposition can then proceed by removal of the HONO, yielding a very reactive dinitrocarbene (DNC) $:C(NO_2)_2$. The formation of DNC during decomposition of nitroform salts has been reported in literature [26]. DNC reacts vigorously with many compounds. Another option is further decomposition to NO_2 and $N_2O + CO_2$, as suggested in Fig. 2.14.

2.4 Quantum chemical calculations

Molecular mechanics and quantum chemical calculations are more and more being employed to obtain information about e.g. molecular equilibrium geometries and transition states. With the current computing power, quantum chemical calculations can be carried out in reasonable amounts of time. Experimental data of the properties and decomposition mechanisms of energetic materials is very difficult to obtain. In this case, quantum chemical calculations are a helpful tool. Modeling approaches have been optimized for energetic material properties and decomposition evaluation, see e.g. Ref. [111].

The least costly methods are the so-called semi-empirical molecular orbital methods. Semi-empirical methods greatly simplify the calculations by dealing with the valence electrons only. It is further assumed that atomic orbitals residing on different atomic centers do not overlap. Semi-empirical parameterizations are based on reproducing a wide variety of experimental data (heat of formation, equilibrium geometry, dipole moments etc). Of the semi-empirical methods, the PM3-parameterization was found to give the best results for nitro compounds [2]. For the determination of equilibrium geometries, the semi-empirical methods are quite successful. However, for the evaluation of thermochemical and kinetic properties ab-initio calculations are favored.

For HNF both semi-empirical and ab-initio calculations have been carried out. Goal of this work is to determine the molecular structure, determine unknown thermophysical properties, and to evaluate some hypothetical decomposition mechanisms. In all the calculations an isolated HNF molecule is considered. The interaction between HNF-molecules is neglected.

2.4.1 Semi-empirical calculations

For the semi-empirical calculations the MOPAC computer program was used [144]. Geometry optimization with the PM3 hamiltonian resulted in the structure as shown in Fig. 2.15. The calculations show that in the nitroform ion two NO_2-groups are in an almost flat surface. The third NO_2-group is staggered. Hydrogen bonds are indicated by the

dashed lines. The calculated heat of formation is $\Delta H^0_{f(g)} = -57$ kJ/mole. The difference between the gas phase heat of formation, and the condensed phase heat of formation is the sublimation energy. Using the literature value $\Delta H^0_{f(c)} = -72$ kJ/mole, it is found that $H_{subl} = 15$ kJ/mole. This value is about 6× smaller as the value derived from vapor pressure data (Eq.(2.3)). This large difference indicates that high order interaction is considerable or that the semi-empirical approach is not very well suited for this kind of molecules. Configuration interaction corrections did not change the values significantly. Whenever differences are used in stead of absolute energy levels, effects tend to cancel, and semi-empirical methods can still be very useful.

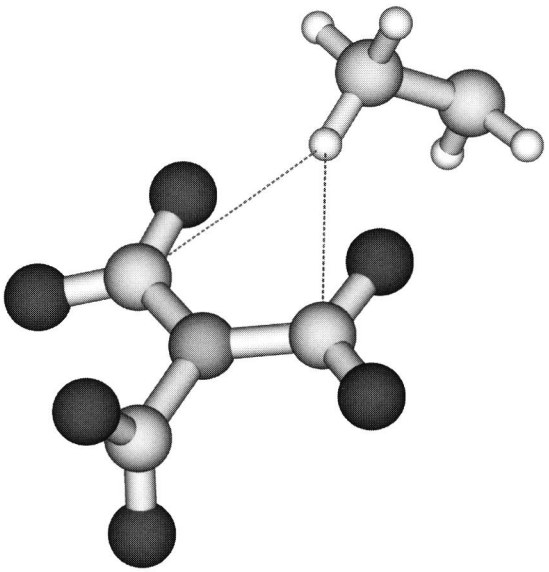

Figure 2.15: *Hydrazinium nitroformate ($N_2H_5C(NO_2)_3$) geometry optimized with PM3 Hamiltonian.*

Also the decomposition of HNF has been studied using semi-empirical calculations. Three different mechanisms have been considered here:

1. C-NO_2 homolysis: rupture of one of the C-NO_2 bonds,
2. H-transfer from hydrazine to the C-atom of nitroform,
3. H-transfer from hydrazine to one of the NO_2-groups.

Each of these decomposition mechanisms was evaluated by calculating the transition state (TS) of each decomposition step with the PM3 hamiltonian. The transition state is the point with the highest energy during the decomposition step. For the above mechanisms the heats of formation of the transition states were found to be respectively: 225 kJ/mole, 40 kJ/mole and 28 kJ/mole. The energy barrier is the lowest for the hydrogen transfer from the hydrazine ion, to one of the NO_2-groups of the nitroform. This transition state

is shown in Fig. 2.16. The hydrogen transfer to the C-atom is hindered by the NO_2-groups. Therefore this step has a higher energy than the hydrogen transfer to one of the NO_2-groups.

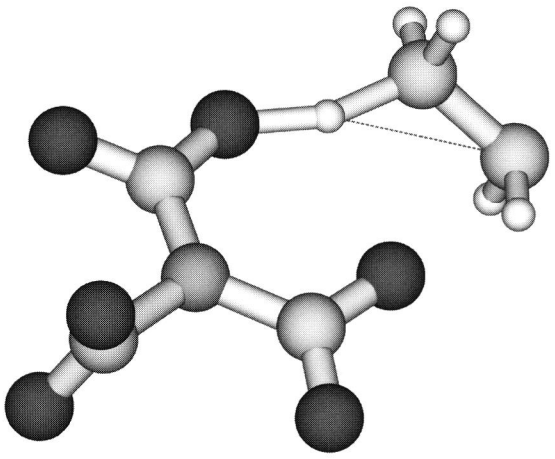

Figure 2.16: *Transition stage of hydrogen transfer from hydrazine to NO_2-group.*

For the PM3 hamiltonian the energy levels of the several stages of the decomposition according to Fig. 2.14 have been calculated. Figure 2.17 shows the energy diagram. The first decomposition step to form aci-nitroform and hydrazine seems reasonable, and has a total barrier of 84 kJ/mole. This value should be compared with the value found by of Williams and Brill (see page 17) for melted HNF $E_a = 105$ kJ/mole, and that of Koroban for solid HNF $E_a = 167$ kJ/mole. The lower activation energy for the melted material can be explained by the fact that in case of melted material the HNF molecules are not aligned in the crystal lattice anymore. When HNF is fixed in the lattice, a proton transfer from the positive hydrazine is hindered by a neighboring negatively charged nitroform group. In case of melted material the barrier is less, because there is no real alignment of molecules anymore. When the HNF is in the gas phase, as assumed by the PM3 calculations, no barrier is present. This then yields the lowest activation energy. The fact that the molecule alignment is important is also seen from the fact that the HNF material decomposes as soon as it melts.

The next transition stage (C-HONO homolysis) has a very high energy level, with a total activation energy of 364 kJ/mole. This is not very likely to occur at low temperatures. At storage temperatures further reaction of aci-nitroform with e.g. the released hydrazine is a more probable scenario. The aci-nitroform reaction with hydrazine may progress rapidly yielding species that were found experimentally such as N_2O, NO and H_2O [65, 163].

2.4.2 Ab initio calculations

The ab initio calculations were performed with the 6-31G basis set, using the PC version of the GAMESS program [41]. This basis set was the most extended set that yielded converged results within acceptable computational time (less than 50 hours). Figure 2.18

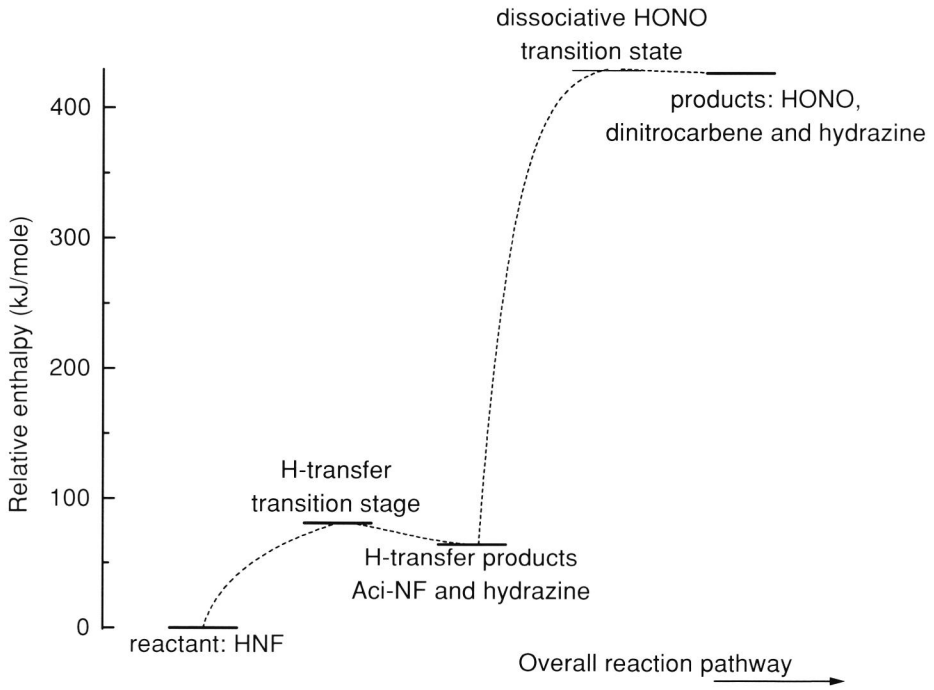

Figure 2.17: *Reaction pathway for decomposition of HNF (semi-empirical PM3 calculations).*

shows the calculated equilibrium structure of HNF. Compared to the semi-empirical results the hydrazinium ion is now more closely directed to one of the NO_2-groups, rather then being shared among two groups. These calculations also show that the third NO_2-group is rotated with respect to the other two groups.

2.5 Conclusions

The decomposition of HNF was studied by UV and visible absorption measurements. HONO is a first gaseous product. The HONO is followed by the formation of NO_2. N_2O is also identified in the decomposition products. NO was only detected if the HNF ignited. An intermolecular hydrogen atom transfer from the hydrazine ion to an NO_2-group of nitroform is proposed to describe the initial HNF decomposition.

Quantum chemical calculations confirm that the hydrogen transfer has the lowest energy barrier. The calculated activation energy is 84 kJ/mole. The calculations show that the formed aci-nitroform and hydrazine probably react, rather than further decomposition of the aci-nitroform into HONO and dinitrocarbene.

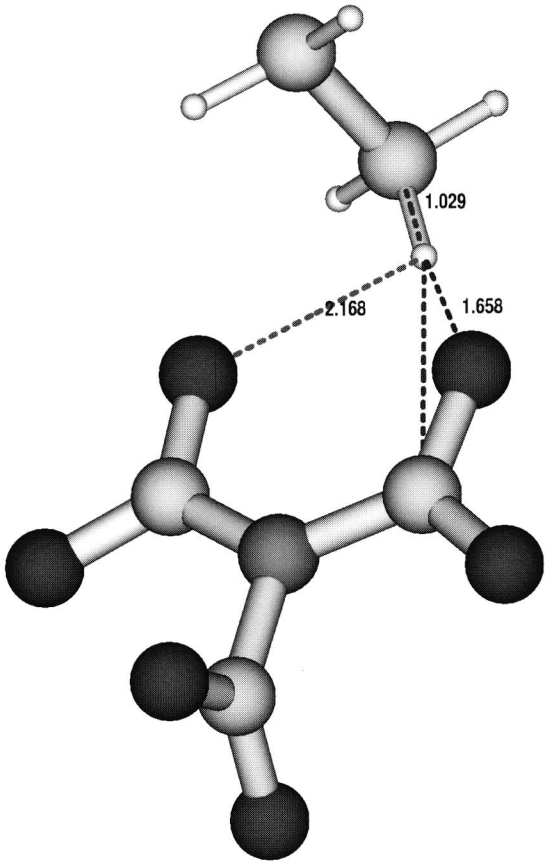

Figure 2.18: *HNF structure optimized at 6-31G level (distances in angstrom).*

Chapter 3

Experimental approach

3.1 Introduction

From an experimental point of view, the combustion of solid rocket propellants usually takes place in a difficult environment. Solid particles in the gas phase, large amounts of chemiluminescence from the flames, high temperatures and high pressures prevent the use of simple methods often employed for rather neat laboratory flames. Not only the gas phase differs from the situations normally encountered, the processes in the condensed phase are also very different from e.g. the combustion of a normal solid material, like coal. The condensed phase is heated by the gas phase and condensed phase reactions under unusual high heating rates, up to 10^6 K/s. It is well known that the decomposition of materials is largely affected by the heating rates. So, the use of common (low heating rate) apparatus for decomposition studies is questionable. Because of the presence of energetic materials and oxidizing species in the condensed phase, subsurface reactions may occur, which affect the combustion behavior of the propellant.

Because of all these difficulties, the experimental techniques that have been employed are very specific techniques to study the combustion of energetic materials. This Chapter describes the experimental techniques used in this study. The Chapter starts with a description of the preparation of the pressed samples (section 3.2) and sandwiches and propellants (section 3.3). Laser-induced fluorescence is used for visualization of radical concentrations, and is discussed in section 3.4.1. Absorption of light can be used to determine absolute species concentrations, and temperature. This technique is discussed in section 3.4.2. Temperatures in the combustion wave are measured with micro-thermocouples. This technique is discussed in section 3.4.3. The experimental setup is addressed in section 3.5. The PML strand burner is briefly described in section 3.6.

3.2 Pressed samples

For the study of neat HNF combustion, HNF is pressed under high pressure to form consolidated pellets. This method allows quick manufacturing of samples with a high density. Also additives can be mixed with the HNF powder to study the effects of additives on the combustion of HNF. This section describes the process of making pressed samples, and also addresses the properties of the formed samples.

Pressing of neat HNF

Experiments with HNF in China Lake (NAWC) have shown that pressing of neat HNF pellets can be done safely [46, 123]. The pressure employed at NAWC is 40-60 kPsi (276-414 MPa). Because HNF presses relatively easy (soft material), most pellets are pressed at 40 kPsi. Theoretical maximum density, TMD, of these pressed samples is 93-96%.

For our experiments, the majority of the pellets that are used have a diameter of 6 mm. These samples are pressed with the die-press shown in Fig. 3.1. Up to 6 mm diameter a 5 kN hydraulic press is used. Larger pellets (e.g. 9 and 12 mm diameter) are pressed on a 100 kN press.

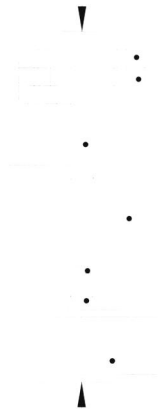

Figure 3.1: *Press for pressing pellets.*

For most samples fine HNF (S-grade) is used as starting material. It is expected that the cracking of small particles generates the lowest amount of heat, and forms the most homogenous samples. With the existing 5 kN press available at TNO/PML a pressure of 174 MPa can be obtained for the 6 mm samples. The pressure is held at its maximum for 10 seconds. Then it is reduced gently.

To verify how the TMD varies with pressing pressures pellets were pressed at different pressure, see Fig. 3.2. The TMD at 236 MPa has been obtained by pressing with the 100 kN press and 9 mm samples. HNF can be pressed very nicely. The result is a smooth sample with a shiny surface (Fig. 3.3).

Structure of the pressed pellets

With the bare eye the pressed pellets seem to have a very uniform structure. However under an ordinary light-microscope the individual crystals can still be identified. As the crystals have a random orientation during pressing, the crystal orientation in the pellet is random. This intensifies the color differences between the original crystals, due to the crystal axis dependent index of refraction. Figure 3.4 shows the fracture of a pellet, as obtained with a light-microscope with diffuse lighting (original: 128× enlargement). Note that it is very difficult to capture the visual image on a camera.

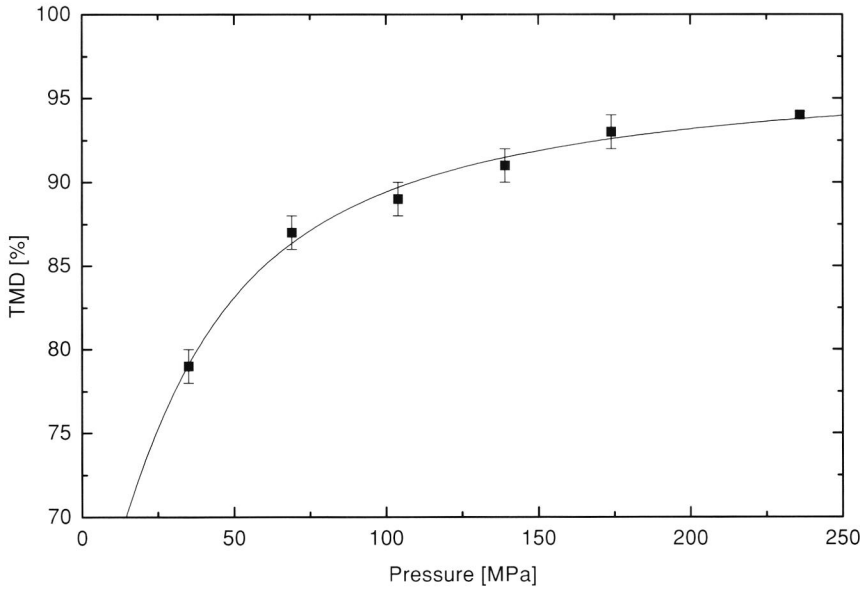

Figure 3.2: *Neat HNF TMD as function of applied pressing pressure.*

When studied through an electron-microscope the image is very different. The electron-microscope image is not sensitive to the index of refraction, and shows a very smooth structure, see Fig. 3.5. The individual crystals (app. 100 μm) are not observed anymore, and the pellet looks like a single crystal (with small voids). It should be noted that HNF's tendency to evaporate under the vacuum applied in the electron-microscope makes it important to quickly obtain the desired images, before the HNF starts to evaporate.

Vacuum pressing

The results from Fig. 3.2 suggest that very high pressing pressures are needed to obtain

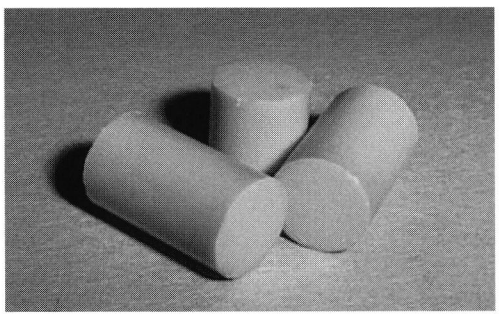

Figure 3.3: *Pressed HNF samples (9 mm diameter).*

Figure 3.4: *Fracture of a HNF pellet (light-microscope, diffuse lighting).*

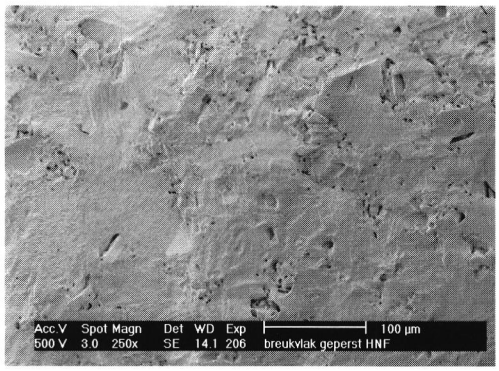

Figure 3.5: *Fracture of a HNF pellet (electron-microscope).*

a TMD close to 100%. However, the maximum pressure is limited by the structural strength of the press. The tempered steels used for the press dies allow up to about 400 MPa. In an attempt to obtain densities closer to the theoretical maximum density, some samples have been pressed under vacuum conditions. By pressing in vacuum there is no air trapped inside the press. This trapped air was speculated to cause the voids as seen in Fig. 3.5.

The available press setup does not allow to press under vacuum conditions. Therefore a small plastic bag is placed around the pellet press. This bag is attached to a hose connected to a vacuum pump. First the pump evacuates the bag. During this pumping action the upper die is already softly pressed into the cylinder, because of the shrinking bag. Then the actual pressing takes place. Some samples with a diameter of 12.3 mm. were pressed at 168 MPa (20 kN). Table 3.1 summarizes the densities of the pellets.

From Table 3.1 it becomes clear that the samples pressed under vacuum do not have a higher density, than the ones pressed under atmospheric pressure. As a matter of fact, the vacuum pressed samples have a lower density then the atmospheric pressed pellets. This is probably caused by the variation in the pressing force, rather than an effect of the vacuum. It is seen that the pellet-to-pellet density variation is larger then the density accuracy.

The vacuum pressed pellets have not been studied with the electron-microscope. It is expected that similar voids are present in both type of pellets. The small voids present in

Condition	Pellet nr.	Density [g/cm^3]
Atmospheric	1	1.745 ± 0.002
	2	1.733 ± 0.002
Vacuum	1	1.730 ± 0.002
	2	1.719 ± 0.002

Table 3.1: *Vacuum vs. atmospheric pressing of pellets.*

between the needle-shaped crystals are thought to be the origin of the voids in the pressed pellets. During pressing only the touching crystal surfaces melt and crack, and form a very strong structure. This structure is locally stronger then the applied pressure, and prevents the voids from collapsing (like the arches of a bridge).

Hazard properties of pressed pellets

The microscopic images of the pellets indicate that the original needle-shaped structure of the powder is altered by the pressing action. In the pressed pellets the crystals are melted together, generating one large amorphous "crystal". To verify whether the hazard characteristics of HNF pellets are essentially different from HNF powder, the friction and impact sensitivity of the pellets have been determined. These two tests are generally accepted to determine the sensitivity of a substance to most common external stimuli (e.g. dropping hardware or mixing in a propellant).

The friction and impact tests are carried out according to a standardized method (UN ST/SG/AC.10/11). According to this method, the sample material is pulverized before testing. However, crushing the pellets may not yield the desired sensitivity parameters of the pellets. Because of this reason two types of material have been evaluated:

- Sanded HNF pellets; some HNF pellets were sanded on #100 sanding paper. This yields very small crystals ($\sim 8 - 10\,\mu$m) which are not needle-shaped anymore, see Fig.'s 3.6 and 3.7. Because of the sanding action very rough surfaces are produced. During sanding no ignition, or tendency to ignite was observed. The hazard testing was carried out exactly according to the standardized method.

- Neat HNF pellets; as pressed. Because of the shape of the samples, these tests are not according the standardized method. For the impact testing, 6 mm diameter, 3 mm tall pellets were used. For the friction tests small HNF disks were pressed, 12.3 mm diameter, and 1 mm thickness, see Fig. 3.8. The disks are placed on the porcelain plate, and the porcelain pin is moved over the disk surface. The disks did not move during the pin-movement, and therefore it was not necessary to make provisions to prevent sample movement.

The results of the hazard assessment tests are summarized in Table 3.2 [5, 78]. It is concluded that the friction sensitivity is hardly changed by the pressing. However the impact sensitivity changes significantly. The pellets show a decreased sensitivity to impact, whereas the sanded pellets are very sensitive to impact. This can be attributed to the amount of energy per unit mass which is absorbed on impact. It is remarkable how small

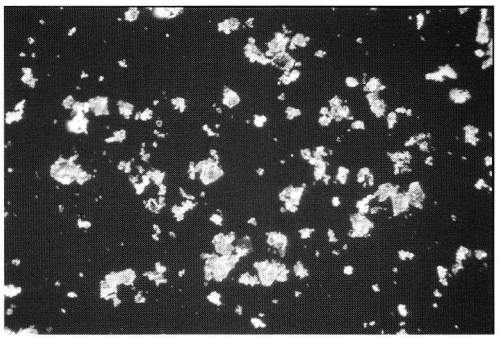

Figure 3.6: *Sanded HNF (light-microscope, diffuse lighting, original image* $100\times$ *enlarged). Typical particle size is* $\sim 8 - 10\mu m$.

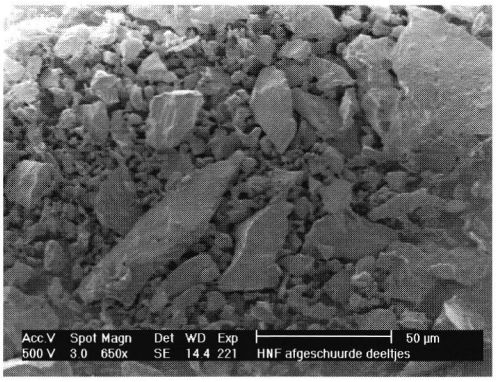

Figure 3.7: *Sanded HNF (electron-microscope).*

the effect of the physical geometry is on the friction sensitivity. This indicates that the friction sensitivity is species determined, rather than geometry determined. It is therefore expected that the friction sensitivity of HNF can not be further decreased by changing the crystal shape. Off course the purity of HNF may still be an important parameter.

Pressing to improve crystal morphology

The microscope images indicate that the HNF is fractured during the pressing action, before the consolidation takes place. This lead to the idea to interrupt the pressing action before a firm pellet is formed [100]. If the pressing is stopped at a pressure of 5-6 MPa loose HNF particles with small L/D are obtained, see Fig. 3.9. The solid loading of propellants with a mixture of pressed S-16 and C12 was improved. The tap density of untreated C-12 is 0.88 g/cm^3, and for S-16 it is 0.65 g/cm^3. For the treated material, an tap density of 1.25 g/cm^3 was obtained for a bimodal mixture with 65-70% C-12. A solid loading of 78% was possible with this bimodal mixture for a HTPB-based propellant (HHU-1).

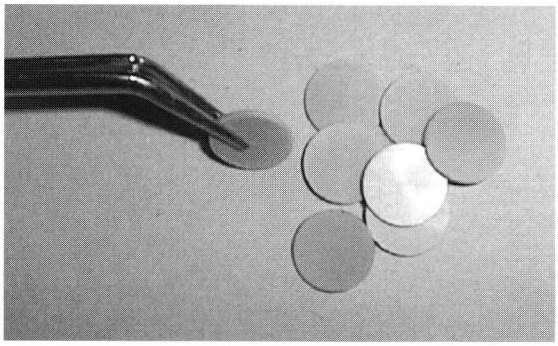

Figure 3.8: *Thin HNF pellets for friction hazard testing, 12.3 mm diameter, 1 mm thickness.*

Material	Friction [N]	Impact [Nm]
HNF S13 powder	16-24	2-4
HNF S13 sanded pellet	20	<1
HNF S13 pellets	16	10

Table 3.2: *Overview of hazard assessment tests.*

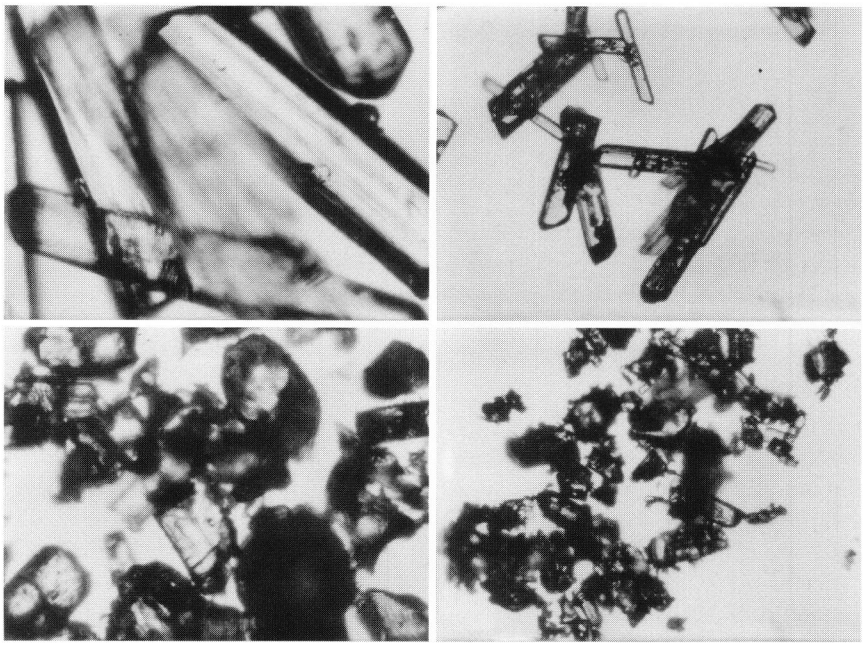

Figure 3.9: *HNF C and S grades before and after pressing to improve morphology. Left: HNF C12, right HNF S16, top: untreated material, bottom: after pressing.*

3.3 Propellant manufacturing

3.3.1 Sandwiches

Sandwiches are stacks of alternating layers of binder and oxidizer. For this work, sandwiches consist of two oxidizer slabs, with a thin layer of binder in between. The sandwich structure is a simplification of the surface region of the oxidizer and binder. Because it is a simple 2D structure, it greatly simplifies the experiments, and allows better determination of binder-oxidizer interaction in the gas phase [127].

Sandwiches were prepared by curing binder slabs between two HNF pellets with a diameter of 6 mm, and a thickness of 2 mm each. Two of these pellets are then glued together with an uncured mixture of binder ingredients. The sandwich thickness is controlled by spacers between the two halves. To prevent movement of the samples the pressed samples are mounted between cardboard slips. Aluminum foil is used as a spacer. Figure 3.10 shows an assembly of cured samples. After curing the spacer material is carefully removed.

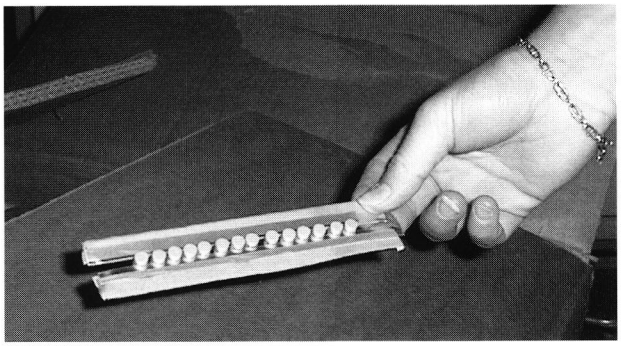

Figure 3.10: *HNF/GAP/HNF sandwiches after curing. Note the aluminum spacer material which determines the binder thickness.*

Initial experiments with a mixture of GAP and an isocyanate showed migration of binder ingredients into the oxidizer pellets. This migration is mediated by the capillaries of the oxidizer samples (see Fig. 3.5). The result was breakdown of the pressed HNF pellets. In the end only a small amount of red liquid material remained. This red material was attributed to the formation of nitrolic acids [74]. The incompatibility of HNF with isocyanates explains this degradation reaction [135]. The problem of migration was solved by adding more curing catalyst to the binder mixture. Sandwiches of good quality were obtained when using a binder mixture with a pot life of less than 20 minutes at room temperature. After curing, two flat sides are sanded to the sandwich at the location of the spacer material. The sandwich is then mounted upright on one of the flat sides. The other flat side (top) is ignited by the CO_2-laser. Figure 3.11 shows an assembled HNF/GAP sandwich (binder about 1 mm width). Two sandwich combinations were selected: one containing a non-energetic binder (HTPB), and the other containing an energetic binder (GAP). All sandwiches were made with a binder slab thickness of 250μm.

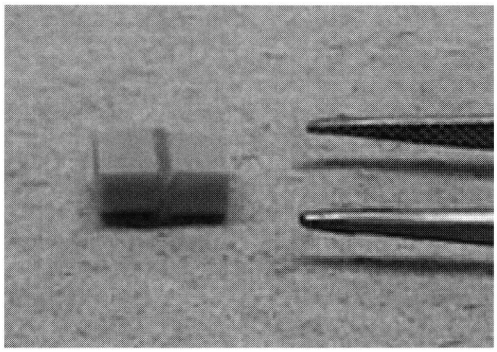

Figure 3.11: *HNF/GAP/HNF sandwich. The sample is ignited on the flat top side. The flat bottom is used for mounting the sample. The flat sides are obtained by sanding the HNF and binder after the sandwich structure has been assembled and cured.*

3.3.2 Propellants

The propellants were prepared in a small mixer in 300 gram batch size (TNO/PE facilities). Mixing took place under vacuum conditions. After mixing, the propellants are poured in a casting mold and cured to a single piece of propellant with dimensions of $30 \times 40 \times 150$ mm^3, Fig. 3.12. The propellant is then cut into strand burner samples ($\sim 7 \times 7 \times 125$ mm^3), and slices of 4 mm thickness. From these slices cylindrical samples with a diameter of 6 mm are made which are used for experiments in DUT setup.

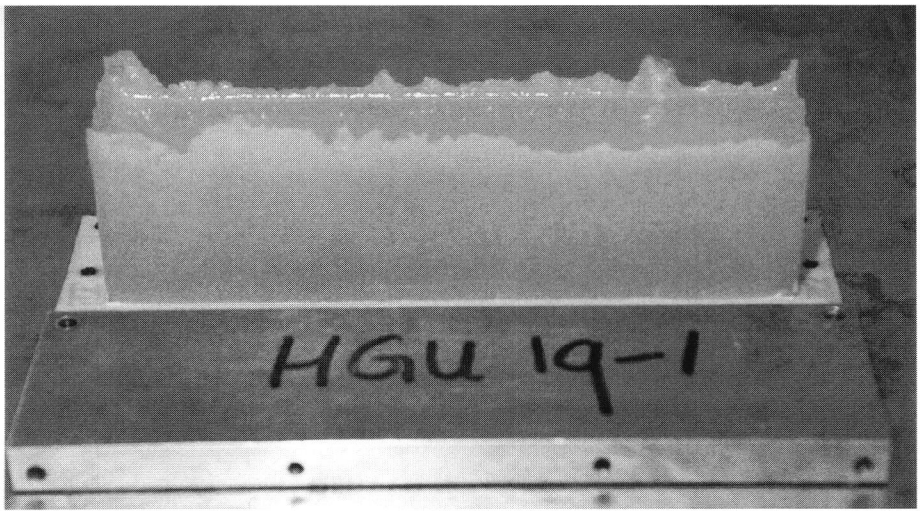

Figure 3.12: *Cast and cured HNF/GAP propellant before cutting into samples.*

3.4 Diagnostic techniques

This section describes experimental techniques that have been used in this work.

3.4.1 Laser induced fluorescence

Laser-induced fluorescence (LIF) is an active optical technique which is often applied to study combustion processes. This technique is based on resonance absorption. When light photons (e.g. from a laser) have the proper wavelengths, they can excite atoms or molecules to excited states. The atom or molecule can lose this excitation energy by re-emission of light as fluorescence. LIF is a powerful technique for the study of solid propellant flames because [122]:

- LIF experiments can be carried out under conditions comparable to those found in a solid rocket motor (pressure, heating rate, etc.).
- It is nonintrusive. No probes in the gas phase are needed, so there is no disturbance of the flow. Although photo-dissociation due to the high laser power may occur, the overall effect on the combustion is small, as the pulse time is very short.
- LIF is temporally and spatially resolved.
- Because both the absorption and emission of light are resonant, LIF diagnostics are species selective via dual choice of laser and detection wavelengths.
- By using pulsed lasers and gated detection, the background flame emission and particle caused black body radiation can largely be reduced.

Lasers used in LIF experiments typically have 5 to 20 ns pulse widths. Although the fluorescent lifetimes can be greater than 50μs, the LIF signal width for measurements is limited to the latter pulse width (or slightly longer), because of quenching. The natural lifetime of the excited species is many orders of magnitude longer than the time between gas-phase collisions. Thus, the sensitivity of LIF experiments is severely compromised by collisional quenching, the nonradiative decay of excited-state energy. As the pressure increases, the collision rates increase, hence the quenching rates increase. At high pressures most excitation energy is lost by quenching and LIF signals become very weak.

Besides quenching, the LIF signal strength may also be reduced by radiation imprisonment. This is the case when the emitted fluorescent signal from the molecules in the center of the flame is reabsorbed by the molecules of the same species in the outer region of the flame, on the way towards the detector.

Consider the two-level system of Fig. 3.13. The rate equation governing the population density of the upper energy level $N_2(t)$ is given by

$$\frac{dN_2(t)}{dt} = N_1(t)\left(B_{12}I_\nu + Q_{12}\right) - N_2(t)\left(B_{21}I_\nu + Q_{21} + A_{21}\right) , \tag{3.1}$$

where $N_1(t)$ is the population density of the lower level, Q_{12} and Q_{21} are collisional coefficients, I_ν is the laser spectral intensity, B_{12} and B_{21} are the Einstein coefficients for stimulated absorption and emission and A_{21} is the rate of spontaneous emission from

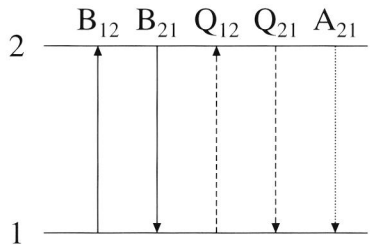

Figure 3.13: *Isolated twolevel system. B represents absorption and stimulated emission, Q quenching and A spontaneous emission (=fluorescence).*

molecules in the upper energy level. This rate equation is found from the general equation for a set of levels [139].

The upper level typically has a negligible population prior to the laser pulse, so the initial condition $N_2(t=0)=0$, is applied to Eq.(3.1). Additionally, there is a conservation constraint on the total population

$$N_1(t) + N_2(t) \;=\; \text{constant} \;=\; N_1^0, \tag{3.2}$$

where N_1^0 is the initial population of N_1. The two laser-coupled energy levels are typically separated by a few electronvolts, and thus collisional excitation (Q_{12}) can be neglected in most combustion environments. From Eq.(3.1) the steady-state fluorescence rate R_p is found to be [146]

$$R_p \;=\; N_2 A_{21} \;=\; N_1^0 B_{12} I_\nu \frac{A_{21}}{A_{21}+Q_{21}} \frac{1}{1+I_\nu/I_\nu^{sat}}\,, \tag{3.3}$$

where the saturation intensity I_ν^{sat} is defined as

$$I_\nu^{sat} \;=\; \frac{Q_{21}+A_{21}}{B_{21}(1+g_1/g_2)}\,, \tag{3.4}$$

where g_1 and g_2 are the degeneracies of the lower and upper level respectively. The degeneracies are introduced in the equation because of the condition of detailed balance for the laser-stimulated rates $g_i B_{ij} = g_j B_{ji}$. For a laser intensity much smaller than the saturation energy ($I_\nu \ll I_\nu^{sat}$), Eq.(3.3) can be simplified to give

$$R_p \;=\; N_2 A_{21} \;=\; N_1^0 B_{12} I_\nu \frac{A_{21}}{A_{21}+Q_{21}}\,. \tag{3.5}$$

This is the so-called linear fluorescence equation, as the fluorescence is linearly proportional to laser intensity. The factor $\frac{A_{21}}{A_{21}+Q_{21}}$ is known as the Stern-Vollmer factor, or fluorescence yield. This equation shows that LIF may be considered to be a measure of the lower-state population, modified by the fluorescence yield. As quenching is sensitive to pressure, temperature and composition, variations in Q_{21} may be difficult to predict in some reacting flows, thereby limiting the quantitative application of LIF for species concentration determination.

If the laser power is sufficiently high, the rates of absorption and stimulated emission become much faster than the quenching and the spontaneous emission rates. For this situation Eq.(3.1) becomes

$$N_1 B_{12} I_\nu = N_2 B_{21} I_\nu \, . \tag{3.6}$$

So the population of the excited state becomes equal (to within degeneracy factors and Einstein coefficients) to that of the ground state. Therefore the fluorescence emission is proportional to the ground state emission, independent of quenching. The technique of saturation of the transition is called laser saturated fluorescence (LSF), and can be applied to overcome the problem of quenching.

One of the drawbacks of the LIF technique is its limited scope. Only a subset of species of interest in propellant combustion will show fluorescence in the wavelength range accessible by current laser systems. Some typical examples are OH, NO, NO_2, CN, CH, H_2CO, H, O, and CO. Several important species for rocket propellant applications which cannot be measured using LIF are H_2, CO_2, N_2, H_2O, N_2O, HCN and NH_3. Molecules with three or more atoms have many degrees of rotational and vibrational freedom, more complex and overlapping spectra, and smaller relative populations in any chosen state, due to the increase in density of states. Because of the smaller relative populations, the LIF signal strength decreases. Therefore LIF experiments are often limited to diatomic species.

Planar laser-induced fluorescence

If the diagnostic laser beam is transformed into a thin sheet, and the fluorescence is collected with an imaging detector, and two-dimensional images are obtained. This technique is called planar laser-induced fluorescence (PLIF). By selection of the laser sheet position, planar slices can be made through the flame. Fig. 3.14 shows a schematic of a PLIF setup. The species are excited by a tunable UV laser. The beam of this laser is converted to a planar sheet, which is then passed through the combustion gases above the sample. The LIF signal is measured at angle by e.g. an intensified CCD camera, which is gated with the dye laser. The sample may be placed in a pressurized window bomb, to allow for measurements at elevated pressures. Interference filters can be used to select the spectral region of interest and reduce the scattered laser signal.

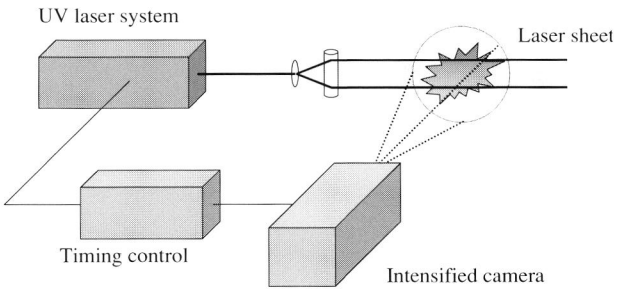

Figure 3.14: *Schematic of a PLIF setup.*

3.4.2 UV-Vis absorption

The problem of quenching limits the use of LIF-techniques to determine absolute species concentrations. Absorption spectroscopy can be used as a complementary tool to determine absolute concentrations. The set-up used for the experiments is similar to that for decomposition species detection, see Fig. 2.8. The absorption is dependent on species volume concentration (pressure, temperature, mole fraction) and pathlength. A reverse method is applied to determine the absolute mole fractions and temperature from the determined absorption profile, by fitting the measured spectra to theoretically calculated spectra. For more information, see the results discussed in section 4.4.

3.4.3 Micro-thermocouples

The combustion zones of solid propellants operating under normal conditions are very narrow with a thickness of several millimeters at most. Visual observations have been applied to e.g. determine dark zone length dependence on pressure. However, a very important piece of information is the temperature distribution throughout the combustion wave. The measurement of this temperature profile is possible by embedding very fine thermocouples within the propellant samples, see Fig. 3.15. The use of thermocouples to determine the temperature profile in a combustion zone is a rather old technique, which is still in use today [59, 71, 83, 129].

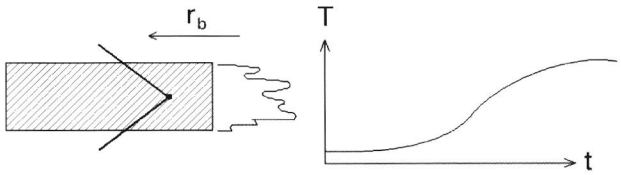

Figure 3.15: *Embedded thermocouple in a solid propellant (left). As the propellant regresses the temperature registered by the thermocouple increases up to the final flame temperature (right).*

The response time of a thermocouple, which is determined by its bead size, is a very important parameter. If the response time of a thermocouple is too large it will not follow the high temperature transients during combustion, and will not resolve the true nature of the combustion. If the characteristic time of the thermocouples is t^*_{tc}, and the characteristic time of combustion is t^*_c, then the thermocouple bead size must be such that

$$\frac{t^*_c}{t^*_{tc}} \gg 1 \,. \tag{3.7}$$

The characteristic time for combustion is given by $t^*_c(p) = \alpha_c / r_b^2(p)$, where α_c is the thermal diffusivity of the condensed phase, and $r_b(p)$ the regression rate at pressure p. Hence, t^*_c decreases with increasing pressure, which limits thermocouple experiments to a maximum pressure. The above condition ensures that the errors due to thermocouple

finite response time are negligible. Apart from this, also the spatial resolution of the thermocouple must be checked.

Besides from the finite response time, several *systematic* errors can be identified when applying the thermocouple technique:

- *Heat conduction through leads:*
  Because the conductivity of the thermocouple wires is about three orders of magnitude larger than that of the propellant, there is a heat loss into the thermocouple leads. This heat loss may be overcome by placing the thermocouple wires parallel to the burning surface. But because the propellant surface is never perfectly planar, the thermocouple leads may burn before its bead. Therefore wires are normally placed under an angle. In a theoretical study, it was shown that the heat loss through the wires increases for a decreasing thermocouple lead diameter [145]. However, to determine fine details of the combustion zone and to minimize response time, very fine thermocouples (and thus fine leads) are desirable. When the angle between two thermocouple wires is selected to be large ($> 120°$), the heat loss can be reduced without introducing problems due to surface irregularities.

- *Catalytic effects:*
  Thermocouples may show catalytic effects on the combustion and decomposition behavior. By comparing the measurements between coated and uncoated thermocouples, or different thermocouple materials, the possible catalytic effects can be evaluated.

- *Flow disturbance:*
  Ribbon (foil) thermocouples have a low thermal response time, but affect the flow because of their size.

Several techniques have been employed to position the thermocouples in the propellant sample. Sabadel et al. developed a technique for embedding the thermocouples directly into uncured strands of propellant [129]. For this a propellant with a very low viscosity and fine oxidizer particles was found to be necessary. Kubota et al. pressed two propellant halves together with the thermocouples in between [83]. Dumas et al. pierced the propellant with a thin needle, and placed the thermocouples in the small hole [40].

3.5 Experimental facility

An experimental facility was created at Delft University of Technology. All experiments take place in a high-pressure bomb (Fig. 3.16), which was designed and machined at the Delft University of Technology workshop. This bomb is equipped with 4 synthetic sapphire (alumina) windows of 50 mm diameter and 6 mm thickness, which are capable of withstanding pressures up to 5 MPa with a safety factor of 3. These UV transparent windows are used for optical access of the laser beams, for transmission of the fluorescence signals and allow the monitoring of the combustion process. The sapphire windows are able to withstand the high UV laser intensities. The (1000) crystal axis is along the laser light direction, to minimize absorption. Before, during and after the combustion the bomb is purged with nitrogen. Ignition and laser- assisted burning is accomplished by a CO_2 laser

pulse which enters the bomb through a 10 mm thick zinc selenide (ZnSe) window on top of the bomb. The ZnSe window is flushed with nitrogen to prevent hot combustion gases reaching the window. Baffles are installed to prevent recirculation of the combustion gases. Pellets are placed on a post, which can easily be inserted through the bottom of the bomb.

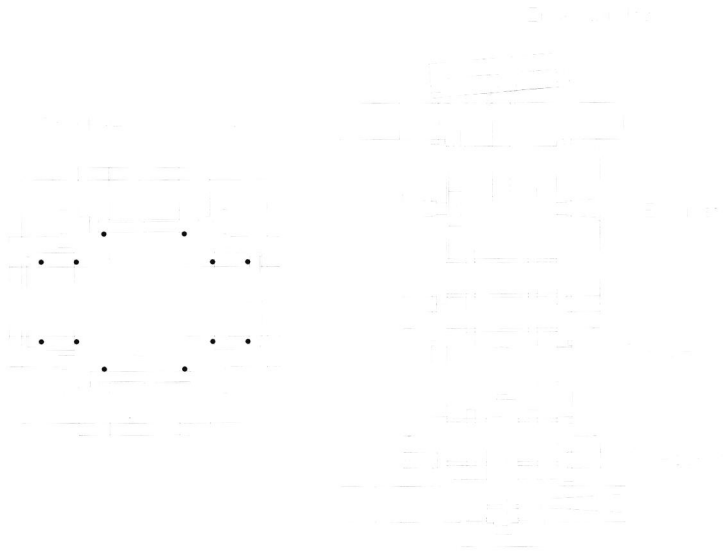

Figure 3.16: *High-pressure bomb for optical diagnostics.*

Figure 3.17 shows a schematic overview of the experimental setup. A Coherent Diamond G-50 CO_2-laser with an average output power of 50 W is used to ignite the pellets. The CO_2-laser is able to instantaneously ignite the samples at the burning surface. The laser is controlled by an AED LC-C50 controller, which allows modulation of the laser signal. A negative ZnSe lens diverges the laser beam to the pellet diameter. The pressure in the bomb is measured with a pressure transducer (Omega PX213; range 1-1000 Psi). The combustion process is monitored by a video camera (Hunt HTC-340) with 135 mm macro objective. This also allows for the determination of the regression rates. The laser source for the laser-induced fluorescence measurements consists of a pulsed XeCl excimer laser (Lambda Physik EMG 200) pumping a dye laser (Lambda Physik LPD3000). The output of the dye laser may be frequency doubled to generate deep-UV laser pulses (using either a KDP or BBO-I crystal). The laser power is measured with a pyroelectric detector (Ophir PE25 with Nova display). The fluorescence is collected and focused on the entrance slit of a high-resolution spectrometer (Jobin-Yvon THR-1000; 2400 gr/mm grating) equipped with an intensified diode array detector (Spectroscopy Instruments IRY 1024). The fluorescence can also be monitored on a low-resolution spectrometer (Jarrel Ash Monospec 18; 1200 gr/mm) also equipped with an intensified photodiode array detector (Princeton Instruments IPDA 1024). Both diode arrays use separate pulsers (Princeton Instruments FG-100) and share a common controller (Princeton Instruments ST-120). A reference flame

and photo multiplier tube (PMT) are used to tune the dye laser to resonance. The fluorescence from the laser sheet can be monitored two-dimensionally with an intensified CCD camera (Princeton Instruments ICCD; 576 × 384 pixels). The camera uses a pulse/delay generator (Princeton Instruments FG-100) producing a 20 ns gate for the intensifier and is controlled by a ST-138 controller. A Stanford Research System pulse/delay generator (DG535) functions as a master clock and controls the experiment timing. Timing is monitored with a digital oscilloscope (LeCroy 9361). Analog measurements are carried out using a 12-bit, 8 channel data acquisition board (National Instruments PCI-1200). The typical sampling rate is 1 kHz. The data acquisition and timing control software is written in LabVIEW.

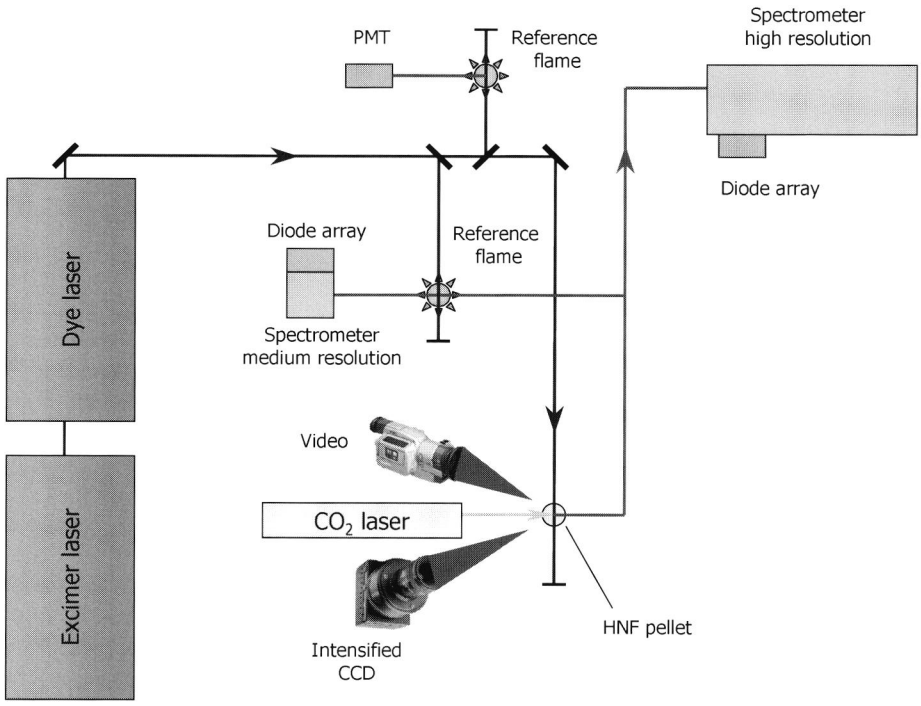

Figure 3.17: *Schematic of the experimental setup.*

The experimental room, HCl excimer gas cabinet and combustion gases are evacuated to the roof. Preparation of the samples and laser dyes takes place under a fume hood. The samples are stored in a safe.

3.6 Strand burner

High pressure (> 5 MPa) regression rate experiments are carried out at the TNO/PML facility. For these experiments a window bomb is used, see Fig. 3.18. The windows are

made of 12 mm thick polycarbonate, which limits the maximum pressure to 20 MPa. During the experiment, the bomb is flushed with nitrogen gas. Lead fuse wires and/or video recordings are used to determine the regression rate. The samples are ignited by a nichrome wire.

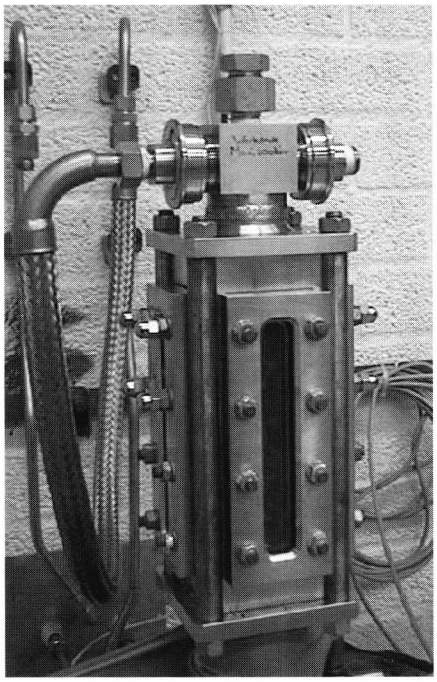

Figure 3.18: *Window strand burner at TNO/PML for high pressure experiments.*

The burn rate results are obtained as follows. Fuse wires are mounted at 20 mm distance. Typically 4 fuse wires are used. The accuracy of placement is ± 0.5 mm. The burn-through of the fuse wires is measured with a frequency of 200 Hz, yielding a timing error of ± 0.005 s. After the experiment the data is grouped as burned distance v.s. time. A linear regression is than applied for each experiment to determine the burn rate. For a typical propellant burning at 20 mm/s, the error in the burn rate at each individual 20 mm segment is then ± 0.6 mm/s. Because three segments are present, and the linear regression rate is applied, the total error in the determination of the burn rate is lower: $\pm 0.3 - 0.4$ mm/s. For lower burn rates the error becomes smaller (± 0.05 mm/s at 5 mm/s burn rate), and at higher burn rates the error increases (± 1 mm/s at 50 mm/s burn rate).

During processing of the experimental results, it was observed that the typical scatter of the burn rate measurements was higher than the expected variations. Propellant inhomogeneities are the most likely cause for this, as mixing took place in small batch sizes. A better estimation of the errors in the burn rate measurements was found to be the standard deviation of the linear fit to the position versus time graphs for each individual pressure. This gives a better idea of the irregularities during a single experiment. The error bars indicated in this thesis, are obtained from the standard deviations of the linear fits.

3.7 Conclusions

This Chapter discussed the preparation of samples, experimental techniques that have been employed and the experimental setup that was constructed. Despite HNF's sensitivity, the pressing of HNF was done on a routine basis without problems. Pressed samples with a density of 94% of the density of HNF crystals were obtained. Microscope images show that the HNF crystals fracture during the pressing action. In a later stage the crystals fuse together because of the high pressures. The friction sensitivity of the pressed samples is comparable to that of the neat HNF. The pressed samples are less sensitive to impact than the HNF material. HNF material which has been pressed and sanded to yield small crystals has similar friction sensitivity as the virgin material. The sanded material is more sensitive to impact. An interrupted pressing process yields HNF material that has a significantly lower L/D and is very well suited as a propellant ingredient. For this study planar laser-induced fluorescence (PLIF) is used as the major diagnostic method. PLIF allows nonintrusive visualization of the flame structure, and by using gated detection and pulsed lasers, the contribution of the natural emission of the flame is reduced.

Chapter 4

HNF combustion

4.1 Introduction

In terms of mass content the oxidizer is the main ingredient of a composite propellant. The combustion of a composite propellant is therefore largely determined by the combustion of the oxidizer itself. This is especially true when the oxidizer has a high energetic content, like HNF. In this Chapter the combustion of neat HNF is addressed. The Chapter starts with a literature review. Then the results of experiments are presented: neat HNF regression rate, micro-thermocouple experiments, emission and absorption spectroscopy, gas phase temperature profile and temperature sensitivity. The combustion characteristics of HNF mixed with several additives are presented at the end of this Chapter. These mixtures are essentially premixed mixtures and show the effect of additives on the combustion of HNF and can be regarded as simple propellants.

4.2 Background

In Table 4.1 the adiabatic flame temperature T_f and the most important final products of HNF solid monopropellant combustion are given (results from NASA SP-273 chemical equilibrium calculations). Due to the shifting equilibrium composition, the flame temperature increases with increasing pressure due to the further oxidation of fuel species (H, H_2, OH, and CO). Note that the effect of pressure on the flame temperature is considerable. From 0.1 to 10 MPa the temperature increases from 2766 to 3112 K.

Table 4.2 shows the results of chemical equilibrium calculations for some other oxidizers and energetic ingredients. HNF is quite unique, as it has a flame temperature comparable to that of the explosive ingredients (HMX, RDX and CL-20), but has a significant amount of oxygen left after combustion. This combination of properties, affects the way in which HNF participates in combustion.

Because of the highly exothermic HNF decomposition, selfdeflagration of HNF monopropellants is possible, at least in the experimental pressure range of 0.025 to 10 MPa [42, 102]. The quantity characterizing this selfdeflagration is the regression rate, or burning rate r_b. The burning rate of HNF monopropellants was determined by McHale and von Elbe [110]. They determined the burning rate of HNF, filled in pyrex tubes at approximately 75% of the theoretical maximum density (TMD). Because of safety aspects, the

p (MPa)	T_f (K)	H	H_2	O	O_2	OH	CO	CO_2	N_2	NO	H_2O
0.01	2578	0.017	0.023	0.022	0.113	0.048	0.047	0.090	0.338	0.014	0.288
0.1	2766	0.010	0.018	0.016	0.108	0.046	0.040	0.100	0.342	0.017	0.304
1	2949	0.005	0.012	0.010	0.103	0.041	0.030	0.112	0.345	0.021	0.321
10	3112	0.002	0.070	0.005	0.099	0.033	0.019	0.125	0.349	0.025	0.337
100	3237	0.001	0.003	0.002	0.095	0.024	0.010	0.136	0.351	0.028	0.349

Table 4.1: *Adiabatic flame temperature (T_f) and the most important species concentrations (mole fractions) of HNF monopropellant combustion at several pressures (p).*

Oxidizer	Chemical composition	Heat of formation [kJ/mole]	T_f [K]	$\%O_2$
HNF	C 1 H 5 N 5 O 6	-72.0	2766	10.8
RDX	C 3 H 6 N 6 O 6	+61.5	2923	0.6
HMX	C 4 H 8 N 8 O 8	+75.0	2919	0.6
CL-20	C 6 H 6 N 12 O 12	+415.5	2963	2.6
ADN	N 4 H 4 O 4	-140.1	2039	19.5
AP	N 1 H 4 Cl 1 O 4	-295.3	1381	29.2
AN	N 2 H 4 O 3	-365.1	1247	14.3

Table 4.2: *Adiabatic flame temperature of several oxidizers and energetic fillers (ambient pressure).*

HNF was only loosely packed in the pyrex tubes, and not pressed. More recently Atwood et al. measured the regression rate of pressed HNF, with 96% TMD [4, 46]. The results of both experiments is shown in Fig. 4.1. In equations:

$$\begin{array}{lllll} \text{McHale, and von Elbe} & 75\%\ \text{TMD} & r_b = 6.00 \cdot p^{1} & [\text{mm/s}], \\ \text{Atwood} & 96\%\ \text{TMD} & r_b = 6.22 \cdot p^{0.828} & [\text{mm/s}], \end{array}$$

where the pressure, p, is in MPa. For the low TMD experiments the pressure exponent, n, was found to be 1, whereas for the high TMD, $n = 0.828$, see Fig. 4.1. The differences in n can be attributed to the differences in loosely packing of the HNF, the purity of HNF, and the effect of turbulence of the gaseous products on the loosely packed HNF [42]. The low TMD experiments are further characterized by a slope break at 0.3 MPa. Below this pressure the pressure exponent was found to be 0.3. This slope break is assumed to be caused by the loosely packing, as the high TMD results correlated well on a single line.

The high TMD experiments are considered to be more representative of a real application of HNF combustion. Laser-assisted (increased burning rate due to laser heat flux) and laser-recoil (unsteady combustion due to varying laser heat flux) experiments have been carried out by Finlinson [46]. Results of these experiments are reported in sections 6.2 and 7.3.5, where they are compared with modeling results.

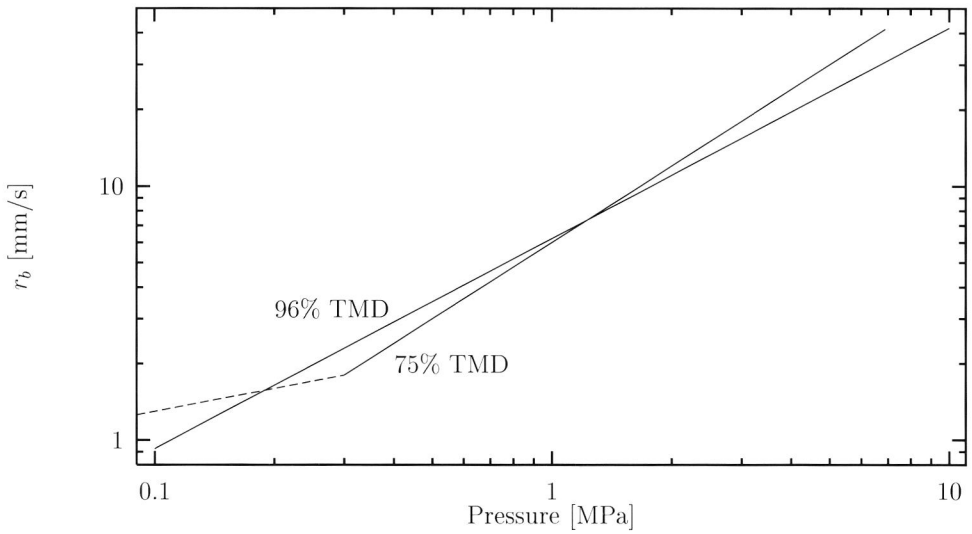

Figure 4.1: *Experimentally determined regression rates of HNF monopropellants for two different TMD values. The begin and end point of the lines indicate the experimental pressure range.*

The temperature sensitivity of the burn rate of a propellant expresses the sensitivity of the regression rate to the propellant's initial temperature. The temperature sensitivity, σ_p, is defined by [147]

$$\sigma_p = \left(\frac{\partial \ln r_b}{\partial T_0} \right)_{p=\text{constant}} . \tag{4.1}$$

The temperature sensitivity is a function of both initial temperature and pressure. For many energetic propellant ingredients σ_p has been found to decrease with increasing pressure, and increase with increasing initial temperature [4]. The temperature sensitivity of 96% TMD HNF monopropellant combustion is given in Fig. 4.2 (From Ref. [4]). The temperature sensitivity of HNF is comparable to that of HMX and RDX, and about 3 times lower than that of ADN at 2 MPa [4]. The low value of the temperature sensitivity implies that the condensed phase reactions play a rather unimportant role in the combustion of HNF [81].

Von Elbe et al. took motion pictures of the burning strands to determinate the regression rate and make visual observations of the burning surface [42]. HNF was observed to melt prior to gasification in the combustion zone. The depth of the molten zone was found

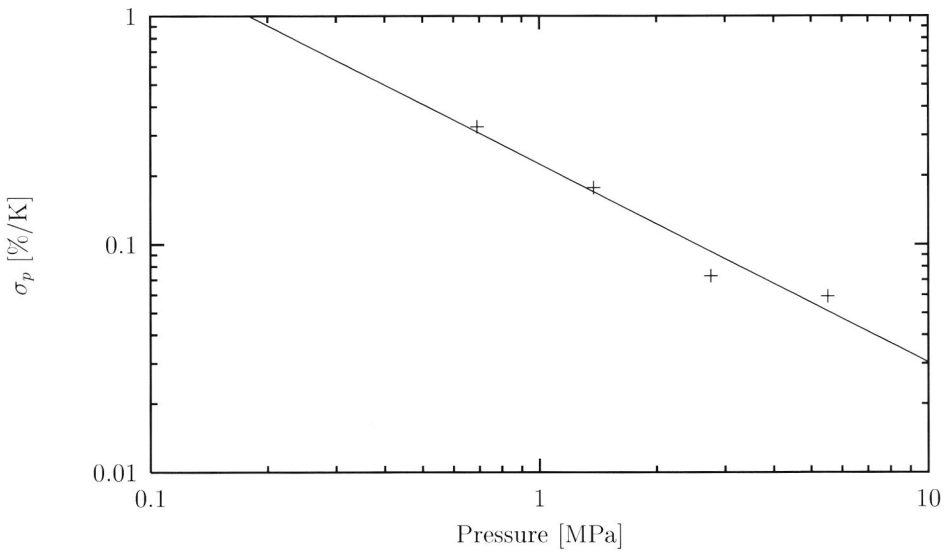

Figure 4.2: *HNF monopropellant temperature sensitivity at 96% TMD (from Ref. [4]).*

to vary inversely with the burning rate, ranging from several millimeters at sub-atmospheric pressures, to fractions of a millimeter at higher pressures.

To further investigate the combustion wave structure of HNF monopropellants, micro-thermocouples were embedded in the loosely packed HNF [42]. Pt-Pt/Rh thermocouples with a bead diameter of approximately 25 μm were used for this. In the initial part the temperature rises from the ambient temperature to approximately 120°C. This zone was found to be characteristic of the regular temperature rise in the preheat zone of a combustion wave. Above 120°C, the material melts and decomposes, generating gas bubbles and acquiring a foam structure. The temperature rise in the foam zone is fairly gradual until the thermocouple records a temperature of about 260°C, at which the gasification process very rapidly goes to completion, and the temperature rises sharply. Then the thermocouple melts, and the temperature signal becomes unusable. In the preheat zone, the temperature slope shows a *convex* curvature toward the x-axis, that is d^2T/dx^2 is positive. The temperature rise in this zone is governed by heat conduction. The steady-state solution of the energy equation for the non-reacting situation, fits the measured temperature profile very well, for the thermal diffusivity $\alpha_c = k_c/(\rho_c c_c) = 0.001\,\mathrm{cm}^2/\mathrm{s}$. This confirms that in the first zone only preheating takes place. In the second, foam, zone, the average slope shows a *concave* curvature towards the x-axis, which signifies correspondingly that heat is lost by conduction, but that the loss is overbalanced by chemical heat evolution. When the thermocouple enters the third zone of complete gasification, the temperature rises abruptly. Because of the high flame temperatures, the thermocouple melts before registering the final flame temperature.

Experiments with pressed HNF material were carried out by Parr and Hanson-Parr [123]. Emission images at ambient pressure showed an extremely short dark zone (ca. 40 μm), followed by a complex flame structure. The first visible flame, starting at 40 μm centered

at 180 μm, with a FWHM (full width at half maximum) of 180 μm, showed whitish on video, and was assumed to be the NH_2^* radical. Within this flamesheet, and extending beyond, are emissions from CN^*, NH^* and CH^*.

Planar laser induced fluorescence (PLIF) measurements confirm the observations of the emission experiments. The CN profile was found to peak at 360 μm, and the NH at 300 μm, see Fig. 4.3. The OH PLIF profile rose rapidly through and outside the CN flamesheet and then transitioned to a more gradual rise in the burnt gas region. PLIF-temperature was also measured. Fig. 4.3 shows that the temperature does not reach the adiabatic flame temperature, and continues to rise at a slower rate beyond the CN flamesheet.

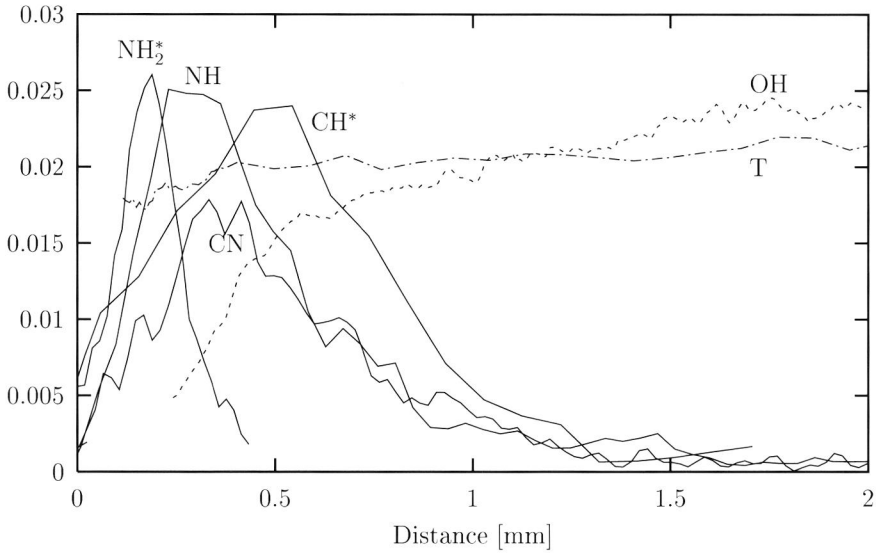

Figure 4.3: *PLIF measurements of HNF monopropellant combustion at ambient pressure. NH, NH_2 and CH^* concentration in arbitrary units, OH concentration in mole fraction, CN mole fraction in ppm, and temperature T in 10^5 K (from Ref. [123]). Results were obtained by averaging measured LIF intensities in zones parallel to the burning surface (ambient pressure).*

In their HNF monopropellant experiments, it was found by Von Elbe et al., that a critical tube diameter exists below which the HNF deflagration is quenched [42]. This diameter depends on the pressure. The critical diameter for quenching was found to be about 20 ... 30 times larger than α_c/r_b. It was hypothesized that in a propellant particles larger than the critical diameter would deflagrate individually ahead of the pyrolysis and gasification of the embedding organic matrix, whereas at low pressure, the propellant would deflagrate via interaction of fuel and oxidant in the condensed phase. It was argued that the physical change of the combustion mechanism could become visible by a change in slope in the burn rate equation.

4.3 Neat HNF combustion

This section addresses the experimental findings of the combustion of neat HNF.

4.3.1 Burn rate

Neat HNF burns with a very high burn rate, and high burn rate exponent. Figure 4.4 shows the measured regression rate of neat pressed HNF pellets. The two different window bombs already described have been used to measure the regression rates (6 mm samples: DUT facility, 9 mm: TNO facility). The figure shows a slope break around 2 MPa from n=0.95 to n=0.85 at higher pressures. Below 2 MPa no inhibitor was used. At higher pressures, the samples were coated with a thin layer of Molycote 111 silicon grease. Also shown in the figure is the data obtained at NAWC [46]. The agreement with this data is good. Below 1 MPa the NAWC-data shows a slightly higher burn rate.

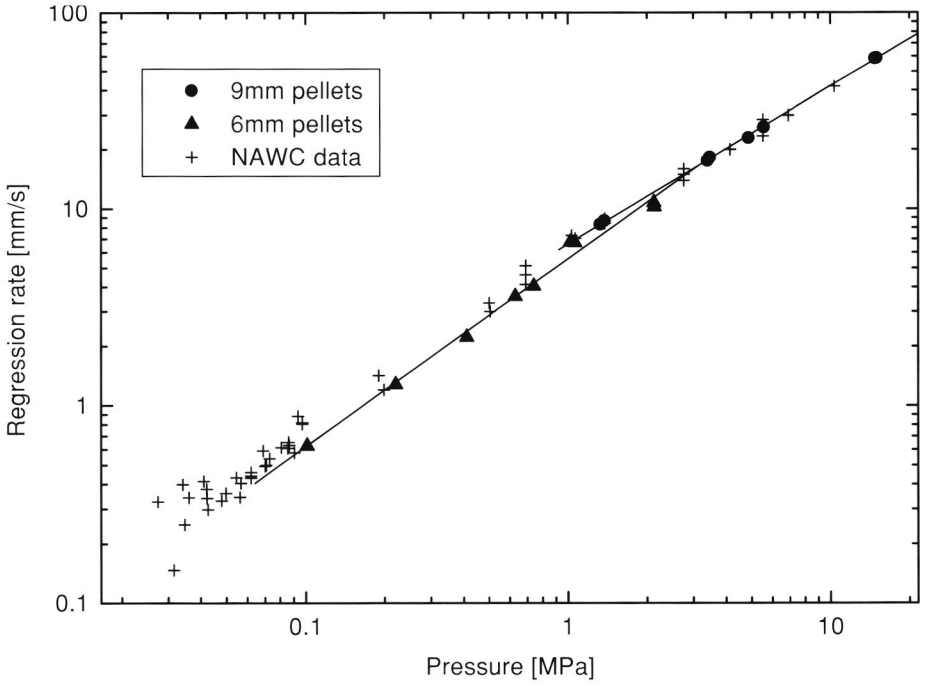

Figure 4.4: *HNF monopropellant regression rate as determined from video recordings. NAWC data below 0.2 MPa was obtained from short samples (2-3 mm) only, explaining the increased scatter at these pressures.*

The combustion of HNF was also studied at sub-atmospheric pressures. It had already been observed in previous work, that the flame front of HNF is very close to the surface. At reduced pressure the flame zone is broader, which makes it easier to use optical diagnostics. At sub-atmospheric pressures, down to 0.06 MPa reliable ignition could be obtained with

longer CO_2 pulse-time. However at lower pressures, increase of the pulse time was not found to be sufficient anymore. The HNF extinguishes due to the sudden drop in radiation at laser shut-off (de-radiative extinguishment). Reliable ignition could be obtained by following the ignition pulse with a linear decrease during 500 ms of the laser power. With this ignition pulse, the samples could be ignited at pressures as low as 0.03 MPa. Occasionally, it has even been possible to ignite and sustain combustion of the samples at pressures as low as 0.02 MPa.

The measured regression rates at sub-atmospheric pressures are also shown in Fig. 4.4 (NAWC data below 0.1 MPa). At low pressures the amount of scatter is large, although the HNF burns stably. During several experiments the HNF was regressing, but did not show a luminous flame. The regression rate was significantly lower in these cases, and these experiments are therefore not shown in Fig. 4.4. It is assumed that the HNF regresses because of some exothermic reactions in the condensed phase. The temperature of the decomposition gases seems to be too low to obtain ignition in the gas phase in these cases. It should be noted that yellow condensate was found in the window bomb and in the exhaust tube. The amount of material was found to increase with decreasing pressure. Also before ignition of the HNF, yellow condensate is seen to come from the surface see Fig. 4.5. This condensate is speculated to be HNF vapor, in correspondence with the findings of section 2.3.2.

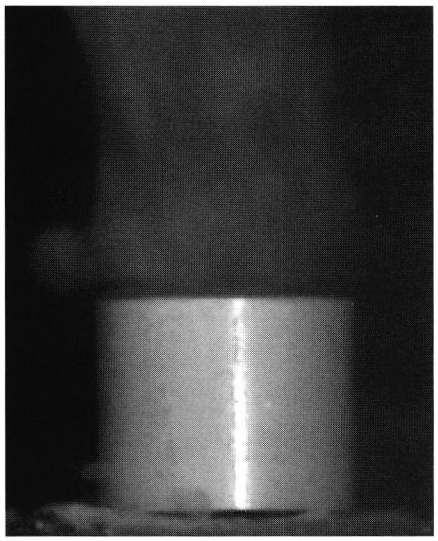

Figure 4.5: *Yellow condensate coming from the surface of a HNF pellet before ignition.*

4.3.2 Micro-thermocouple measurements

The condensed phase temperature profiles were measured by micro-thermocouples (5μm foil, type K, RdF corp.). The thermocouples are assembled between two pellet halves. To ensure that the thermocouple junction emerges at the surface first, pellets were pressed

with two opposing angles, see Fig. 4.6. To reduce heat loss a large angle of 160° was chosen. The two halves are held together by a small amount of paraffin wax around the outside of the sample. Melted paraffin is applied while the two halves are pressed together. After solidification, the samples are mounted on a modified sample holder, with thermocouple feed-through. Throughout the signal chain from the thermocouple to the amplifier, compensation wires and connectors are used.

Figure 4.6: *Ribbon thermocouple between two pressed HNF samples. Note the bright yellow off-center flame due to traces of sodium chloride in the HNF.*

A typical thermocouple trace at ambient pressure is shown in Fig. 4.7. After ignition by the CO_2-laser the condensed phase is heated by conduction from the burning surface. At 340-350 K a bend in the curve appears. At that moment the thermocouple is not yet visible at the burning surface. Around 400 K the thermocouple becomes visible. However, the thermocouple is not yet at the burning surface but is observed through the transparent burning surface. The melting temperature of HNF is 396 K, which agrees very well with the first observation around 400 K. Because of the surface tension, the ribbon foil sticks to the burning surface, resulting in a reasonably constant temperature. The tension at the thermocouple wires becomes stronger because of the regressing surface. If the tension is high enough, the thermocouple enters the gas phase with a very high temperature gradient.

The measured surface temperature as a function of pressure is shown in Fig. 4.8. The surface temperature is seen to increase with increasing pressure. Because of the very steep temperature gradients in the condensed and gas phase of HNF, we did not succeed in determining the surface temperature at pressures above 1.0 MPa. McHale and von Elbe measured a surface temperature of 553K at ambient pressure of loosely packed HNF [110]. The pressed samples show a surface temperature of 530K at 1 atm.

It is difficult to estimate the accuracy of the thermocouple experiments. Due to the large angle and the low temperatures in the condensed phase, the conductive and radiant

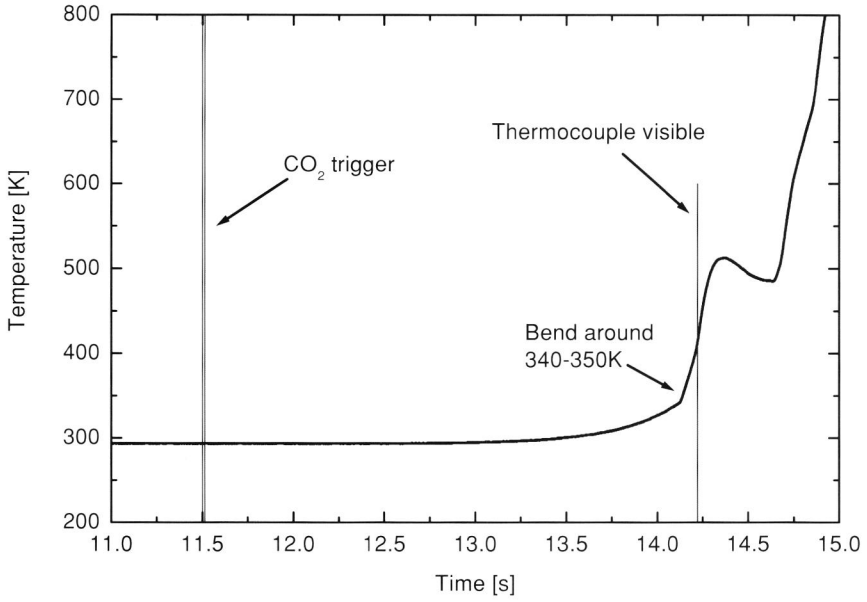

Figure 4.7: *Thermocouple trace of micro-thermocouple embedded in HNF pellet (0.1MPa).*

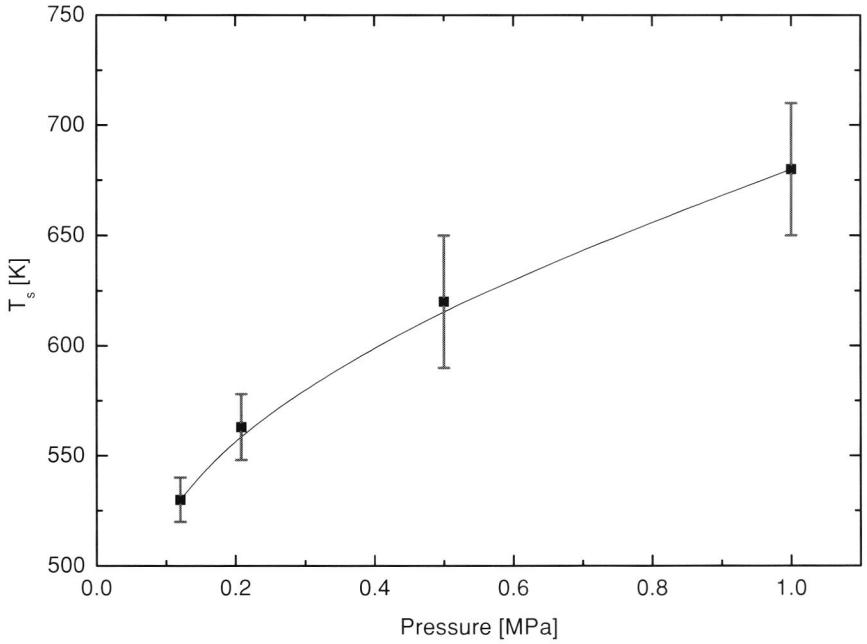

Figure 4.8: *Surface temperature of burning neat HNF as function of pressure.*

heat losses are small (estimated less than 25 K). Because of the laborious preparation of the thermocouples in the samples, only a few experiments were carried out at each pressure. The points shown in Fig. 4.8 are the result of the experiments that showed nice and flat regression behavior at the video images. At each pressure, the experiment was repeated until a satisfactory result was obtained. In many cases the samples started burning on the sides, or ignited off-center. The error bars shown in Fig. 4.8 are based on the amount of variation of the temperature at the plateau, as seen in Fig. 4.7. These variations were found to be at least larger than the estimated measurement error.

The strange bend around 350 K in Fig. 4.7 is caused by an interaction between the combustion wave and mechanical effects in the condensed phase. Because of the non-uniform heating in the combustion wave, stresses build up in the sample. If the stress is strong enough a crack parallel to the burning surface is formed. This causes an increased thermal resistance which explains the upward bend in the measured temperature profile. DSC measurements of HNF do not show any indication of a phase transition at 80°C. Therefore it is assumed that the sudden expansion is caused by the release of stresses present due to the pressing of the pellets. Also "crystal rearrangement" has been mentioned, but there is no further evidence of this. The cracks were only observed in the 9 mm samples, and not in the 6 mm samples. The larger samples have a larger volume to area ratio. This causes higher internal stresses in the larger samples. For more details on the cracking, see Chapter 7.

4.4 Flame structure

4.4.1 Emission spectroscopy

Spectroscopy is a helpful tool to survey the presence of specific atomic and molecular (mostly diatomic) species and their distributions in a flame. The emitted or absorbed light is dispersed in a spectrometer and electronic transitions are identified from the literature.

The neat flame HNF has already been described in Ref [124]. Apart from the narrow flame zone above the surface, the flame was found to be yellowish and bluish. The yellow emission was attributed to chemiluminescence from NO_2. The bluish emission was attributed to a mixture of CH, CN and NH. To evaluate the presence of these radicals the emission spectrum of HNF was measured with the low resolution spectrometer.

The UV emission spectrum in Fig. 4.9 shows some important diatomic combustion intermediates. It shows the well-known OH (280 and 310 nm) and CH (430 nm, blue natural gas flame) emission bands. In addition, it shows the NH (340 nm) and CN (380 nm) bands that are typically found in propellant emission spectra. In the deep-UV (200-270 nm) intense emission bands of NO and O_2 are visible.

When HNF is observed during combustion, sometimes a bright yellow flame emerges from the surface. This flame is attached to the burning surface, and seems to "dance" on the surface. The emission of this flame was attributed to the emission of sodium [156]. An example of this is shown in Fig. 4.6. The explanation for the presence of sodium in the HNF, is the fact that sodium chloride is used to extract water from the nitroform during the production process.

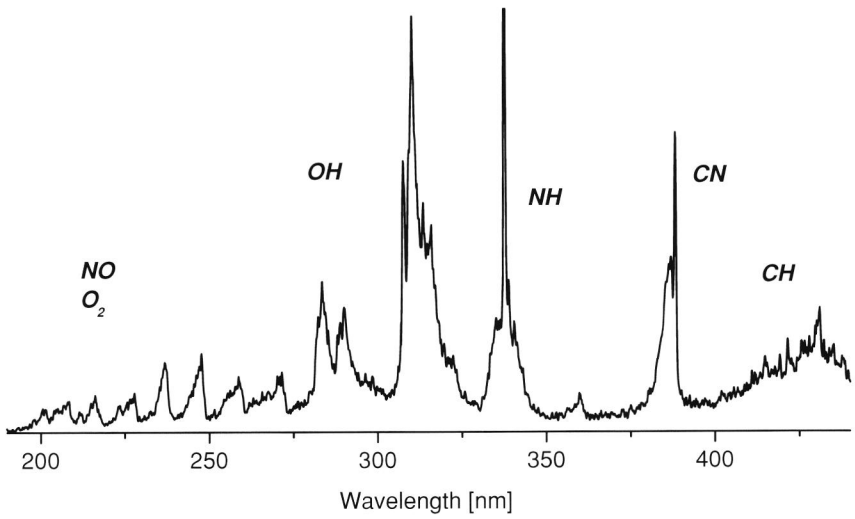

Figure 4.9: *HNF emission spectrum (combustion at ambient pressure).*

4.4.2 Absorption spectroscopy

[1]The absorption spectrum depends on several parameters: number of absorbing molecules per volume (i.e. pressure, temperature and species concentration), and path length. To determine the species mole fractions, it is necessary to know the pressure, path length, and temperature. The temperature is obtained from relative peak heights (assuming a Boltzmann distribution). Given the path length for the absorption, the species concentration can then be determined by comparison of the measured spectra to simulated spectra generated from experimental results [37, 38, 43, 51, 109, 131].

The flame structure of HNF burning at ambient pressure is shown in Fig. 4.10. The flame shows four different zones [123]. First a whitish flame, which is attributed to NH_2*-emission. Then a bluish flame, from CN* and CH* emission. A dark zone follows this flame. Finally, there is a large reddish zone. Emission from this zone was attributed to NO_2*. With increasing pressure, the emission becomes stronger and the narrow flame above the burning surface collapses to the burning surface.

NO profile

In a previous study by the Parr's [123], it was found that the flame temperature of HNF rises rapidly above the burning surface, but does not reach its final adiabatic flame temperature (see Fig. 4.3). It was assumed that the low flame temperature, was caused by

[1]The results of this section were obtained during a visit to NAWC and have been reported in Ref. [102].

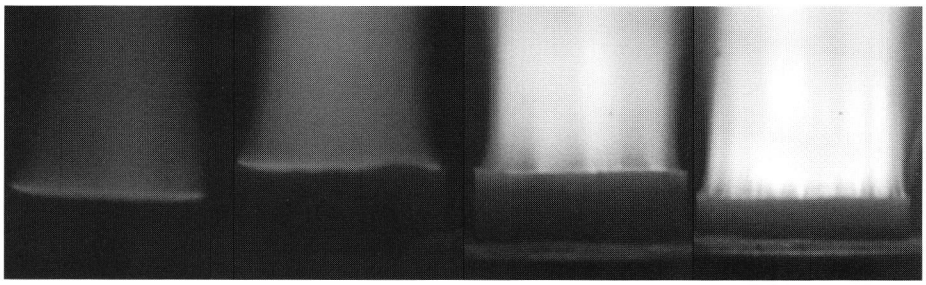

Figure 4.10: *Video images of neat HNF combustion. From left to right:0.1 MPa, 0.3 MPa, 0.9 MPa and 2.0 MPa.*

slow NO-reactions. To further resolve the NO-structure of HNF, UV- absorption experiments were carried out. The spectrometer was set up to cover the (0,0), (0,1), (0,2) (0,3), (1,1) and (2,2) NO bands of the $A^2\Sigma^+ \rightleftharpoons X^2\Pi$ transition.

During the analysis of the data, the absorption of the (0,0) band appeared to be too high. This was explained by the fact that cold NO surrounding the HNF flame also absorbs part of the UV-beam. This cold NO is probably present due to recirculation of the combustion gases in the bomb. Because of this, the (0,0) absorption was not used for reduction of the data. In all of the experiments the lines were broadened because of the high temperatures and pressures (collisional and Doppler broadening). Therefore in none of the experiments absorption flattening (nonlinear behavior of absorption vs species mole fraction due to shadowing) was important, and it was left out of the data fitting.

The measured maximum value of the NO mole fraction above the propellant surface as a function of the combustion pressure is given in Fig. 4.11. This figure shows that the maximum NO mole fraction decreases with increasing pressure. The relative absorption peak heights indicate that the temperature was close to adiabatic, and therefore the adiabatic flame temperature was used in the calculation of the absolute mole fractions. For all pressures the NO fraction strongly exceeds the theoretical adiabatic NO fraction, which varies from 1.6 to 2.2% for the pressure range of Fig. 4.11. This implies that the adiabatic conditions are not reached yet. This may seem to contradict the fact that the adiabatic flame temperature has already been reached. However, thermodynamic calculations show that it is possible to reach temperatures close to the adiabatic flame temperature, and still have a large NO fraction [103]. The reason for this is that HNF is an oxidizer, and no fuel species are left to react with the NO. Therefore the only way to reach equilibrium conditions, is that the NO decomposes to O_2 and N_2. This reaction is almost energetically neutral, and hardly contributes to an increase in the flame temperature. Note that the final flame process is fundamentally different from those of final flames of nitramines. In these flames the NO is reduced to N_2 by e.g. reaction with HCN. This reaction with fuel species causes the NO-fraction to reduce much faster for nitramines. Figure 4.12 shows the decrease of the NO concentration above the HNF surface (ambient pressure). The NO mole fraction is seen to decrease only very slowly above the burning surface.

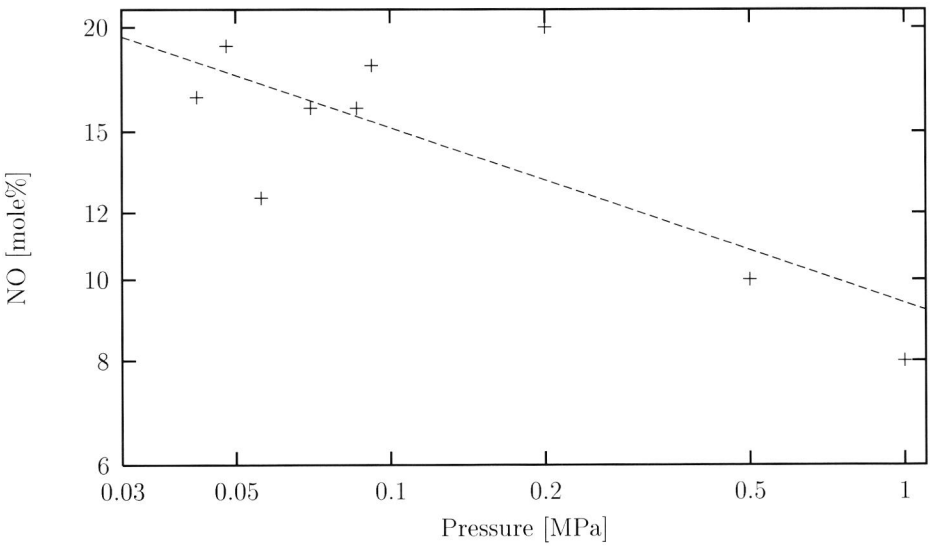

Figure 4.11: *Maximum NO mole fraction in a HNF monopropellant flame measured by absorption.*

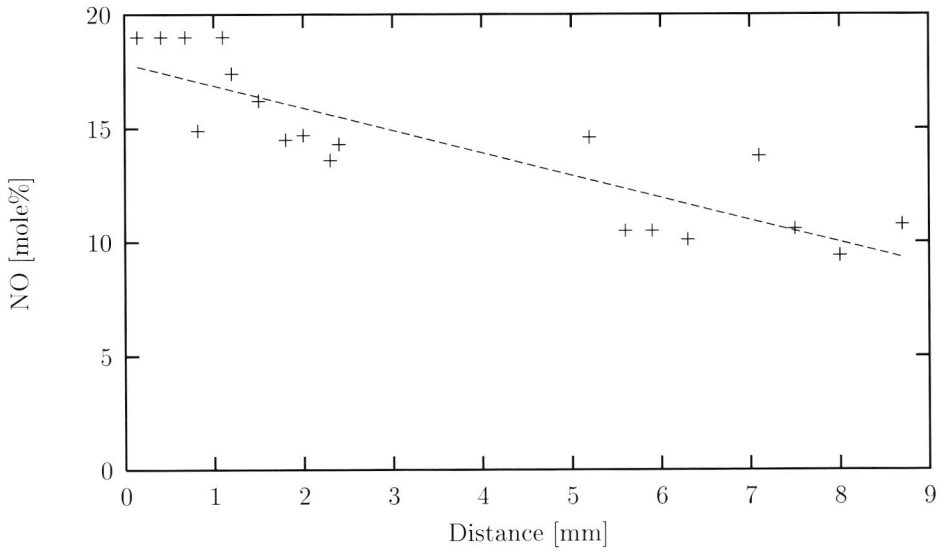

Figure 4.12: *NO mole fraction measured by absorption (ambient pressure).*

4.4.3 PLIF experiments

OH-PLIF in neat HNF

It was decided to excite the OH-radicals at the $A^2\Sigma^+(v' = 1) \leftarrow X^2\Pi(v'' = 0)$ band around 282 nm. The fluorescence from the $A^2\Sigma^+(v' = 0) \rightarrow X^2\Pi(v'' = 0)$ band around 308 nm can then be monitored and allows blocking of the laser light by filtering. In the dye-laser Coumarine 153 dye dissolved in methanol was used. This dye requires frequency doubling to obtain the desired laser light around 282 nm. The excimer output was about 300 mJ/pulse. The fundamental light at 586 nm had an energy of 17 mJ per pulse. After frequency doubling by a KDP crystal, 1.2 mJ/pulse remained at 283 nm. In front of the camera lens a WG305 and UG11 Schott filter combination was placed. This forms a band filter that blocks scattered laser light and the natural flame emission above 400 nm. The $Q_1(6)$-transition ($\lambda = 282.927$ nm) was pumped. This transition yields strong LIF signals, and is independent on temperature. Figure 4.13 shows the measured excitation spectrum around 282 nm in a methane/air Bunsen burner in comparison with theoretical spectra from the LIF-base program [107]. By comparing the theoretical and experimental spectra it is confirmed that the correct radical is excited. Furthermore, the dye laser grating can be calibrated with these results. The dispersed OH fluorescence spectrum for excitation at the $Q_1(6)$-transition is shown in Fig. 4.14.

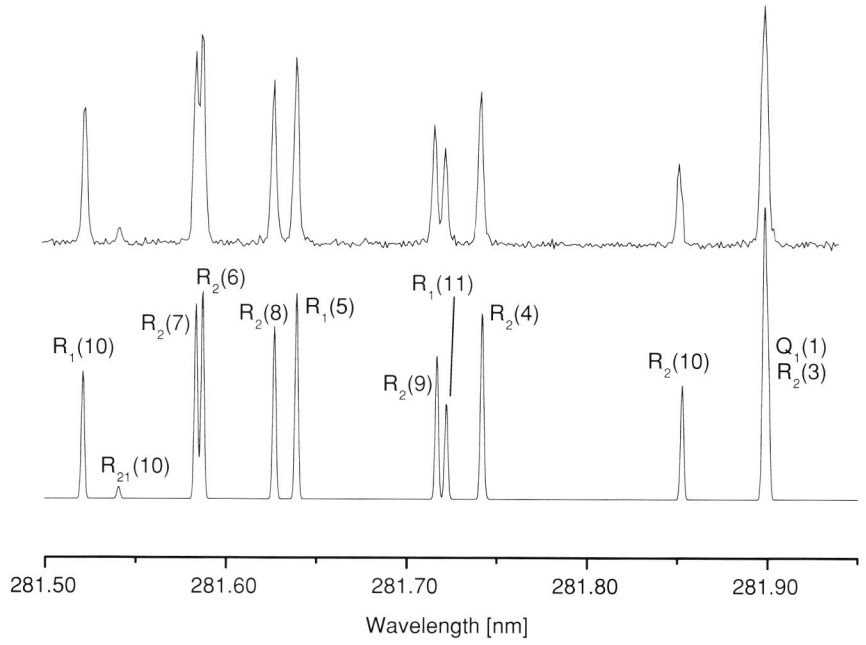

Figure 4.13: *OH excitation spectrum in a methane/air Bunsen burner. The fluorescence was monitored around 308 nm. Top: measurements, bottom: LIFbase calculations.*

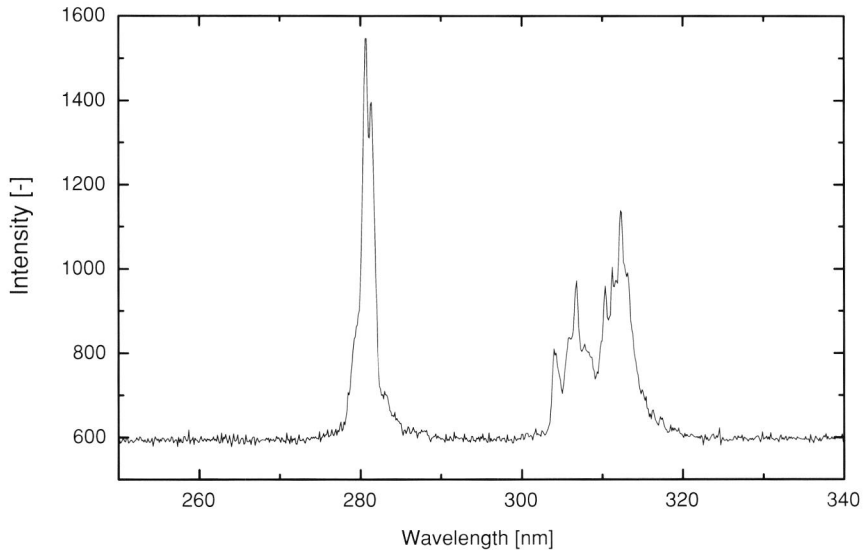

Figure 4.14: *Dispersed OH fluorescence signal in a methane/air Bunsen burner. Excitation at the $Q_1(6)$ line of the OH transition.*

The UV laser light from the dye laser is first magnified by a telescope with two positive lenses ($f_1 = 25$ mm and $f_2 = 50$ mm). The light is then transformed into a small sheet by a cylindrical lens ($f = 200$ mm). The lens is aligned in such a way that the focal point of the sheet is located behind the sample. All images presented in this thesis have been corrected for the varying laser intensity by dividing by the laser sheet intensity. Intensity profiles were obtained from the Rayleigh scattered light with the window bomb filled with 2 MPa nitrogen, and averaging over 100 laser pulses.

Figure 4.15 shows OH PLIF-images of the gas phase of HNF at different pressures. With increasing pressure the OH density increases. Furthermore the equilibrium OH concentration also increases with pressure (see Table 4.1). Both effects have a stronger effect than the decrease of the LIF signal due to enhanced quenching at elevated pressures, and the overall LIF signal is seen to increase with pressure. All images show a monotonous increase of the OH LIF-signal above the sample. Some of the sheet inhomogeneities are still visible.

CN-PLIF in neat HNF

The CN-radical was excited at the P(0,0) bandhead (388.37 nm) of the $B^2\Sigma^+(v' = 0) \leftarrow X^2\Sigma^+(v'' = 0)$ band. The fluorescence of the $B^2\Sigma^+(v' = 0) \rightarrow X^2\Sigma^+(v'' = 1)$ transition was monitored around 420 nm using a Melles Griot interference filter with a center frequency of 420 nm, and FWHM of 10 nm. QUI dissolved in dioxan was used as laser dye. This allows direct generation of the 388 nm light. At the entrance window of the bomb the power was 2 mJ/pulse. In the methane/air Bunsen flame the CN concentration

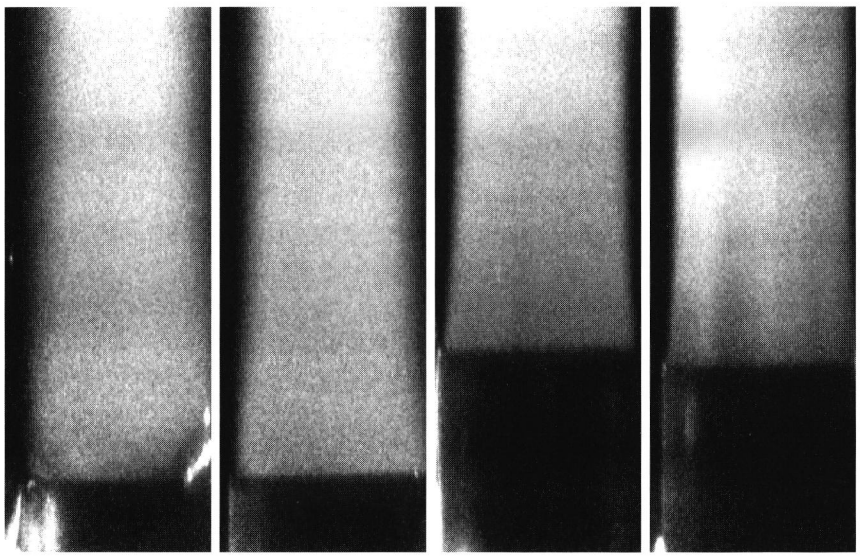

Figure 4.15: *OH-PLIF images in neat HNF. From left to right: 0.12, 0.22, 0.58 and 1.10 MPa. The images are binned in horizontal direction; one pixel represents 4 original pixels.*

is low, and the CN-LIF signal was very weak. In a hot fuel rich oxygen/acetylene flame the outer edges of the flame mix with air, forming large amounts of CN because of the nitrogen in the air. Figure 4.16 shows the measured CN excitation spectrum in a conventional oxygen/acetylene welding torch in comparison with spectrum calculated by LIF-base [107]. The dispersed fluorescence from this flame for excitation of the P(0,0) bandhead is shown in Fig. 4.16.

CN PLIF-experiments were obtained with 2×2 binning of the images to be able to measure at faster laser repetition rates. With this binning the images were 288×192 and the excimer laser could be run at its fastest rate of 10 Hz. Figure 4.18 shows some typical images of CN PLIF-images of neat HNF. The CN radicals were found immediately above the burning surface. By tuning the dye laser off-resonant (0.1 nm above the maximum LIF signal strength) the CN-signal completely vanishes.

At different pressures the CN profiles were averaged by summing the pixels counts in horizontal direction, see Fig. 4.19. The thickness of the CN layer decreases with increasing pressure. In contrary to the OH LIF-signal, the CN LIF-signal strength decreases with increasing pressure.

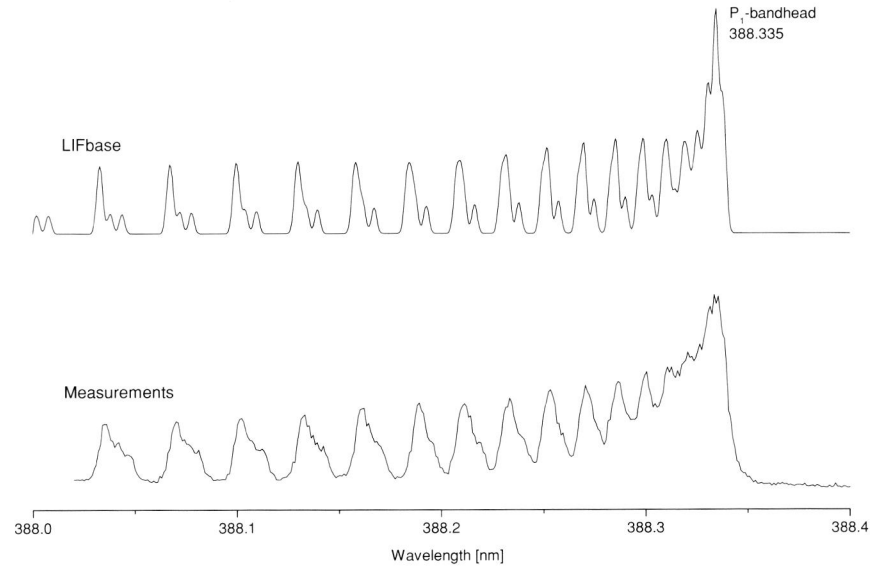

Figure 4.16: *Theoretical CN excitation spectrum and experimental determined spectrum in an oxygen/acetylene welding torch. The fluorescence was monitored around 420 nm.*

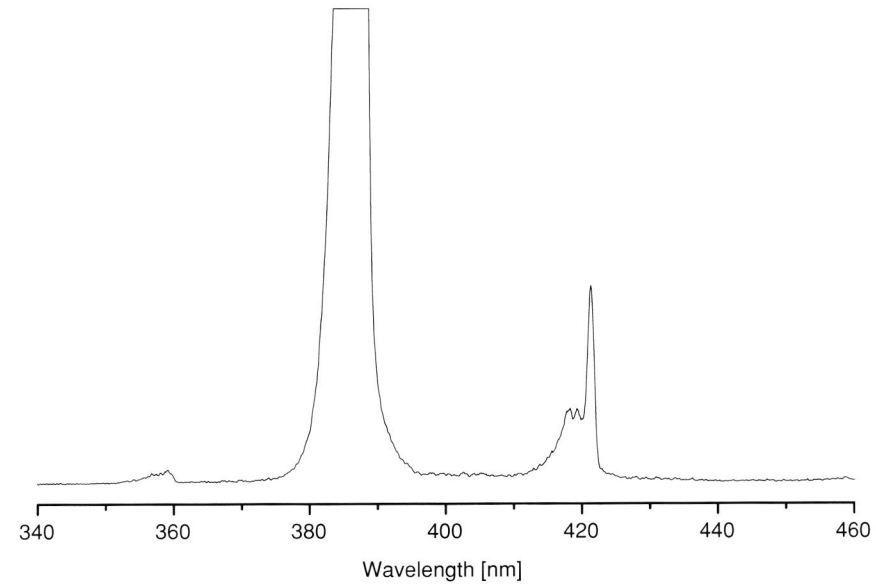

Figure 4.17: *Dispersed CN fluorescence signal in an oxygen/acetylene welding torch. Excitation at the P(0,0) bandhead. The large peak is from the scattered laser light at 388 nm.*

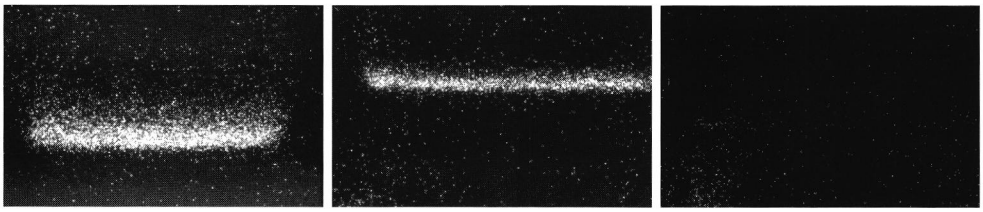

Figure 4.18: *CN PLIF images of neat burning HNF. From left to right: 0.16 MPa, 0.30 MPa and 0.30 MPa non-resonant (image size:* 6.2×4.1 mm^2*).*

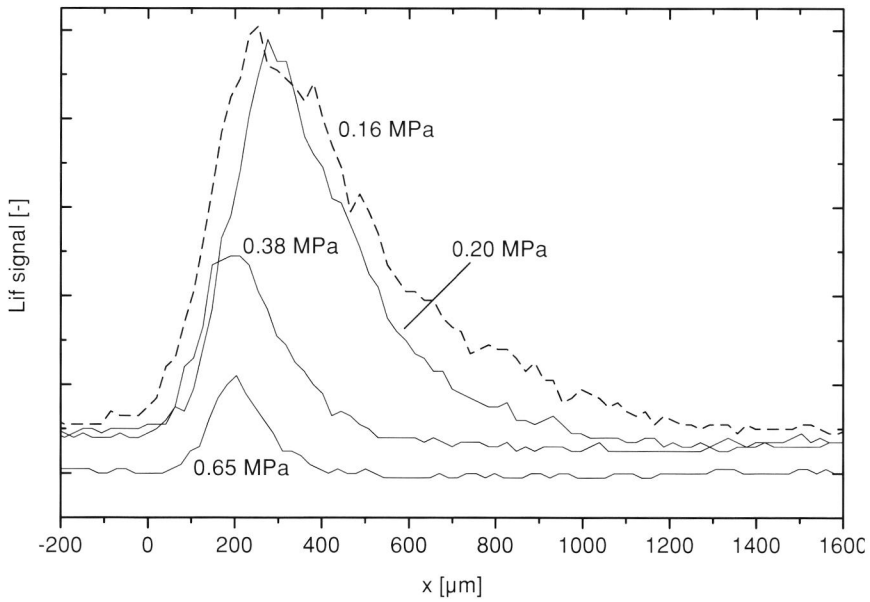

Figure 4.19: *CN-profiles obtained from PLIF images.*

4.4.4 Temperature profile

For a few samples the temperature profile in the gas phase of HNF was measured using the existing CARS (Coherent Anti-Stokes Raman Spectroscopy) [108, 155]. With small samples of 6 mm diameter, the measurements turned out to be unreliable, with very bad fitting of the theoretical spectra to the measured spectra. With larger samples, 9 mm diameter, this problem was solved, and some successful experiments were carried out.

In an attempt to measure the temperature gradient very close to the sample surface, the CARS beams were aligned such that the pellet was hit on the side. The surface of the regressing pellet would pass the probe volume, and the gradient could then be resolved. However, due to the thermal stress build up the pellets exploded after a couple of laser shots. Therefore only measurements starting from about 1 mm above the sample surface have been carried out. A typical result is shown in Fig. 4.20. The error bar indicates the single-shot error (13%) of the CARS technique in this experiment. It is seen that the temperatures are close to the adiabatic flame temperature of HNF (2766 K at ambient pressure).

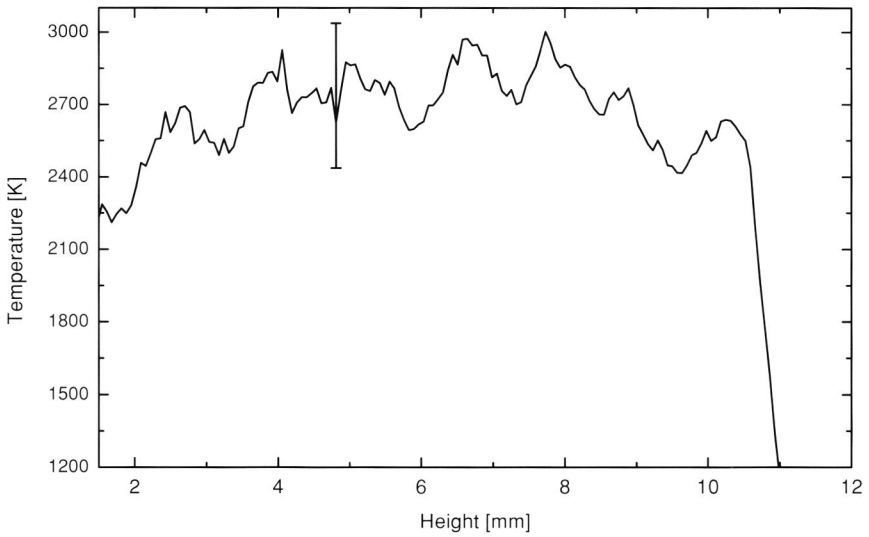

Figure 4.20: *CARS temperature measurement in neat HNF flame.*

Previous three-line LIF temperatures measurements by Parr et al. indicated a temperature in the HNF flame, of not more than 2000 K. Later, these measurements were found to be unreliable, due to the automatic gain control of the used camera. The relative NO absorption peak heights also indicate that the temperature was close to adiabatic. Hanson-Parr et al. used spontaneous Raman spectroscopy to determine the temperature above the HNF surface [56]. These measurements show $\sim$ 1800 K at 0.35 mm above the surface. At 1.2 mm above the surface, the N_2 contour was consistent with a temperature of 2766 K (with an N_2 concentration of 32%, and an H_2O concentration of 30%). In summary it can be concluded that the temperature rises rapidly above the HNF burning surface. Within experimental errors, the flame temperature is reached within 1-2 mm. Significant

gas phase reactions take place after this initial zone, but hardly affect the temperature.

4.5 Radiation enhanced combustion

Radiation which is absorbed below the condensed phase reaction zone in the propellant has a similar effect on the temperature profile as a higher initial temperature. This similarity is called the *equivalence principle* [62]. Mathematically this equivalence is given by

$$r_b(p, T_0, Q_r) \;=\; r_b(p, T_0^*, 0) \text{ , with } T_0^* = T_0 + \frac{(1-r)Q_r}{\rho_c c_c r_b} \text{ ,} \tag{4.2}$$

where Q_r is the radiant heat flux that reaches the surface (in W/m^2), and r the surface reflectivity. It is tacitly assumed that all radiant energy is absorbed in the propellant, and no transmission through the propellant takes place. For an absorption coefficient $K_a \sim 1000$ cm^{-1}, more than 99% of the energy is absorbed within 100 μm below the surface. For more details about the absorption in HNF, see sections 6.2.2 and 7.3.1. The equivalence principle has been found to hold within experimental error for several propellants [142].

HNF temperature sensitivity

Recently laser recoil experiments with pressed neat HNF oxidizer pellets were carried out by Finlinson [46]. As part of this study, also laser assisted steady state regression rates were determined. The results of these experiments will be used here to determine HNF's temperature sensitivity by applying the equivalence principle.

Table 4.3 summarizes the measurement results, and the determined values of T_0^* and σ_p from these results. The steady state burning rate without laser flux is given by $r_{b,1}$. The laser assisted regression rates, $r_{b,2}$, are determined from the fits as given by Finlinson at a laser flux of 50 W/cm^2. Finlinson accounted for a total of 5% for absorption in the gas phase and surface reflection. The density of the pressed pellets was 1.774 g/cm^3.

Pressure (MPa)	$r_{b,1}$ (cm/s)	$r_{b,2}$ (cm/s)	T_0 (K)	T_0^* (K)	σ_p (%/K)
0.10	0.065	0.085	304	609	0.087
0.20	0.136	0.154	304	487	0.068
0.31	0.199	0.219	304	437	0.072
0.41	0.259	0.276	304	412	0.059
0.64	0.381	0.419	304	377	0.131

Table 4.3: *Temperature sensitivity σ_p as determined from the laser assisted regression rate data.*

Fig. 4.21 compares the temperature sensitivity as determined by the equivalence principle with existing temperature sensitivity data. It is seen that the temperature sensitivity from the equivalence principle is much lower than the experimental determined value. An explanation is the fact that the radiation is not absorbed far below the surface, but in the

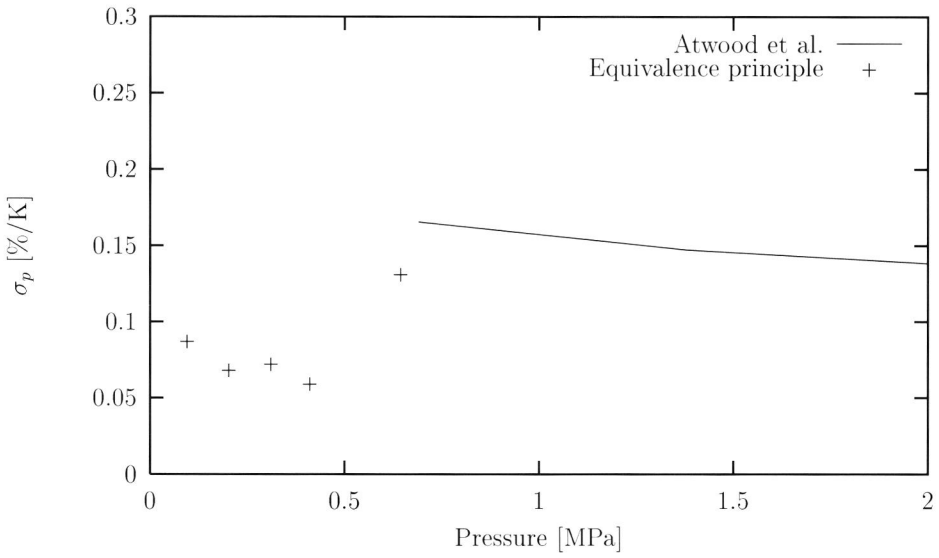

Figure 4.21: *Comparison of σ_p determined by equivalence principle, and as determined by using temperature conditioned samples.*

surface region. In this case the equivalence principle no longer holds. These results suggest that the absorption coefficient of HNF for CO_2-laser radiation is high. Experimental results that will be presented in Chapter 7 confirm this. Another explanation is a high reflection coefficient of the HNF burning surface. Further comparison between experimental and numerical results indicate that the reflection coefficient of HNF during combustion is higher than that of non-burning HNF, see section 6.2. The value of σ_p determined via the equivalence principle increases with increasing surface reflectivity.

4.6 Mixtures containing HNF

Several simple additives have been mixed with HNF and pressed to pellets. The effect of these additives on the combustion was determined. The intention of this study is to obtain a better knowledge of the combustion of HNF propellants. First the experimental set-up will be discussed. Then the manufacturing of the samples is addressed. This includes some hazard assessment tests of the obtained material. Experimental results on measured regression rate, condensed phase temperature profiles, and flame observations will then be discussed.

HNF - Aluminum

Aluminum is often added in a propellant to increase the flame temperature, thereby increasing the performance of a propellant. The effect of adding aluminum on the perfor-

mance of HNF propellants is illustrated in Fig. 1.3. Figure 4.22 shows the effect on the burning rate of adding 20% of aluminum to HNF (average Al particle diameter 20 μm). These experiments have only been carried out with 6 mm pellets.

The addition of aluminum enhances the burning rate approximately 30%, and increases the burning rate exponent from 0.95 to 1.02, see Fig. 4.22. This indicates that the aluminum participates actively in the combustion process, rather than being an inert heat sink. The monopropellant flame of HNF has a very high temperature compared to e.g. AP (2766 K vs. 1377 K at 1 atm). This fact, and the fact that HNF has a very short flame, may cause the aluminum to ignite already at the burning surface. Aluminum is efficiently oxidized by OH [10]. The OH-mole fraction above HNF is high, which also leads to efficient aluminum combustion. At low pressures there was some residue after combustion of the samples. The amount of residue decreased with increasing pressure. At pressures of 2 MPa no residue was observed. The more efficient aluminum combustion at higher pressures, causes an enhanced heat feedback to the burning surface with increasing pressure, and can explain the increase of the burn rate exponent.

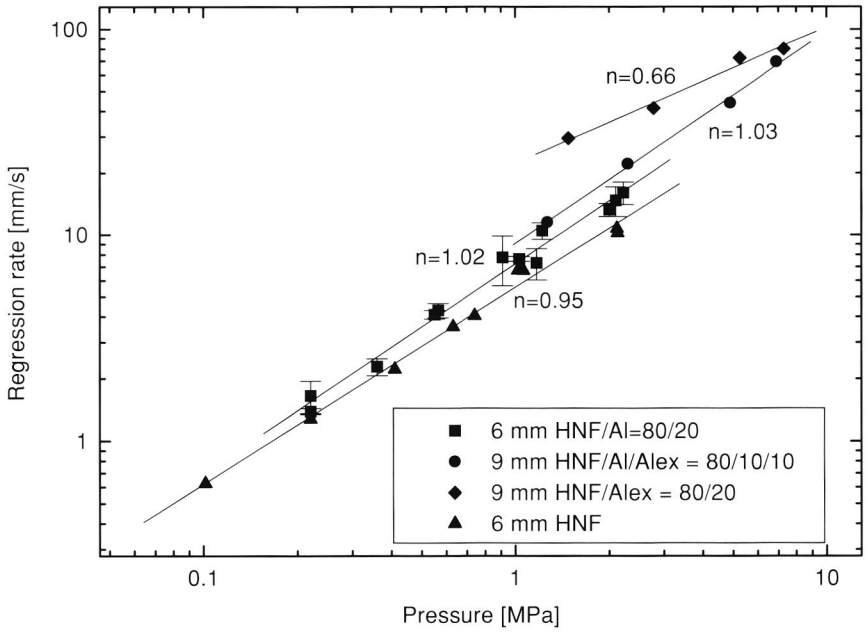

Figure 4.22: *Regression rate of pressed HNF with 20% aluminum additive.*

Also mixtures with ultrafine aluminum (Alex, $\sim$ 180 nm, from Argonide Inc.) have been made. This material is obtained by exploding aluminum wires by a high-current pulse in an argon atmosphere. Because of its small particle size, it is highly reactive. In a series of experiments with different propellant combinations based on an energetic binder, Alex was found to reduce the burn rate exponent of AP-based propellants. The propellant that contained 18% Alex even showed a negative n [140]. In propellants based on a mixture of AP/HMX (27% and 35% respectively) only the burn rate prefactor increased by replacing

conventional aluminum by Alex. These experiments indicate the possible use of Alex to modify the combustion behavior of propellants. Especially the lowering of the burning rate exponent is an interesting aspect with respect to HNF-propellants.

Figure 4.22 shows that a mixture 80/20 HNF/Alex burns very fast, with a mild burn rate exponent, $n = 0.66$. Because Alex is a very fine powder, it is impossible to make propellants with a high solid loading at 20% aluminum loading. A solution for this would be to partially replace the aluminum by Alex, e.g. 50/50 Alex/normal aluminum. However, as seen from Fig. 4.22, this combination also yields a high burn rate exponent, $n = 1.03$.

It should be noted that the burn rates of Alex mixtures are so high, that video recordings did not allow determination of the regression rate. For these experiments the burn rate was determined from the length of the pressure peak, and the sample length. This method was validated by comparing results for neat HNF-samples using video and pressure recordings.

CN-PLIF images for samples with aluminum and Alex are shown in Fig. 4.23. The mixtures with aluminum show similar behavior to that of neat HNF: a narrow CN-band of 400 μm width centered about 400 μm above the burning surface. The width of this CN-band decreases with pressure, while the intensity increases with pressure, see Fig. 4.24. The off-resonant signal is very small, while the natural emission of the flame is strong. The CN-PLIF images of HNF/Alex mixtures show a strong signal. Agglomerates are seen to come off the surface. The non-resonant image has a similar appearance as the resonant image. The strong signals in case of a non-resonant laser, are caused by laser scattering. When the laser is blocked the signals almost vanish. The signal level in the "tails" of the burning aluminum particles is higher for the resonant case. The PLIF images show that the Alex is burning at the surface. The liquid droplets of aluminum are ejected in the gas phase. Due to their velocity lag, hot gasses around the burning particles are entrained in the surrounding flow and form tails. Due to the short exposure time of 50 ns the images are frozen. This observation could only be made with the PLIF-camera. With the video-camera only over-exposed blurred images were obtained. For the mixture with conventional aluminum, the PLIF images show that the aluminum is not burning at 0.14 MPa. This is in agreement with the burnrate measurements, that show that the burn rate at ambient conditions is close to that of neat HNF (see Fig. 4.22).

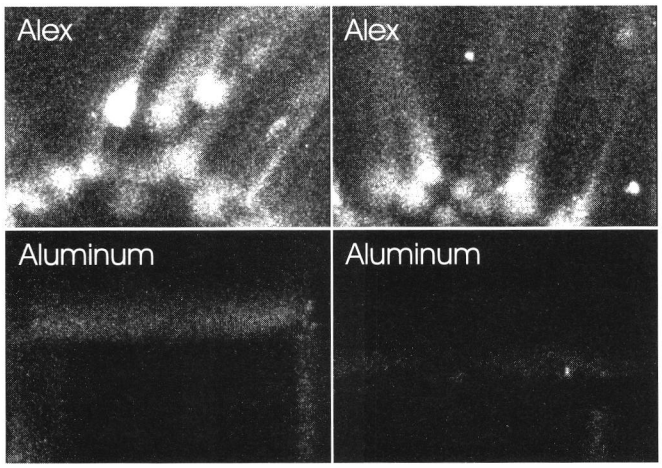

Figure 4.23: *CN-PLIF images of HNF mixtures with Alex (0.16 MPa) and aluminum (0.14 MPa). Left: resonant, right: non-resonant. All images on same intensity scale. Image size:* $6.2 \times 4.1\ mm^2$.

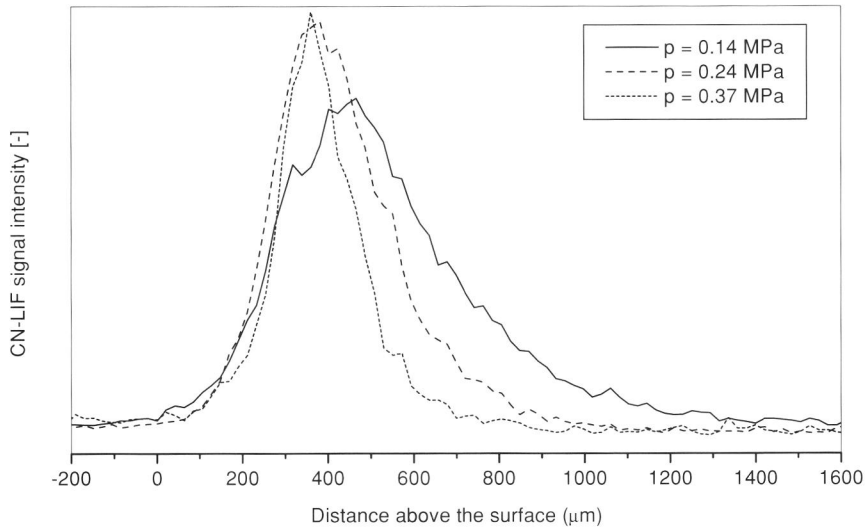

Figure 4.24: *CN-profiles for HNF/Al=80/20 mixture obtained by averaging PLIF images in horizontal direction.*

HNF - Graphite

The addition of small amounts of carbon containing materials to double-base propellants is known to influence their combustion characteristics [82]. In view of the NO_x-chemistry, the gas phase of HNF has similarities with double-base and nitramine propellants. It was decided to add 5% of graphite to HNF to evaluate the effect. At low pressures the burn rate exponent decreases from n=0.95 for neat HNF to n=0.81 for HNF/graphite, see Fig. 4.25. This is caused by the higher burn rate at low pressures. At high pressures the effect disappears and the regression rates become equal.

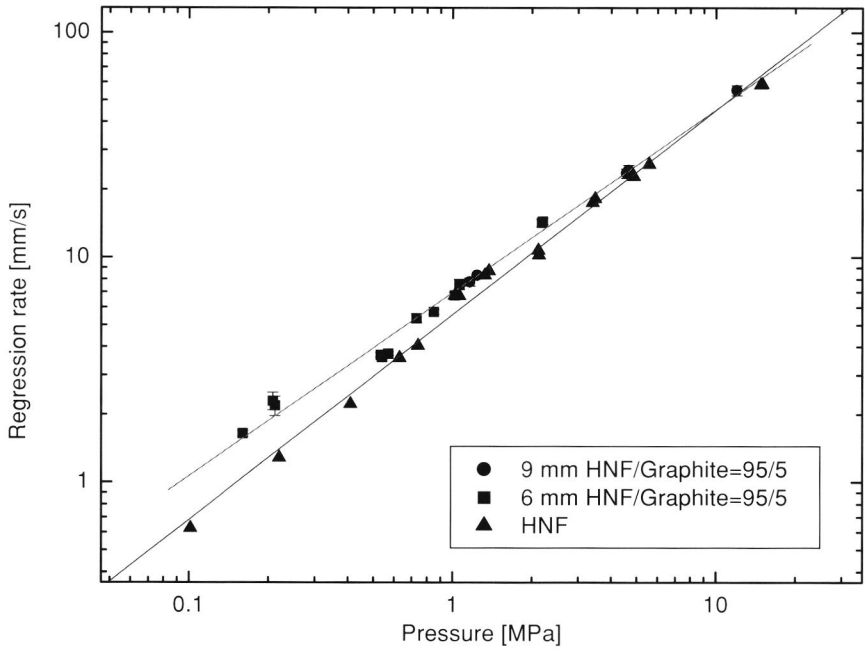

Figure 4.25: *Regression rate of pressed HNF with 5% graphite additive.*

The combustion of HNF-mixtures has been modeled using a modified PREMIX-code for 1D premixed gas flames [66] (see section 6.3). A few simple initial decomposition steps model the condensed phase. In the gas phase Yetter's kinetics for nitramines, together with the GRI-mech for hydrocarbon combustion are used [16, 165]. The calculations show that the reactions are faster in the gas phase close to the surface when graphite is added. This is caused by the combustion of the graphite by the excess oxygen of HNF. This explains the higher burn rates when graphite is added. At higher pressures the HNF flame is already very close to the surface. The graphite reaction is too slow under these conditions, and does not further increase the burn rate.

HNF-Paraffin

As a simplification for binder materials, paraffin has e.g. been used to study the combustion of ADN [159]. Paraffin wax is also compatible with HNF. Paraffin with a melting temperature of approximately 55°C was melted and mixed with HNF. After solidification the mixture was pressed to pellets.

Figure 4.26 shows the regression rate for a mixture containing 10% paraffin. This figure shows a large difference between the two experimental setups. At low pressures a thick paraffin melt layer is formed at the burning surface. The small samples are not inhibited on the outside. As a result, the melted paraffin partially drips along from the sides, away from the burning surface. This may explain the slope break between the low and high pressure experiments, n=0.81 and n=1.09 respectively. The flame standoff is considerably larger than for neat HNF, although the adiabatic flame temperature is slightly higher (2810 K vs 2766 K). At ambient pressure the flame standoff is $\sim 900\mu$m.

Figure 4.27 shows measured CN-profiles for HNF and mixtures with graphite and paraffin. The peak of the CN-profile does not shift when adding carbon black. In case of paraffin the CN-peak shifts away from the burning surface and becomes broader. In section 6.3 calculations of the combustion of HNF and additives are further discussed.

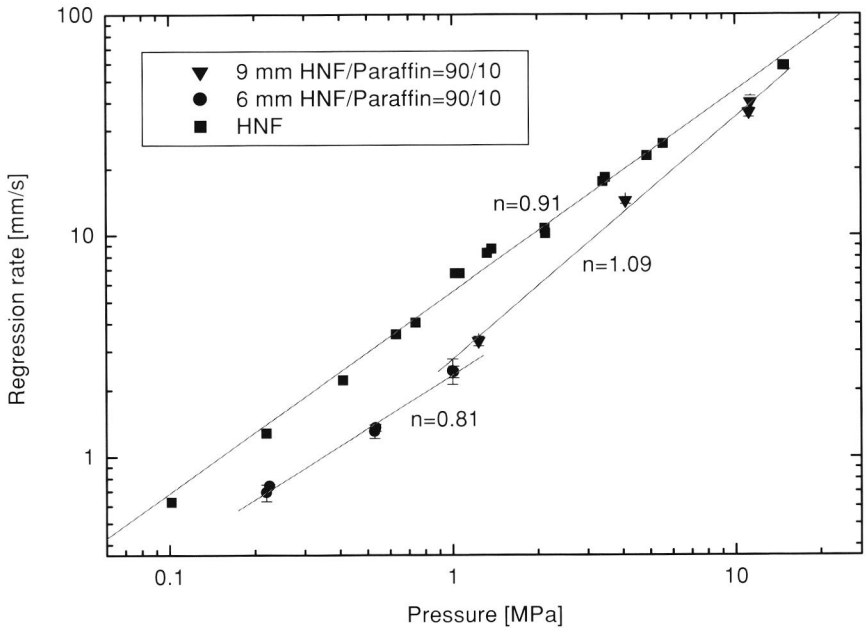

Figure 4.26: *Regression rate of pressed HNF with 10% paraffin additive.*

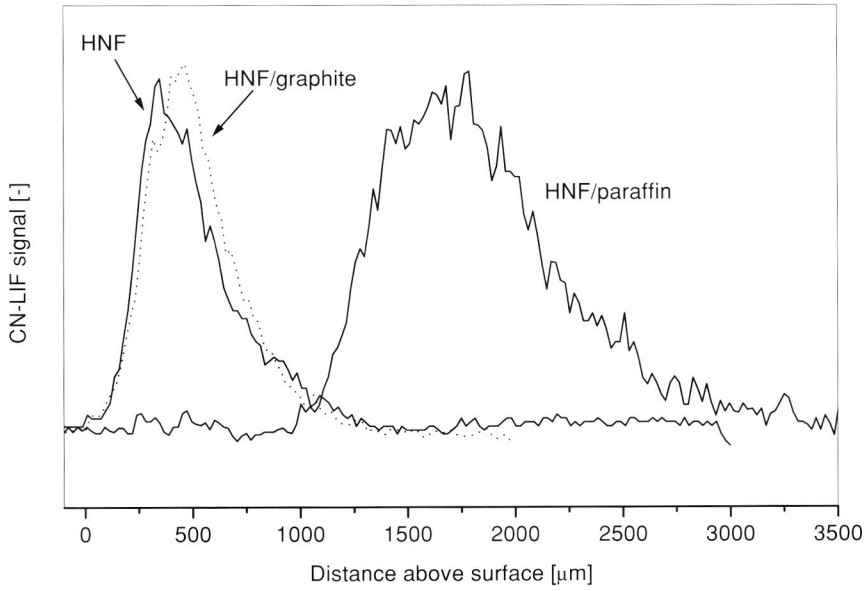

Figure 4.27: *CN-profiles obtained from PLIF images (pressure $\sim$ 0.15 MPa).*

4.7 Conclusions

Neat HNF pellets burn with a high regression rate. A slope break is observed around 2 MPa (from 0.95 to 0.85). The surface temperature increases with increasing pressure: at 0.1 MPa T_s=530 K and at 1 MPa T_s=680 K. The thermocouple measurements show a bend in the condensed phase temperature profile. This bend is attributed to cracks that form during combustion. Because of these cracks a thermal resistance is introduced in the condensed phase, leading to sharp bends in the condensed phase temperature profile.

NO, O_2, OH, NH, CN and CH radicals were identified in the flame by emission measurements. Absorption experiments show that the NO mole fraction decreases slowly above the burning surface. Within 1-2 mm above the burning surface the flame temperature is close to adiabatic. At 9 mm above the burning surface the NO mole fraction is still not at adiabatic conditions.

Samples containing 20% aluminum have about 30% higher burn rate at 1 MPa than neat HNF. The burn rate exponent is $n = 1.02$. At low pressures, a small amount of residue was found after combustion. However, at 2 MPa the pellets combust without residue. Mixtures with 20% Alex (ultra-fine aluminum powder) burn with a very high burn rate, and moderate burn rate exponent $n = 0.66$. Mixtures with 80/10/10 HNF/Alex/aluminum also show a high burn rate exponent $n = 1.03$.

Samples containing 5% graphite have a lower pressure exponent, n=0.81. This is caused by a higher regression rates at lower pressures. Around 10 MPa the burn rate is equal to that of neat HNF. Also paraffin-based combination burn with low pressure exponent n=0.81 at low pressures. However, at higher pressures an increase in pressure exponent was found, n=1.09.

Chapter 5

HNF sandwiches and propellants

5.1 Introduction

In the previous Chapter the combustion of neat HNF was addressed. This Chapter deals with the combustion of HNF in sandwiches and propellants. Sandwiches are alternating stacks of binder and oxidizer slabs. Because this is a simple 2D structure, combustion diagnostics are greatly simplified in comparison to propellants. Sandwiches are especially useful for visualization of diffusion flame structures between binder and oxidizer decomposition products [127]. In this Chapter the combustion of sandwiches of HNF/GAP and HNF/HTPB is studied. Propellants with coarse and fine HNF were formulated. The effect of the particle size on the combustion is studied. The study focuses on the combustion of GAP-based propellants, but also some results of HNF/HTPB-propellants are presented. Flame visualization was done by emission imaging and planar laser-induced fluorescence.

The Chapter starts with a discussion of some typical binder materials, like GAP and HTPB. This gives some more background on the materials that form the propellants and sandwiches. Most attention is paid to GAP, because that is the main focus of this work. The literature review for GAP combustion and decomposition is also used as input for the modeling in Chapter 6. In section 5.3 the combustion of sandwiches is presented. In section 5.4 HNF-propellant combustion is addressed.

5.2 Binders

5.2.1 Glycidyl azide polymer

The development of advanced solid propellants requires the use of energetic binders. For example, for the maximum performance gain at practical solid loads, HNF-propellants require the use of a binder different from the conventional polybutadienes because of the low oxygen balance of HNF compared to that of AP. The azido group may contribute to increase the energy content of many energetic materials, because of its positive heat of formation of 310 ... 400 kJ/unit [48]. Research programs in the late seventies showed that it was possible to make a relatively stable hydroxyl-terminated azido prepolymer, which was very suitable for use as a solid propellant binder: glycidyl azide polymer GAP). GAP is less oxygen deficient as hydroxyl terminated polybutadiene (HTPB). The oxygen balance

in combination with the energetic azide groups, makes it a high performance binder for HNF-propellants. Furthermore, GAP is an ideal binder for HNF as it contains no double bonds, which have been reported to be incompatible with HNF (see Chapter 2. The performance gain might even be higher when other energetic binders are employed, but GAP was chosen during initial HNF research at TNO because it was the only energetic binder that was commercially available in the beginning of the 90's.

Properties

The molecular structure of GAP is shown in Fig. 5.1. GAP is manufactured by polymerization of epichlorohydrin (ECH) to polyepichlorohydrin (PECH), followed by the conversion of PECH to GAP by reaction with sodium azide. In this last step, the C−C bond of PECH is replaced with a C−N_3 bond giving NaCl as a secondary product. The chain is terminated by OH. The bond energy of the N_3 groups is reported to be 378 kJ per azide group [84].

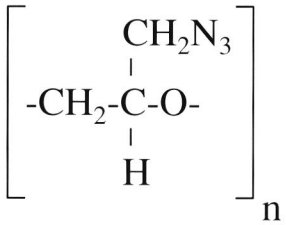

Figure 5.1: *Molecular structure of GAP.*

The azido groups in GAP increase the free volume in the polymer, because of the side group motion [143]. This lowers the glass temperature of GAP, compared with PECH. However, the mechanical properties of GAP at low temperature are poor, because of chain stiffening. Hence, GAP propellants can only meet the structural requirements at low temperature by heavy plasticization. Typical plasticizers employed are diglycol dinitrate (DEGDN), triethyleneglycol dinitrate (TEGDN), and methyltrimethylolmethane trinitrate (TMETN), which have been found compatible with GAP. Also azide terminated GAP (called GAP-A) is successfully employed. In the GAP-A plastizicer the OH-groups are replaced by N_3-groups. The most important properties of GAP are summarized in Table 5.1 (from Ref's. [48, 84]).

Monopropellant combustion

Like many other energetic binders GAP is characterized by its ability of selfsustained combustion. This is caused by the heat released during scission of the $-N_3$ bond structure to form N_2. Because of the high oxygen deficiency a lot of carbonaceous material is formed during *combustion* (actually it is an exothermic decomposition) of GAP monopropellant. At 5 MPa the theoretical equilibrium composition consists of (mole fractions) [84]:

N_2	$C_{(s)}$	CO	CO_2	CH_4	H_2	H_2O
22.38	28.47	13.95	0.13	2.15	32.19	0.71

Molecular formula		$C_3H_5N_3O_1$	
Molecular weight (weight average)	M_w	2097	g/mole
Molecular weight (number average)	M_n	1668	g/mole
OH-Functionality	f_{OH}	1.98	
Density	ρ_c	1300	kg/m^3
Glass point	T_g	-45	°C
Heat capacity	c_c	1.61	kJ/kgK
Thermal diffusivity	α_c	$\sim 1 \cdot 10^{-8}$	m^2/s
Heat of formation	ΔH_f	+118	kJ/mole
Adiabatic flame temperature (at 5 MPa)	T_f	1465	K
Oxygen balance		-121.09	%
Impact sensitivity		20	Nm
Friction sensitivity		324	N
Electro Static Discharge (10/10 no fire)		6.25	J

Table 5.1: *Overview of properties of GAP (from Ref's. [48, 84]).*

Although the adiabatic flame temperature of GAP is low (1465 K at 5 MPa, because the energy contained in the unit mass of GAP is small), the regression rates of GAP monopropellants are high, when compared with conventional solid propellants. Fig. 5.2 shows the regression rates at three different temperatures (from Ref.[84]). At 293 K the regression rate is given by

$$r_b = 5.27 \cdot p^{0.44} \quad [\text{mm/s}] , \tag{5.1}$$

where the pressure p is in MPa.

From Fig. 5.2 is becomes clear that the regression rate of GAP propellants is very dependent on the ambient temperature. The temperature sensitivity was found to be $\sigma_p = 1\%/\text{K}$, which is three times larger than that of conventional propellants. Furthermore the regression rates of GAP propellants are very sensitive to the amount of curative [48]. It has also been reported that the regression rate of GAP gumstock is profoundly affected by the type of isocyanate used for curing [47]. A typical example is shown in Fig. 5.3, which shows the effect of curing GAP with HMDI and N100 type isocyanate. It is seen that the burn rate of the HMDI system is about three times higher, without significant changes in the burn rate exponent. Another important aspect is the fact that the burn rate of the this - American - GAP/N100 propellant is about twice as low, as that of the - Japanese - GAP/N100 propellant of Fig. 5.2.

To understand the combustion behavior of GAP, thermocouple experiments have been carried out by Kubota and Sonobe [84]. These experiments show that the combustion wave of GAP propellants can be divided into three zones:

1. Nonreactive heat conduction zone.

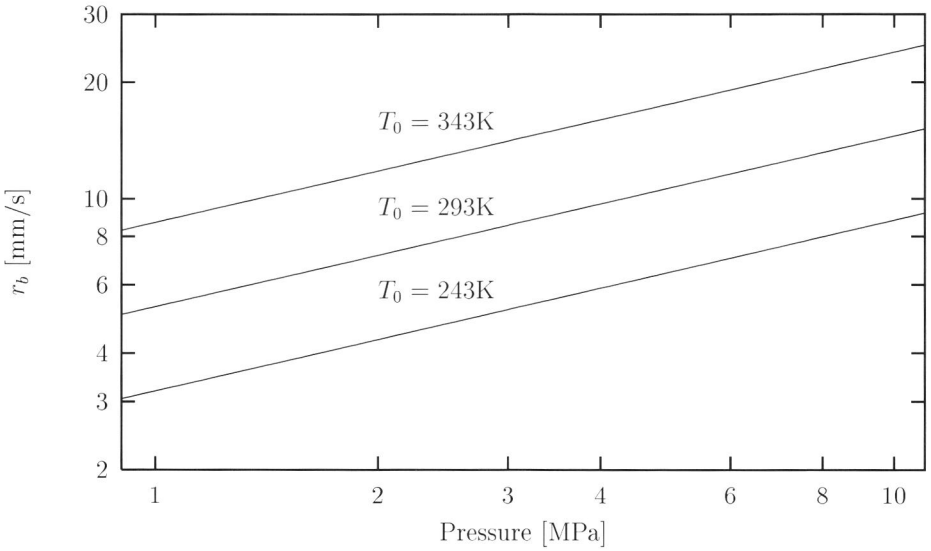

Figure 5.2: *Burning rate characteristics of GAP/N100 propellant showing high temperature sensitivity of the burning rate (from Ref. [84]).*

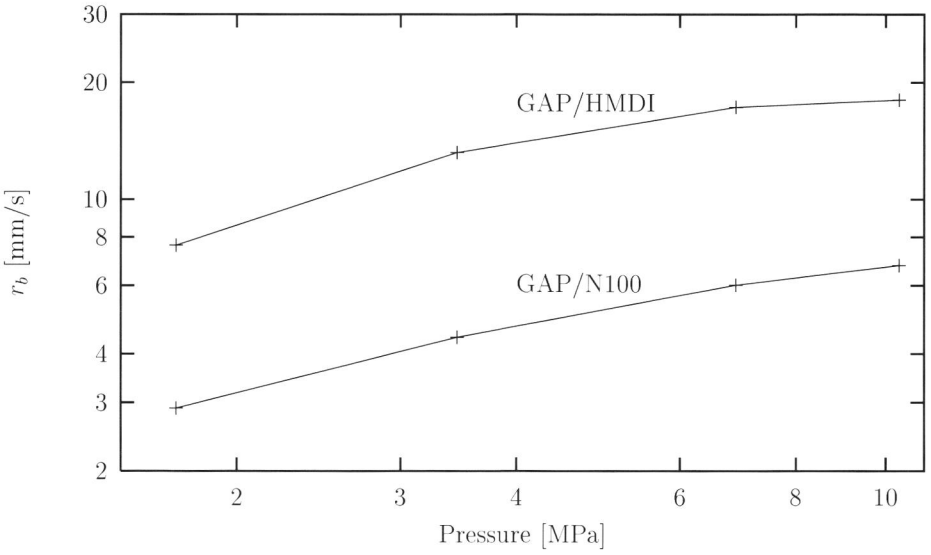

Figure 5.3: *Regression rate of GAP gumstock for different curatives (from Ref. [47]).*

2. Condensed phase reaction zone, starting when the decomposition temperature T_d is reached.

3. Gas phase reaction zone, in which the final combustion products are formed. Complete gasification occurs at the surface, which has temperature T_s.

It was found that T_d and T_s are relatively pressure insensitive.

The heat release in the condensed phase, Q_c, was determined to be 624 kJ/kg. The ratio between the heat feedback from the gas phase to the condensed phase heat release was determined to be 0.08 at 0.6 MPa. This result indicates that the exothermic reaction in the condensed phase, is the major heat source throughout the combustion wave of GAP propellants.

Since the regression rate of GAP is controlled mainly by the decomposition reaction at the burning surface, the kinetic decomposition rates obtained from decomposition experiments can be used to describe the combustion process of GAP. Using a value of $E_c = 87$ kJ/mole, the regression rate of GAP is given by the following 0-th order Arrhenius law

$$r_b(T_s) = Ae^{-E_s/RT_s} = 9.16 \cdot 10^3 e^{-8.7 \cdot 10^4/RT_s} \quad [\text{m/s}] , \tag{5.2}$$

where R is the universal gas constant. Differentiating Eq.(5.2) with respect to the initial temperature T_0 it is found that

$$\left(\frac{\partial T_s}{\partial T_0}\right)_p = \sigma_p \frac{RT_s^2}{E_s} . \tag{5.3}$$

Substituting the value of all parameters it is found that $(\partial T_s/\partial T_0)_p = 0.481$ at $p = 5$ MPa. From the above calculation of $(\partial T_s/\partial T_0)_p$, it is seen that an increase in the initial temperature, leads to a increase surface temperature which is almost half the initial temperature increase. Because of the high activation energy, this has a large effect on the regression rate.

In Fig. 5.4 the regression rate of GAP gumstock obtained in the TNO-PML strand burner is shown. When compared to the literature results for GAP/N100 (e.g. Fig. 5.2 and 5.3), it is seen that there is a large spread in the results. This difference is attributed to the different source of the GAP. Kubota's results have been obtained with GAP produced in Japan (JP). The results of Fig. 5.3 were obtained with GAP produced by 3M in the United States of America (US). The GAP of TNO comes from SNPE in France. With increasing pressure the pressure exponent is found to decrease. A fit to the TNO measurements above 2 MPa yields

$$r_b = (7.3 \pm 0.4) \cdot p^{(0.46 \pm 0.03)} \quad [\text{mm/s}] , \tag{5.4}$$

where the pressure p is in MPa (errors indicate the standard deviation of the parameters of the curve fit).

Decomposition

In a series of thermochemical analysis, Kubota and Sonobe have shown that the decomposition behavior of GAP propellants is a two stage process [84]. In the first stage, thermogravimetry (TG) shows a decrease of mass by 42% in the temperature range from

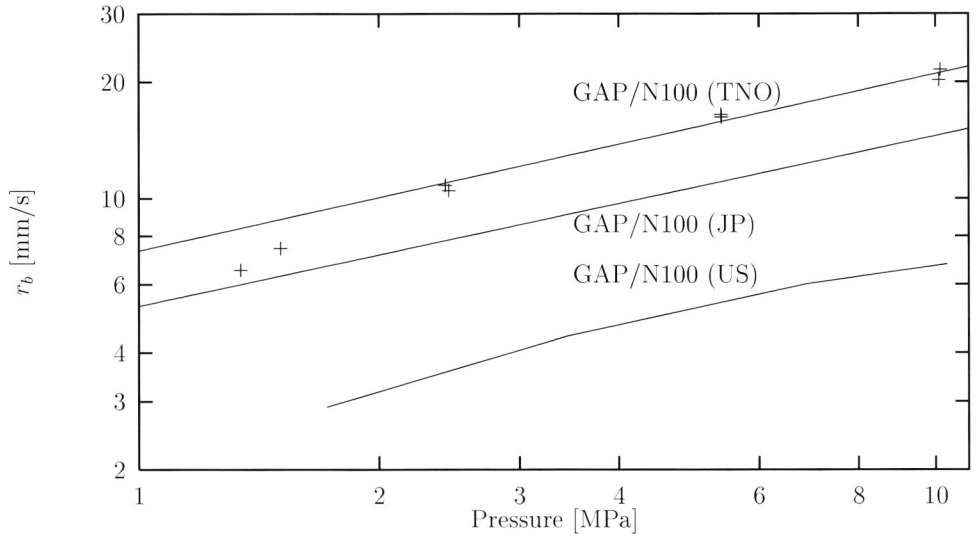

Figure 5.4: *Measured regression rate of GAP/N100 gumstock (TNO) in comparison with results from other experimenters (JP and US), see also Fig.'s 5.2 and 5.3.*

475 to 537 K. In this temperature range, differential thermal analysis (DTA) shows an exothermic reaction. The second stage starts at 537 K. In this stage there is a gradual decrease of mass, without heat liberation.

The results indicate that the exothermic reaction of GAP occurs only in the early stage of decomposition. It was verified that after the first decomposition stage, no N_3 was left in the sample. The initial decomposition of GAP is considered to be caused by the decomposition of the molecular structure $-CH_2-N{=}N_2$ to $-C{\equiv}N + N_2 + H_2$. This decomposition is highly exothermic, 685 kJ/mole. Accordingly, an acrylonitrile structure is formed in the initial stage of the decomposition process. Succeeding decomposition of the molecular structure liberates carbon and oxygen atoms.

Similar results were found by Krause and Pfeil [79]. They also investigated the differences between cured and uncured GAP on the decomposition mechanism. No differences were found between cured GAP (at several NCO/OH ratios), and uncured GAP. These results indicate that the decomposition of GAP is determined by the $N{-}N_2$ group scission.

The above mentioned decomposition experiments agree well with recent measurements of Hori and Kimura [61]. By replacing part of GAP by polypropylene glycol (PPG), which is very similar to GAP (less the azido group), they were able to validate the following simple model for GAP combustion

$$\text{GAP} \overset{\text{N}_2^{\uparrow},\, Q_c}{\longrightarrow} \text{Fragments} \overset{\text{Oxidation},\, Q_f}{\longrightarrow} \text{Final products}\,, \tag{5.5}$$

where Q_c is the heat released during the the first stage condensed phase decomposition, and Q_f the heat released during the second stage. Q_c is used to heat up the propellant to its

surface temperature T_s, and Q_f is used to heat it further from T_s to the flame temperature T_f. Again it was concluded that $Q_f \ll Q_c$.

Kubota determined the activation energy from DTA curves at various heating rates by Kissinger's method [69, 84]. The activation energy was determined to be 174 kJ/mole. This result agrees well with the estimated dissociation energy of 170 kJ/mole of the $N-N_2$ bond [79]. It has been reported that the *apparent* activation energy during linear (regression) pyrolysis is half of that measured in bulk degradation experiments, such as DTA and TG analysis [21]. Thus the value of the activation energy for condensed phase decomposition during combustion is $E_c = 87$ kJ/mole. To evaluate the effect of heating rate and pressure on the decomposition pathways of GAP, experiments at varying heating rates and pressure have been carried out [121]. It was found that both pressure and heating rate have little effect on the composition of the decomposition products of GAP.

Decomposition differences between OH terminated, GAP-OH, and azide terminated, GAP-A, have also been studied [120]. The azide terminated GAP was found to have a higher decomposition rate. The activation energy of bulk decomposition was found to be equal. This indicates that the azide groups at the terminal position of the chain decompose independently of the polymer chain, and other azide groups on the main chain. If it is assumed that the heat of decomposition if fully generated by the reaction of the azide group, one azide group was found to generate 316 kJ in case of GAP, and 315 kJ in case of GAP-A.

5.2.2 Hydroxyl terminated polybutadiene

Nearly all composite solid propellants that are manufactured today use polybutadiene (PB) binders. Three types are used: polybutadiene-acrylic acid-acrylonitrile (PBAN), carboxyl-terminated polybutadiene (CTPB), or hydroxyl-terminated polybutadiene (HTPB). Because of the improved mechanical properties at low temperatures, and lower mixing viscosities leading to propellants with higher solid loading than with other polybutadienes, HTPB is now the preferred binder. HTPB is commonly cured by reaction with isocyanates to produce polyurethanes. The chemical structure of HTPB is shown in Fig. 5.5.

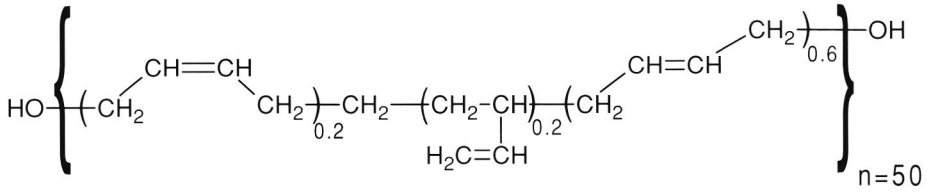

Figure 5.5: *Chemical structure of HTPB.*

5.3 HNFsandwiches

In this section the experimental results of the combustion of HNF-sandwiches are presented.

5.3.1 Emission imaging

HNF/GAP sandwiches with a 250 μm binder lamina were burned at different pressures [97]. The video images of these experiments are shown in Fig. 5.6. The images were obtained using different lens aperture settings due to the increasing flame luminosity with increasing pressure. The experiments show that the GAP binder regresses along with the HNF surface. At the binder/oxidizer interface, the HNF regresses faster than at some distance from the binder. However a diffusion flame is not visible in the wavelength range of visible light.

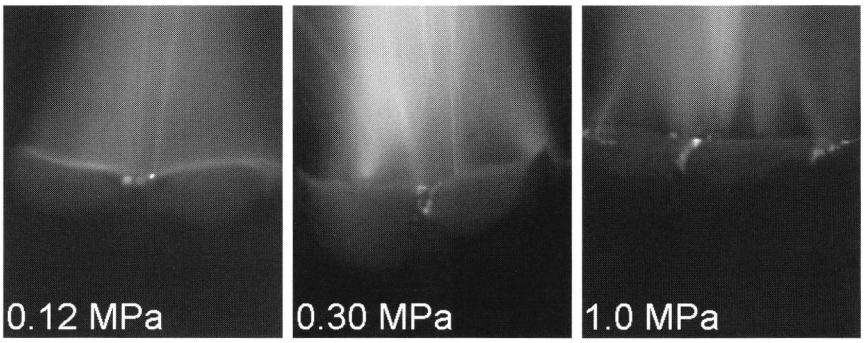

Figure 5.6: *Video images of sandwiches of HNF and GAP at 0.12, 0.30 and 1.0 MPa (image size = 8.4 × 6.9 mm^2). The GAP slab is centered in the middle, surrounded by the HNF. Direction of the regression is from top to bottom.*

To further resolve a possible diffusion interaction in these sandwiches, emission images were obtained for different radicals. An interference filter centered at 241.5 nm, and a FWHM of 18 nm was used to visualize the chemiluminescence of the γ-bands of NO. The chemiluminescence of the A←X transition of OH was determined by an interference filter centered at 310 nm with a FWHM of 20 nm. Emission from CN was detected through a combination of Shott filters UG-11 and GG-375. This combination forms a band pass filter, centered at 385 nm with a FWHM of approximately 20 nm. This passes the chemiluminescence of the B←X transition of excited CN at 388 nm.

Figure 5.7 shows the CN, OH, and NO emission images of HNF / GAP sandwiches at 0.12 MPa. All three radicals show an intense bright emission above the burning surface of HNF. CN and OH also have a continuous emission above the burning surface. Only the NO emission reveals the diffusion interaction pattern. The sequences shown in Figure 5.8 and 5.9 allow further comparison of the OH emission images and NO emission images. These sequences also show that the NO emission yields more information about the flame structure of the diffusion flame.

As mentioned, the HNF/GAP sandwiches show a higher regression rate near the binder-fuel surface. The regression rate of GAP is higher than that of HNF at low pressures.

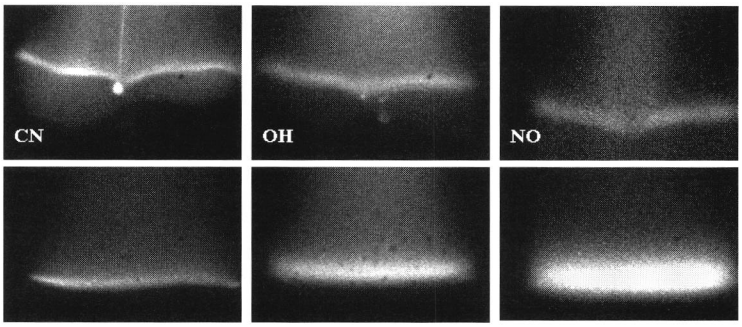

Figure 5.7: *Emission of HNF/GAP sandwich at 0.12MPa. From left to right: CN, OH, and NO emission. As a reference the emission images of neat HNF are also given at the lower row. Image size* $= 4.1 \times 6.2\ mm^2$*).*

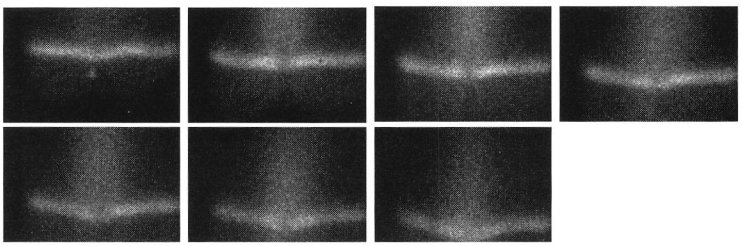

Figure 5.8: *Sequence of NO emission of HNF/GAP sandwich at 0.12 MPa (image size* $= 4.1 \times 6.2\ mm^2$*).*

Assuming that the HNF and GAP burn independently, it is plausible that the V-shape forms. This results in an increasing V-shape during combustion (see e.g. Fig.'s 5.8 and 5.9). It has been reported that the regression rate of HNF with additives is higher than that of neat HNF [98]. The cause of this is a higher heat feedback to the burning surface, due to a steeper temperature profile in the presence of a fuel. A similar mechanism might enhance the burning rate of the HNF/GAP interface even more. Because NO emission shows the diffusion pattern most clearly, it was decided only to measure NO emission images for the HNF/HTPB sandwiches.

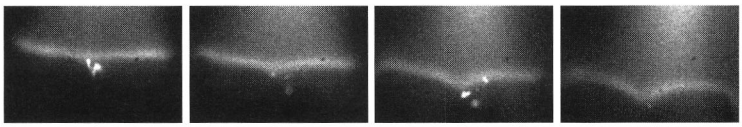

Figure 5.9: *Sequence of OH emission of HNF/GAP sandwich at 0.12 MPa (image size* $= 4.1 \times 6.2\ mm^2$*).*

Video images of HNF/HTPB sandwiches are shown in Fig. 5.10. These images show that the HTPB binder slab extends above the burning surface of HNF. Above the HTPB binder a very bright diffusion flame is visible. The flame standoff (from binder surface to luminous flame) and binder protrusion decrease with increasing pressure, see Fig. 5.11.

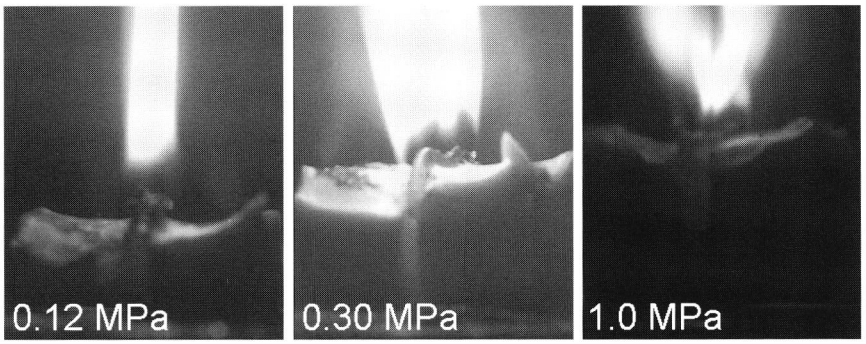

Figure 5.10: *Video images of HNF/HTPB sandwiches at 0.12, 0.30 and 1.0 MPa (image size* $= 8.4 \times 6.9$ *mm*^{2}*).*

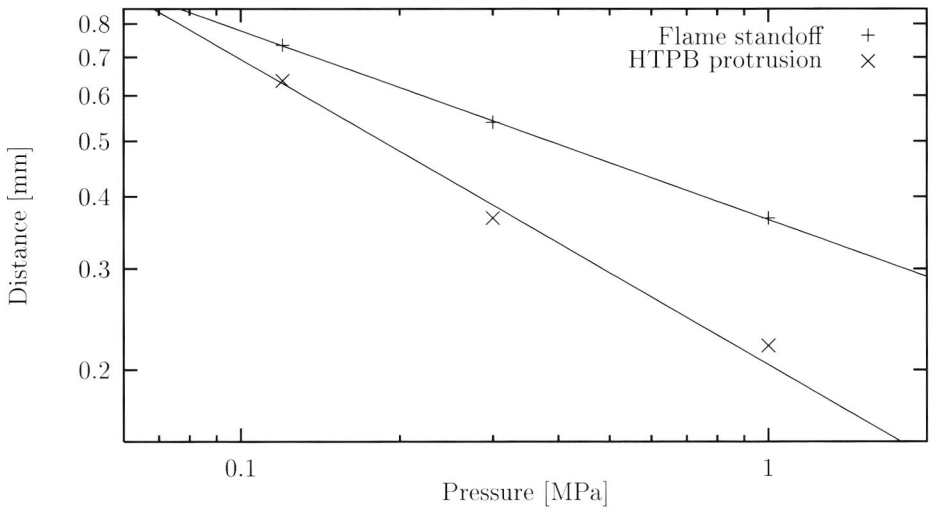

Figure 5.11: *Flame standoff and binder protrusion of a HNF/HTPB sandwich.*

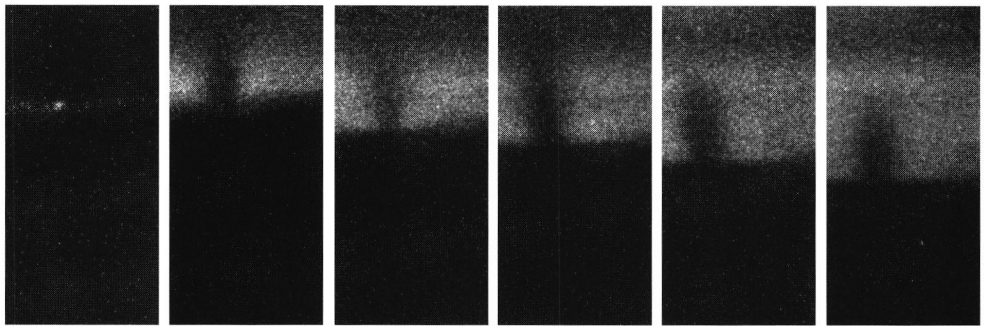

Figure 5.12: *OH PLIF image of HNF/GAP sandwich at 0.35 MPa (image size* $1.9 \times 4.1\ mm^2$*).*

The NO emission images showed a very bright diffusion flame. The emission from the luminous flame makes it difficult to detect the emission from NO in the neat HNF flame. The diffusion flame with the HTPB binder is further away from the burning surface, and less pronounced that that with a GAP binder. These observations are in agreement with the results from Parr and Hanson-Parr [123].

The flame-standoff of the HTPB-sandwich is larger than that of neat HNF: 200 μm vs 800 μm, at atmospheric pressure. This implies that there is no extra heat feedback from the diffusion flame, and the surface is only cooled due to the endothermic HTPB decomposition and capacitive heat loss. In the section 5.4 it is reported that the burning rate of a HNF/HTPB formulation is considerably lower than that of a HNF/GAP formulation. This is in agreement with the findings for the sandwiches.

5.3.2 PLIF experiments

The emission experiments only image the excited species. The LIF-technique allows detection of all species, which makes direct comparison with modeling results possible. It was therefore decided to also obtain PLIF-images of sandwich combustion. Both OH and CN-PLIF images of sandwiches were obtained. The detection and excitation schemes were similar to that for the neat HNF PLIF-experiments of section 4.4.3.

OH-PLIF

Figure 5.12 shows a single OH-PLIF sequence of a HNF/GAP sandwich at 0.35 MPa. Above the HNF (outer slabs) there is OH. Above the GAP there is no OH, because the GAP decomposition products are fuel rich. There the OH is rapidly consumed by the fuel rich gases.

With increasing pressure the mixing becomes more and more difficult. This results in a smaller 'non-OH' zone above the GAP slab, see Fig. 5.13. The width of the zone without OH is defined as the distance between the points where the OH-signal drops to half the value above the sandwich. For the pressures of Fig. 5.13 this zone width is shown in Fig. 5.14. The error bars shown in this figure represent the standard deviations of the

average (i.e. the standard deviation of the measurements at each pressure, divided by the square root of the number of images used to determine the average).

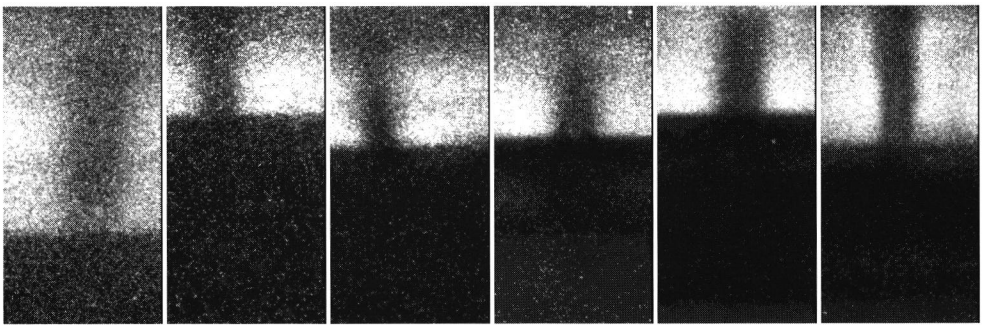

Figure 5.13: *OH PLIF images of HNF/GAP sandwiches. From left to right: 0.11 MPa, 0.24 MPa, 0.35 MPa, 0.47 MPa, 0.53 MPa and 1.07 MPa (image size* 1.9×4.1 mm^2*).*

At pressures below approximately 0.3 MPa the GAP in the sandwiches does not seem to burn steadily. During experiments at these pressures the images that are obtained show either a homogeneous OH structure, or the clear diffusion structure. In Fig. 5.15 a typical example of such intermittent combustion is shown. Neat GAP gumstock did not show selfsustained combustion below $\sim$ 0.4 MPa in the high pressure bomb. This agrees with the fact that the intermittent combustion is observed during sandwich combustion.

CN-PLIF

The CN PLIF-images are the complement of the OH images. Above the HNF there is only a small narrow band where CN is found. Above the GAP the CN sticks out above the surface, see Fig. 5.16. The CN LIF-measurements also show intermittent combustion of the GAP, see Fig. 5.17.

The width of the CN zone above the GAP slab as function of pressure is shown in Fig. 5.18. With increasing pressure the CN zone thickness approaches the binder slab thickness because the diffusion decreases with pressure. Also in this figure the error bars indicate the standard deviation of the average at each point. The point at 0.8 MPa does not have a standard deviation, because only a single image was available.

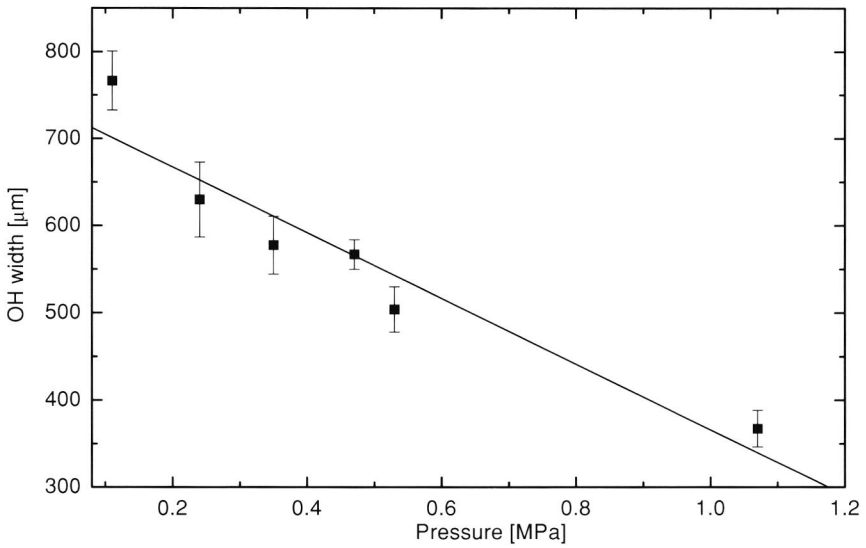

Figure 5.14: *Width of the zone without OH above the sandwich. GAP binder slab thickness is* $\sim 280\mu m$.

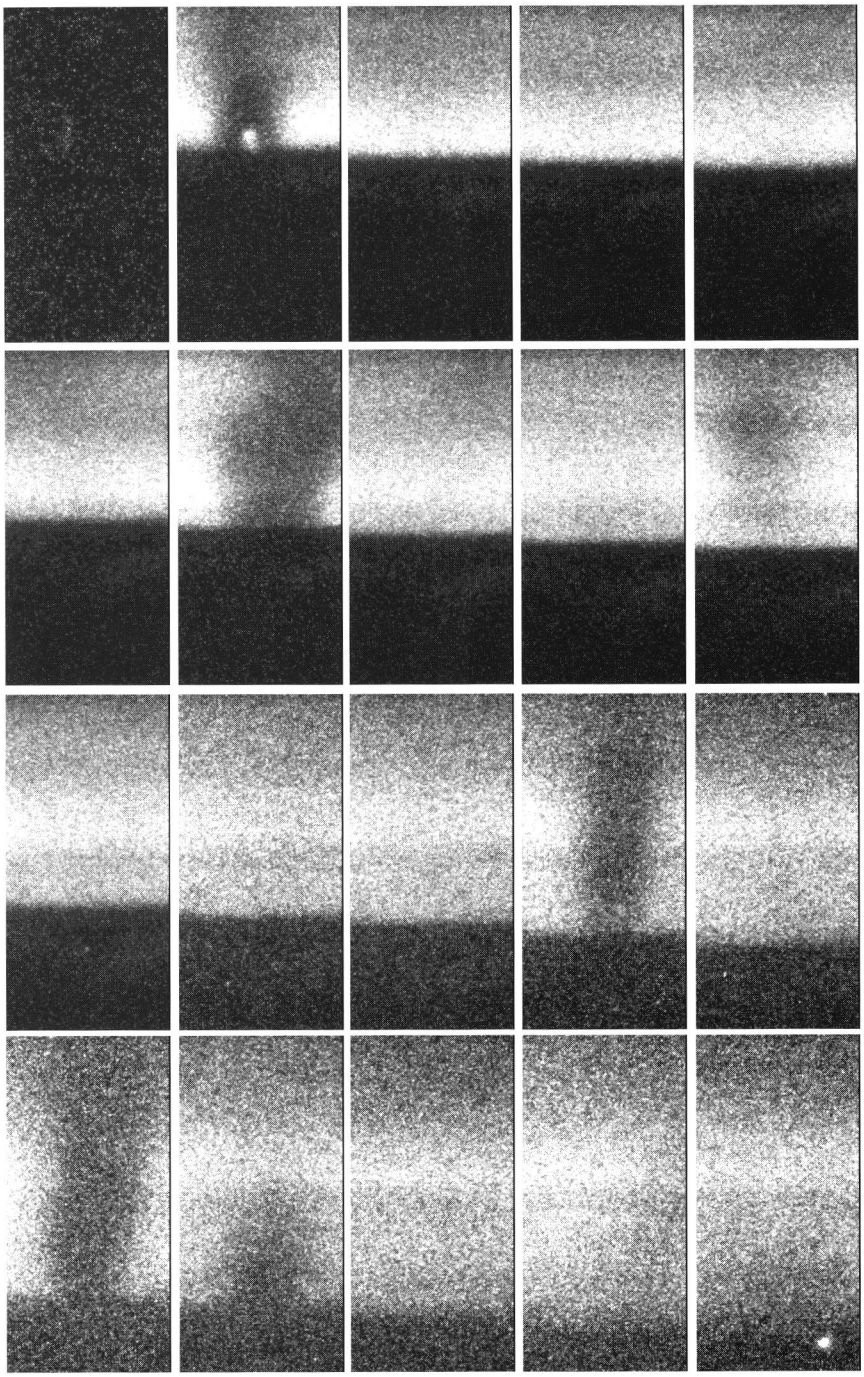

Figure 5.15: *OH-PLIF sequence of a HNF/GAP sandwich at 0.11 MPa. Laser repetition rate is 3 Hz. Note the intermittent combustion of the GAP.*

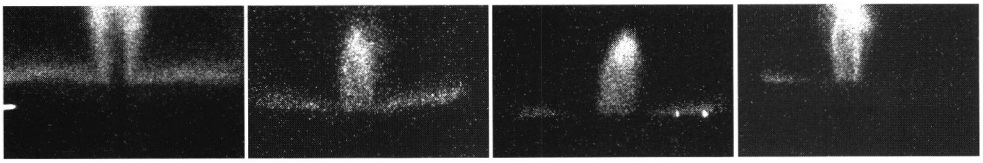

Figure 5.16: *CN PLIF images of HNF/GAP sandwiches. From left to right: 0.14 MPa, 0.28 MPa, 0.40 MPa, 0.47 MPa (image size* 1.9×4.1 mm^2*).*

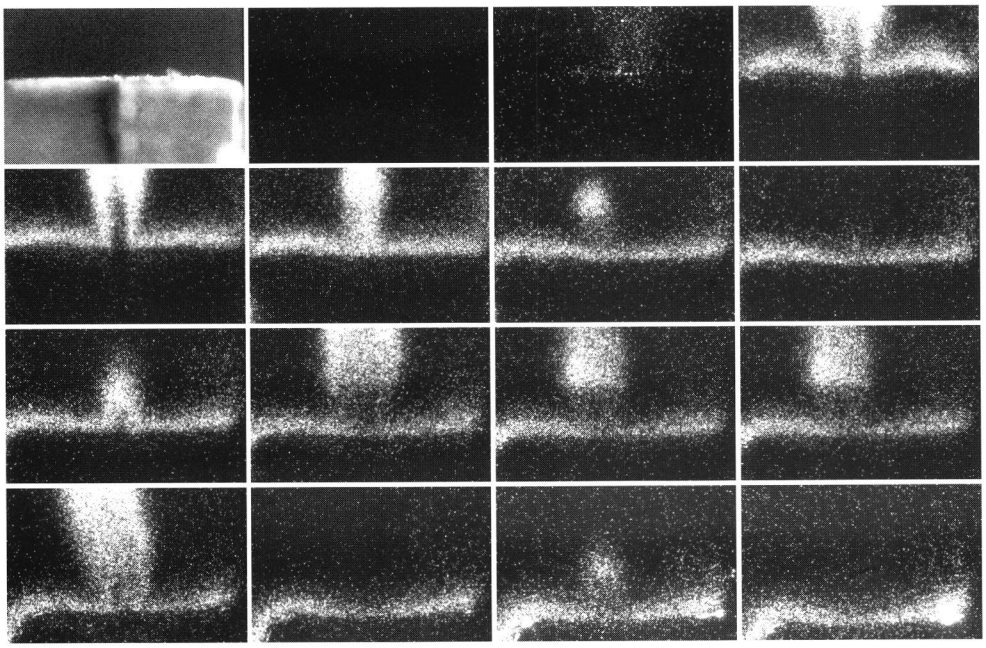

Figure 5.17: *CN PLIF images of HNF/GAP sandwiches at 0.14 MPa. The first image shows the sandwich (in UV). The laser repetition rate is 8 Hz.*

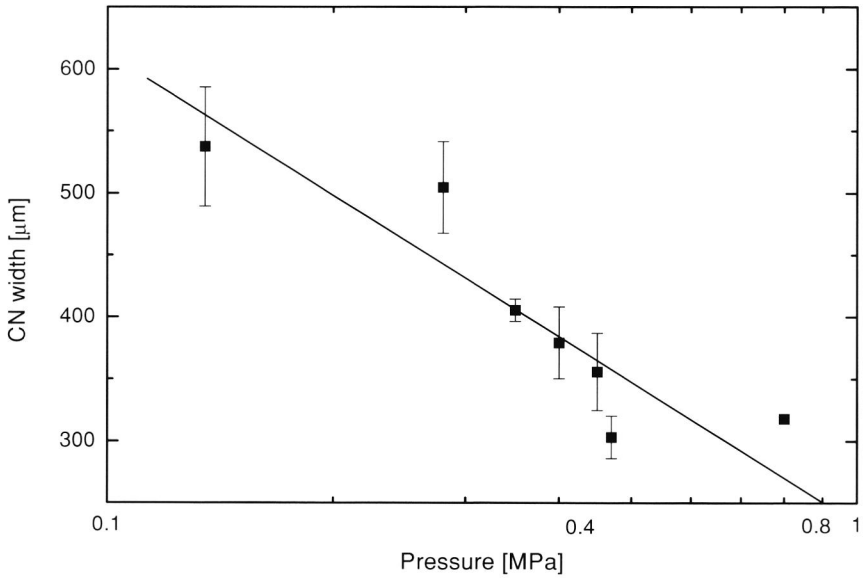

Figure 5.18: *Thickness of the CN zone above the GAP slab as function of pressure.*

5.4 HNF propellants

Two types of HNF propellants were used in this work. The first is a HTPB-based propellant with a solid loading of 75%. This propellant contains a bimodal mixture of coarse HNF (474μm, type C15) and fine HNF (100μm, type S16). The particle size is based on an equivalent spherical volume. The HNF particles are needle shaped. These two grades have an L/D ~5. Consequently the solid loading was limited to 75%. The propellant formulation is summarized in Table 5.2.

Material	Composition [%]
HNF C15 + S16	73
Additives	2
Binder	
HTPB + isocyanate + plasticizer	25

Table 5.2: *Formulation of HTPB-based propellant HHU-2-1 (mass percentages).*

The other propellant formulations contain the energetic binder GAP. To determine whether the HNF particle size affects the burn rate, two propellants were manufactured with the above mentioned different HNF types available. To allow for a good comparison, the solid loading for both propellants was the same. Because of the monomodal particle size distribution and the viscous GAP binder, the maximum solid loading that could be obtained was 55%. Table 5.3 summarizes the composition of the HNF/GAP-propellants.

Material	Propellant 1 HGU-19-1	Propellant 2 HGU-20-1	Propellant 3 HGU-23-1
HNF			
HNF C15 (coarse)	55		35
HNF S16 (fine)		55	15
Aluminum			18
Binder			
GAP + isocyanate	45	45	32

Table 5.3: *Formulation of GAP-based propellants (mass percentages).*

A third HNF/GAP-propellant (HGU-23) with aluminum was also casted. To increase the solid load, the HNF was treated to form more spherical crystals by the method described in section 3.2. The total solid loading was 68%, which includes 18% aluminum. For successful curing the amount of curing catalyst had to be doubled with respect to the propellants HGU-19 en HGU-20. It was also attempted to formulate propellants containing 68% HNF. However, these propellants did not cure satisfactory. It seems that the curing process using isocyanates becomes more difficult when the HNF loading or HNF surface area is high.

5.4.1 Burn rate

The regression rate of both HNF/GAP propellants is shown in Fig. 5.19. For the propellant with coarse HNF C15 the burning rate exponent is $n = 0.71 \pm 0.03$ (the error is the standard deviation of the curve-fit). Within experimental accuracy, the propellant containing fine HNF has the same burn rate exponent $n = 0.67 \pm 0.01$. For reference the regression rates of neat HNF and GAP are also shown (both TNO-data). The difference in regression rate between the coarse and fine HNF is very small. At 5 MPa the absolute difference is 0.7 mm/s, with an average regression rate of 17.5 mm/s.

The propellants burn faster than neat HNF at low pressures. Above 2 MPa the burn rate is lower than that of neat HNF. With respect to the burn rate of neat GAP, the situation is opposite. There are two mechanisms for this behavior. At low pressures, the higher burn rate of GAP enhances the burn rate of the propellant, and at higher pressures the slow GAP combustion limits the burn rate. More details about this mechanism are outlined in section 8.2. The other mechanism, enhances the burn rate of the propellant at low pressure. The addition of fuel to HNF causes a steeper temperature gradient, causing the burn rate to be higher than that of neat HNF. As the pressure increases, the NO reactions become faster, and the effect of additional fuel reduces [98]. The sandwich experiments also show that around the HNF/GAP surface the burn rate is higher. So, at low pressures the burn rate is further enhanced by the presence of fuel decomposition products of GAP.

The effect of adding aluminum in a propellant is shown in Fig. 5.20. At low pressures the burn rate is slightly higher than that of the non-aluminized propellants. With increasing pressure this difference decreases. The burn rate exponent is $n = 0.65 \pm 0.05$. It is concluded that the effect of the addition of aluminum on the burn rate is small. This result is

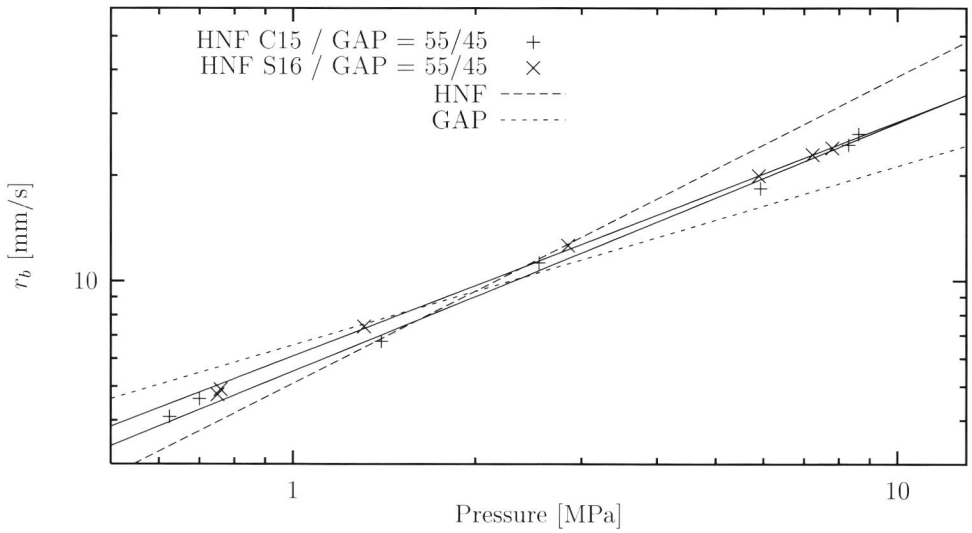

Figure 5.19: *Regression rate of HNF/GAP propellants, compared to that of neat HNF and GAP.*

in agreement with earlier experimental findings for HNF/polyNIMMO propellants with different aluminum loading [92]. Also for these propellants the effect of aluminum loading on the burn rate was found to be negligible compared to experimental errors.

The measured burn rate of the HTPB propellant is shown in Fig. 5.21. Compared to the GAP- based propellant the burn rate is much lower, although the HNF oxidizer content is 73% compared to 55% in the GAP propellant. This is in agreement with the sandwich results which showed a protruding HTPB binder that does not take part in the combustion process close to the burning surface. The burn rate exponent of this propellant is also higher n=1.01±0.05. This pressure exponent resembles that of neat HNF (0.85-0.90). The small differences are probably caused by heat losses due to the use of HTPB.

The propellant containing HTPB left a residue after combustion. Due to this residue it was impossible to determine the structure of the flame zone from video or emission imaging. Figure 5.22 shows the remaining mass residue as a function of combustion pressure. Below 0.5 MPa the combustion is smoldering, producing a yellow sooth in the combustor. Most probably this is HNF vapor, which has also been observed during neat HNF combustion [102]. Above 0.5 MPa flames become visible. The residue above 1 MPa is probably caused by 1% of non-combustible additive that is present in this propellant. When this propellant was burned in air, luminous flames were also observed below 0.5 MPa.

Within the CEPA-14 program a HNF-polyNIMMO propellant was formulated. This propellant contained 68% HNF. The binder consisted of polyNIMMO with GAP-A plasticizer. The regression rate of this propellant is shown in Fig. 5.23. The pressure exponent is n=0.99. Which is comparable to that of the HTPB propellant, although the polyNIMMO propellant contains less HNF. The regression rate of the polyNIMMO propellant

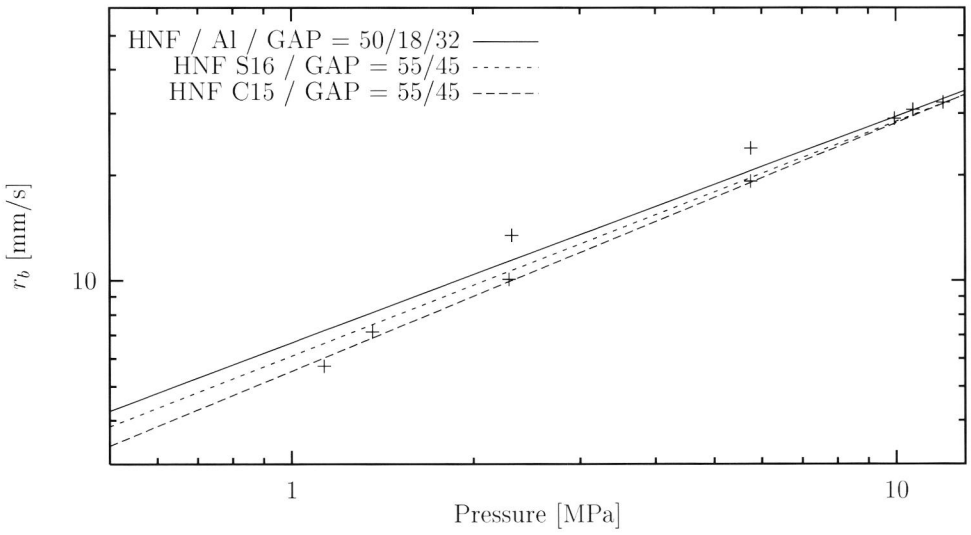

Figure 5.20: *Regression rate of HNF/Al/GAP propellants, compared to that of two propellants without aluminum.*

is higher. The burn rate of neat polyNIMMO was not found in literature. Because of its energetic content, it seems plausible that polyNIMMO can burn self-sustained (especially when plasticized with GAP-A). The overall regression rate of the propellant seems therefore largely affected by the burn rate of the binder as well. Note however, that for all these academic propellants the solid loadings are low. For more practical propellants the amount of binder will almost have to be halved. Thereby probably reducing the effect of the binder.

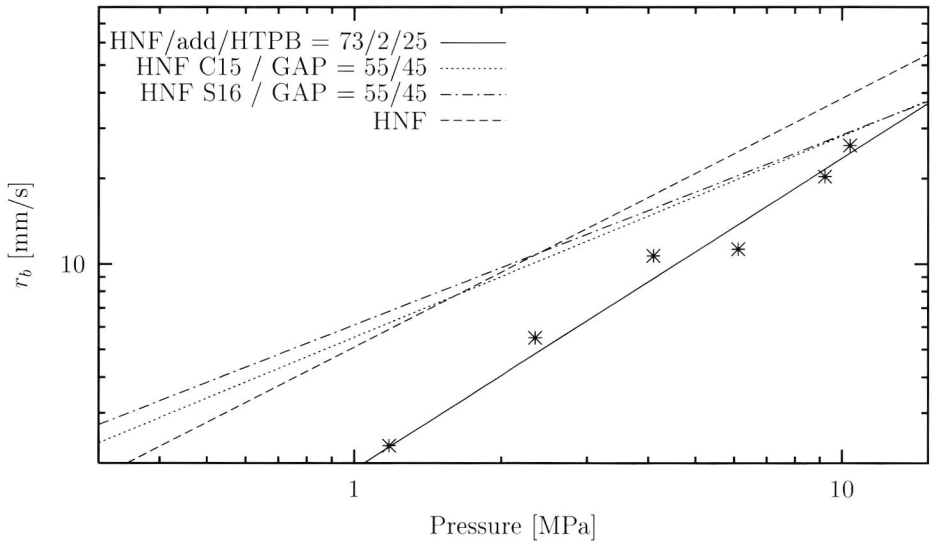

Figure 5.21: *Regression rate of HNF/HTPB propellants, compared to that of neat HNF, and HNF/GAP propellants.*

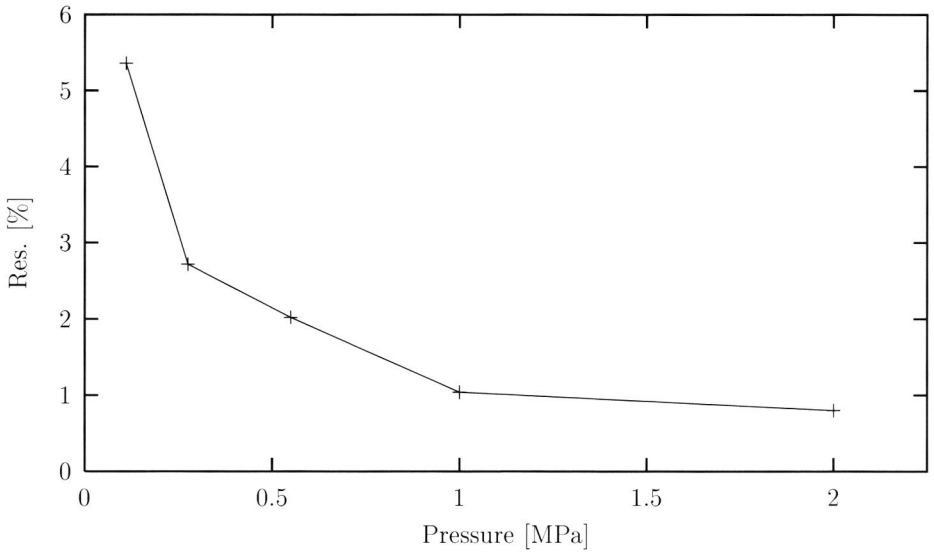

Figure 5.22: *Mass residue of HNF/HTPB propellant.*

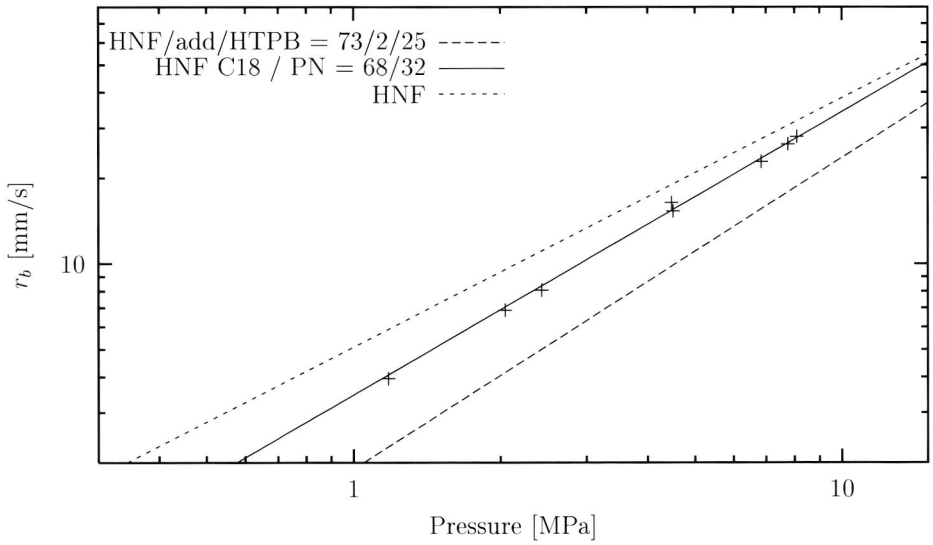

Figure 5.23: *Regression rate of HNF/polyNIMMO propellants, compared to that of a HNF/HTPB propellant and neat HNF.*

5.4.2 Emission imaging

Figure 5.24 shows video images of the HNF/GAP propellants for the two different types of HNF (C15 coarse, S16 fine) in comparison with images of neat HNF. The propellant with fine HNF did not burn self-sustained when the CO_2-laser was switched off below 0.3 MPa. The image at 0.12 MPa for this propellant was obtained with the CO_2-laser operating.

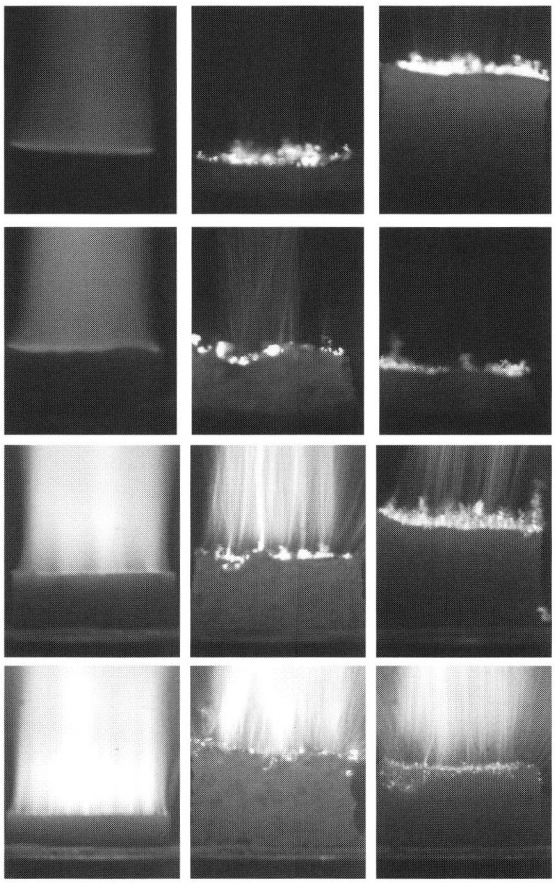

Figure 5.24: *From left to right: Video images of HNF, HNF C15/GAP, and HNF S16/GAP. From top to bottom: 0.12 MPa, 0.3 MPa, 0.9 MPa, and 2.0 MPa. The image at 0.12 MPa with HNF S16 was obtained with the CO_2-laser switched on (image size = 8.4×6.9 mm^2).*

The flame of neat HNF is brighter than that of the HNF/GAP propellants. The neat HNF has a bluish color at all pressures. This emission comes from CN* and CH* radicals [27, 98]. This bluish color only becomes visible at elevated pressures in the HNF propellants. The propellant with the coarse HNF shows a heterogeneous flame structure. Except for the CN* emission, the emission from neat HNF is stronger than that of the

propellants. This is caused by the continuous emission from the protruding binder. The UG-11 filter used for the CN emission also passes some light around 600 nm. Therefore the CN*-emission has to be interpreted carefully for bright flames.

When emission images are compared, it becomes clear that in case of the coarse HNF not the whole surface of the propellant is burning. Only at localized spots there is emission from the surface. A typical example of this is shown in Fig. 5.25. The size of the emission spots matches the HNF particle size. Another example is shown in Fig. 5.26. This shows the OH emission image of a HNF propellant burning at an angle. The needle-shaped particles can be recognized at some points in this figure. The propellant with the fine HNF shows a much more homogenous emission from the burning surface.

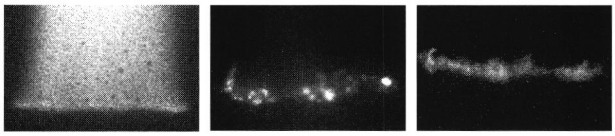

Figure 5.25: *OH emission at 0.3 MPa. From left to right: HNF, HNF C15/GAP, and HNF S16/GAP (image size* $= 4.1 \times 6.2$ *mm*^{2}*).*

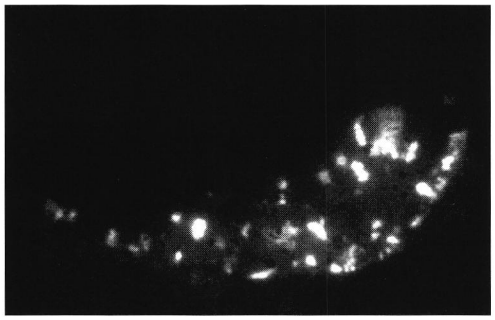

Figure 5.26: *OH emission of a HNF-C15/GAP propellant (coarse HNF) at 0.15 MPa (image size* $= 4.1 \times 6.2$ *mm*^{2}*).*

5.4.3 PLIF experiments

Analogous to the sandwiches, it was tried to obtain PLIF-images from HNF propellants. Experiments were carried out for the OH and CN radicals. In all experiments, the signal intensities were low, and the images were blurred. Several reasons can be given for the "bad" quality of the images. First, the propellants are all very fuel rich. PREMIX calculations show that the OH concentrations are low, typically less than 0.1 mole%. This is 10× lower as for neat HNF. Because of the low solid loadings the temperatures are low, and also the CN concentrations are low. The three dimensional flame structure also causes beam steering through the flame. Furthermore, the off-resonant images have about the

same signal levels as the resonant images. Due to the large amount of binder a lot of soot is present in the gas phase and the laser signal is scattered. Because all images are completely random, background subtraction can not be carried out.

5.5 Conclusions

The combustion of hydrazinium nitroformate (HNF) sandwiches and HNF propellants has been studied in window bombs. Sandwich experiments were carried out up to 1 MPa. The binder in HNF/GAP sandwiches regresses along with the HNF. At the interface of GAP and HNF the regression rate is higher than that of neat HNF. Results of kinetic modeling of the HNF/GAP sandwich structure confirm that the final flame temperature is reached closer to the burning surface above the binder slab. The binder in HNF/HTPB sandwiches does not keep up with the oxidizer. The extension above the burning surface is dependent on the pressure. At increasing pressures, the protrusion decreases.

HNF/GAP propellants with both coarse and fine HNF crystals (474 μm and 100 μm, based on an equivalent spherical volume) were made with a solid loading of 55%. Both propellants have a burn rate exponent $n \sim 0.68$. The difference in burn rate is very small: the propellant with fine HNF burns 4% faster at 5 MPa. The burn rate exponent of a HNF/HTPB propellant containing 73% HTPB is $n = 1.01 \pm 0.05$. The HTPB propellant has a lower regression rate than the GAP propellant.

NO*, OH* and CN* emission images show that only the GAP sandwich has a clear diffusion flame, close enough to the surface to affect burning rate. Emission images of propellants containing coarse HNF show that only part of the surface is burning simultaneously. The propellant containing fine HNF has a more homogeneous emission from the surface.

Chapter 6

Modeling

6.1 Introduction

This Chapter deals with the modeling of the combustion of HNF and HNF-compositions. First a very simple model for neat HNF combustion is presented. The condensed phase chemistry is treated by a single reaction step with a high activation energy. Two approaches are followed: a gas phase with low activation energy, and a gas phase with high activation energy. The low activation energy model yields good results for steady-state and laser-assisted combustion of neat HNF. The simplified model lacks detailed information about the flame structure of HNF. Section 6.3 discusses a model with a detailed kinetical mechanism for HNF combustion. The results of this model help to understand the gas phase structure of HNF. The other two sections of this Chapter describe modeling efforts for the combustion of HNF/GAP propellants. In section 6.4 a global model based on the BDP-model for AP-combustion is presented. This model allows determination of the burn rate as function of solid loading and HNF particle size. The BDP-type propellant model does not yield detailed information about the diffusion flame structure above the propellant surface. As a simplification of a propellant, experimental results of "sandwiches" have already been discussed (see section 5.3). The last section of this Chapter shows results obtained with a detailed kinetical model for sandwich combustion. For these calculations the `BIGMIX` computer code is used. The work of sections 6.4 and 6.5 was carried out as a engineering thesis, and therefore only the most important issues are mentioned here. For more details and main results is referred to Landman [87].

6.2 Simplified model for HNF combustion

In this section, modeling results using simplified approaches are presented. The goal of the model is maximal predictive capability and accuracy, coupled with minimal complexity. This is achieved by using essential physics and chemistry only, yielding tractable models. The condensed phase is treated by a high-activation-energy approximation method. The gas phase is treated in two ways: the classical high-activation-energy limit (Denison-Baum-Williams, DBW, model) [33, 161], and the recently introduced low-activation-energy limit (Ward-Son-Brewster, WSB, model) [157]. Both limits allow for an analytical solution of the gas phase energy equation. The WSB approach was found to match the experimental

observations much better than the DBW models for HMX and double base propellants [20]. It is the intention of this section to verify whether the new WSB-approach also gives better results for HNF combustion.

6.2.1 Model

The combustion of HNF is modeled as a one-dimensional, steady-state process. The condensed phase is described by an unimolecular, irreversible, zero-order decomposition reaction

$$\mathrm{A} \rightarrow \mathrm{B}\,, \tag{6.1}$$

where A represents the solid HNF, and B some kind of unstable intermediate species (such as the observed NO_2, HONO and N_2O). B reacts further according to the following bimolecular, irreversible, gas phase reaction

$$\mathrm{B{+}M} \rightarrow \mathrm{C{+}M}\,, \tag{6.2}$$

where C represents intermediate gas phase products, such as NO. M represents unstable species such as N, H and OH. The kinetic scheme represented by Eq.'s (6.1) and (6.2) is an ad hoc global description. This model was not derived from a detailed kinetic scheme, but from a conceptual point of view. The above mentioned species represented by B and C are representative for HNF kinetics, and help to clarify the idea behind the global description.

The reactions represented by the second step (B+M→C+M) consume the intermediate radical species. These reactions are characterized by high exothermicity and low activation energy barrier. M can be viewed as a pool of unspecified chain carriers, whose mass fraction is constant, and negligibly small compared to the main species B and C [157]. The reaction is second-order overall, and first order with respect to B. For purposes of modeling species conservation, no distinction is made between the M species that appear on the left and right hand sides of Eq.(6.2). The process is assumed to be a bimolecular exchange reaction, which for species bookkeeping purposes, assumes only two gas species, B (reactant) and C (product). The above interpretation relates to the WSB-model. For the DBW-model the kinetic interpretation is one of a gas phase thermal decomposition, and M is interpreted in the usual sense, as any species.

The molecular weights of the various species are assumed to be equal, and mass diffusion in the gas phase is assumed to be described by Fick's law. The specific heat capacity and thermal conductivities are assumed to be constant. The gas phase and condensed phase specific heat capacity are assumed to be equal. To simplify the solution of the gas phase equations, the Lewis number is assumed to be unity, $Le = k_g/\rho_g D c_p = 1$. The propellant may be illuminated with an external laser heat flux, with radiative energy Q_r (in $\mathrm{W/m^2}$). This heat flux is absorbed in the condensed phase according to Beer's law (absorption coefficient K_a). The gas phase laser flux absorption is assumed to be zero. Reactions in the condensed phase have a total heat release Q_c. The gas phase is assumed to obey the ideal gas law. Mass diffusion in the condensed phase is neglected.

Condensed phase

With the above assumptions, the condensed phase is described by the following energy equation

$$mc_c\frac{dT}{dx} = \lambda_c\frac{d^2T}{dx^2} + Q_c\epsilon_c + f_rQ_rK_a\exp(K_ax) \ , \tag{6.3}$$

with boundary conditions

$$T(0) = T_s \ , \quad \text{and} \ \lim_{x\to-\infty} T(x) = T_0 \ , \tag{6.4}$$

with m the mass flux (kg/m^{2}s), and f_r the fraction of laser energy absorbed below the surface. The value of f_r can be estimated from $f_r = \exp(-K_ax_R)$, where x_R is the reaction zone length, approximated by $x_R = (k_c/(\rho_cc_c))/(E_c/(2RT_s))$ [62]. As a zero-order condensed phase reaction was assumed, the reaction rate is given by

$$\epsilon_c = \rho_cA_c\exp\left(-\frac{E_c}{RT}\right) \ . \tag{6.5}$$

The thermocouple experiments of section 4.3.2 show that the condensed phase of HNF has a thin reactive zone, i.e. a high activation energy for the decomposition process as given by Eq.(6.1). This means that activation energy asymptotics (AEA) may be used to find the mass flux from Eq.(6.3). The well known (implicit) solution is [62, 90]

$$m^2 = \frac{A_cRT_s^2\lambda_c\rho_c\exp(-E_c/RT_s)}{E_c(c_c(T_s-T_0) - Q_c/2 - f_rQ_r/m))} \ . \tag{6.6}$$

Gas phase

Solution of the gas phase equations is less straightforward. Most early models are based on the flame sheet approach, i.e. a very thin reactive zone, where all the gas phase heat release occurs. This process is typical for gas phase kinetics with high activation energy ($E_g \to \infty$). Mathematically the heat release can be approximated by a Dirac delta function [23]. It was recently argued by Ward et al. that a very low gas phase activation energy ($E_g \to 0$) is more physical [157]. Their perspective is based on the fact that the temperature profile of HMX could be much better replicated by $E_g = 0$, than by $E_g = \infty$. Analogs in gas phase combustion provide further evidence that such an approach is not unrealistic. Most of the energy of a hydrogen/oxygen system is released during the recombination/termination step, which has a low activation energy barrier [168]. Both limit cases ($E_g = 0$ and $E_g = \infty$) will be discussed here, to see the overall effect on the model.

The energy equation in the gas phase is

$$mc_c\frac{dT}{dx} = \lambda_g\frac{d^2T}{dx^2} + Q_g\epsilon_g \ , \tag{6.7}$$

with the reaction rate given by

$$\epsilon_g = \rho_g^2B_gYT^2\exp\left(-\frac{E_g}{RT}\right) \ , \tag{6.8}$$

where Y is the mass fraction of B, B_g a constant and Q_g the total heat release in the gas phase. The density of the gas phase, ρ_g, is found from the ideal gas law. The interface

conditions are found from energy conservation at the surface (the total amount of energy to heat the condensed phase from T_0 to T_s originates from subsurface heat release and the conductive heat from the gas phase)

$$T_s = T_0 + \frac{Q_c}{c_c} + \frac{1}{mc_c}\left[\lambda_g \left(\frac{dT}{dx}\right)_{x=0} + Q_r\right] , \tag{6.9}$$

and

$$T_f = T_0 + \frac{Q_c + Q_g + Q_r/m}{c_c} . \tag{6.10}$$

The species equation of the gas phase is

$$m\frac{dY}{dx} = \rho_g D_g \frac{d^2Y}{dx^2} - \epsilon_g , \tag{6.11}$$

Where D_g is the gas phase diffusion coefficient. For the species equation, the boundary conditions are

$$Y_s = 1 + \frac{\rho_g D_g}{m}\left(\frac{dY}{dx}\right)_{x=0} , \tag{6.12}$$

and

$$\lim_{x\to\infty} Y = 0 . \tag{6.13}$$

Because of the assumption $Le = 1$, the gas phase energy equation and species equation are uncoupled, and can be written as two similar nondimensional equations (nondimensional quantities denoted by *) [157]

$$m^*\frac{dT^*}{dx^*} = \frac{d^2T^*}{dx^{*2}} - D_g^*(T_f^* - T^*)\exp\left(-\frac{E_g^*}{T^*}\right) , \tag{6.14}$$

and

$$m^*\frac{dY}{dx^*} = \frac{d^2Y}{dx^{*2}} - D_g^* Y \exp\left(-\frac{E_g^*}{T_f^* - YQ_g^*}\right) . \tag{6.15}$$

The boundary equations transform accordingly. For arbitrary values of E_g^*, Eq.(6.14) has to be solved iteratively with Eq.(6.6) to yield T_s^* and m^*. Note that solution of this set requires solution of a 2nd order differential equation. For the two limiting cases, $E_g = 0$, and $E_g \to \infty$, it is possible to obtain an analytical solution.

The first limit is that of a very low activation energy in the gas phase, $E_g \to 0$. For this case an analytical solution of Eq.(6.14) can be obtained

$$\frac{T^* - T_f^*}{T_s^* - T_f^*} = \exp\left(-\frac{x^*}{x_g^*}\right) . \tag{6.16}$$

In this equation x_g^* is a dimensionless characteristic gas reaction zone thickness, given by

$$x_g^* = \frac{2}{\sqrt{m^{*2} + 4D_g^*} - m^*} . \tag{6.17}$$

Using different approximations, Miller derived similar results for the gas phase [113]. In Miller's work the gas phase reaction is described by a first order reaction, and a constant

temperature reaction rate. Since M is assumed constant in this work, reaction (6.2) is in essence also first order. The constant temperature reaction rate approximation corresponds with a constant, temperature independent, reaction rate, i.e. $E_g = 0$.

In summary: In the limit of a high condensed phase activation energy, coupled with a low activation energy gas phase, the analytical solution of the problem is given by the (nondimensional) form of Eq.(6.6)

$$m^{*2} = \frac{A_c^* T_s^{2*} \exp(-E_c^*/T_s^*)}{E_c^*(T_s^* - T_0^* - Q_c^*/2 - f_r J)} \,. \tag{6.18}$$

This equation is solved simultaneously with Eq.(6.17) The energy balance is given by the nondimensional result of Eq.(6.9)

$$T_s^* = T_0^* + Q_c^* + \frac{Q_g^*}{x_g^* m^* + 1} \,. \tag{6.19}$$

For the high activation energy gas phase ($E_g \to \infty$), the regression rate is given by Williams's gas phase controlled analytical solution (for $E_g/RT_f \gg 1$) [62]

$$m^2 = \frac{2\lambda_g B_g M^2 p^2 c_c T_f^4}{E_g^2 Q_g^2} \exp\left(-\frac{E_g}{RT_f}\right) \,. \tag{6.20}$$

This expression indicates that the mass flux is determined by gas kinetics only, and not by decomposition kinetics. There is no dependence on T_s or E_c. Note that actually Q_r affects T_f (Eq. (6.10)), which affects m. For this case the energy balance yields

$$T_s^* = T_0^* + Q_c^* + Q_g^* \exp\left(-x_g^* m^*\right) \,. \tag{6.21}$$

For the high activation energy limit case, the AEA result, Eq.(6.18), is still used for the determination of the surface temperature T_s^*. Results of this traditional analytical limit case will be compared with the new concept of $E_g = 0$ to show the overall improvements of the model's predictive capability.

6.2.2 Results

The model input used for the calculations are summarized in Table 6.1. During all calculations these values are held constant. The condensed phase activation energy $E_c = 75\,\mathrm{kJ/mole}$ was found to give good results in the whole pressure range of interest. This value is close to the 84 kJ/mole required to break-up HNF into hydrazine and nitroform via a hydrogen transfer (section 2.4). The values of the Arrhenius prefactors, A_c and B_g, were determined from the experimental observation that $T_s = 523\,\mathrm{K}$ [104] and $r_b = 0.77$ mm/s at 0.1 MPa [46, 104]. After this *calibration* of the model at a single burning condition, the regression rate is calculated at different pressures, without modification of any of the other parameters. The density of the pressed HNF pellets was 1740 kg/m^3 [104]. The thermophysical properties of solid HNF were recently measured [57]. The specific heat capacity and thermal conductivity were found to have a slight temperature dependence. However, the effective thermal conductivity was found to decrease near the burning surface, due to cracks during combustion [99] (see also Chapter 7). In this model constant values at 100°C are used.

Symbol		Value	Unit
Q_g		2429	kJ/kg
Q_c		-30.0	kJ/kg
A_c		$1.67 \cdot 10^9$	1/s
B_g	$E_g = 0$	$4.45 \cdot 10^{-2}$	m^3/kgK^2s
	$E_g = \infty$	$1.06 \cdot 10^4$	m^3/kgK^2s
c_p		0.97	kJ/kgK
λ_g		0.054	W/mK
λ_c		0.15	W/mK
E_g		167	kJ/mole
E_c		75	kJ/mole
ρ_c		1740	kg/m^3
M		25.6	kg/kmole

Table 6.1: *Input values used for neat HNF monopropellant calculations with the WSB and DBW-models.*

Steady state HNF combustion

Figure 6.1 shows the results of the calculated regression rate for both models, compared with experimental data (from Ref.[4], and Chapter 4). Like many energetic materials, HNF's regression rate can be described by $r_b = ap^n$. The high activation energy limit yields $n = 1$, because $m = \rho_c r_b \propto p$, see Eq.(6.20). Experimentally $n = 0.89$ was found for HNF combustion (least-squares fit to all data points in Fig. 6.1). Because the regression rate was gauged at 0.1 MPa, the flame sheet overpredicts the regression rates above 0.1 MPa. The WSB approach shows good agreement with the experimental results. This model predicts $n = 0.87$ (by calculating the burn rate at 1 MPa and at 1.01 MPa).

However above 0.7 MPa, there is an increasing difference between the WSB-results and the experimental data. This difference can be attributed to the fact that not only the gas phase kinetics change with pressure, but also the flame temperature. At 0.1 MPa the flame temperature of HNF is $T_f = 2766\,\mathrm{K}$. When the pressure is increased, the flame temperature of HNF increases considerably, e.g. $T_f = 2949\,\mathrm{K}$ at 1 MPa, and $T_f = 3112\,\mathrm{K}$ at 10 MPa. This is due to the fact that the equilibrium composition is dependent on the pressure, see Table 4.1. The higher flame temperature results in an extra heat feedback to the surface, not accounted for by the model. This varying flame temperature can be introduced into the model, by varying Q_g as function of pressure, so that the calculated adiabatic flame temperature is reached, $T_f = (Q_g + Q_c)/c_c + T_0$. The rest of the parameters is kept constant. The result is an improved agreement between the WSB-model and the experimental results, see Fig. 6.2. For reasons of simplicity this modification of the model will not be used throughout the rest of this paper, and from now on constant Q_g values will be used.

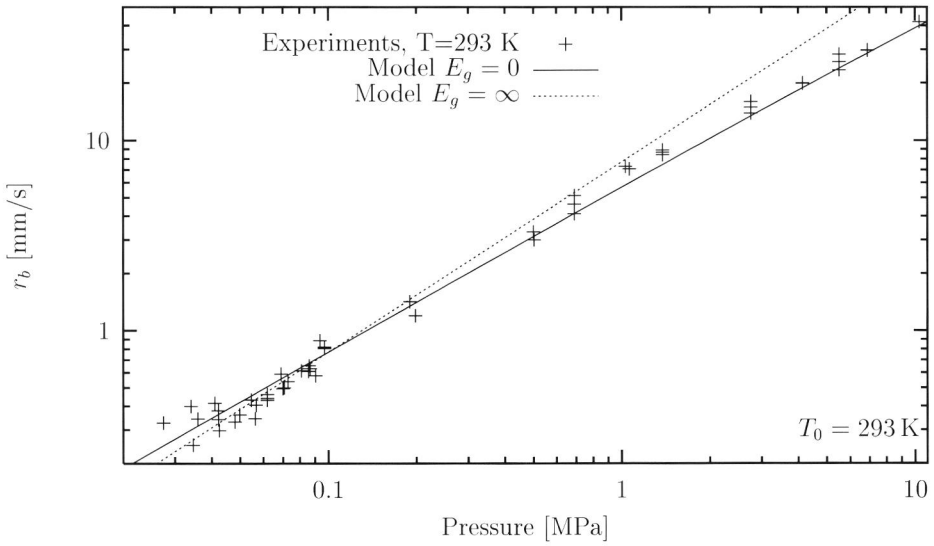

Figure 6.1: *Comparison of calculated and measured regression rate of neat HNF samples.*

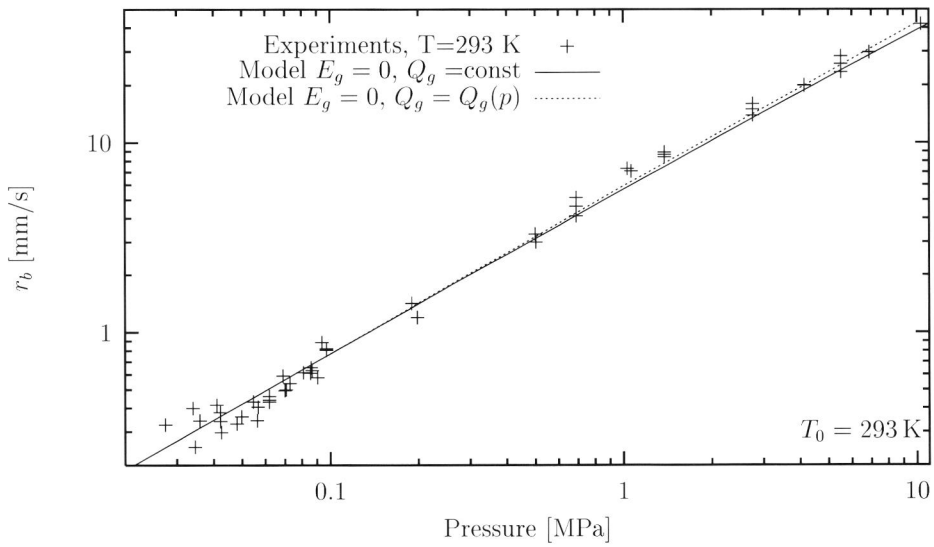

Figure 6.2: *Effect of introducing pressure dependent Q_g to account for the varying flame temperature with pressure.*

Also for low and high initial temperatures, the WSB-model has good agreement with the experimental results, see Fig. 6.3. This sensitivity of the burning rate to the initial temperature, is defined by the following expression

$$\sigma_p = \frac{1}{r_b}\left(\frac{\partial r_b}{\partial T_0}\right)_p . \tag{6.22}$$

By determining the regression rate at 292 K and 293 K HNF's temperature sensitivity was determined for both the DBW and the WSB model, see Fig. 6.4. This graph also shows the experimental determined temperature sensitivity from the data points of Fig. 6.3. This is done in two ways: First, *direct* determination of σ_p at each pressure by a fit of $\ln(r_b)$ vs. temperature. The second method uses the least-squares power law fit to the regression rates. Then the temperature sensitivity is determined from the differences between these fits at each pressure. If the propellant burns nicely according to $r_b = ap^n$, then the second method will give more accurate results.

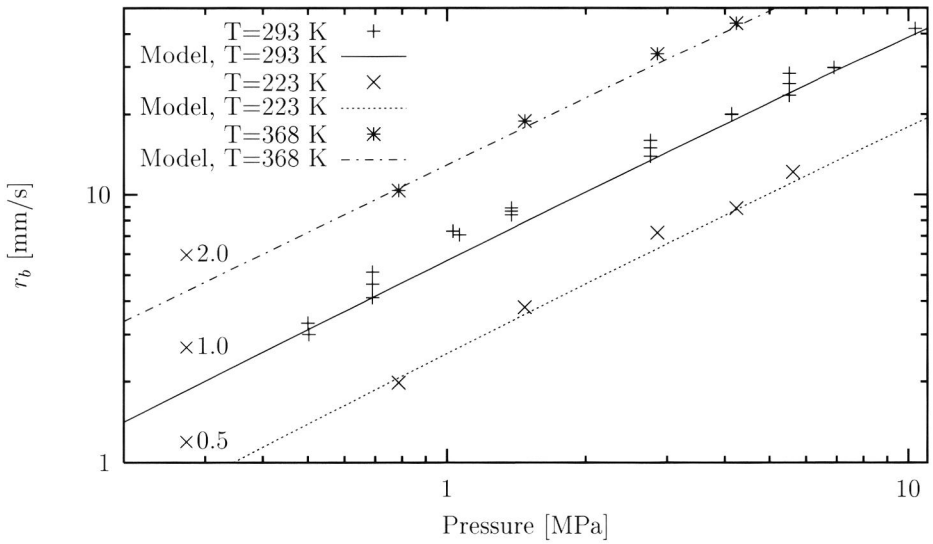

Figure 6.3: *Comparison of calculated (WSB-model) and measured regression rate of neat HNF samples. (Note the multiplication factors, which are introduced to prevent overlap of data.)*

From Fig. 6.4 it is seen that the low activation energy limit predicts a pressure dependence of the temperature sensitivity. This limit case shows reasonable agreement with the direct determined values for σ_p. The agreement with the temperature sensitivity as determined by the second method is very good. The $E_g \to \infty$ model is not capable of capturing a pressure variation of σ_p. Unfortunately the large errors from the direct method make it impossible to favor one of the two modeling approaches. The temperature sensitivity as determined from fitting power laws first, agrees better for the WSB-approach, than for the DBW-model.

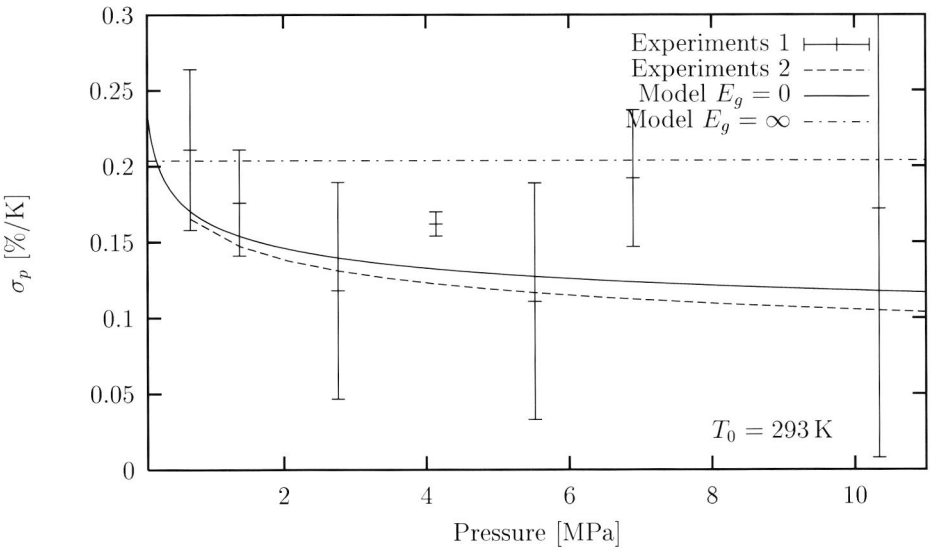

Figure 6.4: *Experimental vs. theoretical temperature sensitivity of HNF for both modeling approaches (errorbars indicate the standard deviation from the* $\ln(r_b)$ *vs. T fit). For explanation of the two different methods of experimental* σ_p *evaluation see the text. Within the* $E_g \to \infty$ *approach only a constant temperature sensitivity is calculated,* $\sigma_p = (T_f + E_g/2RT_f)/T_f$.

The variation of the surface temperature, T_s, with pressure is depicted in Fig. 6.5. Although both models share the same condensed phase equations, the predicted surface temperatures are different, because both models predict a different mass flux for each pressure. The figure also shows some experimental results which were obtained with thermocouples [104].

Figure 6.6 compares the temperature profile as found from both limit cases, and with that of detailed modeling (next section). It is seen that the temperature profile of the simplified WSB-model is close to that of the detailed chemical model. Both simplified models show a temperature profile close to the final flame temperature at $x = 1\,\mathrm{mm}$. The detailed calculations show a lower temperature due to the slow NO reactions, similar to the "dark-zone" in double-base propellants. With a second step in the gas phase, C $\to$ D, the simple models would also be able to calculate this intermediate zone. The final flame temperature of the kinetical model is equal to that of the other models. It was determined by NO UV-absorption and CARS experiments that temperatures close to the adiabatic flame temperature are reached within 1 mm above the surface (see section 4.4). All three modeling approaches confirm this. However, the inaccuracy of the absorption experiments does not allow to reject one of the models.

A closer agreement between the temperature profile of WSB/DBW-models and the kinetic model is obtained by using the intermediate temperature of 2550 K as the final temperature. It was verified that after re-calibration of the WSB-model the effect is small.

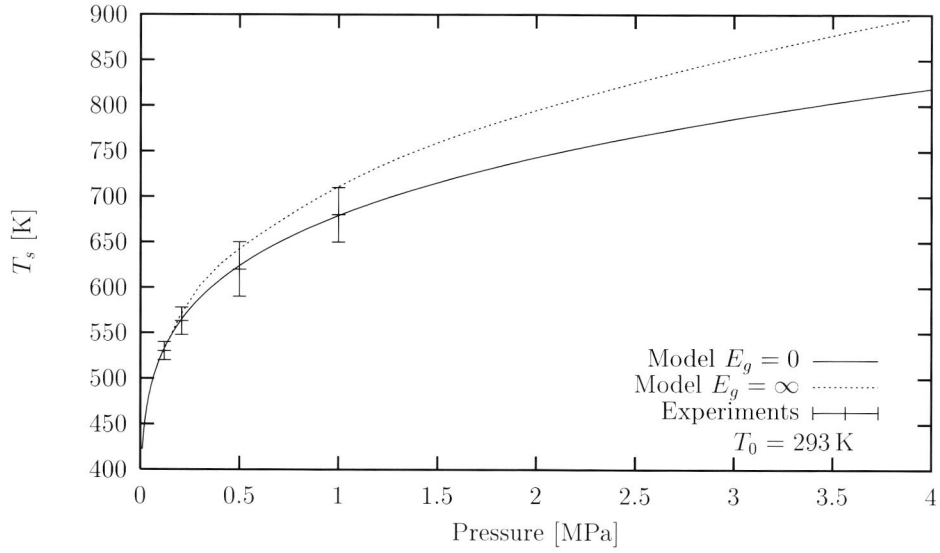

Figure 6.5: *Experimental and predicted surface temperature.*

For the DBW-model there is no effect, as a decrease of Q_g is compensated by a decrease of B_g (see Eq.(6.20)). These results will therefore not be discussed here.

Figure 6.7 shows the position where 63% (= x_g) and 99% of the final flame temperature are reached. These positions are characteristic dimensions for the gas phase reaction zone thickness. In the figure this flame thickness is compared to several experimental results. The flame standoff distances in Fig. 6.7 were obtained from video images as the distance off the surface of the CN chemiluminescent emission. The CN profile peak location was determined by planar laser induced fluorescence (PLIF), which is a more accurate determination of the CN standoff. The CN profile peak does not necessarily coincide with x_g, but should at least follow the same trend, and be of the same order of magnitude. The magnitude is much better predicted by the WSB-model. The DBW-model flame thickness is an order of magnitude too thin (as also the case for HMX). It is seen that both the DBW and WSB-models predict the experimental observed pressure dependence (nearly $1/p$).

Laser-assisted combustion

As part of the study of the transient combustion of HNF, Finlinson determined the laser assisted regression rates of HNF [46]. The laser-assisted regression rate data allows the further validation of the model. During combustion the laser energy is absorbed in the condensed phase near the burning surface, and increases the regression rate. An infra-red 10.6 μm CO_2-laser was used in Finlinson's study. Isbell and Brewster measured the optical properties of several energetic materials [64]. Their results show a large difference, in e.g. the value of the absorption coefficient, K_a. The values varied from $K_a \sim 190\,\mathrm{cm}^{-1}$ for AP, to $K_a \sim 2800\,\mathrm{cm}^{-1}$ and $K_a \sim 5670\,\mathrm{cm}^{-1}$ for RDX and HMX respectively. For HNF, the absorption coefficient for the CO_2-wavelength, has been estimated as $K_a \sim 1000\,\mathrm{cm}^{-1}$[99].

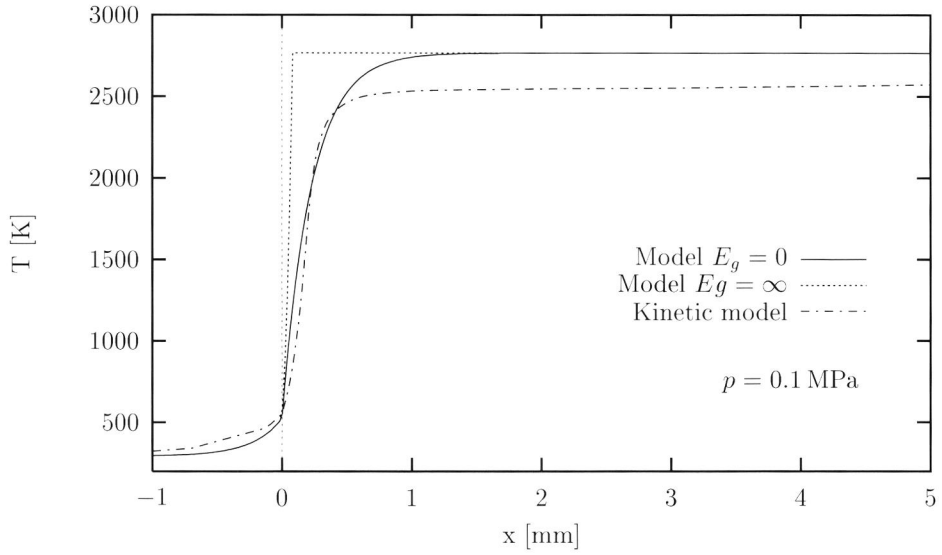

Figure 6.6: *Temperature profile of HNF for both limit models, and a comprehensive detailed kinetical model.*

No absorption or reflection measurements have been carried out for HNF in the 10.6 μm CO_2-laser range used by Finlinson. The reflection coefficient is determined from a best fit to all experimental data. From the previous discussion, it has become clear that the low activation energy limit, WSB, shows best agreement with the experiments. Therefore only this model will be discussed here.

Figure 6.8 shows the laser-assisted combustion of HNF. For all pressures the model predict the trend with increasing external laser heat flux in good agreement with the experimental data. The difference between experiments and the modeling is caused by the small inaccuracies of the model, that are already present at $Q_r = 0$. For these calculations at all pressures a surface reflection of 60% was used. This value is comparable to the values used for HMX modeling [93]. This work uses a surface reflectivity of 50%. However, neat HMX samples show only 15% reflectivity at room temperature. Several explanations for this difference can be given: ions present in the melt layer, enhanced scattering inside the melt layer due to bubbles, or enhanced absorption at the burning surface due to the presence of decomposition products (hence increased reflectivity). If the pressure increases the melt thickness decreases. This implies a lower reflection. The measurements at 0.6 MPa seem to indicate this. However, the number of measurements at this pressure are limited.

6.2.3 Conclusions

Two very simple models for the combustion of HNF have been presented. The gas phase has been calculated by two limit approaches: low (WSB) and high (DBW) gas phase activation energy. The WSB approach shows great predictive capability, in both laser-assisted and

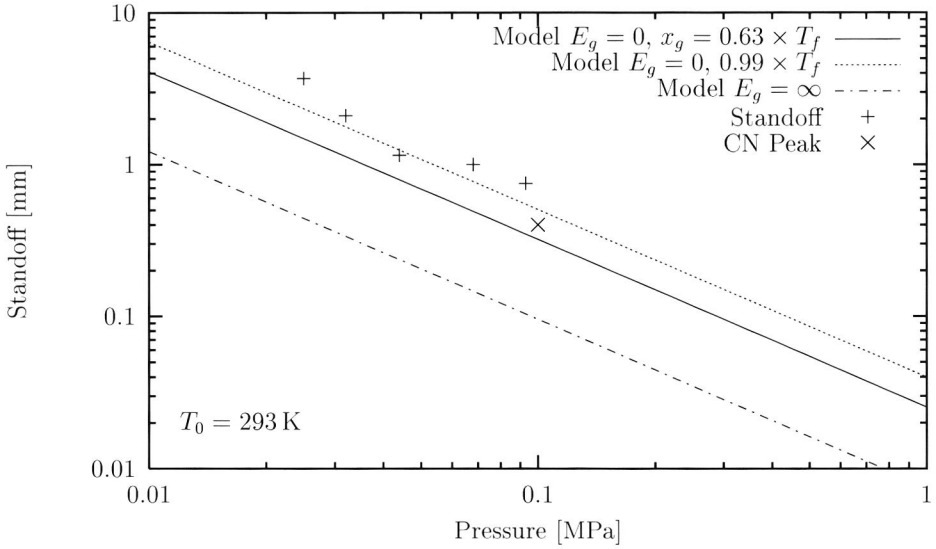

Figure 6.7: *Flame standoff distance as calculated from both models, compared with experimental determined flame standoff (height above the burning surface of CN chemiluminescence), and CN profile peak position (as determined by planar laser induced fluorescence).*

self-sustained regression rates, temperature sensitivity, and surface temperatures. The agreement of these propellant properties is much better than with the usual assumption of large gas phase activation energy (DBW). By introducing HNF's strong pressure dependent adiabatic flame temperature into the WSB-model even better results are obtained. The parameters that gave the best agreement between modeling and experimental results all have realistic values. The condensed phase decomposition activation energy corresponds to HNF decomposition. The overall energy release in the condensed phase is endothermic, which can be explained by the melting and evaporation of the HNF. The gas phase has an effective low activation energy for the primary flame zone, like e.g. HMX-combustion.

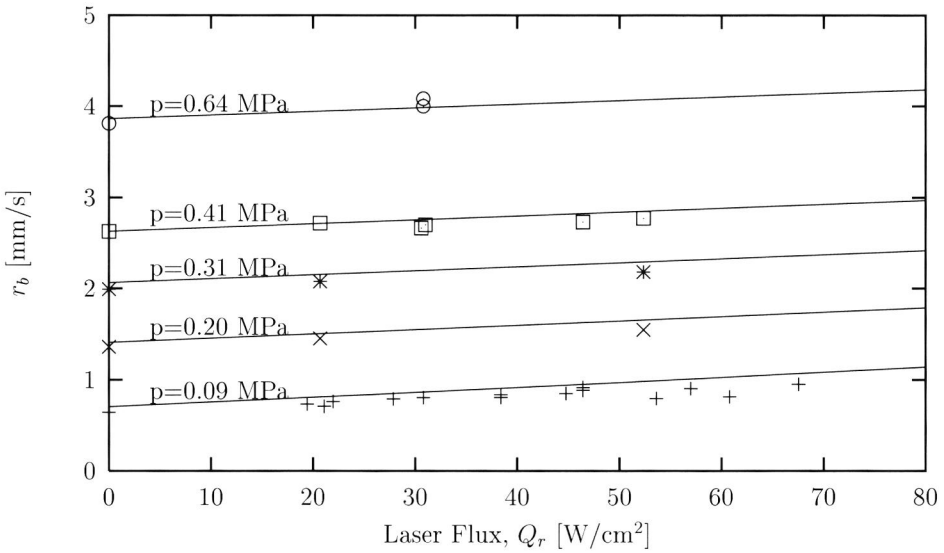

Figure 6.8: *Laser-assisted regression rates of HNF at different pressures. Points: experimental data; Solid lines: WSB-model's results for* $K_a = 1000\,cm^{-1}$*. The WSB model predicts the trend in HNF's burning rate with increasing heat flux accurately for all pressures. The deviation from the experimental results is independent of the value of the heat flux, but is caused by differences already at* $Q_r = 0$*.*

6.3 PREMIX modeling

The models of the previous section do not treat chemistry in detail. By doing more detailed calculations, more insight about the kinetics of the condensed and phase is obtained. The detailed calculations also make a direct comparison with e.g. PLIF results possible. This section describes more detailed calculation of neat HNF combustion. The HNF flame is treated as a premixed flame, with an attached condensed phase.

6.3.1 Description of the model

HNF combustion is characterized by a three phase combustion zone: solid, liquid and gas phase. The model presented here accounts for all three phases, see Fig. 6.9. The HNF combustion is described by a one-dimensional model. The liquid to gas surface is held fixed at $x = 0$. The solid extends to $x = -\infty$, and the gas phase extends to $x = +\infty$. The solid-to-liquid surface is located at an unknown position x_m between $x = -\infty$ and $x = 0$. The computational domain extends from $x_1 < x_m$ to $x_2 > 0$ which are to be chosen such that zero gradient conditions at the boundaries apply.

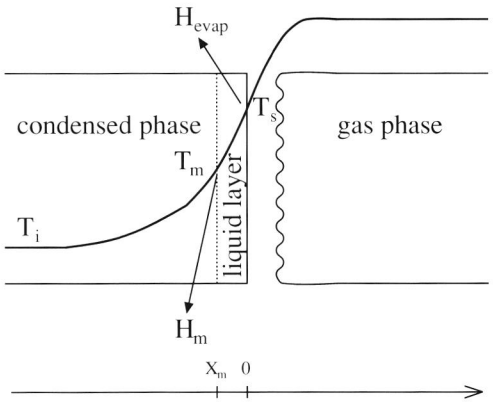

Figure 6.9: *Schematic of the model for HNF solid monopropellant combustion.*

Condensed phase

It is assumed that no chemical reactions take place in the condensed phase. Thermocouple experiments by Von Elbe et al. [42] and in this work show that the temperature traces follow the theoretical solution for heating of a non-reacting solid (section 4.3.2). The governing equations are: mass conservation, species conservation, and energy conservation. In the condensed phase, these conservation equations are respectively given by the following equations [85]

$$\dot{m} = \rho v A = \text{constant} , \tag{6.23}$$

$$Y_k = \delta_{\text{HNF},k} \quad \text{for } k = 1, 2, \ldots K , \tag{6.24}$$

$$\dot{m}c_c\frac{dT}{dx} = \frac{d}{dx}\left(\lambda_c A\frac{dT}{dx}\right) , \tag{6.25}$$

where

$\dot{m}$	total mass flow
ρ	density
v	velocity
A	area
Y_k	mass fraction of the kth species (there are K species)
δ	Kronecker delta
c_c	heat capacity of the condensed phase
λ_c	thermal conductivity of the condensed phase.

Liquid phase

Some reactions take place in the melt layer during HNF combustion [42]. This results in a bubbling surface layer because of the gaseous species released in the liquid phase. However, within the model these bubbles are not explicitly accounted for. A limited set of melt layer reactions is considered. It is assumed that all decomposition products produced in the liquid phase remain dissolved in the liquid. Thus sub-surface evaporation is neglected. This greatly simplifies the equations describing the two phase flow region. A similar approach yielded good results for RDX solid monopropellant combustion [126]. The liquid layer is described by

$$\dot{m} = \rho v A = \text{constant} , \tag{6.26}$$

$$\dot{m}\frac{dY_k}{dx} = A\dot{\omega}_k W_k \quad \text{for } k = 1, 2, \ldots K , \tag{6.27}$$

$$\dot{m}c_l\frac{dT}{dx} = \frac{d}{dx}\left(\lambda_l A\frac{dT}{dx}\right) - A\sum_{k=1}^{K}\dot{\omega}_k h_k W_k , \tag{6.28}$$

where

$\dot{\omega}_k$	molar rate of production by chemical reaction of the kth species (per unit volume)
W_k	molecular weight of the kth species
h_k	specific enthalpy of the kth species
c_l	heat capacity of the liquid phase
λ_l	thermal conductivity of the liquid phase.

The density of the liquid phase is assumed to be equal to that of the condensed phase.

Gas phase

In the gas phase further reaction takes place, until an equilibrium is reached. The governing equations are found by adding the diffusion terms to the equations describing the liquid phase. So, the gas phase is described by

$$\dot{m} = \rho v A = \text{constant} , \tag{6.29}$$

$$\dot{m}\frac{dY_k}{dx} = -\frac{d}{dx}\left(\rho A Y_k V_k\right) + A\dot{\omega}_k W_k \quad \text{for } k = 1, 2, \ldots K \,, \tag{6.30}$$

$$\dot{m}c_g\frac{dT}{dx} = \frac{d}{dx}\left(\lambda_g A\frac{dT}{dx}\right) - A\sum_{k=1}^{K}\rho Y_k V_k c_{g,k}\frac{dT}{dx} - A\sum_{k=1}^{K}\dot{\omega}_k h_k W_k \,, \tag{6.31}$$

where

V_k diffusion velocity of the kth species
c_g heat capacity of the gas phase
λ_g thermal conductivity of the gas phase
$c_{g,k}$ heat capacity of the kth species

The reaction mechanism for the gas phase may be different from that of the liquid phase. The density of the gases is found from

$$\rho = \frac{p\bar{W}}{RT} \,, \tag{6.32}$$

where p is the pressure and $\bar{W}$ the average molecular weight of the species.

Boundary conditions

Boundary conditions are needed to complete the description of the problems. These are given at the boundaries of the computational domain (x_1, x_2), and at the interfaces. At the solid boundary the initial propellant temperature T_i is given by

$$T(x_1) = T_i \,. \tag{6.33}$$

Furthermore, only HNF is present in the condensed phase

$$Y_k(x_1) = \delta_{\mathrm{HNF},k} \quad \text{for } k = 1, 2, \ldots K \,. \tag{6.34}$$

At the gas phase boundary ($x = x_2$), zero gradients are imposed

$$\left(\frac{dT}{dx}\right)_{x_2} = 0 \,, \tag{6.35}$$

and

$$\left(\frac{dY_k}{dx}\right)_{x_2} = 0 \quad \text{for } k = 1, 2, \ldots K \,. \tag{6.36}$$

At the surface the energy boundary condition is found from an energy balance at the liquid-gas interface

$$\dot{m}\left\{(H_{tot})_{0^+} - (H_{tot})_{0^-}\right\} = \left(A\lambda_g\frac{dT}{dx}\right)_{0^+} - \left(A\lambda_l\frac{dT}{dx}\right)_{0^-} - \left(A\sum_{k=1}^{K}\rho Y_k V_k H_k\right)_{0^+} \,, \tag{6.37}$$

where 0^- and 0^+ denote respectively the negative and positive side of the interface. The impulse terms are small, and have been neglected in this equation. The difference in total

enthalpy $H_{tot} = \sum_{k=1}^{K} Y_k H_k$ across the surface is caused by the heat of vaporization of HNF. The diffusion term accounts for the enthalpy flux leaving the surface by mass diffusion. The solid-liquid interface location is not known a-priori. Liquid phase properties are used when the temperature is above the melting point T_m, and solid phase properties when below that point. Energy balance is maintained across the solid-liquid interface by solving Eq.(6.37) without the diffusion velocity term.

Determination of the mass flux

In all the above equations, the mass flux $\dot{m}$ is not known. In general two approaches can be followed to determine the mass flux:

- Determine the difference between rate of evaporation of the liquid monopropellant, and the rate of condensation for the gaseous products.
- Determine the mass flux as an eigenvalue of the problem.

The evaporation and condensation rates are generally empirically derived expressions that involve the temperature and the various species concentration at the interface. For the more common monopropellants like RDX and HMX this data is available. For HNF however, no such data is available. Furthermore, this method is hampered by numerical instabilities because the evaporation and condensation rates are large numbers, with a very small difference.

The approach followed here is that of the eigenvalue method, which is analogous to that of a free flame [66]. Calculation of the mass flux is carried out by introduction of the trivial differential equation

$$\frac{d\dot{m}}{dx} = 0 \,. \tag{6.38}$$

To maintain a well-posed problem, an additional boundary condition for the trivial Eq.(6.38) is needed. Within this model, the boiling point temperature T_s at the liquid-gas interface is given

$$T(x = 0) = T_s \,. \tag{6.39}$$

So, the model is not capable of predicting the surface temperature. Once the surface temperature is reached, any remaining liquid HNF is mathematically vaporized. The value of T_s is obtained from the WSB-model.

Reaction rates

The reaction rates are calculated as follows. Consider I elementary reactions involving K chemical species, given by the following form

$$\sum_{k=1}^{K} \nu'_{ki} \chi_k \rightleftharpoons \sum_{k=1}^{K} \nu''_{ki} \chi_k \quad \text{for } i = 1, 2, \ldots I \,, \tag{6.40}$$

where ν_{ki} are the stoichiometric coefficients, and χ_k is the chemical symbol for the kth species. The production rate $\dot{\omega}_k$ (in mole/m^{3}s) of the kth species can be written as a

summation of the rate-of-progress variable q_i for all reactions involving the kth species

$$\dot{\omega}_k = \sum_{i=1}^{I} (\nu''_{ki} - \nu'_{ki}) q_i \quad \text{for } k = 1, 2, \ldots K \; . \tag{6.41}$$

The rate-of-progress variable q_i for the ith reaction is given by the difference of the forward rates and the reverse rates

$$q_i = k_{f_i} \prod_{k=1}^{K} [X_k]^{\nu'_{ki}} - k_{r_i} \prod_{k=1}^{K} [X_k]^{\nu''_{ki}} \; , \tag{6.42}$$

where $[X_k]$ is the molar concentration of the kth species and k_{f_i} and k_{r_i} are the forward and reverse rate constants of the ith reaction. The forward rate constants are assumed to have the following Arrhenius temperature dependence

$$k_{f_i} = A_i T^{\beta_i} \exp\left[-\frac{E_i}{RT}\right] \; , \tag{6.43}$$

where A_i is the frequency factor, β_i is the temperature exponent, and E_i is the activation energy. The reverse rate constants k_{r_i} are related to the forward rate constants through the equilibrium constants K_{c_i} through

$$k_{r_i} = \frac{k_{f_i}}{K_{c_i}} \; . \tag{6.44}$$

For the calculation of the equilibrium constants the routines of the `CHEMKIN-II` package are used, for more details see e.g. Ref. [67].

Elementary reactions describing the dissociation of a single molecule into two radicals require the presence of a third molecule (M) in order to preserve the momentum and energy of the collision. The same holds for the recombination of two radicals ($\mathcal{M}_1$ and $\mathcal{M}_2$) forming a larger molecule ($\mathcal{M}_3$):

$$\mathcal{M}_1 + \mathcal{M}_2 + M \rightleftharpoons \mathcal{M}_3 + M \; . \tag{6.45}$$

For this situation Eq.(6.42) becomes

$$q_i = \sum_{k=1}^{K} \alpha_{i,k} [X_k] \cdot \left(k_{f_i} \prod_{k=1}^{K} [X_k]^{\nu'_{ki}} - k_{r_i} \prod_{k=1}^{K} [X_k]^{\nu''_{ki}} \right) \; , \tag{6.46}$$

where $\alpha_{i,k}$ is the efficiency factor of the species acting as a third body. The efficiency factors of the current reaction mechanism in are found in Annex B.1, and are denoted as "k enhanced by α_i".

6.3.2 HNF chemistry

HNF gas phase chemistry

The HNF flame chemistry is very similar to that of RDX and HMX. Therefore, Yetter's mechanism for RDX combustion was used for the calculations [165]. This mechanism is

intended to be generally applicable. The most important modifications of this scheme are the removal of several RDX decomposition products, and the introduction of gaseous HNF decomposition steps. As found by Williams and Brill, decomposition of HNF at 260°C yields mostly CO and N_2O at the cost of CO_2 and N_2 [163]. As temperature is increased, the amount of CO and N_2O reduces, and more CO_2 and N_2 are formed (ie. the overall decomposition reaction becomes more exothermic). At lower temperatures the decomposition of HNF is modeled as

$$N_2H_5{\cdot}C(NO_2)_3 \rightleftharpoons 2NO+CO+2H_2O+N_2O + \tfrac{1}{2}N_2+\tfrac{1}{2}H_2 \; . \tag{6.47}$$

At higher temperatures decomposition occurs according to

$$N_2H_5 \cdot (NO_2)_3 \rightleftharpoons 2NO+CO_2+2H_2O+ \tfrac{3}{2}N_2+\tfrac{1}{2}H_2 \; . \tag{6.48}$$

The remaining gas phase reaction scheme consists of 208 elementary reactions, involving 39 species. The reaction mechanism is given in Annex B.1. Compared to the rest of the mechanism, the above description is still a relatively global mechanism, but it is based on the best information available at this moment.

Combustion experiments of HNF solid monopropellants have shown that the flame can be treated as really 1-D at ambient pressure, i.e. the area A above the surface may be treated as constant [124]. It is assumed that also at higher pressures the flame remains 1-D.

HNF liquid phase chemistry

Already at very low temperatures HONO and N_2O have been observed. HNF condensed phase decomposition yields HONO and N_2O. No NO_2 is formed directly according to hot plate and hot cell experiments. The NO_2 was only detected after some time, and is probably formed by the decomposition of HONO. NO was only detected after ignition of the sample material. HNF condensed phase decomposition does not yield NO and NO_2 directly.

According to the above conclusions, the condensed phase decomposition can be summarized as

$$N_2H_5{\cdot}C(NO_2)_3 \rightleftharpoons N_2H_4+HONO+N_2O+CO+O_2 \; . \tag{6.49}$$

The mechanism as presented in Fig. 2.14 is not completely in correspondence with the decomposition according to Eq. 6.49. The formation of N_2O is not explained by the mechanism as presented in the figure, but *was* experimentally observed. Also the indirect formation of NO_2 as suggested by the experiments is not in agreement with the figure. It is however not very unlikely that the N_2O is formed from the released NO_2. The possible slow second step, may be the reason why no NO_2 is detected immediately. All this is highly speculative at the moment, and therefore reaction 6.49 will be used for the calculations. The thermodynamic properties of HNF are not in the standard CHEMKIN database. The values from section 2.2 are used as input for the model.

6.3.3 Solution

The model is very similar to the `PREMIX` model for steady laminar premixed flames developed by Kee et al. [66]. The numerical solution procedure is summarized in Appendix A. For more details is referred to the work of Kee et al.

6.3.4 PREMIX program

The model presented here closely resembles that of the PREMIX model of Kee et al. [66]. Hence, it was decided to adapt the PREMIX Fortran program to account for the different phases and the extra necessary input. The most important changes are:

- During determination of the residual values $F(\phi)$, the phase of grid node j is determined and the proper conservation equation for that node is used. At the boundaries the proper boundary conditions are used.
- Only a certain set of chemical reactions is allowed to take place in the gas phase, while a different set is allowed to take place in the liquid phase.
- Introduction of a few new keywords to the program, to improve convergence rate (e.g. minimum time step increases during timestepping, and maximum number of new mesh points per mesh refinement increases with the number of current mesh points).

The FORTRAN code was compiled on a Pentium-166 MHz running on the Linux operating system. Optimization by compiler options like, "loop unrolling" and "inline functions" decreased the computational times noticeably. Typical execution time for the calculations presented here is 6 hours. A large amount of the computational time (about 1 hour) is used to obtain convergence on the initial grid.

The grid is automatically refined by the program. The refinement parameters η (curvature) and ζ (gradient) were set to 0.5 and 0.2 respectively. The initial grid consists of 59 (almost) equidistant mesh points. A higher mesh concentration near the surface appeared to be necessary for initial convergence. The final grid constructed by the program typically consists of about 200 mesh points. The grid nodes concentrate around the burning surface and the first 10 mm of the gas phase.

6.3.5 Results

Neat HNF

Figures 6.10 to 6.17 show results of the PREMIX calculations. The calculated temperature profile is shown in Fig. 6.10. The final flame temperature is 2777 K which is 0.4% above the adiabatic value of 2766 K. The temperature rises rapidly to ~2550 K above the burning surface ($x < 0.5$ mm). This is the primary flame zone. In the subsequent flame zone ($x > 0.5$ mm), the temperature rises slowly to the final adiabatic value. The first flame zone is the most reactive. The second flame zone is almost energetically neutral. The calculations match the experimental observations of Chapter 4. The flame temperature is close to adiabatic within 1 mm above the burning surface. The difference between the calculated 2550 K and the adiabatic value of 2766 K is within the experimental errors.

In Table 6.2 the calculated mole fractions for several species, at 1 mm above the surface, are compared to the adiabatic values as calculated by the NASA SP-273 code (CET-89). From the table it becomes clear that at 1 mm above the surface most species are already close to their adiabatic value. A real deviation from the adiabatic fraction is only found

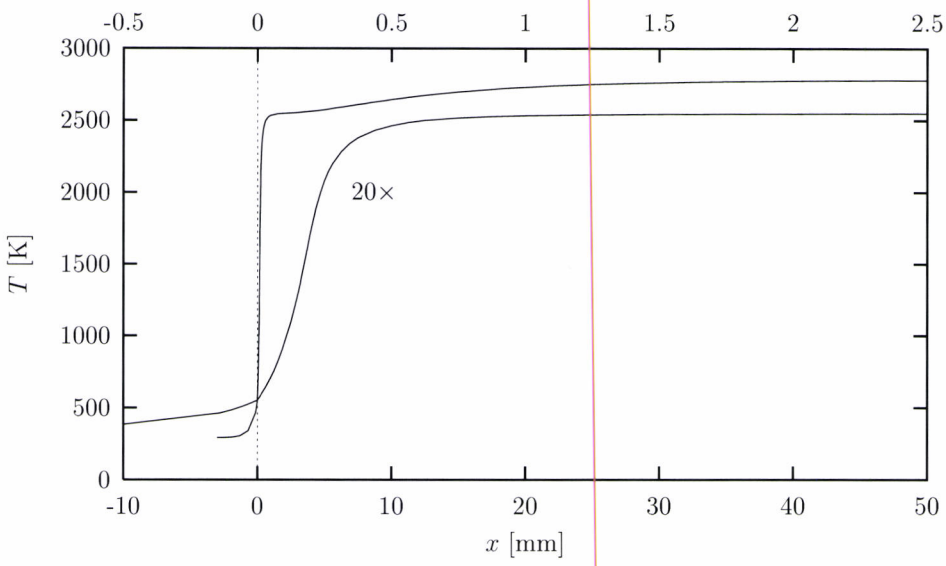

Figure 6.10: *Calculated temperature profile (neat HNF, 0.1 MPa). Graph labeled 20× is enlarged 20 times and uses upper x-axis.*

for the species NO, O_2 and N_2. As will become clear, this is mainly due to the slow NO decomposition reaction.

The species profiles in the first part of the flame are shown in Fig. 6.11. HNF is seen to decompose rapidly. Within 200μm above the surface N_2 and H_2O have formed, and from then on the variation is minimal. Also shown in the figure are the results from spontaneous Raman measurements by Hanson-Parr et al. [56]. These measurements also show that the variation in species concentration between 0.35 mm and 1.2 mm above the burning surface are minimal, although the measurements show that the temperature increases from 1800 K to 2766 K in this region. In the second stage most fuel species have been oxidized, and NO cannot react as an oxidizer. It therefore decomposes to O_2 and N_2, see Fig. 6.12. This

	H_2	O_2	OH	CO	CO_2	N_2	NO	H_2O
adiabatic	0.018	0.108	0.046	0.040	0.100	0.342	0.017	0.304
calculations at 1 mm	0.020	0.002	0.007	0.036	0.112	0.219	0.276	0.321
calculations at 100 mm	0.017	0.114	0.047	0.041	0.103	0.340	0.018	0.292

Table 6.2: *Most important species concentrations (mole fractions) of neat HNF combustion: comparison between calculated species fraction at 1 mm and 100 mm above the surface and the adiabatic values.*

reaction is almost energetically neutral, and has only a minor effect on the temperature. In double-base propellants this second stage flame accounts for about 50% of the heat release, and has a dramatic influence on the combustion properties. For HNF the contribution of the second stage flame is small, and it can hardly affect the combustion. A dark zone, as found in RDX and double-base combustion is absent.

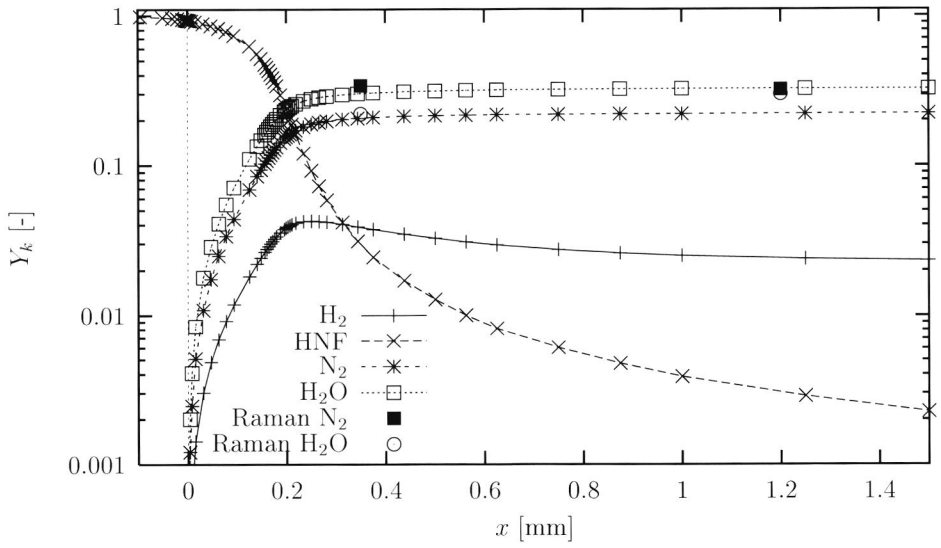

Figure 6.11: *Calculated species profiles (neat HNF, 0.1 MPa). Spontaneous Raman measurements from Ref. [56].*

For several radicals PLIF species profiles have been obtained [123]. The NH, NH_2 and CN profiles are shown in Fig.'s 6.13 to 6.15. In general the agreement with experimental data is good (the location of the maximum, and the shape of the curve). The PREMIX calculations show that the location of the CN-peak moves closer to the burning surface with increasing pressure. This is in agreement with the experimental results of Fig. 4.19. The peak value was found to increase with increasing pressure, which is the opposite of the experimental results. However, due to the enhanced quenching at higher pressures an absolute comparison cannot be made.

Also the calculated shape of the OH and NO profiles matches the experimental findings. However, the absolute OH and NO mole fractions are not in agreement with the experimental results (Fig. 6.16 and 6.17). Similar results have been obtained for RDX combustion. Beckstead et al. reported that models overpredict the measurements by 40% for NO [7]. For the OH concentration similar results were found by Prasad et al. [126]. The measured OH-concentration after the primary flame was about 50% higher than the calculated value. The conclusion is that Yetter's RDX mechanism is reasonably applicable to HNF combustion. OH and NO species concentrations are underpredicted respectively overpredicted. This seems to be a general problem with the model kinetics, rather than mismatch between model calculations and the available experimental data for HNF.

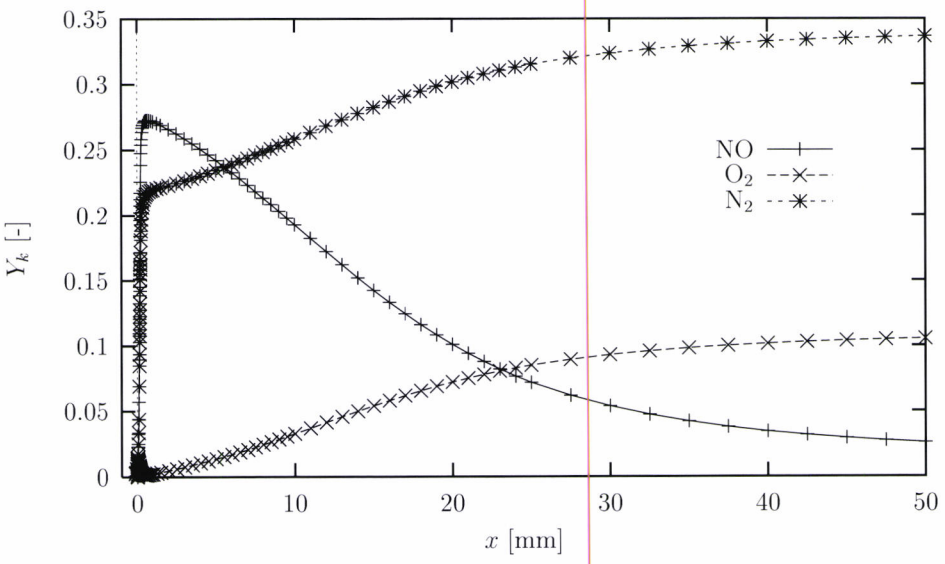

Figure 6.12: *Calculated species profiles of neat HNF combustion, showing the second stage flame zone (0.1 MPa).*

In the second stage most fuel species have been oxidized, and NO cannot react as an oxidizer. It therefore decomposes to O_2 and N_2, see Fig. 6.12. This reaction is almost energetically neutral, and has only a minor effect on the temperature. In double-base propellants this second stage flame accounts for about 50% of the heat release, and has a dramatic influence on the combustion properties. For HNF the contribution of the second stage flame is small, and it can hardly affect the combustion. A dark zone, as found in RDX and double-base combustion is absent.

HNF compositions

In Chapter 4 the combustion of the mixture of HNF with graphite and paraffin was discussed. Because the graphite and paraffin are highly dispersed into the samples, these mixtures can be considered premixed (especially at low pressures). To further investigate the effect of these additions, the mixtures HNF/graphite=95/5 and HNF/paraffin=90/10 were modeled with the PREMIX code. The paraffin was simulated by C_2H_4. Because no experimental data is available, the surface temperature was assumed to be equivalent to that of neat HNF.

Figure 6.18 shows calculated temperature profiles close to the burning surface. The temperature profiles of the HNF and HNF/graphite are comparable, although the burning rate of the graphite mixture is higher. This implies faster reactions for the graphite mixture. The mixture with paraffin shows a slower temperature rise (and lowest regression rate).

The CN-profiles for these mixtures are shown in Fig. 6.19. Both HNF-mixtures show a higher CN fraction than the pure HNF. The location of the CN-maximum is similar for

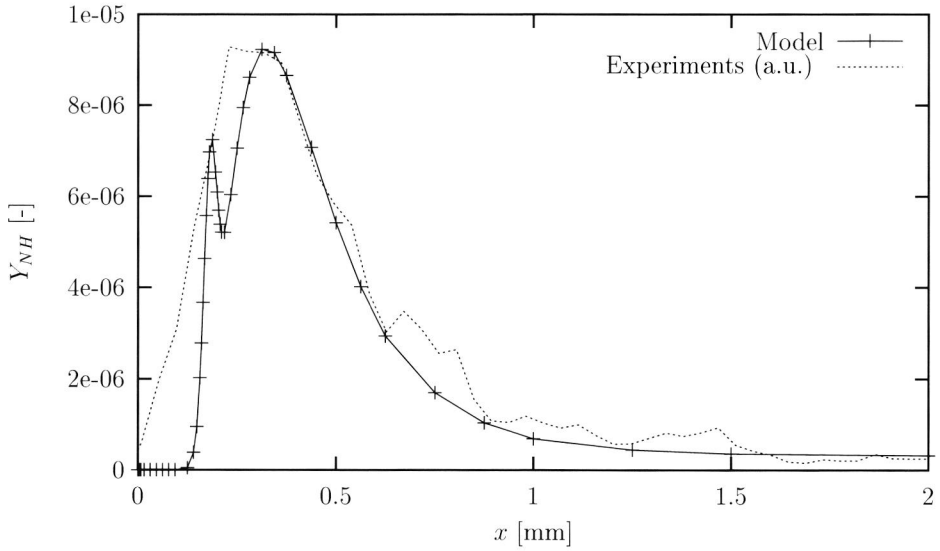

Figure 6.13: *NH mole fraction in HNF flame (0.1 MPa).*

HNF and HNF/graphite. For the mixture with paraffin, this maximum is further away from the burning surface. PLIF experiments (see Chapter 3, in particular Fig. 4.27) confirm these trends.

6.3.6 Conclusions

In this section a combustion model for HNF and HNF-mixtures has been presented. The model is based on the PREMIX-program for premixed flames. The agreement between modeling and experimental results is good. Some discrepancies were found between experimental and calculated OH and NO mole fractions. These differences are caused by the deficiencies of the available chemistry models. The model is especially useful for a better understanding of the flame structure of HNF.

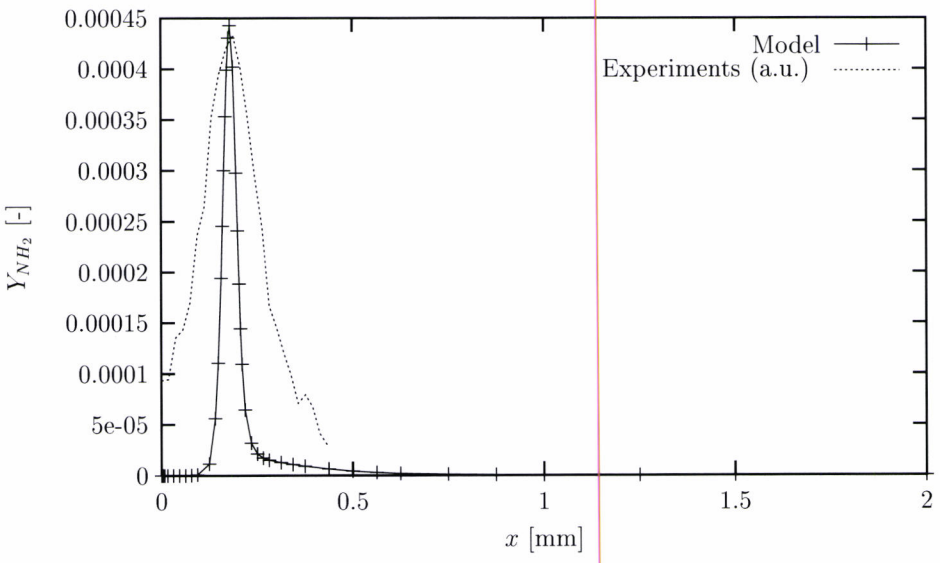

Figure 6.14: *NH_2 mole fraction in HNF flame (0.1 MPa).*

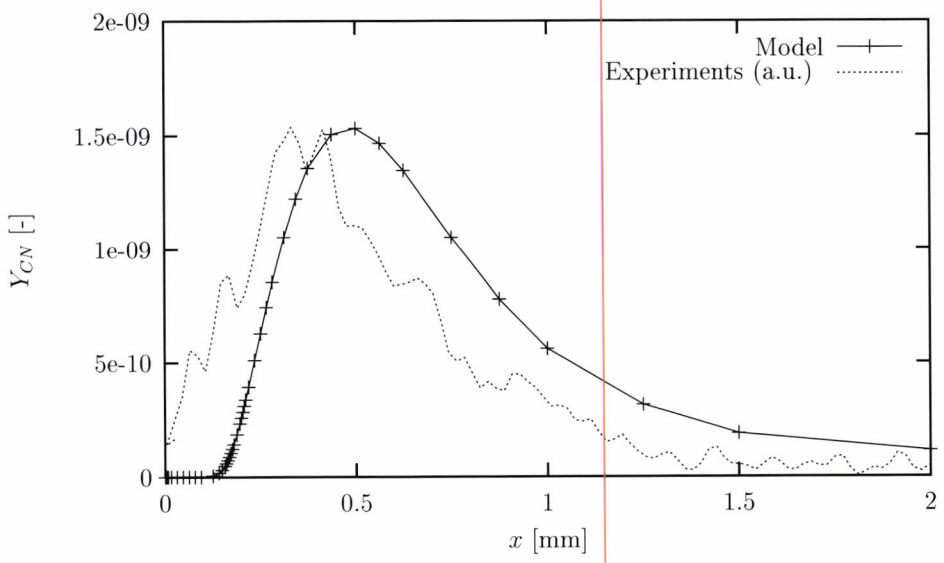

Figure 6.15: *CN mole fraction in HNF flame (0.1 MPa).*

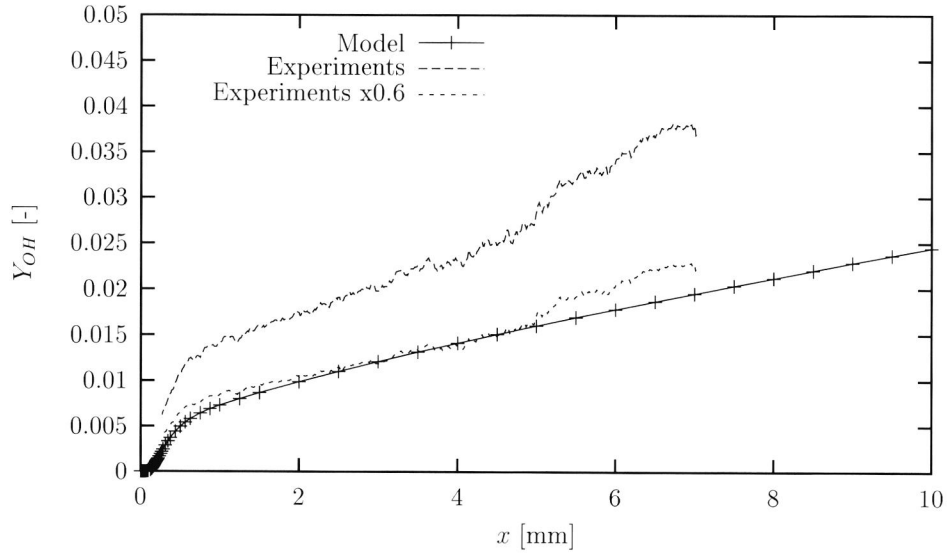

Figure 6.16: *OH mole fraction in HNF flame (0.1 MPa).*

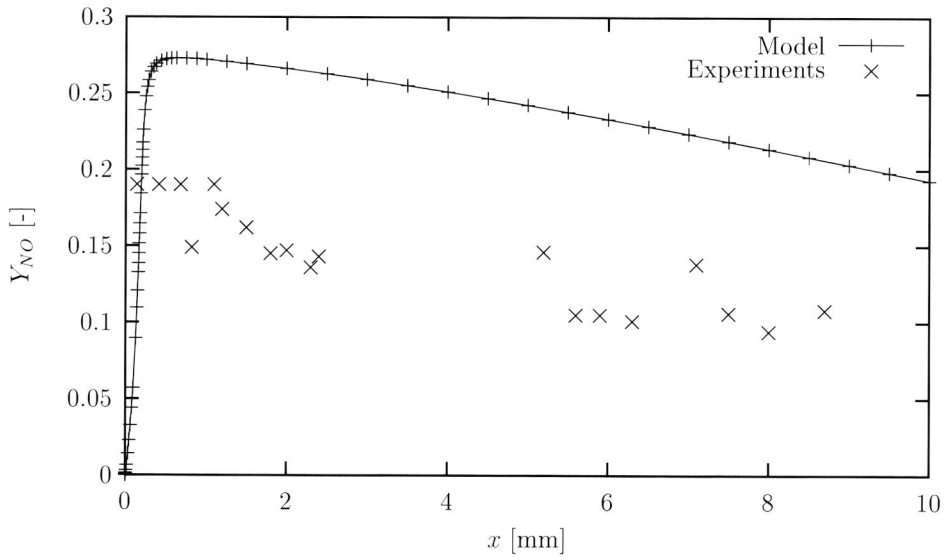

Figure 6.17: *NO mole fraction in HNF (0.1 MPa) (data from Chapter 4).*

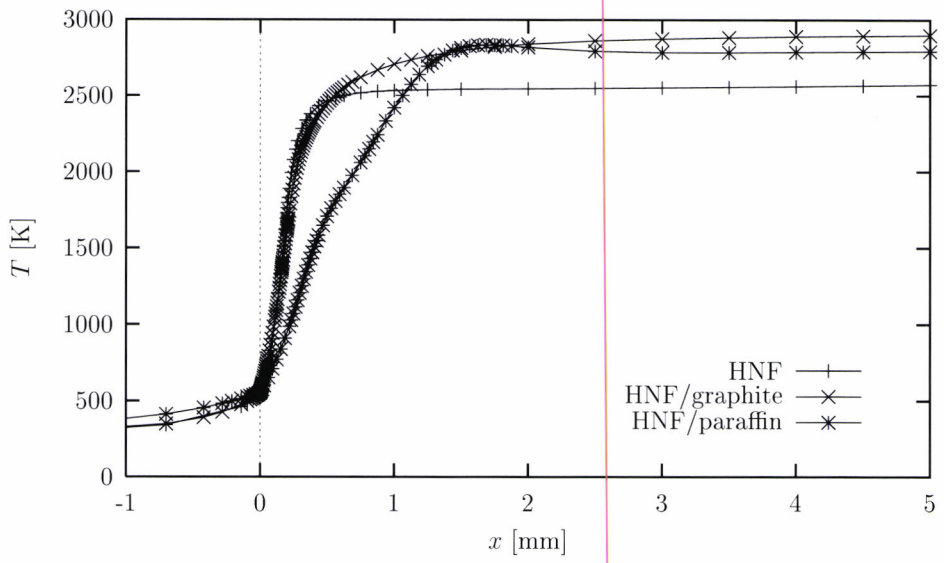

Figure 6.18: *Calculated temperature profiles for HNF, HNF/graphite=95/5 and HNF/paraffin=90/10.*

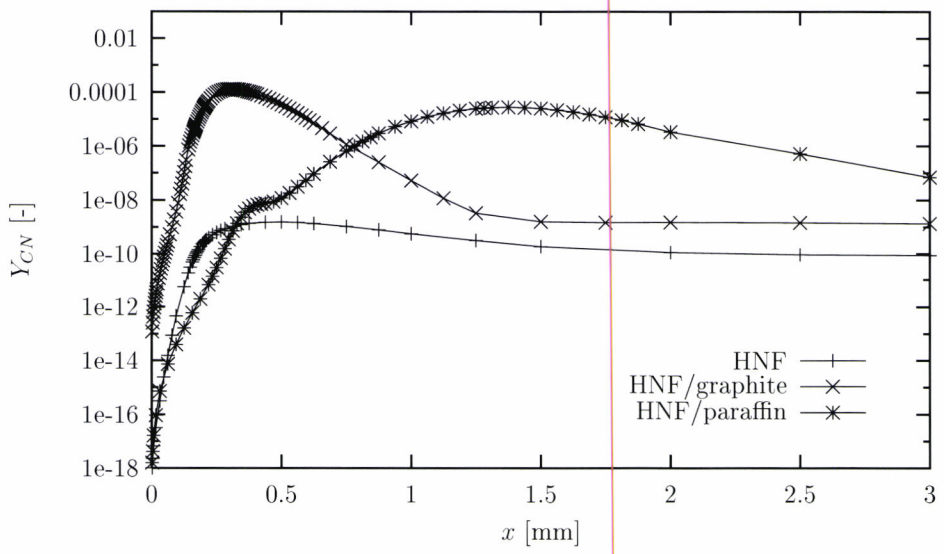

Figure 6.19: *Calculated CN-profiles for HNF, HNF/graphite=95/5 and HNF/paraffin=90/10.*

6.4 BDP propellant model

The Beckstead-Derr-Price BDP-model is based on a conceptual view for AP-propellant combustion [8], see Fig. 6.20. It considers a single oxidizer crystal surrounded by a binder. Interaction between the individual oxidizer crystals is neglected. Several flames are considered, hence the model is often referred to as the multiple-flame model. The monopropellant flame originates from the oxidizer decomposition products. This is a kinetically controlled premixed flame. Along the edges of the oxidizer crystals, diffusion of the binder and oxidizer decomposition products occurs. This flame is called the primary diffusion flame. This flame is controlled by both kinetics and diffusion. The final flame is the flame where the remaining oxidizer products react with the binder decomposition products. As the temperatures are high in this region, this flame is controlled by diffusion only.

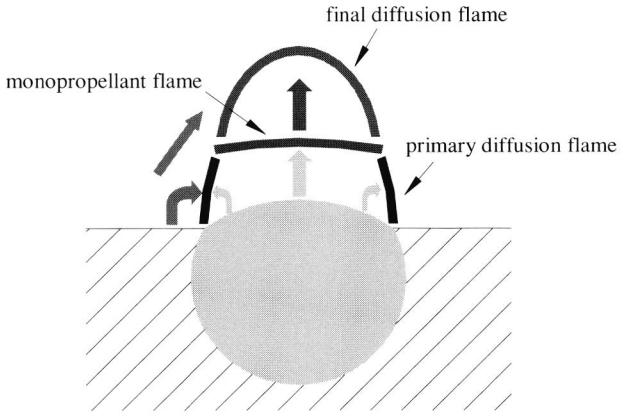

Figure 6.20: *Schematic of the multiple flames of the BDP-model.*

In case of AP-propellants the neat oxidizer flame temperature is low 1381 K (see Table 4.2) when compared to the final flame temperature of $\sim$ 3000 K. If oxidizer and pyrolysis products mix and react before the monopropellant flame occurs, the surface heat feedback is higher than in case of a neat oxidizer flame. This explains why propellants with fine AP particles burn faster.

In this section the results of the application of the BDP-model to HNF/GAP-propellants are presented. Except for some minor changes, this implies only different model input values. The calculations were done with the HYPEM program that was originally written for AP/HMX/HTPB-propellants [14]. The HYPEM computer program is an implementation of the BDP-model. For a more complete description of the model changes and inputs is referred to Landman [87].

6.4.1 Model input

The results of regression rate and surface temperature experiments for neat HNF were fitted to an Arrhenius expression. The HNF-flame coefficients were adjusted to obtain the correct value of the HNF regression rate at 0.1 MPa. For the combustion of GAP, the results of

Kubota and Sonobe have been used [84]. They found that the exothermic decomposition reactions at the surface are the major heat source (93% of the total at 0.6 MPa) for GAP combustion (see also section 5.2.1 for a discussion about GAP combustion).

The BDP-model does not account for the self-sustained combustion of a binder, as is the case for GAP. In the case of a propellant consisting of a binder only there are no flames. The only heat source is the degradation energy of the binder, Q_d. If the degradation energy would be constant, there would not be a pressure dependent burning rate. Therefore the degradation energy was introduced as a function of pressure. The variation of Q_d is relatively small: 612 kJ/kg at 0.1 MPa to 779 kJ/kg at 10 MPa. The experiments of Kubota and Sonobe also indicate a pressure dependent heat release in the condensed phase, but the experimental pressure interval is small. The physical interpretation is that with increasing pressure, more heat is released in the condensed phase, and less in the gas phase.

6.4.2 Results

Effect of oxidizer particle size

The oxidizer particle size affects the relative flame heat contributions. Figure 6.21 shows the calculated heat feedback contributions for a HNF/GAP propellant with a solid loading mass fraction $\alpha = 0.8$. The calculations were carried out at a pressure of 0.2 MPa. At low pressures and small oxidizer crystal size, the primary diffusion flame dominates over the HNF monopropellant flame. All of the oxidizing species react in the primary flame (the fraction that reacts in the primary flame is β_f=1). As the oxidizer particle size increases, the diffusion distances increase. Less oxidizer species react in the primary flame, and β_f decreases. At 0.2 MPa the primary flame disappears totally at a particle size of approximately 200μm. The final diffusion flame starts to come up together with the HNF monopropellant flame. This is because the oxidizing species that are left over from the monopropellant flame, are assumed to react in the final diffusion flame. The relative amount of heat feedback from the final flame is maximally 20% of the total heat feedback. With increasing crystal size the diffusion distance increases, and the final flame moves further away from the surface. The heat feedback of the final diffusion flame decreases for increasing particle size.

The HNF monopropellant flame standoff distance rapidly decreases with increasing pressure ($\sim p^{-1}$). When this distance becomes smaller than the primary flame kinetic standoff distance, β_f becomes zero. This means that all of the HNF reacts in the monopropellant flame, before diffusing into the fuel decomposition gases. At pressures above 0.5 MPa, this is even the case for the smallest crystal sizes in the calculated range 10-1000μm. In that case only two flames remain: the HNF flame and the final diffusion flame. Figure 6.22 shows a typical example of the relative contribution of these two flames in comparison with the calculated burn rate. The relative contribution of the final flame decreases with crystal size due to an increasing diffusion distance. Simultaneously, the relative contribution of the HNF monopropellant flame increases. The burning rate depends on the total amount of heat that reaches the surface. For larger crystals this total amount is lower than for small crystals, because the extra heat from the final flame (with higher flame temperature) is missed. Consequently the burning rate decreases with particle size (see Fig. 6.22). The variation of the burning rate for oxidizer size varying from 10 to

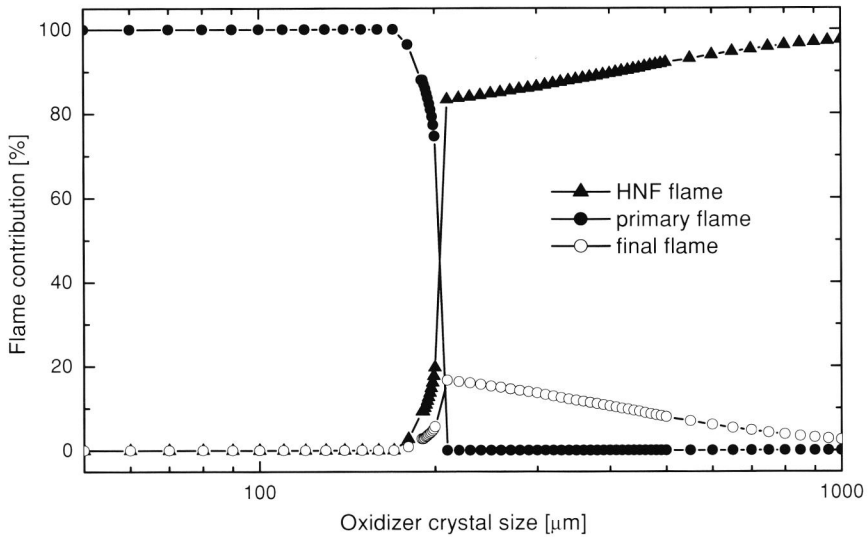

Figure 6.21: *The relative contributions of the three flames to the total heat feedback, for a HNF/GAP=80/20 propellant at 0.2 MPa.*

1000μm is 6%. This difference is very small compared to that of AP-propellants. In the same particle size range and at the same pressure the burning rate for an 88/12 AP/HTPB propellant drops 90% [14].

Pressure dependency

The pressure exponent n depends on several parameters, like the relative amounts of oxidizer and binder (expressed by α), the particle size, and the pressure. Figure 6.23 shows the variation of the burn rate predicted by the BDP-model with the solid loading for two extreme cases: $\alpha = 0.1$ and $\alpha = 0.9$, for a HNF particle size of 100μm. The calculated burn rates follow the $r_b = ap^n$ relation. The variation of the burn rate exponent with solid loading is remarkably small and varies from $n = 0.75$ to $n = 0.87$ for the above mentioned solid loadings. Compared to the assumed burn rate exponent of the GAP ($n = 0.44$), the burn rate exponent of the 10/90 HNF/GAP propellant is high. Figure 6.24 shows the calculated variation of the burn rate exponent with the HNF solid loading. It is seen that even small amounts of HNF in the propellant increase the burn rate exponent of the propellant considerably.

Schöyer et al. reported experimental results of strand burner burn rate measurements with several HNF/GAP formulations [134]. Two of these propellants did not contain burn rate catalysts: HGU-2 (47.5% HNF) and HGU-14 (59% HNF). The HGU-14 propellant also contained 18% aluminum. The measured burning rates of these propellants are shown in Fig. 6.25. The experiments confirm the calculations that the pressure exponent is insensitive to the solid loading. The HGU-2 propellant showed higher burning rates than the calculated value, but the line drawn in Fig. 6.25 is based on only two data points. The

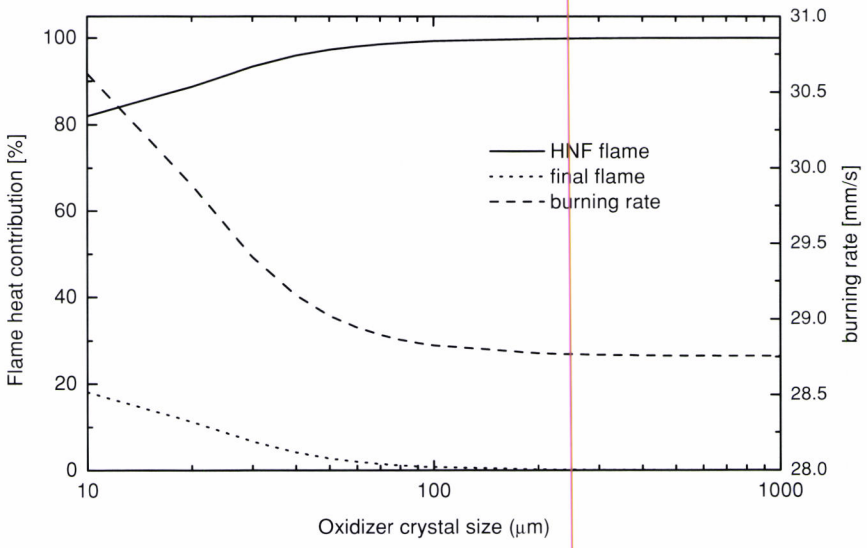

Figure 6.22: *The calculated relative flame heat contributions and burn rate at 6.9 MPa (1000 Psi) and* $\alpha = 0.80$.

calculated results for $\alpha = 0.59$ are in good agreement with the experimental HGU-14 data. For this propellant the aluminum was neglected in the calculations.

In Fig. 6.26 the variation of the burn rate with pressure is shown for two extreme particle sizes. The pressure exponent was determined by a linear fit in the pressure interval 0.4-10 MPa. The calculated points in this range are not shown. They do not deviate from a straight line. The four points shown in the figure demonstrate the effect of the primary diffusion flame on the burning rate of the propellant containing fine HNF. As mentioned before, this effect is only present at low pressures for small particles. The burning rates in the range 0.1-0.4 MPa are increased in comparison with what is obtained when the primary diffusion flame is neglected. In this range a lower pressure exponent is found. The lines in Fig. 6.26 are almost parallel. The absolute difference in the burning rates decreases slightly with pressure: 7.8% at 0.5 MPa to 6.0% at 10 MPa. This slight decrease is caused by the fact that the diffusion becomes more difficult at high pressures. The difference in the burning rate between small and large particles is caused by the difference in the diffusion flame contribution. As a result of the decrease of this contribution, the difference in burning rate decreases with pressure. Therefore the pressure exponent is slightly lower for the small HNF crystals. These modeling results are confirmed by the experiments of section 5.4. The results reported there show a very small effect of the particle size on the burning rate.

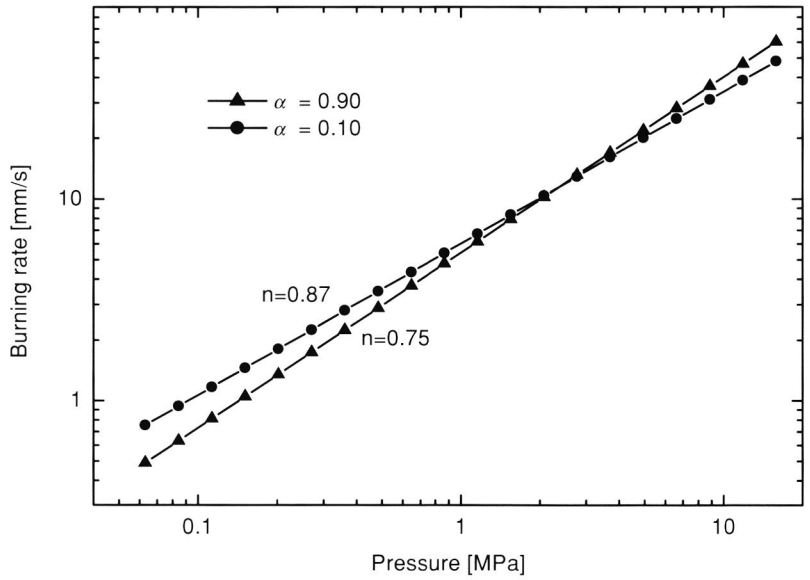

Figure 6.23: *Burning rate as a function of pressure for $\alpha = 0.10$ and $\alpha = 0.90$. The oxidizer particle size is 100μm.*

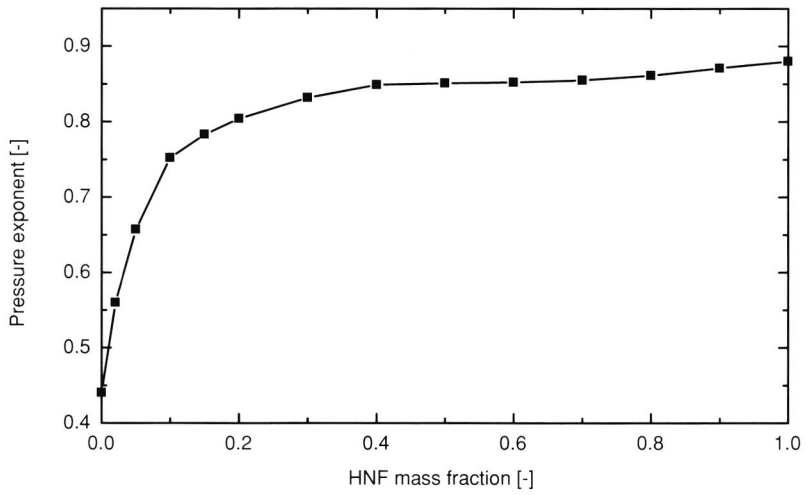

Figure 6.24: *Variation of the pressure exponent as function of the HNF mass fraction.*

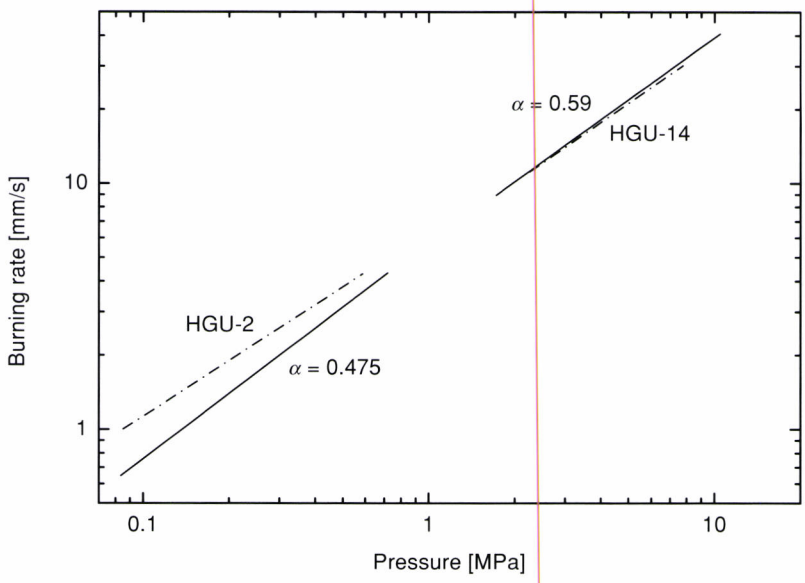

Figure 6.25: *Measured burning rates of propellants HGU-2 and HGU-14 (dashed lines) versus calculated results for matching HNF mass fractions (solid lines).*

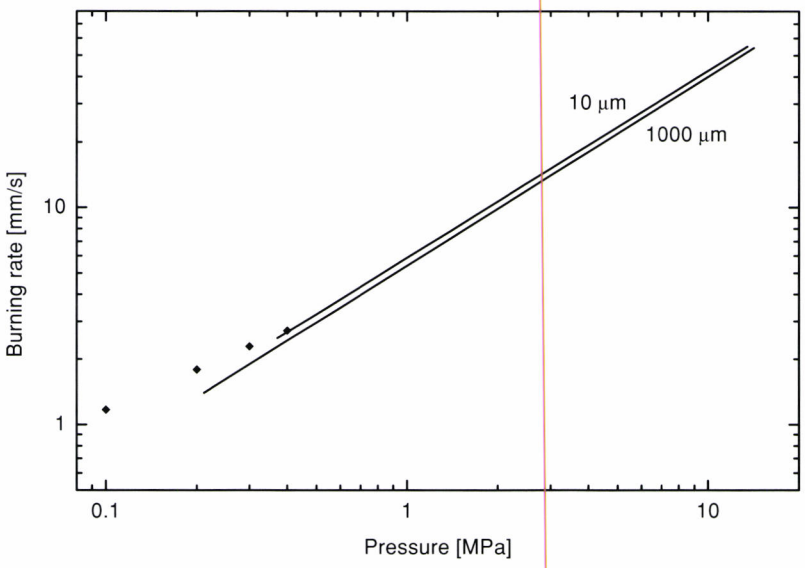

Figure 6.26: *The calculated pressure dependency of a 75/25 HNF/GAP propellant with small (D=10μm) and large (D=1000μm) HNF particles. The primary flame has been neglected ($\beta_f = 0$). The effect of a non-zero β_f is shown by the solid points, and is only observable for small particle sizes and pressures below 0.4 MPa.*

6.5 BIGMIX: 2D computational fluid dynamics model

The BDP-model from the previous section does not allow a-priori calculation of diffusional interaction between HNF and binder decomposition products. For example the diffusion interaction parameter β_f has to be estimated. Also direct comparison with experimental sandwich data is impossible, because the BDP-model does not calculate the complete flame structure. In this section the calculation of the flame structure above a HNF-sandwich is reported. In essence the sandwich structure was modeled as two-dimensional burner. This implies that the regression of the surface cannot be accounted for. Coupling of the gas phase with the condensed phase as for the PREMIX-modeling, would be very expensive in terms of computational time.

6.5.1 BIGMIX modifications

The BIGMIX program was developed to model the combustion of turbulent two-dimensional diffusion flames [125]. The BIGMIX program was adapted to calculate the gas phase structure above a HNF/GAP sandwich [87]. This sections summarizes the most important changes. For more details is referred to Landman [87].

BIGMIX uses a finite volume method. The domain is divided into grid cells. For the HNF/GAP problem a rectangular grid is used, that is uniform along the burning surface (y-axis), and stretched in the direction away from the burning surface (x-axis). The position of the cell walls is precisely in between the grid points. The scalar variables and the thermodynamic and transport properties are evaluated at the grid points. The velocities are evaluated at the cell walls. The finite differences of the PREMIX model are replaced by finite volumes. The differential equations are integrated over these volumes, i.e. a balance over the cell. The steady solution is obtained by time-marching, until a steady solution is obtained. For this particular problem, a fractional time step method was employed to increase convergence. First the non-reactive terms (convection and diffusion) are integrated in time. Then the reactive terms are integrated. The chemical reactions have much smaller time scales than the flow, and can then be solved efficiently using smaller timesteps.

The BIGMIX model was developed for turbulent combustion. For these flows the turbulent mixing is much larger than the diffusional mixing. Diffusional mixing was therefore not included in the BIGMIX program. The sandwich flow is laminar, and diffusion is the only mixing method. Multi-component diffusion [158], or diffusion as treated by Eq.(6.11), $Y_k V_k$, was considered to be too computational expensive. A constant Schmidt number approach was followed, which implies a constant diffusion coefficient was used for all species [162].

6.5.2 Model input

The HNF mechanism of section 6.3 was used as a basis for the kinetic database. To include the reactions of GAP decomposition products, this mechanism is extended with the GRI-mechanism for hydrocarbon combustion. If a reaction was present in both mechanisms, Yetter's parameters were chosen. The additional reactions are given in Appendix B.2. An artificial reaction from solid carbon to gaseous carbon was added. The carbon that is

present in the GAP decomposition products can in this way be consumed by the oxidizing species coming from HNF decomposition. The complete reaction mechanism contains 58 species in 382 reactions.

In the inlets there is a continuous flow of decomposition gases of HNF and GAP. The mass flow rates are obtained from the individual HNF and GAP regression rates, yielding inflow velocities of 0.3 m/s and 8.3 m/s respectively. The results of the PREMIX calculations were used to determine the composition above the HNF surface. The composition above the GAP surface was obtained from the GAP model developed by Davidson and Beckstead [29]. When using mechanism A or B of Davidson and Beckstead unrealistic temperature jumps were found above the burning surface. These steep temperature profiles are caused by immediate reaction of species like CH_2 and C_2H_3. Removing these species and increasing the surface temperature from 620 K to 700 K (in correspondence with the micro-thermocouple results from Kubota [84]), the temperature profile become less steep and compares well with experimental data [87]. Table 6.3 summarizes the inlet boundary conditions for HNF and GAP.

GAP		**HNF**	
T_s	700 K	T_s	553 K
$C_{(s)}$	0.240	$HNF_{(g)}$	0.9137
C_2H_2	0.015	O_2	0.01726
C_2H_4	0.011	CO	0.01726
CH_2O	0.029	N_2O	0.01726
CH_4	0.023	HONO	0.01726
CNO	0.028	N_2H_4	0.01726
CO	0.114		
H_2	0.280		
H_2O	0.009		
HCN	0.069		
N_2	0.160		
NH_3	0.023		

Table 6.3: *Inlet boundary conditions (species concentration in mole fractions).*

Calculations were performed for a sandwich with a total width of 2 mm, and a GAP binder slab of 250 μm in the center. The first three millimeters in the gas phase were calculated. Because of the symmetry of the problem, only half of the domain is calculated (1×3 mm^2). Typically the calculations are performed on a grid of 40×40 cells. The cells are uniform in the y-direction (along the surface) and stretched in the x-direction (perpendicular to the surface). For this grid the smallest cells are 25×25 μm close to the surface, and 166×25 μm on the exit boundary.

6.5.3 Implementation

The BIGMIX program was compiled with the NAGWare Fortran 95 compiler on a Linux Pentium platform. For a grid size of 40×40 cells, a stationary solution took about 300 hours of computational time on a 400 MHz PC. Using this solution as an estimate for a

80×40 cell solution required an additional 150 hours. For the calculations at 0.1 MPa time a time step of 10^{-6} s was used. For higher pressures the time step was reduced to 10^{-7} s and 10^{-8} s for 1 and 10 MPa respectively.

6.5.4 Results

First some results at ambient pressure will be given. These results are important for comparison with the experimental data. In the second part of this section the results from calculations at higher pressure will be discussed. These are more relevant for propellant combustion.

Ambient pressure

The ambient pressure calculations were carried out on the finest grid, 80×40 cells. Figures 6.27 and 6.28 show some typical results that were obtained. The temperature profile shows that the temperature rises more rapidly above the HNF than it does above the binder slab. Just above the HNF surface the isotherms are close together and parallel to the surface. Farther away from the surface the temperature contour has a different shape. The high temperature zone is closest to the surface at approximately 0.5 mm from the sandwich center. This is an indication of a diffusion flame. In the presence of a fuel, a higher flame temperature is reached. The temperature profile also shows that the gradient of the temperature profile (i.e. the heat feedback to the surface) is not higher near the surface.

The second image of Fig. 6.27 shows the u-velocity, i.e. the velocity in the x-direction away from the burning surface. The inlet velocity of the GAP gas stream is much higher than the inlet velocity of the HNF gas stream (8.3 vs. 0.3 m/s). The main cause for this is that the density of the GAP decomposition products is lower than that of HNF (which consists for a large part of HNF vapor). In addition, GAP has a higher regression rate at ambient pressure. Because of the fast decomposition of HNF, the velocity increases rapidly above the HNF surface. The velocity in the y-direction is maximal at approximately 0.5 mm above the surface, somewhat outside the boundary of the GAP and HNF inlet streams. The v-velocity in this region is pointed outwards, because of the diffusion of the GAP decomposition products into the HNF gas stream. Closer to the surface there is a small region where the HNF products diffuse towards the direction of the binder. HNF decomposes very fast above the burning surface. The $C_{(s)}$ mass fraction decreases to zero in less than 1 mm above the GAP surface. The profiles of CNO, C_2H_2, C_2H_4, CH_2O, CH_4, NH_3 and HCN (all GAP decomposition products) are very similar to that of $C_{(s)}$.

The last image of Fig. 6.28 shows the N_2 mass fraction. N_2 is the main decomposition product of GAP, and is also an important species in the HNF flame equilibrium composition (is not directly formed during HNF decomposition). This is clearly seen from the N_2-profile. The final N_2 concentration is reached within 1 mm above the GAP slab. The N_2-concentration above the HNF takes longer to reach equilibrium (not fully reached within the computational domain).

Figure 6.28 shows some more species profiles. The O_2 mass fraction is shown in the first image. Neat HNF combustion yields 13% O_2. In the presence of the binder, the oxygen is consumed in reactions with the fuel products, and only small amounts remain, away from

the binder products. The O_2 is not directly formed during HNF decomposition, and is formed away from the burning surface.

The CO and CO_2 images are almost complementary. The CO mass fraction is the highest in a region about 1 mm above the GAP surface. The lack of oxidizing species, yields predominantly CO. The excess oxygen in HNF, yields mostly CO_2.

The NCO image shows maximum concentrations right above the HNF/GAP interface. This species is a good example of a species that is not found in the HNF and GAP monopropellant flames, but is present in areas where these two mix. Species like NNH, HOCN, HCCOH show similar profiles.

The HNF decomposition product N_2O is reduced by the GAP products, as seen in the fifth image of Fig. 6.28. The NH_2 mass fraction is shown in the last image of this figure. The PREMIX calculations already showed the NH_2 present above the burning surface, see Fig. 6.14. However, much more NH_2 is found above the binder slab. PREMIX calculations for GAP showed that the NH_2 concentration is $\sim 10^{-7}$. For the sandwich structure, the NH_2 concentration is several orders larger.

Elevated pressure

Besides the calculations at 0.1 MPa, also calculations at 1 and 10 MPa have been carried out. In this paragraph the effect of pressure will be evaluated. By increasing the pressure the reactions rates become faster, but diffusion is reduced. The burning behavior of the sandwich is determined by the location of the heat release. To visualize this heat release, the chemical heat release has been calculated. Figures 6.29 to 6.31 show the effect of increasing the pressure. Because the flame zones become smaller with increasing pressure, the computational domain was smaller for 1 and 10 MPa. With increasing pressure, the temperature profiles above the HNF surface become steeper, and the difference with the binder becomes obvious. At 10 MPa there is no complete mixing within the computational domain.

The heat release image of Fig. 6.29 shows the heat release rate at 0.1 MPa. Near the HNF/GAP interface the reaction zone crawls upwards. To resolve the heat release at the HNF/GAP interface, the maximum value of the color legend ($20 \cdot 10^9$ W/m^3) is lower than the actual maximum ($30 \cdot 10^9$ W/m^3) that is reached. For the images of 1 and 10 MPa, the maximum value of the color legend is multiplied by 10 and 100 respectively. In this way the images are comparable, as the heat release is expressed in W/m^3 and the density is proportional to the pressure. In the 1 MPa image, the two thin stripes that extend in vertical direction illustrate the presence of a diffusion flame. The heat release in this region is an order of magnitude smaller than the heat release near the HNF surface. For the high pressure, the heat release in the "diffusion flame" is two orders of magnitude smaller than that at the HNF surface. This fact, and the fact that the HNF flame is very close to the surface, make that the contribution of the diffusion flame is negligible.

To evaluate how much heat is actually transported by conduction to the surface, the conductive heat fluxes ($\lambda_g \partial T/\partial x$) have been determined. Figure 6.32 shows the results. For 0.1 MPa there is a large change in the heat flux, and locally it is even negative. This is caused by numerical errors. Around 0.6 mm from the sandwich center the heat flux is 15% higher than at the HNF outer edge. This effect was already observed in the temperature image (Fig. 6.29), where the upper isotherm is closer to the surface in this region. So, for

low pressures, there is a small diffusion flame effect. The heat flux at 1 MPa shows a more staircase behavior. Just outside the HNF/GAP surface there is a maximum in the heat flux. At 10 MPa the heat flux has a real step behavior. So, it can be concluded that the effect of the diffusion flame is small. At 0.1 MPa the additional heat feedback is about 15%, but it decreases with increasing pressure due to the reduced mixing.

Comparison with experimental results

The BIGMIX results show that the contribution of the heat feedback of the binder-oxidizer diffusion flame in a HNF/GAP-sandwich is small in comparison to the heat feedback of the HNF flame. This is in agreement with the experimental findings of section 5.3.2. Experimentally the HNF/GAP-sandwiches were found to regress evenly, except around ambient pressure where the interface showed a slightly higher regression rate. The results of Fig. 6.32 match these experimental findings.

Also the experimentally determined width of the diffusion flame, in terms of the width of the CN-zone, compares very well with the modeling results. Fig. 6.33 compares the experimental results (from Fig. 5.18) with the results of the BDP model.

Another approach to compare experimental results with the modeling results, is to compare the experimental flame structure with the modeling results. As the HNF/GAP flame does not show a strong bright flame, it is difficult to image the flame (see e.g. Fig. 5.6). In some early experiments, the HNF/GAP sandwiches were not made by curing the GAP in between the HNF samples, but by glueing the stacks together using tiny amounts of cyanoacrylate glue. Due to this glue the flame becomes very bright. From the bright flame it can be determined where the material of the outer edges of the GAP-material has diffused to. The modeling analogy of this is the mean mixture fraction, that is the ratio of fuel to oxidizer: a mixture fraction of one corresponds to GAP, a mixture fraction of zero corresponds to HNF. In Fig. 6.34 the calculated mean mixture fraction is compared to the image of a glued HNF/GAP sandwich. Both shapes show the same outward diffusion above the burning surface, and have a very similar structure.

6.6 BDP vs BIGMIX

In the BDP-model the diffusion flame front is defined as the surface on which the oxidizer/fuel ratio equals the stoichiometric ratio. Consequently the diffusion flame height can be determined from the stoichiometric line of the mixture fraction. From this the HNF/GAP sandwich diffusion flame height at ambient pressure is found to be 2 mm [87]. This compares well with the final diffusion flame distance of 2.4 mm calculated by the BDP-model for a propellant with 2000 μm HNF crystals that resembles the HNF/GAP-sandwich.

A difficulty in the BDP-model is the estimation of the parameter β_f. This parameter describes the fraction of oxidizer species that reacts in the primary flame. In the BDP-model a rough method to calculate β_f is used, based on the geometric projection of the AP-flame on the oxidizer crystal. Applying the similar approach to the HNF-GAP input data showed that β_f becomes rapidly zero with increasing pressures. From Fig. 6.30 it is seen that at 1 MPa the heat release in the primary flame is about 4 times lower as in the

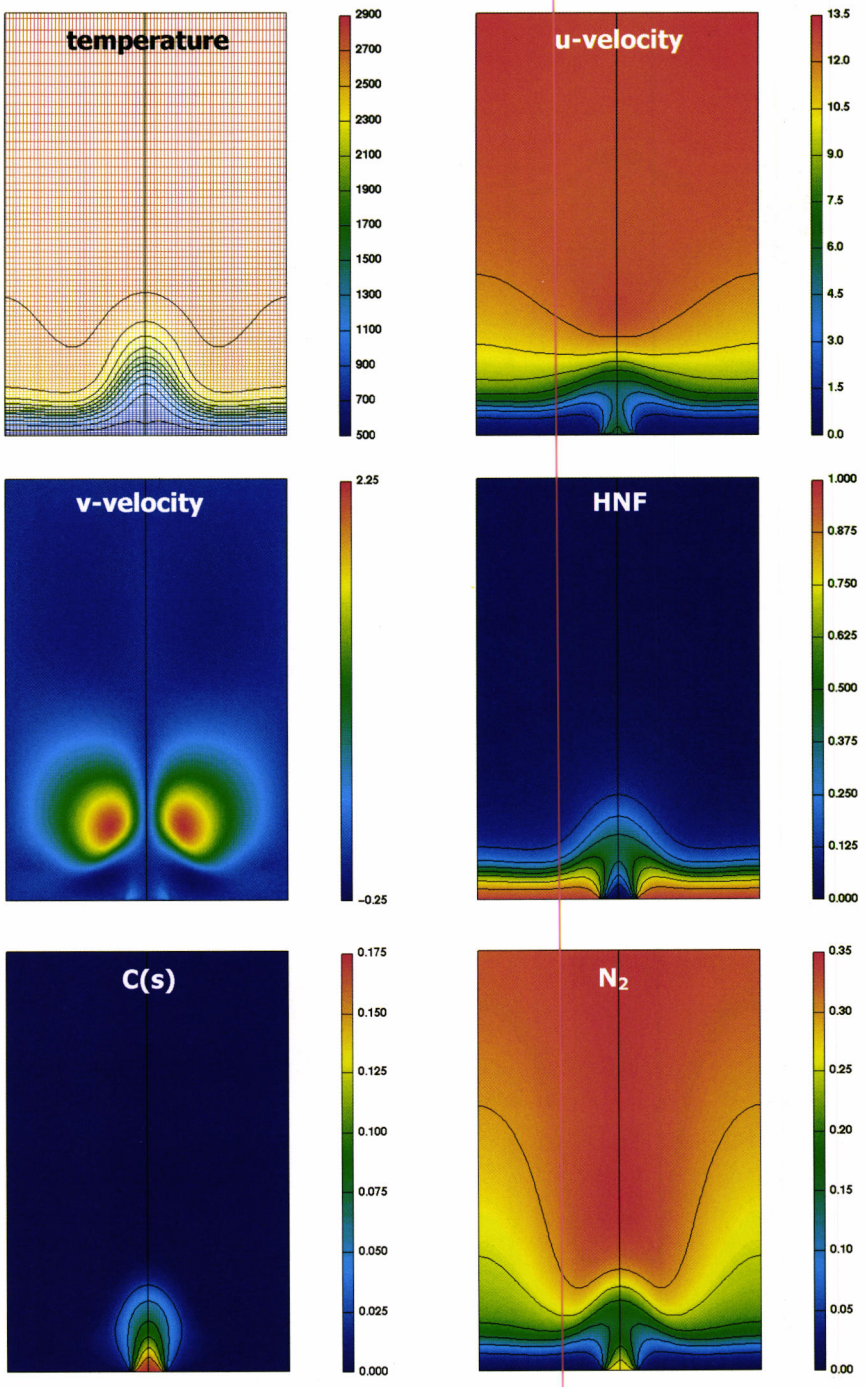

Figure 6.27: *Calculated scalar fields above a HNF/GAP sandwich at 0.1 MPa. Grid size represents* 2×3 *mm*^{2}*. Shown are the temperature (K), u- and v-velocity (m/s), and HNF,* $C_{(s)}$ *and* N_2 *mass fractions.*

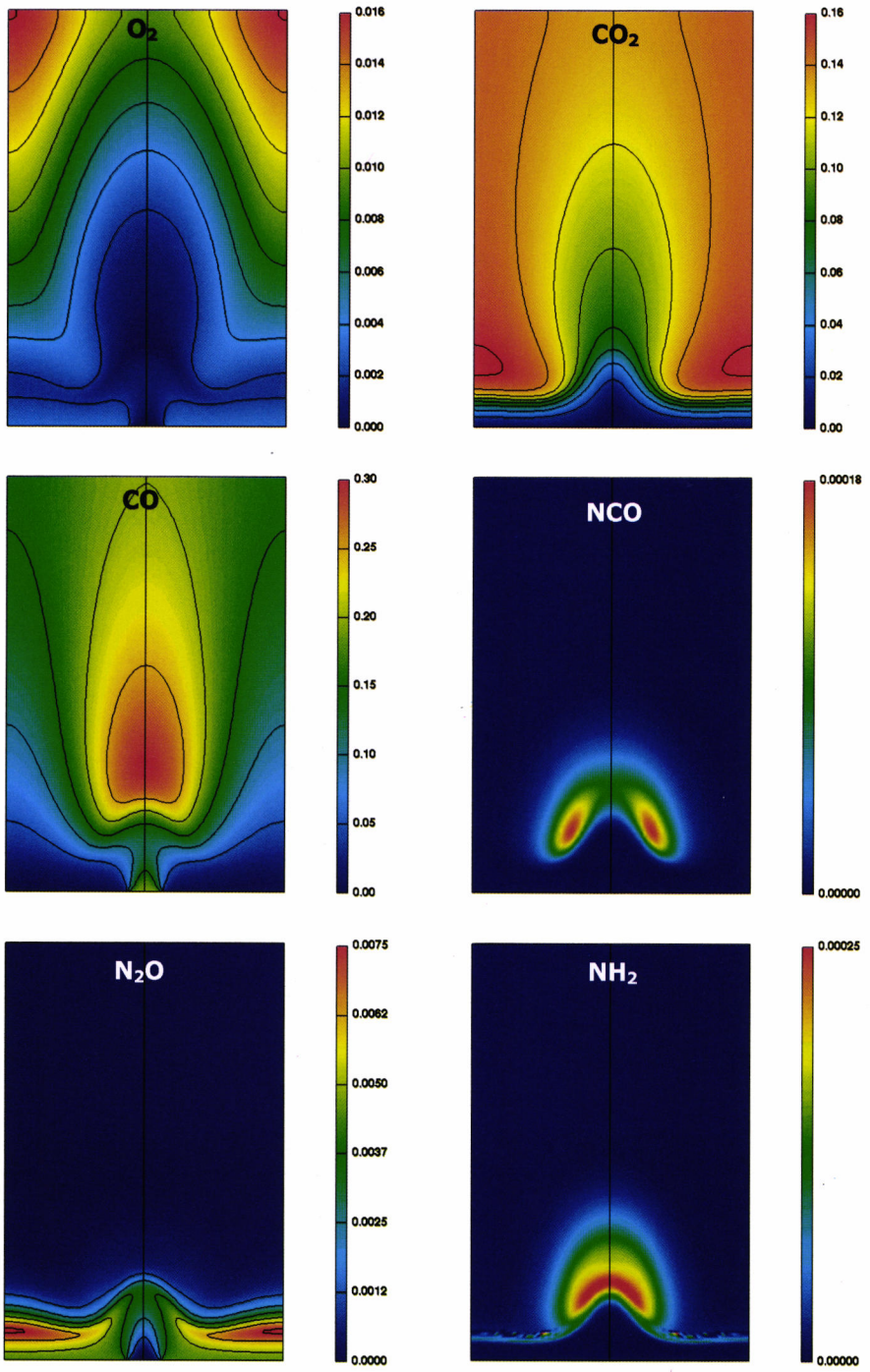

Figure 6.28: *Calculated species mass profiles above a HNF/GAP sandwich at 0.1 MPa. Grid size represents* 2×3 mm^2.

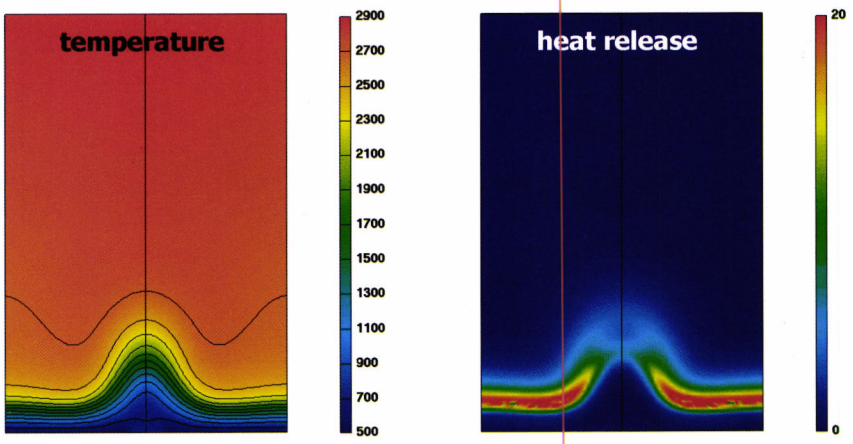

Figure 6.29: *Calculated temperature (K) and heat release rate (TW/m^3) at 0.1 MPa.*

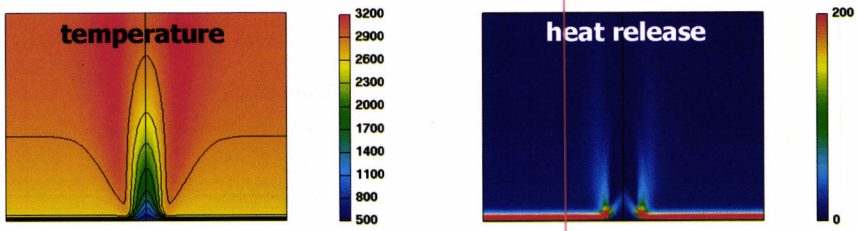

Figure 6.30: *Calculated temperature (K) and heat release rate (TW/m^3) at 1 MPa.*

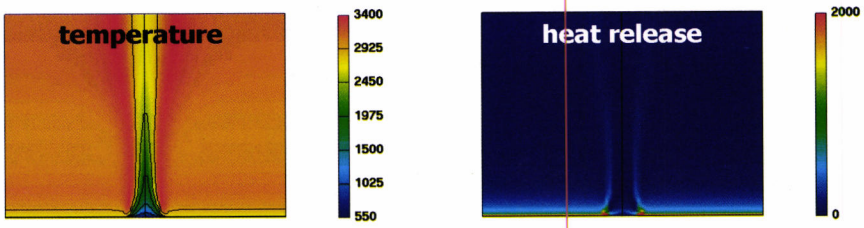

Figure 6.31: *Calculated temperature (K) and heat release rate (TW/m^3) at 10 MPa.*

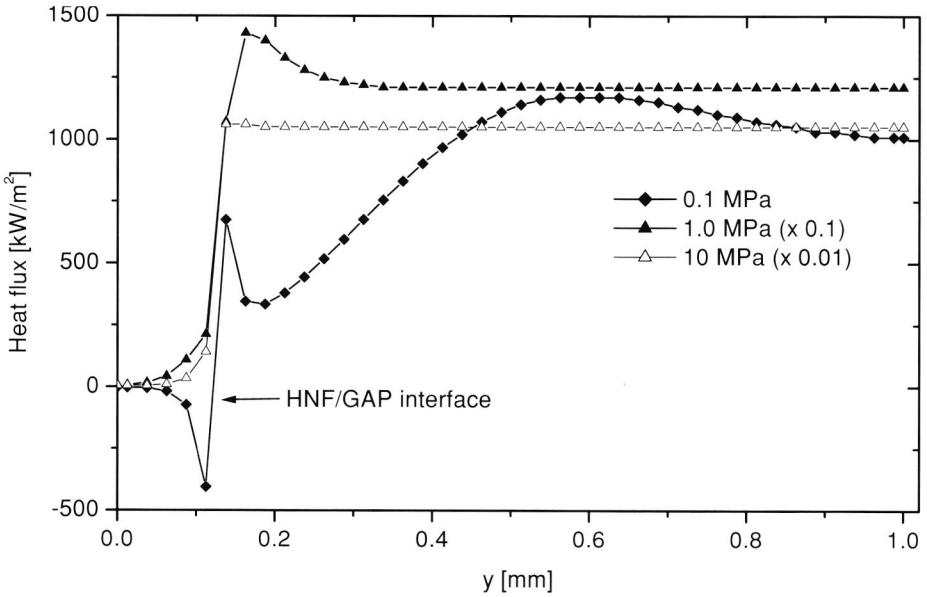

Figure 6.32: *The conductive heat fluxes to the surface of the HNF/GAP sandwich as a function of y (distance from sandwich center). The fluxes at 1 and 10 MPa are divided by 10 and 100 respectively.*

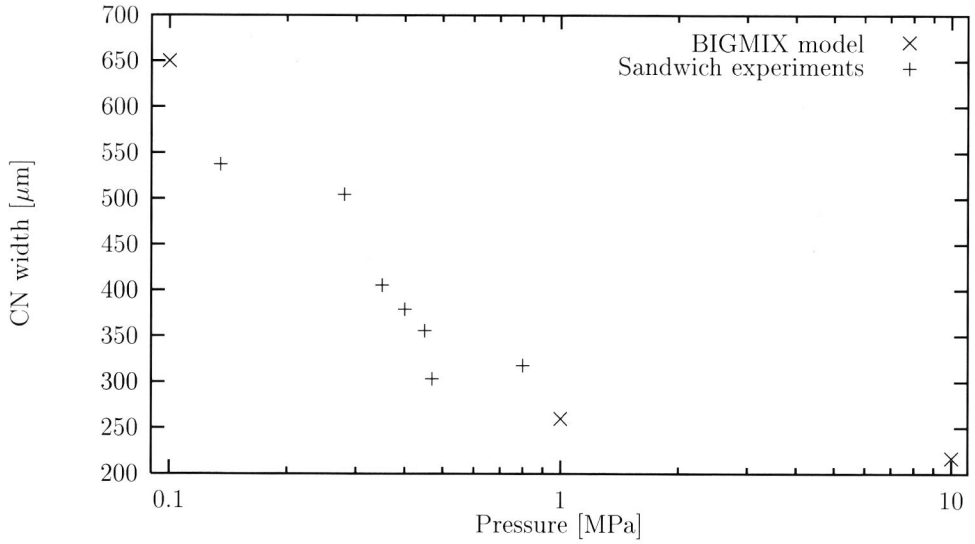

Figure 6.33: *Comparison of CN width as determined by the BIGMIX program and the experimental sandwich results.*

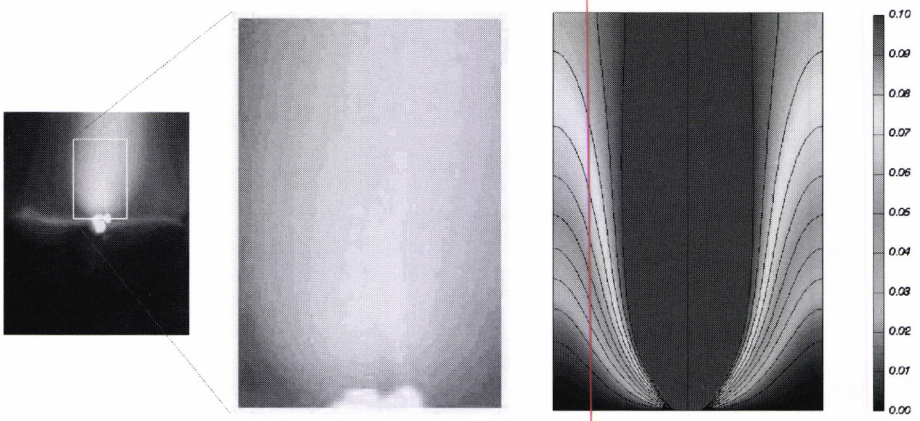

Figure 6.34: *Comparison of video image of the emission of glued HNF/GAP sandwich flame (left) and calculated mean mixture fraction (right). The central figure represents the same dimensions as the calculated mean mixture fraction (all at ambient pressure).*

HNF flame. It is also relatively farther away from the burning surface compared to the situation at 0.1 MPa. This justifies the approach followed by the BDP-calculations of setting β_f to zero.

6.7 Conclusions

In this Chapter several models for the combustion of HNF and HNF-propellants were presented. Each of the models has its own specific assumptions and approximations. Taken together the models help to explain the combustion of HNF and HNF-compositions.

The simplified WSB-approach allows for an accurate calculation of steady state regression rates, temperature sensitivity, laser-assisted combustion and other physical parameters such as surface temperatures and flame standoff distances. The idea behind the WSB-model is a low gas phase activation energy. In comparison with the flame sheet approach (high activation energy) the agreement with experimental data is better. The physical interpretation is that the rate-determining step in the gas phase has an overall low activation energy. Chemically speaking the low activation reactions (e.g. NO_2+H$\rightleftharpoons$NO+OH) are more important for the heat-feedback to the combustion surface than the high-activation energy reactions (like the reactions that further reduce the NO). This observation matches the fact that high temperatures are already achieved in the HNF-flame before NO-reactions have taken place.

The modified PREMIX approach supplements the WSB-model findings. Except for the HNF decomposition steps this model uses elementary reactions for the calculation of HNF combustion. Yetter's mechanism for the combustion of RDX was used. The results show that at 0.1 MPa a temperature of 2550 K is reached at 0.5 mm above the burning surface. At this point the NO mole fraction is at its maximum value of 0.27. Further reduction of the NO only minimally affects the temperature. At ambient pressure the adiabatic

flame temperature (2766 K) is reached at about 30 mm above the burning surface. The calculated composition above the burning surface shows good comparison with chemical equilibrium calculations. Also the agreement with species profiles for several radicals that have been obtained with planar or laser-induced fluorescence further support the model.

Based on the obtained knowledge on the combustion of HNF and available literature on GAP combustion a HNF/GAP propellant model was presented. The BDP-model approach for the combustion of AP-propellants was followed. The model calculations show that the primary diffusion flame (diffusion flame between HNF and GAP decomposition gasses) only plays a role at pressures below 0.5 MPa, for HNF particle sizes from 10 μm to 1000 μm. At typical operating pressures for solid rocket motors (5 MPa and higher) the primary flame can be neglected completely. At these pressures the HNF-flame dominates the surface heat feedback (more than 80% of the contribution). Due to the slight decrease of the final flame heat feedback, the burn rate decreases slightly with increasing particle size. This effect is small. For propellants with HNF particle sizes 10 μm and 1000 μm the variation of the burn rate is 6%. For a similar AP-propellant the burn rate variation is 90%. The pressure exponent only minimally varies with solid loading. Calculations show that already at HNF mass fractions of 0.3 the pressure exponent is higher than 0.8. From the BDP-calculations it may be concluded that the HNF decomposition flame is the dominating heat feedback source to the burning surface. The effect of the binder-oxidizer flame in terms of heat feedback to the propellant surface is negligible compared to the HNF decomposition flame.

In the last part of this Chapter results of the DUT BIGMIX code for the combustion of HNF/GAP sandwiches have been presented. The chemical mechanism for the HNF PREMIX calculations was extended with the GRI-mech for hydrocarbon combustion. The BIGMIX calculations show that the diffusion interaction between oxidizer and binder flame decreases with pressure. At 0.1 MPa there is an enhanced heat feedback due to the hotter diffusion flame. The maximum is located 0.5 mm outside the GAP slab. At 1.0 MPa the maximum still exists, but has shifted to 50 μm outside the binder slab. At 10 MPa there is no further enhanced heat-feedback due to the diffusion flame.

Chapter 7

Ultrasound

7.1 Introduction

Many different methods are currently employed to determine the regression rate of a new propellant, or control the regression rate of propellants in production [28, 70]. The most common method is the strand burner. With this device the burning rate is measured by embedding fuse wires in the propellant which melt when the combustion wave passes. A serious disadvantage of this method is that it requires a laborious preparation of the samples, which makes strand burner experiments expensive. Another possibility is the use of optical access to the burner to determine the regression rate. Both methods have already been described in the previous Chapters.

The measurement of *un*steady regression rates is less trivial. The unsteady combustion is very important for both practical and fundamental reasons. The designer needs to know about the unsteady combustion behavior of a propellant, to safely design a new system. Furthermore, accurate unsteady burning rate data gives much more information about the combustion process of an energetic material than only the steady state regression rate data. Accurate unsteady data can be used to obtain a better insight in the combustion process of the material under study [52].

The strand burner apparatus is unable to resolve the unsteady combustion. Several alternative methods are currently used with a varying degree of success. The regression rate can be determined instantaneously by measuring the momentum generated by the hot gases leaving the propellant surface (recoil). However this method is limited to the use in small laboratory samples. Eigenfrequencies often limit the frequency range of the micro-balances used in these experiments. It is also an indirect method as it requires a conversion of the momentum of the mass efflux to the instantaneous burning rate. For example, in case of metalized propellants this is not trivial [18]. Microwaves have been employed successfully to measure the burning rate. Because of the small wavelength of the waves, this yields good spatial accuracy [17]. However, the microwave technique requires some special equipment which makes it a relatively expensive method. The training requirements of the people, is also a major drawback of this method [164].

The ultrasound technique is an economical alternative to the microwave technique. The ultrasound technique has been used to determine the regression rate of both solid propellants [25, 31, 150], and of hybrid propellants [15, 36, 76, 77, 88]. In most studies, the focus has been on steady combustion. As will be discussed, for steady combustion the data-

interpretation is greatly simplified as compared to the transient combustion experiments.

It is the intention of this Chapter to evaluate the possibilities and difficulties involved in application of the ultrasound technique to unsteady energetic material combustion. In this study, the ultrasound technique will be applied to hydrazinium nitroformate (HNF) combustion. From earlier work TNO has obtained large experience with the application of the ultrasound technique in ramjet and hybrid systems [36, 76, 77]. This resulted in the development of an Ultrasound Regression Rate Analyzer (URRA). The setup that has been used for this work, is very similar to that used in the earlier work.

This Chapter starts with a brief summary of ultrasound (techniques), and the ultrasound properties of HNF in particular. In section 7.3 a combustion model for HNF is presented. This model is needed for the interpretation of the experimental results. Section 7.4 describes the experimental setup and the data-reduction method. Experimental and modeling results are presented in section 7.5.

7.2 Ultrasound

Ultrasound waves are sound waves, not audible to the human ear. In general their frequency ranges from 16 kHz to 1 GHz [114]. Ultrasound waves progress in a plane, or a spherical wave front through a medium. Like other pressure waves, the ultrasound waves can be transversal or longitudinal.

7.2.1 Propagation

Ultrasonic waves are solutions of the wave equation [114]

$$\Delta\Phi = \frac{1}{c^2}\frac{\partial^2\Phi}{\partial t^2} , \tag{7.1}$$

where Φ is the amplitude of the wave, c the ultrasound velocity, and t is time. Depending on the source of the ultrasound wave and the geometry, several types of waves may propagate through the medium: plane waves, cylindrical waves, and spherical waves. For the determination of the thickness of a sample (e.g. of a propellant slab), the plane waves are mostly used.

Plane waves are solutions of the wave equation with

$$\Phi = \Phi_0 f(t \pm \frac{x}{c}) , \tag{7.2}$$

where f is any function which is continuous up to its second order derivative. The most common planar ultrasound waves are the harmonic waves

$$\Phi = A \sin\omega(t \pm \frac{x}{c}) , \tag{7.3}$$

where A is the amplitude, and ω is the angular frequency ($\omega = 2\pi f$, f is the frequency). The sound pressure, P, for these harmonic waves is given by

$$P = \omega A\rho c = \omega A Z , \tag{7.4}$$

where $Z = \rho c$ is the acoustic impedance.

7.2.2 Reflection

When a plane ultrasound wave traveling through a medium with acoustic impedance Z_1 reaches an interface with a different medium (with acoustic impedance Z_2) part of the incident wave is transmitted, and the remainder is reflected. The fraction of the sound pressure which is transmitted is given by [149]

$$T = \frac{P_{\text{transmitted}}}{P_{\text{reflected}}} = \frac{2Z_2}{Z_2 + Z_1} . \tag{7.5}$$

The reflection coefficient is given by

$$R = 1 - T = \frac{Z_1 - Z_2}{Z_2 + Z_1} . \tag{7.6}$$

The above equations show that an incident sound wave on a boundary from liquid or solid to air yields a very high reflection coefficient ($Z_2 \ll Z_1$).

7.2.3 Attenuation

A major restriction of the application of ultrasound for thick media, is the attenuation of the sound wave in the medium. A general expression for the attenuation of the sound wave is

$$P(x) = P_0 e^{-\alpha_{us} x} , \tag{7.7}$$

where α_{us} is the attenuation coefficient. Attenuation of an ultrasound wave is caused by several different physical phenomenon. For solid materials the most important are [114, 149]:

1. **Absorption:** friction of the vibrating particles with the surrounding. If the temperature increases the interaction with the surrounding particles will be larger. This causes an increase of the absorption with temperature.

2. **Heat conduction:** Energy is lost due to heat flows induced by the temperature differences between zones with over and under pressure.

3. **Scattering:** The scattering of ultrasound waves has different reasons: it can be caused by particles (e.g. oxidizer particles in a propellant), or by imperfections in the material. Scattering is especially efficient if the particles (imperfections) dimensions are of the same order as the ultrasound wavelength.

7.2.4 Pulse-echo technique

The pulse-echo technique is the most common method to determine material thickness with ultrasound. Figure 7.1 sketches the the principle of this technique. An ultrasonic pulse is transmitted by the probe at $t = 0$. After passing through the material, the ultrasound wave reflects at the interface. The same probe may be used to receive the echo at $t = \Delta t$. If the ultrasound velocity is constant throughout the material, relation between Δt and the thickness d of the sample is given by

$$\Delta t = \frac{2d}{c} . \tag{7.8}$$

However, if the ultrasound velocity changes through the material, the relation is

$$\Delta t = 2 \int_0^d \frac{dx}{c(x)} . \tag{7.9}$$

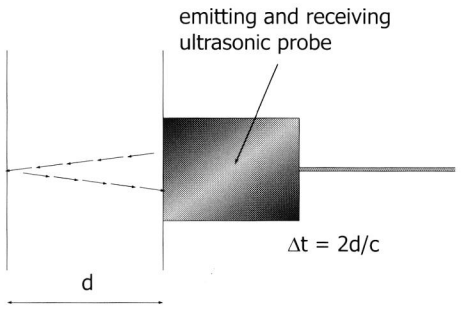

Figure 7.1: *Principle of the ultrasound pulse-echo technique.*

The pulse-echo method can be repeated to determine the regressing surface of a solid propellant (or e.g. hybrid rocket fuel, or thermal protecting layer). For a constant value of the ultrasound velocity, the regression rate r_b is found from $r_b = 2/c \cdot d\Delta t/dt$.

7.2.5 Ultrasound properties of HNF

The discussion in the previous sections, shows that it is important to know the ultrasound velocity in the material under study. Pressure and temperature are known to influence the ultrasound velocity for solid propellants [25]. For HNF no literature values of the ultrasound velocity were found in literature. Therefore HNF's ultrasound properties have been investigated first. The ultrasound velocity was measured as a function of temperature and pressure at an ultrasound frequency of 5 MHz. The samples for these measurements were pressed HNF crystals (S-13 grade). For more details about the experiments and samples is referred to section 7.4 of this Chapter. Figures 7.2 and 7.3 show the results of these measurements. It is seen that the ultrasound velocity is dependent on the temperature. However the pressure was found to have no measurable effect in the pressure range studied (Fig. 7.3). The attenuation of the ultrasound wave was found to be very temperature dependent. At temperatures above 40°C the reflection signal could not be distinguished from the noise anymore.

The error bar in Fig. 7.2 indicates the typical error due to length differences of 20-30 μm within a single sample. These differences are caused by non-squareness of the die-press. For all points in this figure, and that of Fig. 7.3 the error is similar. By calculating this error it has been assumed that the pulse-echo time to voltage conversion factor of the URRA has negligible effect. For determination of the burn rate the inverse relation is applied. As long as the conversion factor of the URRA is constant the effects cancel out. The URRA that was used was calibrated, and according to its specification the URRA error can be neglected.

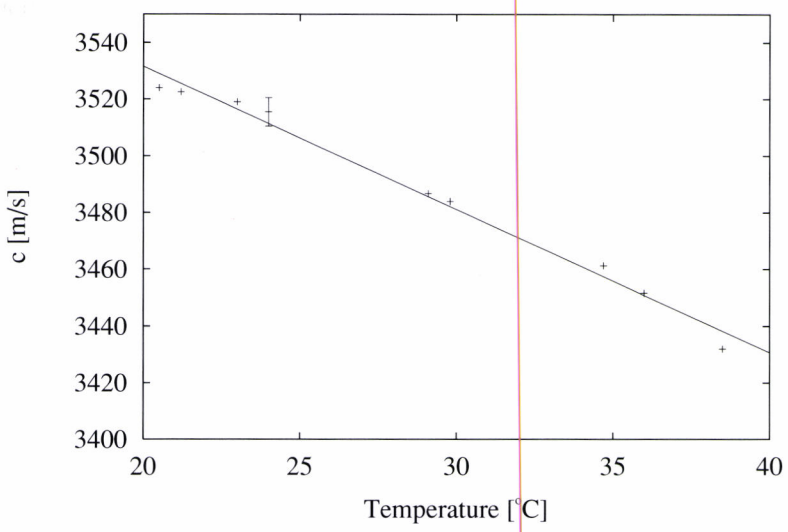

Figure 7.2: *Temperature dependency of the ultrasound velocity of HNF (f = 5 MHz, atmospheric pressure). The error bar represents the typical error due to length differences of 20-30 μm of a single sample.*

7.3 HNF combustion model

It was already discussed in section 7.2.5 that the ultrasound velocity of HNF is dependent on the temperature. Because the ultrasound wave passes through the condensed phase combustion zone, the pulse echo measurements will be biased by the condensed phase temperature profile (difference between Eq.'s (7.8) and (7.9)). For example: due to the decrease in ultrasound velocity when the condensed phase temperature profile builds up, it seems like the propellant "grows" at ignition. For steady burning propellants this is not a problem, as this increase in pulse echo time Δt is constant throughout the burning. The regression rate is determined from $d\Delta t/dt$, which is unaffected.

For transient burning, the condensed phase temperature profile will vary continuously. Therefore it is necessary to measure or model the temperature profile behavior during the transient combustion. Measuring *unsteady* temperature profiles is very difficult, and no measurements exist for HNF. To evaluate the effects of the unsteady temperature profile, a simplified model for the combustion of HNF is used. This model is based on the familiar QSHOD (quasi-steady gas phase, homogeneous one dimensional) models which have been developed for solid propellants [32]. Of particular interest is the accurate calculation of the temperature profile, as this profile directly determines the pulse echo time Δt.

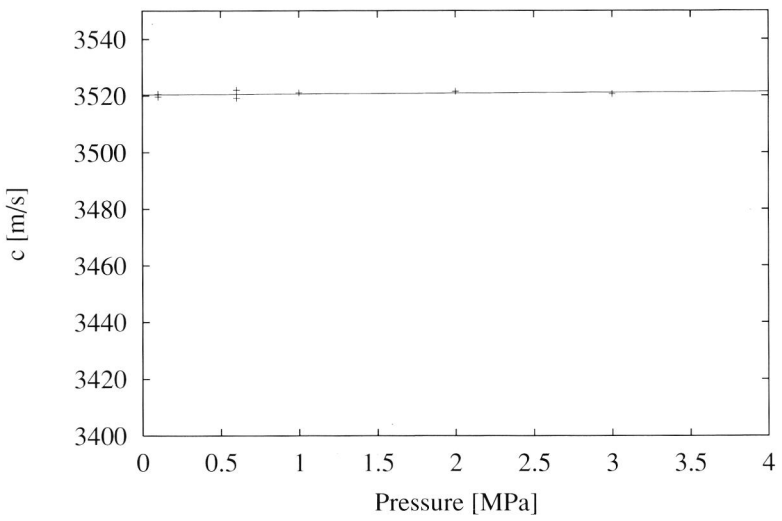

Figure 7.3: *Pressure dependency of the ultrasound velocity of HNF ($f = 5\,MHz$, $T = 293\,K$).*

7.3.1 Condensed phase

The combustion process is described by a one dimensional model. The energy equation for a semi-infinite slab of propellant ($\infty < x < 0$) is given by [32] (see also Eq.(6.3))

$$\rho_c c_c \frac{\partial T}{\partial t} + \rho_c c_c r_b \frac{\partial T}{\partial x} = \lambda_c \frac{\partial^2 T}{\partial x^2} + Q_c \epsilon(T) + Q_r(x) \,, \tag{7.10}$$

where ρ_c is the density of the propellant, c_c is the specific heat capacity, T is the temperature, r_b is the regression rate, λ_c the thermal conductivity of the propellant, Q_c is the total heat release in the condensed phase due to exothermic ($Q_c > 0$) or endothermic ($Q_c < 0$) reactions, ϵ is the chemical reaction rate per unit volume, and Q_r is a possible local heat absorption due to an external radiation source (e.g. a laser). It has been shown that the temperature profile can largely affected by the temperature dependency of the thermophysical properties [94, 95]. It is part of this study to evaluate the effect of these dependencies on the ultrasound pulse echo signal. The thermophysical properties are temperature dependent, i.e. $c_c = c_c(T)$ and $\lambda_c = \lambda_c(T)$. The chemical reaction rate ϵ is given by a zero-order reaction

$$\epsilon(T) = \rho_c A_c \exp\left[-\frac{E_c}{RT}\right] \,, \tag{7.11}$$

where A_c is a frequency factor, E_c is the activation energy for the condensed phase decomposition, and R the universal gas constant. The radiative energy absorption is given by Beer's law

$$Q_r(x) = (1 - r) K_a Q_r \exp\left[K_a x\right] \,, \tag{7.12}$$

where K_a is the absorption coefficient for the radiation, Q_r is the total radiative heat flux, and r is the reflectivity of the burning surface.

The boundary conditions for the energy equation are given by the initial propellant temperature T_0

$$T(-\infty, t) \;=\; T_0 \;, \tag{7.13}$$

and from energy conservation at the burning surface

$$\lambda_c \left(\frac{\partial T}{\partial x}\right)_{0-} \;=\; \lambda_g \left(\frac{\partial T}{\partial x}\right)_{0+} \;, \tag{7.14}$$

where λ_g is the thermal conductivity of the gas phase. Note that in the above equation no surface heat release is assumed. All chemical heat is released in a distributed reaction zone. This relaxation of the surface reactions by the more general distributed reactions, has been shown to have a large effect in calculations, especially during unsteady combustion [166].

The species equation is given by

$$\frac{\partial Y}{\partial t} + r_b \frac{\partial Y}{\partial x} \;=\; -\,\epsilon \;, \tag{7.15}$$

where Y is the HNF mass fraction. The boundary condition for this equation is $Y(-\infty, t) = 1$. The regression rate is found as an eigenvalue of the system [166]

$$r_b(t) \;=\; A_c \int_{-\infty}^{0} \exp\left[-\frac{E_c}{RT}\right] dx + \int_{-\infty}^{0} \frac{\partial Y}{\partial t} dx \;. \tag{7.16}$$

Note that the introduction of the species equation prevents the problem of the (arbitrary) selection of a surface pyrolysis law [19], as the instantaneous regression rate is found as an eigenvalue of the solution of Eq.'s (7.10) and (7.15).

7.3.2 Gas phase

The gas phase is also assumed to be semi-infinite ($0 < x < \infty$) and one-dimensional. For the specific ultrasound problem, the condensed phase temperature profile is of particular interest. The gas phase temperature profile is of less importance. This justifies the selection of a rather simple model for the gas phase heat release. In this work, the heat release is modeled by a KTSS-type of flame, i.e. a constant heat release, uniformly distributed over the reaction zone [80]. It is further assumed that the gas phase reaction zone is attached to the burning surface. The KTSS flame is used to describe the heat feedback from the gas phase to the condensed phase (r.h.s. of Eq.(7.14)). The model is a QSHOD-model: the gas phase is treated quasi-steady. Consequently the heat flux is dependent on pressure and instantaneous regression rate only.

The total heat release in the gas phase, Q_g, is found from energy conservation

$$Q_g \;=\; \int_{T_0}^{T_s} c_c(T) dT + c_g(T_f - T_s) - Q_c \;, \tag{7.17}$$

where c_g is the (constant) specific heat capacity of the gas phase, T_s is the surface temperature, and T_f is the flame temperature. Because he surface temperature fluctuates

during transient burning, the value of Q_g will also vary. In accordance with the QSHOD-theory, the total heat release during transient burning and steady burning is assumed to be constant, i.e. transient effects due to slow kinetics in the gas phase are neglected.

7.3.3 Solution

The Eq.'s (7.10) and (7.15) form a system of coupled nonlinear parabolic partial differential equations. This system is solved by an implicit forward Cranck-Nicholson method. Because the thermophysical properties are temperature dependent, the solution is iterative. To precisely resolve the steep temperature gradient close to the burning surface, the computational grid is non-uniform, with an increasing finer mesh near the surface. For more details see e.g. Ref.'s [50, 94].

In the above Eq.'s (7.10) to (7.17) there is only one really unknown parameter, the exponentional prefactor for the condensed phase decomposition, A_c. This variable is determined from the steady state burning rate at 0.1 MPa, $r_b = 0.68$ mm/s. During the rest of the calculations the value of A_c is kept constant.

7.3.4 Input data

A summary of the input data used for the calculations is given in Table 7.1. The density, ρ_c, of pressed HNF pellets is lower than than of HNF, due to small voids (1740 vs 1860 kg/m^3). The thermal conductivity and specific heat capacity of pressed HNF pellets were measured by Hanson-Parr by a heat pulse method [57]. The temperature dependence of the specific heat is approximated by a linear relation. The thermal conductivity required is more complicated and will be discussed in section 7.5.2. The condensed phase activation energy and heat release are from values as recently proposed for a steady combustion model of HNF [96]. The overall heat release in the condensed phase is endothermic; HNF decomposition into hydrazine and nitroform is endothermic, as is the melting of HNF. The gas phase properties were calculated by the NASA-Lewis CET-89 thermal equilibrium program. The value for the exponentional prefactor, A_c with this dataset is $A_c = 2.49 \cdot 10^9$ 1/s, for a regression rate of 0.68 mm/sec at 0.1 MPa. The only other calibration involved is the surface temperature of 553 K at 0.1 MPa [98]. The surface reflectivity r was set to 0.6 [96]. Note that since the current model calculates $T_s(p)$, no calibration for r_b v.s. T_s is necessary.

7.3.5 Model validation

The model presented here shows large similarity with the analytical steady-state WSB-model presented in section 6.2. This model uses high activation energy asymptotics for the condensed phase, and showed good agreement with experimental data.

Steady combustion

Figure 7.4 shows the calculated steady regression rate of HNF, compared with experimental data [45]. Figure 7.5 compares the experimental data with the results from the model (experimental results from Ref. [46]). The results from these experiments were used to

Property	Symbol	Value	Unit
Condensed phase			
Density	ρ_c	1740	kg/m^3
Specific heat capacity	c_c	$0.83 + 0.0014 \cdot (T - 273)$	kJ/kgK
Conductivity	λ_c	see section 7.5.2	W/cmK
Frequency factor	A_c	$2.49 \cdot 10^9$	1/s
Activation energy	E_c	75	kJ/moleK
Heat release	Q_c	-30	kJ/kg
Absorption coefficient	K_a	1000	1/cm
Surface reflectivity	r	0.6	-
Gas phase			
Specific heat capacity	c_g	1.7466	kJ/kgK
Conductivity	k_g	$2.2418 \cdot 10^{-3}$	W/cmK

Table 7.1: *Overview of model input.*

determine the reflectivity of the HNF burning surface. In correspondence with section 6.2, it is found that $r = 0.6$.

Unsteady combustion

A practical function which describes the sensitivity of a propellant to an external (harmonic) fluctuating signal is the response function R. Two typical external disturbances are pressure and external heat flux, with corresponding response functions R_p and R_q. For small disturbances, $\Delta \ldots$, the response functions are given by

$$R_p = \frac{\Delta r_b / \bar{r}_b}{\Delta p / \bar{p}} , \tag{7.18}$$

and

$$R_q = \frac{\Delta r_b / \bar{r}_b}{\Delta q / \bar{q}} . \tag{7.19}$$

The bars in the above equations indicate time average values.

Most experiments are carried out with a fluctuating heat (laser) flux. Finlinson measured this so-called laser-recoil response from HNF [46]. To be able to compare his results with the model's results, it is necessary to convert the measured force amplitude, $f(t)$, to instantaneous regression rates, $r_b(t)$, using momentum conservation at the burning surface [112]

$$f(t) = (\rho_c r_b(t))^2 \frac{RT_g}{pM} , \tag{7.20}$$

where R is the universal gas constant, T_g is the gas temperature, p is the pressure, and M the molecular weight of the combustion products. The measurement results of Finlinson

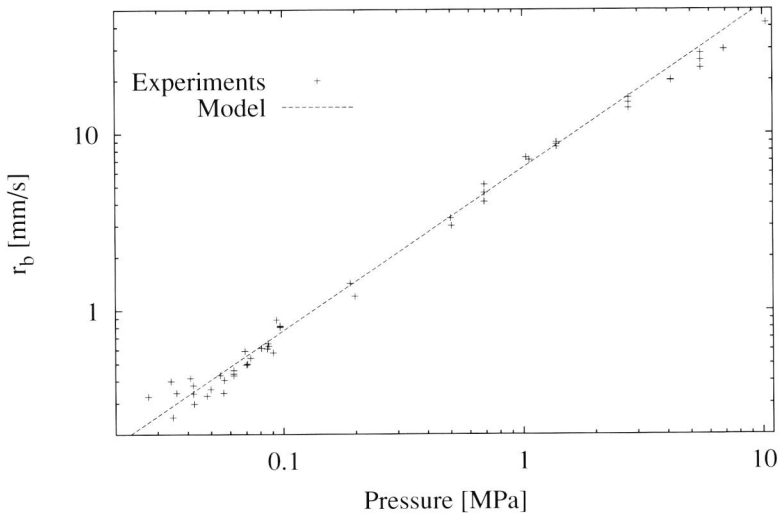

Figure 7.4: *Comparison of measured steady burning rates of HNF with the model's results.*

are represented as peak-to-peak thrust oscillations (f_{pp}). To convert these results to the response function a linearized relation is used

$$R_q = \frac{Mp/(\rho_c^2 \bar{r_b}^2 RT_g) f_{pp}}{\frac{\Delta q_r}{q_r}} = C \frac{f_{pp} p}{\bar{r_b}^2}, \tag{7.21}$$

where C is a constant. Because the temperature and molecular mass are not accurately known at the burning surface, C is determined from comparison between experimental and numerical results. It is found that $C = 0.00013\,\mathrm{cm^4/mgf\,MPa\,s^2}$, for f in $\mathrm{mgf/cm^2}$, and r_b in mm/s.

Figure 7.6 compares the experimental results, which have been processed as discussed above, with the numerical results. The figure shows two different response functions. The dotted line has been obtained from calculations where the propellant is disturbed by a harmonic signal, starting from steady-state. These calculations require that several periods of the laser flux are calculated until a dynamic equilibrium exists [94]. However, because of the limited supply of HNF samples, Finlinson used logarithmically sweeped laser fluctuations. This means that the frequency of the disturbing signal changes continuously in time. In this case no dynamic equilibrium exists. These sweeped measurements have been carried out as "numerical experiments", and are shown as the solid lines in Fig. 7.6. The figure clearly shows the difference between both methods. The agreement with the experimental data is reasonably: The resonance frequency and magnitude of the response function at the resonance frequency is reasonably predicted by the model. Above 40Hz a larger deviation is seen. This deviation is explained by the decrease of the laser power with increasing frequency. This phenomenon was discovered after comparison of modeling

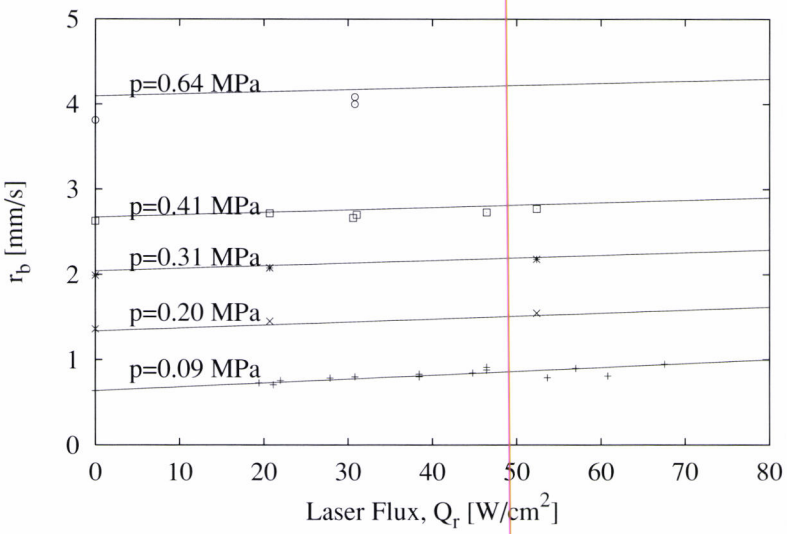

Figure 7.5: *Comparison of measured laser-assisted steady burning rates of HNF (dots) with the model's results (lines).*

and experimental results, and the data was not yet corrected for this effect. At 70 Hz, this effect is about 15%, which matches the deviation between model and experiment at 70 Hz. Further analysis of this phenomenon is necessary for a better comparison between experimental and modeling results.

7.4 Experiments

7.4.1 Description of the experimental setup

Samples of approximately 1 gram of neat S-13 HNF were pressed at 230 MPa in a die with 9 mm diameter. These samples are larger than the ones used for the PLIF-experiments. The reason for this is that the effective beam diameter of the ultrasound transducer is about 5 mm, which is close to the 6 mm for the small samples. The experiments are carried out in the DUT-bomb. The sample holder was modified to contain the ultrasound transducer.

Figure 7.7 details the ultrasound setup. The ultrasound pulses are transmitted and received by a 5 MHz transducer (Harisonic ABT0504). A high frequency is desirable, to obtain a better spatial resolution. On the other hand, damping increases with frequency, which limits the maximum frequency. At 5 MHz the damping of the ultrasound pulses was acceptable. At 5 MHz the wavelength of the ultrasound waves in the HNF is 0.7 mm. This is several orders of magnitude larger than the observed inclusions in the material (Fig. 3.5). It is therefore expected that the ultrasound waves will not be affected by these inclusions.

An ultrasonoscope is used for pulse generation and initial signal amplification (Sonic

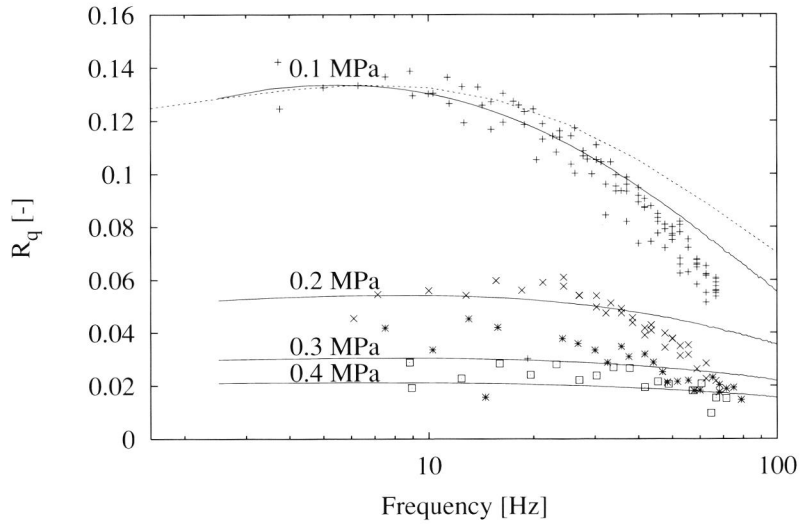

Figure 7.6: *Calculated vs. measured laser-recoil response function of HNF (solid lines: sweep signal, dotted line: harmonic signal).*

FTS Mark IV). The ultrasonoscope emits the pulses at a rate of 1 kHz. The ultrasound pulse-echo time is determined by an Ultrasonic Regression Rate Analyzer (URRA), which has been developed by TNO/PML. This URRA converts the time-of-flight into a measurable voltage. This is done by comparing the reflected and amplified signal with a threshold level. If the measured signal is higher than this threshold value, it is considered to be a reflective pulse. To prevent wrong peak selection, a holdtime can be selected. During this holdtime the comparison is not carried out. In this way reflections of the coupling material can be neglected (see Fig. 7.8). During combustion the sample thickness decreases, resulting in a decrease of the URRA output signal. A typical experimental (steady) run is shown in Fig. 7.9.

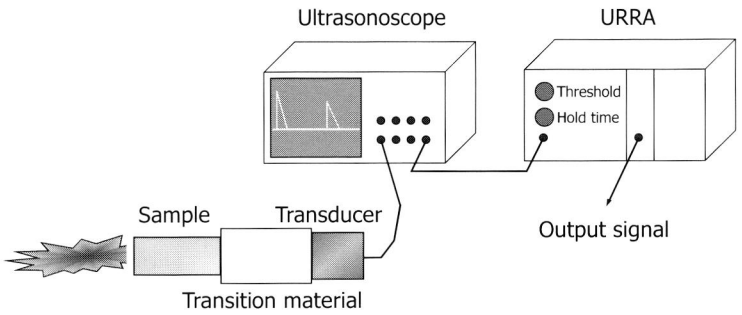

Figure 7.7: *Schematic overview of the ultrasound setup.*

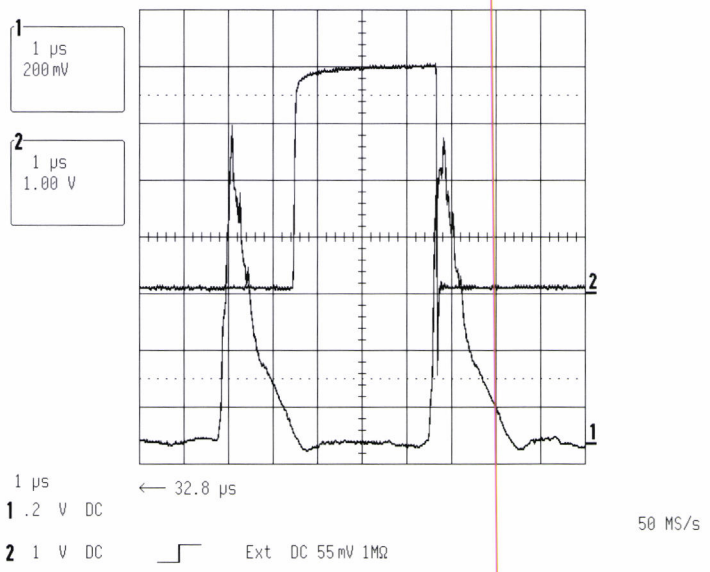

Figure 7.8: *Oscilloscope image showing the reflection at the coupling material (first peak), and the reflection at the HNF surface (second peak). The rectangular pulse defines the beginning of the measurement interval, and the first detected peak. The time lapse between pulses is a measure of the propellant thickness.*

Several materials have been tested as coupling material: brass, aluminum and polymethyl methacrylate (PMMA). Of these materials, the acoustic impedance of PMMA is the most close to that of HNF. According to Eq.'s (7.5) and (7.6), this means the highest transmittance of the ultrasound into the HNF. PMMA was also found to give the best results.

The bonding of the HNF to the coupling material is critical. Due to the incompatibility of HNF with normal coupling gels, alternatives were sought for. Paraffin with a low melting temperature of 55°C, was found to be an excellent alternative. The propellant sample and coupling material are placed in an oven, and are heated to a temperature slightly above the melting temperature of the paraffin. Both pieces are then pressed firmly against each other, with a small amount of paraffin in between. After cooling an excellent acoustic coupling was formed, combined with mechanical fixation of the sample.

The combustion process is also monitored with a CCD video camera (Sony X-777). The video images are recorded on a digital video recorder (Sony DHR-1000). This allows comparison of the regression rates determined by the ultrasound technique, and regression rates determined by the video images. The light emission of the gas flame was also monitored by a diode which is sensitive to the visible light.

Measurements were carried out using a 12-bit, 8-channel data acquisition board (National Instruments PCI-1200). The sampling frequency was 1 kHz. All data-acquisition

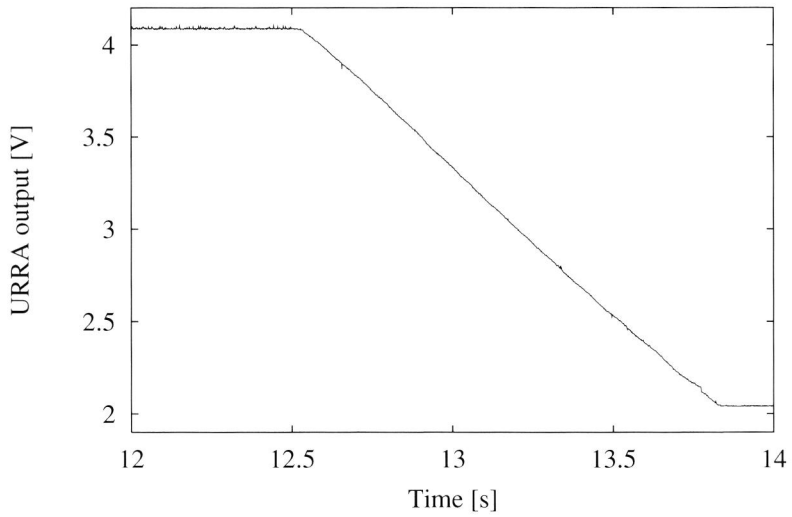

Figure 7.9: *URRA signal during a steady state regression experiment.*

and processing software was written in LabVIEW. The analog signals were filtered at 500 Hz with 24db/octave low-pass Butterworth filters (Krohn-Hite 3202).

7.4.2 Ultrasound data reduction

Filtering of the ultrasound signal is critical due to the fact that determination of the regression rates involves determination of the time derivative of the measured signal. For the steady state experiments the processing software was as follows:

1. The measured URRA signal is filtered with a low-pass second order Butterworth filter, with a cut-off frequency of 25 Hz. The function of this filter is reduction of electronic and ADC-quantization noise. This filtering is carried out in two different stages; First a first order filter with the measured data, and then filtering of the reversed data. This two-stage filtering procedure reduces the phase errors.

2. The time derivative of the filtered signal is determined, and is converted to the burning rate.

3. Because of the high amount of noise after determination of the time derivative, the signal is filtered again. A 8th order Bessel low-pass filter with a cutoff frequency of 25 Hz proved to give good results, without introducing overshoots during ignition and burnout. This filtering is also carried out in two stages, with signal reversion between the first and second stage.

During unsteady combustion the cutoff frequencies of steps 1 and 3 are adjusted, so that the frequency of interest is below the filter cutoff frequency.

7.5 Results

7.5.1 Model results

The effect of the temperature dependent properties on the pulse-echo time Δt is depicted in Fig. 7.10. This figure shows the result of radiation driven transient burning at 0.1 MPa (10 Hz sinusoidal laser power, average 10 W/cm^2, amplitude 5 W/cm^2). It is seen that the temperature dependence of the sound velocity has the largest effect on the pulse-echo time Δt. These calculations illustrate the need for the strong interaction between the experimental results and modeling to be able to determine unsteady regression rates: the pulse-echo time traces for the variable properties would give completely different results if treated as a constant-properties trace.

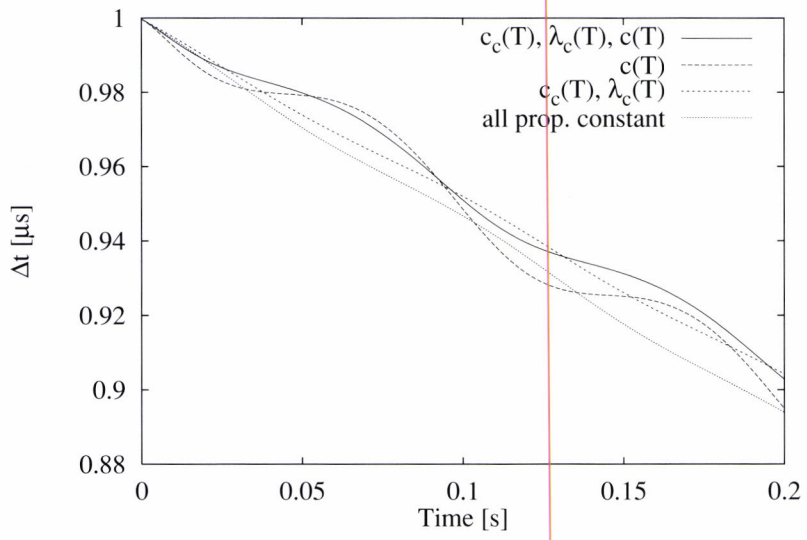

Figure 7.10: *Calculated pulse-echo time for both temperature dependent and temperature independent properties. The selected initial sample length corresponds to an arbitrarily chosen value of the pulse-echo time of 1 μs.*

7.5.2 Experimental results

Pulse-echo reflection signal quality

The strength of the reflection of the ultrasound wave at the HNF-surface was found to be very dependent on the pressure. At low pressures (less then ~ 0.2 MPa), it was impossible to obtain a reflection signal stronger than the background noise. At low pressures HNF has a melt layer, and a thick thermal layer. It was observed during the determination of the ultrasound velocity, that the absorption of the ultrasound signal increases with temperature (as for most materials). The absorption in the condensed phase is the most

probable cause for the bad signal quality at low pressures. In none of the experiments an extra reflection peak caused by the liquid-solid interface was observed. Increasing the pressure above 0.3 MPa gave reflection signals which could very well be distinguished from the background noise.

The maximum pellet length used in the experiments was 20 mm. Compared to the normal pellet of app. 10 mm length, this required an extra 10 dB signal amplification (i.e. $\alpha_{us} = 0.12\,\mathrm{mm}^{-1}$). With 20 mm tall samples the reflection signal was still clearly detectable. Taller pellets will probably not cause problems. However, with the current press-die it is not possible to make such tall pellets.

Steady state regression rate

First it has been evaluated if the ultrasound technique is applicable to the determine the steady regression rates of HNF. This is done by comparing the ultrasound results with the regression rates as determined from a video sequence. In this optical method the burning surface regression is determined as a function of time. A linear least-square fit to these points then yields the regression rate. The absolute error in these measurements is found as three times the standard deviation of the fitting coefficient.

Figure 7.11 compares the regression rates as determined from the ultrasound experiments with the optical method. At high pressures a large deviation from the optical measurements is seen to occur. This difference is probably caused by the transient coning of the propellant samples: directly after ignition the sample is burning faster in the middle of the sample, and then the outside starts to catch up (see also video sequence of a burning pellet, Fig. 7.12). As the video camera is looking perpendicular at the burning samples, the regression of the outer surface determines the burning rates. In case of coning after ignition, this means a higher regression rate. The experimental error in the video experiments, seems confirmed by the regression rate data of Atwood et. al. [46] (also shown in Fig. 7.11). The ultrasound measurements compare very well with this data.

Apparent oscillations during steady burning

In all of the "steady" experiments, relatively high regression rate oscillations were found after processing of the ultrasound signals. A typical example is shown in Figure 7.13. At first, these oscillations were thought to be caused by intrinsic instabilities. However, the frequencies are far too low for gas phase instabilities, considering the short flame structure of HNF.

Self-sustained unstable condensed phase combustion was also evaluated as a possible source of these fluctuations. This type of self-sustained combustion has e.g. also been found in neat HMX deflagration [68]. In case of self-sustained oscillations it is expected that the frequency of the oscillations is determined by the characteristic time of the condensed phase: $f_{\mathrm{osc}} \sim 1/t_c^* \sim (\alpha_c/r_b^2)^{-1} \sim p^{2n} \sim p^2$, where n is the burn rate exponent. However, it was found that the frequency of the oscillations is proportional to p^n ($n = 0.85$), see Fig. 7.14. This indicates a process determined by the characteristic length-scale $x_c^* = \alpha_c/r_b$ in the propellant, rather than a characteristic time-scale. The formation of cracks was identified as the relevant process.

During combustion of the HNF pellets cracks were seen to form in advance of the regressing surface, Fig. 7.15. These cracks can be explained by the large expansion coef-

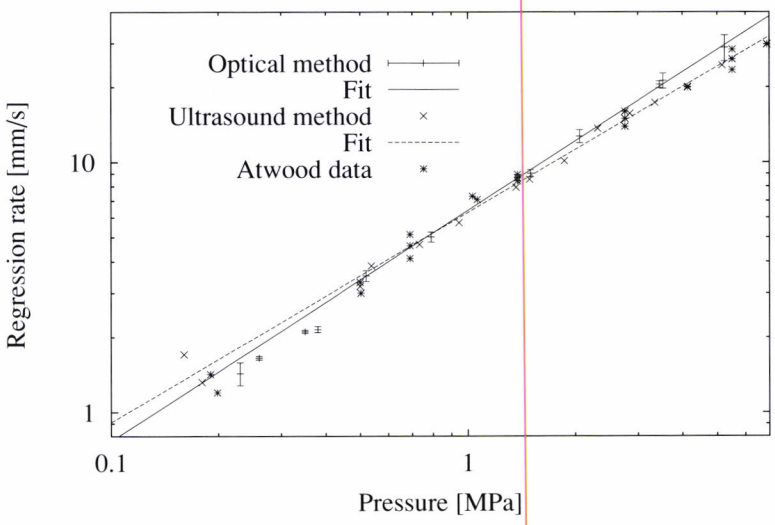

Figure 7.11: *Measured regression rates determined by the ultrasound method, and by an optical method.*

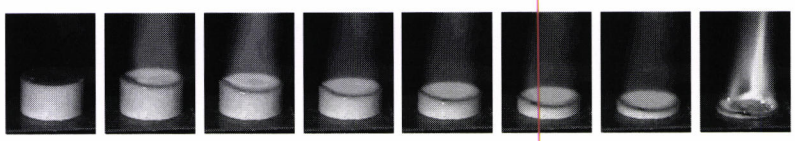

Figure 7.12: *Video sequence of a burning HNF pellet.*

ficient of HNF pellets around 80°C (see Fig. 7.16). Because of the inelastic character of the pressed pellets, cracks are formed. After cracking, the internal stress starts to build up again. As the ultrasound velocity of a material is dependent on the internal stresses, the ultrasound velocity in the burning surface region is continuously changing. This causes the apparent regression rate fluctuations. The typical time scale to burn past the formed crack zone is proportional to the burning rate r_b^{-1}, and hence $f_{\mathrm{osc}} \sim r_b \sim p^n$. It was verified that the cracks were not caused by the ultrasound energy. The cracks were also observed when no ultrasound was applied to the sample. It should be remarked that in principle the high expansion coefficient has to be accounted for when determining the ultrasound velocity from a sample with known length. Below 80°C the effect of expansion is about an order of magnitude smaller than the temperature effect, but in the transition region, the effect becomes significant.

The cracks formed in the HNF pellet are also considered to be the reason for a sudden change in the thermal diffusivity for combusting HNF. This phenomenon was already reported earlier (thermocouple experiments of section 4.3.2), but never explained [95]. Measurements of heated HNF pellets do not show this sudden change in thermophysi-

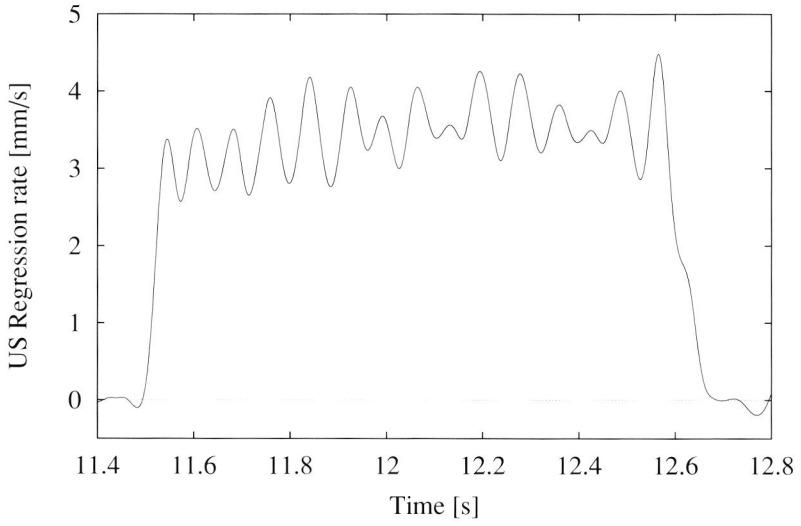

Figure 7.13: *Apparent oscillation of the regression rate ($\bar{p} = 0.73MPa$) during steady burning.*

cal properties [57]. No cracks are formed in this type of experiments, as the pellets are uniformly heated.

By comparing the measured and calculated temperature profile in the condensed phase, the effective decrease of the thermal conductivity was found to be 60%. Of course, the thermal conductivity does not really change, but there is a thermal resistance due to the crack. In the model, the effect of the cracks is lumped in the decrease of thermal conductivity of HNF to 0.4× the thermal conductivity at room temperature. The value of the specific heat ratio is independent of the presence of cracks, but is temperature dependent.

The sudden change in thermal conductivity shifts the peak of the response functions along the frequency axis. For the calculations as presented in Fig. 7.6, the resonance peak would be around 4 Hz, whereas a higher frequency was found experimentally. This is another indication of the sudden change in thermal conductivity.

Determination of the absorption coefficient K_a

During combustion the ultrasound wave traverses the condensed phase temperature profile, and delayed by the higher temperature present in the conductive-reactive zone. So, the pulse-echo delay time is a fingerprint of the integral over the temperature profile in the condensed phase. This allows the use of the ultrasound technique as an indirect *non-intrusive* diagnostic method for the condensed phase.

An illustrative example of the indirect method, is the determination of the absorption coefficient K_a from the ultrasound pulse-echo trace. For example: during laser-assisted burning, the condensed phase temperature profile is modified by the sub-surface radiant

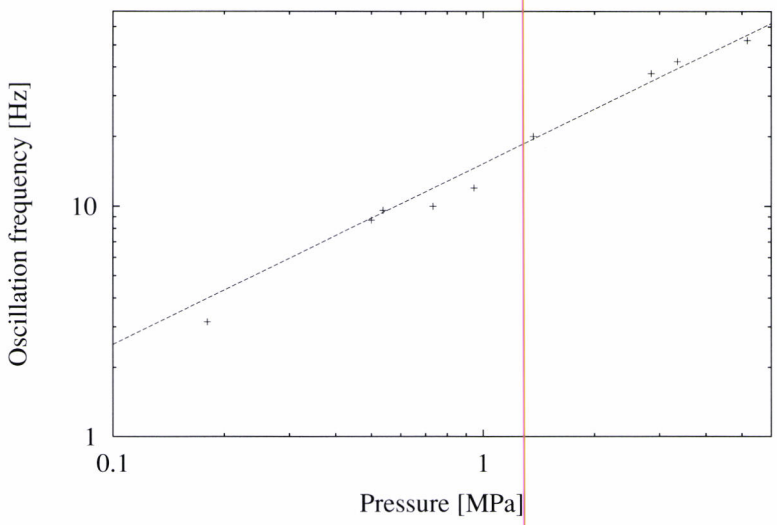

Figure 7.14: *Frequency of the apparent oscillations of the regression rate during steady burning.*

energy absorption. When the laser is switched off, the propellant transients to the new situation. During this transition, the pulse-echo time follows the condensed phase temperature profile.

Model calculations show that the pulse-echo time Δt-trace is sensitive to the absorption coefficient K_a. By comparison of the measured and modeled Δt-trace for various values of K_a, K_a can be estimated. Figure 7.17 shows the result of such a calculation. Measurements do not show a transient phase, but a sudden change in the slope of the ultrasound signal. This indicates a high absorption coefficient, $K_a \sim 1000\,\mathrm{cm}^{-1}$.

Response function

The measurement of unsteady regression rates by the ultrasound technique is a logical follow-up of the measurement of steady regression rates. As discussed, (sinusoidal) modulation of the CO_2-laser is an easy method to introduce transient burning. However, the observed cracks during the combustion of the pellets introduce oscillations which have to be distinguished from the real unsteady fluctuations.

Another problem is that of the varying thermal layer thickness. This causes fluctuations of the ultrasound pulse-echo signal, which are not solely caused by the unsteady regression (see Fig. 7.10). A correction is needed. This correction is dependent on the environmental conditions, like pressure, average laser power and modulation amplitude.

In theory the best approach of reduction of the ultrasound measurements is iterative solution of the measurements together with a model (e.g. like the model presented). However, the noisy ultrasound signals coupled with the long calculation time reduces the practical application of this method. Therefore, a correction based on model results is used. Model

Figure 7.15: *Cracks in the pressed HNF pellet.*

calculations are run to give simulated pulse-echo time traces. These are processed like the experimental determined traces to give burn rates. Because of the temperature dependent properties of the condensed phase, there will be a difference with the burn rates directly determined from the simulations. The ratio of these burn rates and the burn rates from the simulated pulse-echo traces are used to correct the experimental data.

A series of model calculations was run for the experimental settings: $p = 0.2\,\mathrm{MPa}$, $Q_r(t) = 31 \pm 30\sin(\omega t)\,\mathrm{W/cm^2}$. The peak-to-peak oscillation of the regression rate is compared to the peak-to-peak regression rate fluctuations obtained from the *theoretical* ultrasound pulse-echo signal, computed assuming constant properties. The ratio of these two different fluctuations is dependent on the frequency of the disturbance, see Fig. 7.18. The results of these calculations are then used to correct the experimentally observed fluctuations by ultrasound, to actual regression rate fluctuations. The differences between these two signals originates from the temperature dependent ultrasound velocity.

Several laser-stimulated unsteady experiments were run. Figure 7.19 shows a typical example. With the results from the model calculations these were corrected as discussed above. The harmonic oscillations were obtained by a band-pass filter, centered around the disturbance frequency. This reduces noise and fluctuations caused by the cracking. The results of these measurements are summarized in Fig. 7.20. This figure clearly shows the need for the correction of the ultrasound data. As seen, the error for these measurements can be almost an order of magnitude (factor 10). The reason for this is the low pressure of 0.2 MPa which was chosen. Due to the limited available laser power, the regression rate fluctuations were found to be very small at higher pressures. At higher pressures the signal quality was much better, resulting in smaller errors. The error bar in Fig. 7.20 indicates the estimated absolute error due to variations in the measured ultrasound regression rate fluctuations during unsteady burning.

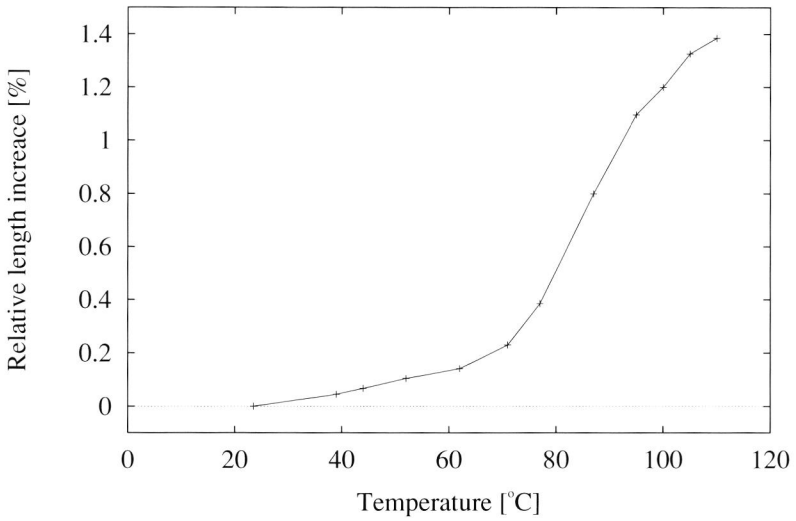

Figure 7.16: *Relative length increase of a HNF pellet.*

7.6 Conclusions

The practical application of the ultrasound technique for (un)steady regression rate measurements has been evaluated. A HNF monopropellant was selected to simplify the required combustion model. Small pressed samples of neat HNF, with a diameter of 9 mm, and a length of 10 mm were used for the experiments. To support the measurements, and to process the obtained results, a transient model for the combustion of HNF has been developed. The model shows good correlation with experimental results (expressed as the laser-assisted response function).

The ultrasound velocity of HNF was found to be 3532 m/s at 293 K. The ultrasound velocity is a strong function of temperature, decreasing by 5 m/s/K. At pressures below 0.2 MPa the ultrasound reflections are too weak to be able to measure the regressing surface. Above 0.3 MPa signal quality was good.

The steady regression rate of HNF has been determined by ultrasound and by video recordings. The correlation between both methods is good. The small deviations are explained by the transient coning of the small samples. Oscillations were found in the ultrasound signals during steady burning. These oscillations are explained by cracks in the pellets. Unsteady regression rate measurements were carried out by laser stimulated combustion. The effect of the temperature dependence of the ultrasound velocity is large. When this effect is not accounted for, the regression rate fluctuations are overestimated by a factor 10 at 50 Hz.

Apart from the determination of the regression rate, the ultrasound technique may also be used as an non-intrusive method to determine the integral over the thermal layer in the condensed phase. This method has been employed to determine the absorption coefficient, K_a of HNF for CO_2-laser light. It is found that $K_a \sim 1000\,\mathrm{cm}^{-1}$.

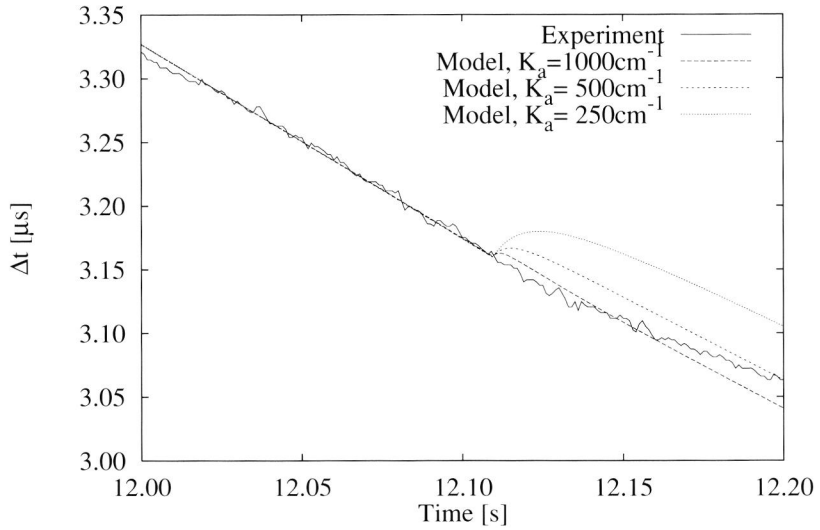

Figure 7.17: *Calculated and measured pulse-echo time around end of laser-pulse for different values of K_a.*

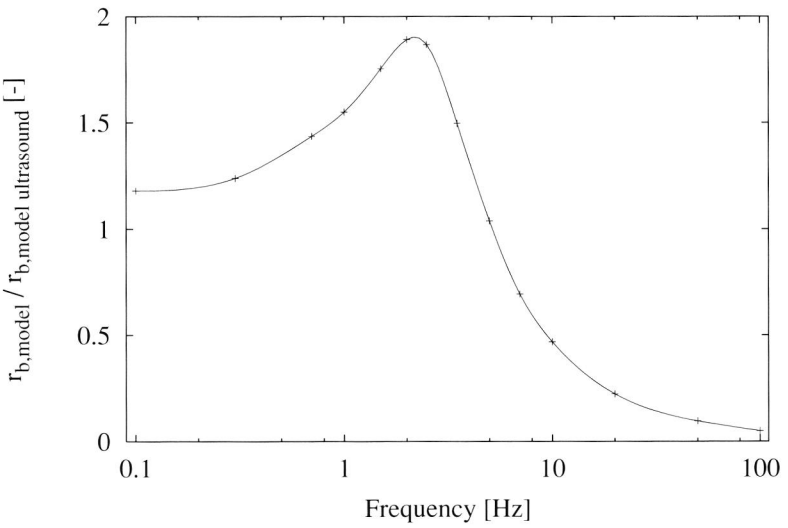

Figure 7.18: *Ratio of calculated unsteady regression rate fluctuations (peak-to-peak) and unsteady p-t-p regression rate fluctuations obtained from the theoretical ultrasound pulse-echo time (markers are calculated points).*

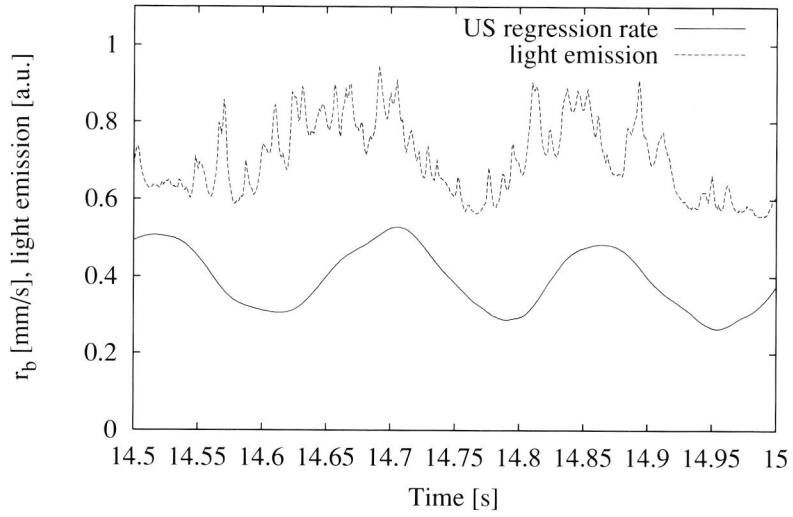

Figure 7.19: *Uncorrected ultrasound regression rate signal and light emission ($p = 0.2\,MPa$, harmonic laser fluctuation at 5 Hz). Note the phase difference between both signals.*

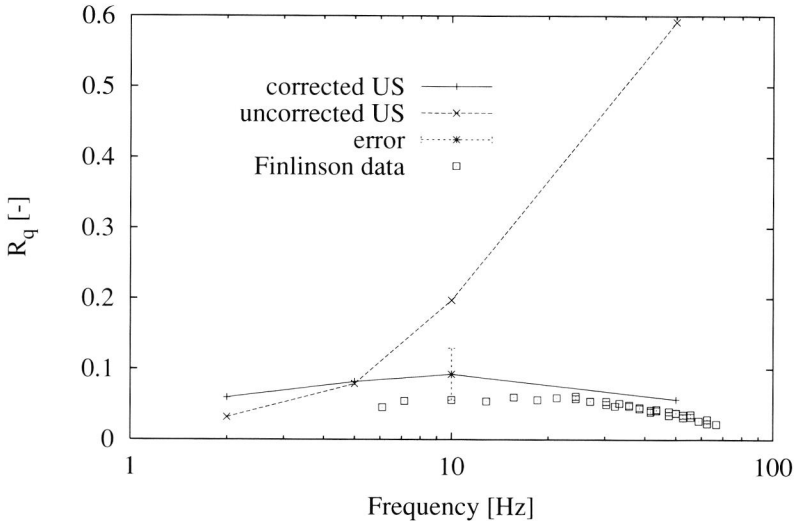

Figure 7.20: *Laser-recoil of HNF at 0.2MPa measured with ultrasound. Shown are the corrected and uncorrected response function for varying thermal layer thickness.*

Chapter 8

Combustion modification

8.1 Introduction

The previous Chapters have shown that the burn rate exponents of HNF-propellants are high. For practical applications a pressure exponent below 0.7 is needed. In this Chapter a simple model for the combustion of HNF-propellants is presented, given the burn rates of the binder and oxidizer. This model helps to understand the high burn rate exponent of HNF-propellants. The reason for the high burn rate exponent of HNF is outlined in the second part of this Chapter. In the last part of this Chapter some introductory experiments of HNF with additives are presented. This Chapter has been included as a starting point for future work towards the combustion modification of HNF-propellants.

8.2 Time-averaged combustion

The combustion of energetic filler materials in an energetic binder has been studied by several researchers [35, 91]. Results of these studies show that in many cases the binder and energetic filler burn independently, and the regression rate is the time-average of the burn rates of the components. For these systems the regression rate is given by [91]

$$\frac{1}{r_b} = \frac{\xi_{ox}}{r_{b,ox}} + \alpha \Delta t_{ox} + \frac{(1 - \xi_{ox})}{r_{b,binder}} , \tag{8.1}$$

where ξ_{ox} is the volumetric oxidizer fraction, and $r_{b,ox}$ and $r_{b,binder}$ are the regression rates of the oxidizer and binder respectively. The factor $\alpha \Delta t_{ox}$ accounts for the ignition delay of the oxidizer particles, and is generally dependent on the diameter of the oxidizer crystals. This equation is easily derived by calculating the burn time of a unity length of propellant. The burn rate is then found as the inverse of the total burn through time, i.e. the right hand side of Eq.(8.1). This explains the series-averaging of the individual component burn rates. In the above expression the binder ignition delay has been neglected, based on experimental evidence for HMX-based systems. For HMX/HTPB propellants, the non-energetic binder does not burn in a nice linear fashion, but also large amounts are shedded from the surface [9]. For these types of propellants, additional terms in Eq.(8.1) are required to account for these effects.

The HNF-propellant emission images suggest that the HNF and GAP are also combusting in an independent alternating way (see Chapter 5). The regression rates of neat

HNF and GAP were used to compute the regression rate of a HNF/GAP=55/45 propellant. The results of these calculations are shown in Fig 8.1. For these calculations the ignition delay was neglected, $\Delta t_{ox} = 0$. Comparing the results of the computations against the experimental results of Fig. 5.19, it is seen that agreement is very good: For both the experimental results and the calculations, the burn rate curves cross around a pressure of 2 MPa. At low pressures the burn rate is enhanced by the high regression rate of GAP. At higher pressures the GAP reduces the burn rate of the propellant. The time-averaged combustion is supported by the experimental and numerical results for sandwich combustion of Chapters 5 and 6. These results also showed that the diffusion flame contribution can be neglected compared to that of the neat HNF flame, and the exothermic subsurface reactions in GAP, and that the binder and oxidizer burn independently.

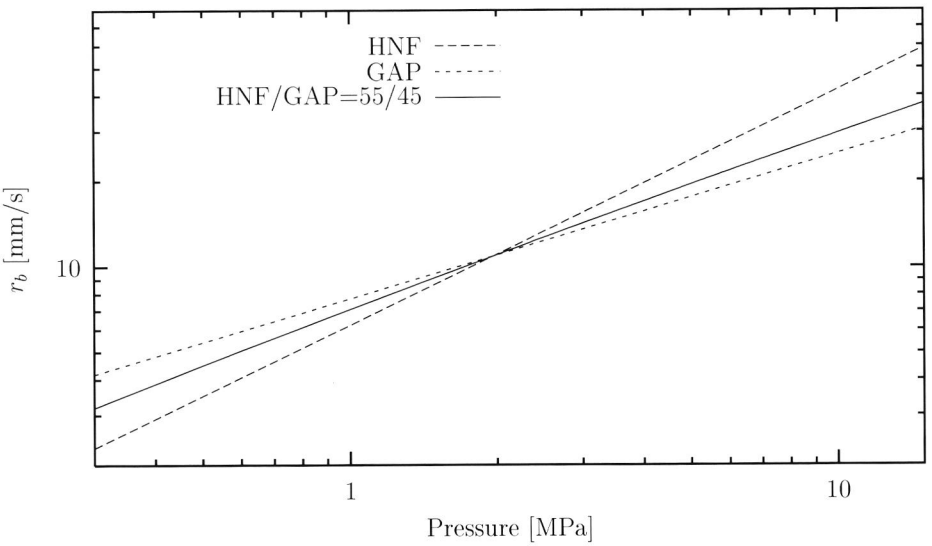

Figure 8.1: *Calculated regression rate of a HNF/GAP propellant assuming time-averaged combustion of HNF and GAP.*

When evaluating Eq.(8.1) it is found that the effect of the oxidizer ignition delay time is most relevant at higher pressures. The ignition delay time decreases the burn rate exponent at higher pressures. The best agreement with experiments is obtained for an ignition delay time of zero. However, in reality there will always be some delay time. This means that at higher pressures the pressure exponent will decrease (assuming that the HNF and GAP do not show slope breaks). Unfortunetly, data at high pressures is not available to verify this.

The model for time-averaged combustion always predicts a pressure exponent lower than that of the neat oxidizer combustion. In Chapter 5 it was reported that HNF-propellants with polyNIMMO and HTPB binder have a burn rate exponent close to n=1. With the simple model of Eq.(8.1) this cannot be explained. Consequently the combustion mechanism of these propellants must be different from that of the GAP-based propellants.

One major difference between GAP-propellants and the HTPB and polyNIMMO based propellants is the bonding of the HNF to the binder. GAP propellants show good bonding. In case of HTPB and polyNIMMO based propellants, the HNF does not bond to the binder. During handling of these propellants, the HNF crystals easily fall out of the binder matrix. The propellants are also more sensitive to tearing, which becomes clear during sample cutting and placement of the fuse wires for the strand burner.

The mechanical properties of HTPB and polyNIMMO propellants can explain the high pressure exponents of these propellants. Because the HNF flame is very small, it easily penetrates into voids between binder and crystals. At that moment the burn rate becomes higher than that of time-averaged combustion. Similar effects have also been found with early HNF/GAP-propellants, which did not match the mechanical properties of the current propellants [49]. For these HNF-propellants the pressure exponent was n=0.72 at low pressures ($<$ 1 MPa), and n=1.06 when the results of all experiments were taken into account ($0.2 < p < 6$ MPa). With increasing pressure, the mechanical degradation becomes more important, and the burn rate of the propellant changes due to this degradation. This mechanism is considered also to be the cause of the high pressure exponents of HTPB and polyNIMMO-based propellants. It is expected that the use of a bonding agent will reduce the pressure exponent of these propellants.

8.3 Pressure exponent reduction

It can be concluded from the previous section that combustion modification of HNF-propellants is most logically done via modification of the combustion of HNF itself. The result of the DBW-model already showed that the pressure exponent of HNF is n=1, see Eq.(6.20), and close to n=1 for the WSB model. These results originate from the initial assumption of a second-order gas phase reaction, and can be more generalized for a reaction order δ. For the WSB and DBW type of models the result is always n$\sim \delta/2$, see e.g. [6, 133]. Beckstead derived an analytical solution for the pressure exponent for a simple model assuming a flame sheet with flame standoff ξ^*, a constant specific heat capacity c, and surface activation energy E_s [6]

$$\mathrm{n} = \frac{\delta + \left(\dfrac{E_g}{RT_f} + \dfrac{cT_f}{Q_g \xi^*}\right) \dfrac{\partial \ln T_f}{\partial \ln p}}{2 + \dfrac{RT_s}{E_s} \dfrac{cT_s}{Q_g \xi^*} \exp(\xi^*)} . \tag{8.2}$$

This equation shows that for a constant flame temperature T_f, the pressure exponent is a little smaller than $\delta/2$ because of the second term in the denominator. The fact that a pressure dependent flame temperature ($\partial \ln T_f / \partial \ln p$ is non-zero) affects the pressure exponent was already discussed in section 6.2. For a high surface activation energy, and a constant flame temperature the result n=$\delta/2$ is retrieved.

These simple models show that the effect of the condensed phase on the pressure exponent is very small. Only the reaction order of the gas phase determines the burn rate exponent. So, the most logical approach to reduce the pressure exponent is to reduce the reaction order of the gas phase reactions. However, for HNF the gas phase reaction zone is very small at elevated pressures. This means that the catalyst has to function in a very

narrow zone (e.g. < 25 μm), and consequently the catalyst particle size must be small in comparison to the length of this zone. Unfortunetly, no simple recipe can be given to reduce the reaction order of the gas phase reactions.

Because of the similarities of the chemical composition of HNF with double-base, HMX and RDX, typical catalysts used for these propellants have been evaluated in the past. Several typical double-base modifiers were introduced in HNF/polyNIMMO propellants [92]. For these propellants no significant burn rate variations were observed in comparison to the control propellant without additives. According to Lengellé, a staged flame structure allows combustion modification by adequate additives, like salts of lead, copper, bismuth etc. [91]. These will enhance the secondary flame reactions, involving NO, creating super-rate effects and plateau effects. For nitramines (HMX, RDX, and HNIW) the secondary flame is close to the surface, and there is no possibility of creating super-rates and plateau burning. Also for HNF it can be stated that there is no real staged flame zone, and that conventional double-base additives will not work. More research is necessary in this area.

In a propellant development program for Rocketdyne, high-energy HNF propellants were formulated [128]. Carboxy-terminated polybutadiene (CTPB) was used as binder. The propellants contained about 10% beryllium and had solid loadings of 86% and more. Because these propellants had a pressure exponent of about unity, an attempt was made to modify the combustion behavior. Reducing the solid load reduced the pressure exponent, but lead to unacceptable performance loss. Several additives were tried, such as: $CaCO_3$, Cr_2O_3, Fe_2O_3, V_2O_5, $K_2Cr_2O_7$ and $(NH_4)_2Cr_2O_7$. In all cases the pressure exponent remained close to unity, although with some additives the burning rates were increased. Dilution of the oxidizer by replacing the HNF with AP or AN reduced the pressure exponent. For a propellant containing 22% HNF and 50% AP the pressure exponent was reduced to 0.74. This experimental matches the findings of the BDP-model, which predicts a high burn rate exponent already at low HNF loadings, see Fig. 6.24.

Boron hydrides (B_nH_n) were found to have a pronounced effect on the burn rate of propellants containing nitramines [138]. Very high burn rates (> 100 mm/s) have been obtained by adding these hydrides. The mechanism is not very well understood. It seems that the hydrides are good proton donors. Hydrogen of the hydride reacts with the NO_2 groups of the nitramine, yielding HONO. A similar scenario is not unlikely for HNF and boron hydrides, because HNF decomposition was found to start with a proton transfer. It seems therefore interesting to carry out some experiments with HNF-B_nH_n mixtures.

8.4 Initial experiments

In an attempt to reduce the pressure exponent of HNF, samples with additives were pressed and regression rates were measured in the TNO/PML strand burner. Compared to vacuum casting and curing propellant samples, this is less laborious. The choice of additives is limited to the materials that are compatible with HNF. This restriction largely affected the selection.

Materials that were selected are graphite, boron, bismuth oxide (Bi_2O_3), ammonium perchlorate, lithium fluoride (LiF), molybdenum vanadium oxide (MOVO), and ultrafine aluminum, Alex. The results for graphite and Alex were already presented in section 4.6. Boron has been observed to reduce the pressure exponent of AP-propellant by exothermic

reactions close to the burning surface [86]. For a similar reason the Alex was chosen. Bismuth oxide was found to be one of the few metal oxides that is compatible with HNF. Bismuth oxides are known for catalyzing double-base propellants [34]. Lithium fluoride has a high latent melting heat, and acts as a cooler on the burning surface. The 'catalysts' were added at 5% level. Alex was mixed at 20% level, comparable to the amount of aluminum in a propellant. The HNF/AP-mixture was selected to contain 50% AP.

Figure 8.2 shows the regression rates of different HNF mixtures. Compared to the neat HNF combustion only the mixtures containing Alex and AP show a considerable decrease of the burn rate exponent ($n = 0.66$ and $n = 0.75$ respectively). All the other additives have some effect on the absolute value of the burn rate, or an adverse effect on the pressure exponent. The addition of Alex increases the burn rate dramatically. The addition of AP reduces the burn rate (exponent) because of the dilution of the HNF.

The reason that the Alex is more effective than e.g. conventional aluminum and boron can be explained by the short flame of HNF. PREMIX calculations show that at 10 MPa a flame temperature of 2500 K is achieved within 15 μm above the burning surface. This distance is of the same order of magnitude as typical aluminum particles in a composite propellant. So, when conventional aluminum is added, the HNF still combusts according to its normal mode, which has a pressure dependency $n \sim 0.85$. In this case the aluminum does not contribute to the combustion significantly. However, when very fine aluminum is added, reaction between the highly reactive Alex and HNF decomposition gases can occur before the energy is released via the normal reaction path in the gas phase. Then the combustion mode changes from a homogeneous gas phase reaction, to a heterogeneous reaction at the burning surface of the HNF. This reaction is quite different from the normal gas phase reactions, and in general has a different pressure dependence. Note that the HNF-flame still reacts with the coarse aluminum at about 15 μm from the surface. But, at elevated pressures this distance to the burning surface is too large to affect the burn rate.

8.5 Conclusions

A simple model has been presented to describe the combustion of HNF-propellants based on the idea of independent, sequential, combustion of the binder and oxidizer. The results of this model show good agreement with experimental data, and help to understand the combustion of HNF-propellants. The model shows that the burn rate exponent of HNF-propellants can be modified by altering the neat HNF combustion, or that of the binder.

The most logical method to reduce the burn rate exponent of HNF, is to reduce the reaction order of the gas phase reactions. Unfortunetly no real recipe exists for the reduction of the reaction order. Several additives with HNF were tested to evaluate the effect on the combustion. No real 'catalyst' has been found. HNF-Alex mixtures burn with n=0.66, at 20% Alex loading. All other additives hardly affected the burn rate exponent, except for a dilution effect in the case of a HNF/AP=50/50 mixture.

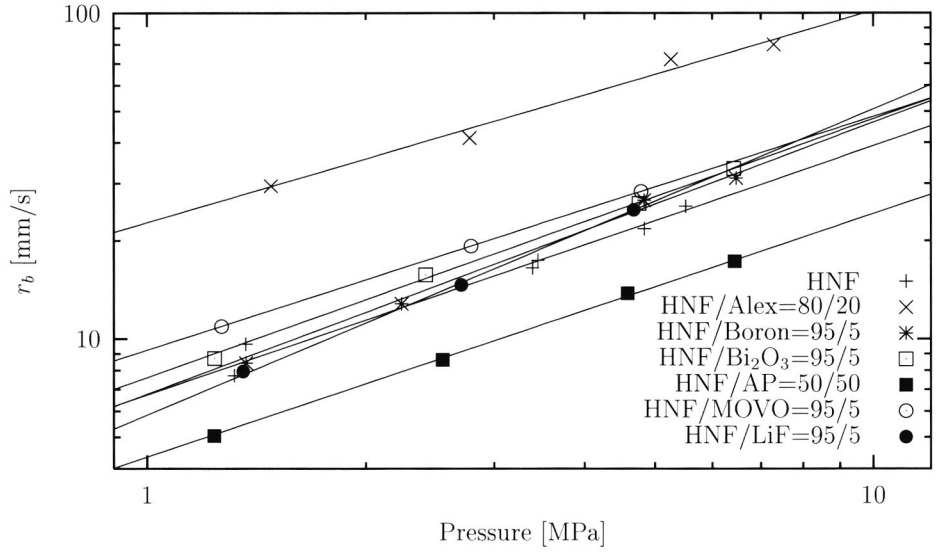

Figure 8.2: *Regression rates of pressed samples containing HNF.*

Chapter 9

Conclusions

In this thesis the decomposition and combustion of hydrazinium nitroformate (HNF) is addressed. HNF's high energetic content makes it a very attractive candidate for future propellants. Most of the work that has been carried out in other programs focused on the production of stable HNF and HNF-propellants. It is the intention of this work to obtain a better understanding of the combustion of HNF and HNF-propellants

Decomposition experiments showed that the most probable initial step for HNF decomposition is an intramolecular hydrogen transfer from the hydrazinium ion to one of the NO_2-groups of the nitroform. The calculated activation energy (for a single molecule in the gas phase) for this step is 84 kJ/mole. In comparison with the activation energy for other energetic materials this is a low value. After the proton transfer highly reactive hydrazine and aci-nitroform remains. Further decomposition of aci-nitroform to HONO and dinitrocarbene was speculated but the calculated activation energy for this step is too high to actually take place, at least at low temperatures. Further decomposition is more probable by reaction of the aci-nitroform with the released hydrazine, or different species that were found during other decomposition steps. Typical species that are formed in these steps are N_2O, NO, H_2O, etc.

HNF crystals were pressed to consolidated samples with a density of approximately 94% of the crystals. Microscopic images of these pellets revealed that during the pressing action the needle-shaped HNF crystals break and are then fused together because of the high pressing pressure ($\sim$200 MPa). Hazard assessment experiments showed that the friction sensitivity of HNF crystals and HNF pellets is equal. HNF pellets were less sensitive to impact than the original HNF material. In this work the pressed HNF pellets are used to study the combustion of neat HNF and to manufacture HNF/binder sandwiches to study oxidizer/binder diffusion flame interactions.

The neat HNF pellets burn with a high burn rate and high pressure exponent. At 10 MPa the burn rate is $\sim$60 mm/s. The pressure exponent decreases slightly with pressure. At pressures below 2 MPa the pressure exponent was found to be 0.95. Above this pressure the pressure exponent is 0.85. The surface temperatures have been measured by micro-thermocouples. The surface temperature increases from 523 K at 0.1 MPa to 680 K at 1.0 MPa. The thermocouple traces show sudden bends in the temperature profile. The bends are attributed to the cracking of the HNF pellets because of thermal stresses. Due to these cracks a thermal resistance is introduced, leading to sharp bends in the temperature profiles.

Absorption experiments in the gas phase of HNF show that the maximum NO mole fraction at ambient pressure is 20%. The NO is very slowly consumed. The reason for the slow consumption of NO is the fact that HNF combustion yields oxygen rich decomposition products. NO is only consumed by decomposition to N_2 and O_2, not by a reaction with fuel species. During combustion HNF vaporizes at the burning surface, and then decomposes in the gas phase. At low pressures, or during ignition, a yellow condensate was observed to come of the surface. This material was identified to be HNF.

To study the HNF/binder interaction, sandwiches of HNF and binder were made. The flame structure was visualized by planar laser-induced fluorescence (PLIF). The PLIF-images show a small diffusion effect at ambient and slightly elevated pressures. With increasing pressure the diffusion vanishes, and the two components burn independently. Above $\sim$ 1 MPa no significant diffusion was found. It was attempted to image the flame structures of HNF-propellants by PLIF as well. However, due to the significant amount of non-resonant signal, these experiments did not yield useful information about the flame structure.

HNF propellants with a glycidyl azide polymer (GAP) binder were formulated. To evaluate the effect of HNF particle size, two propellants with an equivalent solid load of 55%, but different HNF particle size (100μm and 474μm) were formulated. Within experimental errors the burn rate exponent was found to be equivalent, $n = 0.7$. The propellant with the fine HNF particles has a slightly higher burning rate. At 5 MPa the difference is 0.7 mm/s, with an average regression rate of 17.5 mm/s. The burn rate of HNF-propellants is insensitive to the addition of aluminum. A 68% solid load HNF/Al/GAP propellant containing 18% aluminum was found to have similar burn rates as the other non-aluminized propellants with 55% solid load.

Several models for the combustion of HNF and HNF-propellants have been presented. Each of the models has its own specific assumptions and approximations. Taken together the models help to explain the combustion of HNF and HNF-compositions. The simple Ward-Son-Brewster (WSB) model allows for an accurate calculation of steady state regression rates, temperature sensitivity, laser-assisted combustion and other physical parameters such as surface temperatures and flame standoff distances for neat HNF combustion. The idea behind the WSB-model is a low gas phase activation energy. In comparison with the flame sheet approach (high activation energy) the agreement with experimental data is better. The physical interpretation is that the rate-determining step in the gas phase has an overall low activation energy. Chemically speaking the low activation reactions (e.g. NO_2+H$\rightleftharpoons$NO+OH) are more important for the heat-feedback to the combustion surface than the high-activation energy reactions (like the reactions that further reduce the NO). This observation matches the fact that high temperatures are already achieved in the HNF-flame before NO-reactions have taken place.

The modified PREMIX approach supplements the WSB-model findings. Except for the HNF decomposition steps this model uses elementary reactions for the calculation of HNF combustion. The results show that at 0.1 MPa a temperature of 2550 K is reached at 0.5 mm above the burning surface. At this point the NO mole fraction is at its maximum value of 0.27. Further reduction of the NO only minimally affects the temperature. At this pressure the adiabatic flame temperature (2766 K) is reached at about 30 mm above the burning surface. The calculated composition above the burning surface shows good comparison with chemical equilibrium calculations. Also the agreement with species pro-

files for several radicals that have been obtained with planar or laser-induced fluorescence further support the model.

Based on the obtained knowledge on the combustion of HNF and available literature on GAP combustion, a HNF/GAP propellant model was presented. The BDP-model approach for the combustion of AP-propellants was followed. This model allows to study the combustion of a HNF/GAP-propellant using global reactions. A laminar diffusion flame between the HNF and GAP decomposition gases is assumed. The model calculations show that the primary diffusion flame (diffusion flame between HNF and GAP decomposition gases) only plays a role at pressures below 0.5 MPa (for HNF particle sizes between 10 μm and 1000 μm). At typical operating pressures for solid rocket motors (5 MPa and higher) the primary flame can be neglected completely. At these pressures the HNF-flame dominates the surface heat feedback (more than 80% of the contribution). Due to the slight decrease of the final flame heat feedback, the burn rate decreases slightly with increasing particle size. This effect is small. For propellants with HNF particle sizes between 10 μm and 1000 μm the variation of the burn rate is only 6%. For a similar AP-propellant the burn rate variation is 90%. The pressure exponent varies minimally with solid loading. Calculations show that already at HNF mass fractions of 0.3 the pressure exponent is higher than 0.8. From the BDP-calculations it may be concluded that the HNF decomposition flame is the dominating heat feedback source to the burning surface. The effect of the binder-oxidizer flame in terms of heat feedback to the propellant surface is negligible compared to the HNF decomposition flame.

Finally, modeling results were obtained with the DUT BIGMIX code for the combustion of HNF/GAP sandwiches. The BIGMIX code calculates the two dimensional flame structure above the sandwich using elementary reactions. The chemical mechanism for the HNF PREMIX calculations was extended with the GRI-mechanism for hydrocarbon combustion. The surface regression is neglected in the BIGMIX model. The BIGMIX calculations show that the diffusion interaction between oxidizer and binder flame decreases with pressure. At 0.1 MPa there is an enhanced heat feedback due to the hotter diffusion flame. The maximum is located 0.5 mm outside the gas slab. At 1.0 MPa the maximum still exists, but has shifted to 50 μm outside the binder slab. At 10 MPa there is no further enhanced heat-feedback due to the diffusion flame.

The combustion of HNF was also studied by ultrasound. A pulse-echo technique was employed to determine instantaneous sample thickness, hence the burning rate. The steady state combustion results agree very well with the strand burner results. Apparent oscillations during steady state combustion were found to have the same pressure dependence as the burning rate. From this, the oscillations were identified to be caused by periodic cracking of the HNF pellets. Due to cracks, the thermal profile in the condensed phase changes, leading to varying pulse-echo times. Because the pulse-echo time is dependent on the thermal profile in the condensed phase, the ultrasound method can be employed to obtain non-intrusive temperature information of the condensed phase. Because of the coupling between the temperature profile and the pulse-echo time, a computer code was made to process the unsteady regression rate data. Using the same parameter set as for the simplified HNF-model, good agreement with existing laser-recoil data was obtained.

When comparing the regression rates of neat HNF and GAP with that of HNF-GAP propellants, it can be concluded that the regression is determined by the time-averaged combustion of the binder and the oxidizer. Combustion modification of HNF/GAP pro-

pellants is most efficiently done by modifying the combustion of HNF. In an attempt to reduce the pressure exponent of HNF, HNF was mixed with several additives. HNF samples pressed with 20% aluminum (particle size 20 μm) have a 30% higher regression rate at 1 MPa than the pure HNF. The pressure exponent for this mixture is 1.02. Below 2 MPa the HNF mixtures burn with residue. At higher pressures, no residues remained after combustion. HNF mixed with ultrafine ($\sim$ 180 nm) aluminum in a HNF/Al=80/20 ratio, burn with a moderate pressure exponent of 0.66. The regression rate of this composition is significantly higher than that of HNF. Several other additives were pressed with HNF, but none of them showed a large effect on the pressure exponent.

It is concluded that there is a very promising agreement between the experimental data and the theoretical analyses: the absence of an effect of crystal size on the burning rate of HNF propellants, the temperature sensitivity, and the overall decomposition of HNF. For steady state processes, it is fair to state that most fundamental aspects of the combustion of HNF and HNF propellants are well understood now.

Bibliography

[1] J.P. Agrawal. Recent Trends in High-Energy Materials. *Prog. Energy Combustion Science*, 24:1–30, 1998.

[2] Y. Akutsu and S. Tahara. Calculations of Heats of Formation for Nitro Compounds by Semi-empirical MO Methods and Molecular Mechanics. *Journal of Energetic Materials*, 9(3):161–171, 1991.

[3] Atlantic Research Corporation. Final Report on the Spherical High-Energy Solid-Propellant Rocket Motor. Technical Report ARC-SR-23A1, Atlantic Research Corporation, Alexandria, Virginia, 1963.

[4] A.I. Atwood, T.L. Boggs, P.O. Curran, T.P. Parr, D. Hanson-Parr, and C.F. Price. Burning Rate of Solid Propellant Ingredients, Part 2: Determination of Burning Rate Temperature Sensitivity. *Journal of Propulsion and Power*, 15(6):748–752, 1999.

[5] E. Bal. Resultaat stoot- en wrijvingsgevoeligheid HNF samples. Technical report, TNO Prins Maurits Laboratory, 1997. COMPANY CONFIDENTIAL.

[6] M.W. Beckstead. A model for double base propellant combustion. 16th AIAA/SAE/ASME Joint Propulsion Conference, June 30-July 2, Hartford, CT, AIAA Paper 80-1164, 1980.

[7] M.W. Beckstead, J.E. Davidson, and Q. Jing. A Comparison of Solid Monopropellant Combustion and Modeling. In K. Kuo, editor, *Challenges in Propellants and Combustion, 100 years after Nobel*, pages 1116–1132. Begell House Inc., New York, 1997.

[8] M.W. Beckstead, R.L. Derr, and C.F. Price. A Model of Composite Solid-Propellant Combustion Based on Multiple Flames. *AIAA Journal*, 8(12):2200–2207, 1970.

[9] M.W. Beckstead and K.P. McCarty. Modeling calculations for HMX composite propellants. *AIAA Journal*, 20(1):106–115, 1982.

[10] M.W. Beckstead and J. Widener. Aluminium combustion modeling in solid propellants. AIAA Paper 98-3824, 1998.

[11] M. Ben-Reuven and L.H. Caveny. Nitramine Flame Chemistry and Deflagration Interpreted in Terms of a Flame Model. *AIAA Journal*, 19:1276–1285, 1979.

[12] R.R. Bennet. Clean Propellants and the Environment. AIAA Paper 92-3398, 1992.

[13] R.P. van den Berg, J.M. Mul, and P.J.M. Elands. Monopropellant system. European Patent Application EP 0 950 648 A1, 1999.

[14] F.S. Blomshield. Nitramine Composite Solid Propellant Modelling. Technical Report TP 6992, Naval Air Weapon Center, China Lake, 1989.

[15] T.A. Boardman, L.G. Porter, F.W. Brasfield, and T.M. Abel. An Ultrasonic Fuel Regression Rate Measurement Technique for Mixture Ratio Control of a Hybrid Motor. AIAA Paper 95-3081, 1995.

[16] C.T. Bowman, R.K. Hanson, D.F. Davidson, W.C. Gardiner Jr., V. Lissianski, G.P. Smith, D.M. Golden, M. Frenklach, and M. Goldenberg. GRI-Mech V1.2. `http://www.me.berkeley.edu/gri_mech/`, 1999.

[17] V.S. Bozic, D.D. Blagojevic, and B.A. Anicin. Measurement System for Determining Solid Rocket Propellant Burning Rate Using Reflection Microwave Interferometry. *Journal of Propulsion and Power*, 13:457, 1997.

[18] M.Q. Brewster, M.H. Hites, and S.F. Son. Dynamic Burning Rate Measurements of Metalized Composite Propellants Using the Laser-Recoil Technique. *Combustion and Flame*, 94:178–190, 1993.

[19] M.Q. Brewster and S.F. Son. Quasi-Steady Combustion Modeling of Homogeneous Solid Propellants. *Combustion and Flame*, 103:11–26, 1995.

[20] M.Q. Brewster, M.J. Ward, and S.F. Son. New Paradigm for Simplified Combustion Modeling of Energetic Solids: Branched Chain Gas Reaction. AIAA Paper 97-3333, 1997.

[21] T.B. Brill. Multiphase Chemistry Considerations at the Surface of Burning Nitramine Monopropellants. *Journal of Propulsion and Power*, 11:740–751, 1995.

[22] T.B. Brill, P.J. Brush, and D.G. Patil. Thermal Decomposition of Energetic Materials 58: Chemistry of Ammonium Nitrate and Ammonium Dinitramide Near the Burning Surface Temperature. *Combustion and Flame*, 92:178–186, 1993.

[23] J.D. Buckmaster. *An Introduction to Combustion Theory. In: The Mathematics of Combustion, Frontiers in Applied Mathematics.* SIAM, Philadelphia, 1985.

[24] D. Campbell, A.S. Cumming, and E.J. Marshall. Development of insensitive rocket propellants based on ammonium nitrate and polynimmo. In *84th Symposium on Environmental Aspects of Rocket and Gun Propellants*, pages 14–1–14–9, Aalesund, Norway, 29 August - 2 September 1994. Agard Conference Proceedings 559, Propulsion and Energetics Panel (PEP).

[25] F. Cauty. Solid Propellant Combustion Response Function from Direct Measurement Methods: a Review of ONERA's Experience. Int. Workshop on Combustion Instability of Solid Propellants and Rocket Motors, Politecnico di Milano, 16-19 June, 1997.

[26] I.E. Chlenov, M.V. Kashutina, S.L. Ioffe, S.S. Novikov, and V.A. Tartakovskii. The possibility of generating dinitrocarbene from the trinitromethane anion. *Translated from: Seriya Khimicheskaya*, 9:2085–2086, 1969.

[27] B.T. Chorpening and M.Q. Brewster. Flame Structure of AP/Binder Sandwiches from Emission Imaging. AIAA Paper 99-0594, 1999.

[28] A. Davenas. *Solid Rocket Propulsion Technology.* Pergamon Press, Oxford, England, 1993.

[29] J. Davidson and M.W. Beckstead. A Mechanism and Model for GAP Combustion. AIAA Paper No. 97-0592, 1997.

[30] L.L. Davis and K.R. Brower. Shock-Initiation Chemistry of Nitroarenes. APS Topical Conference on Shock Compression of Condensed Matter, Amherst, MA, July 28-August 1, 1997.

[31] D. Deepak, R. Jeenu, P. Sridharan, and M.S. Padmanabhan. Determination of Pressure Dependence of Burning Rate in Solid Motors Using Ultrasonic Technique. *Journal of Propulsion and Power*, 14:290–294, 1998.

[32] L. DeLuca. *Theory of Nonsteady Burning and Combustion Stability by Flame Models in: Nonsteady Burning and Combustion Stability of Solid Propellants, edited by L. Deluca, E.W. Price, and M. Summerfield*, volume 143 of *AIAA Progress in Astronautics and Aeronautics.* AIAA, Washington, 1992.

[33] M.R. Denison and E. Baum. A simplified model of Unstable Burning in solid Propellants. *ARS Journal*, 31:1112–1122, 1961.

[34] A.P. Denisyuk, L.A. Demidova, Yu. G. Shepelev, B.M. Baloyan, and V.E. Telepchenkov. Highly efficient low-toxicity catalysts of combustion of double-base powders. *Combustion, Explosion and Shock Waves*, 33(6):688–694, 1997.

[35] A.P. Denisyuk, V.S. Shabalin, and Yu. G. Shepelev. Combustion of condensed systems consisting of hmx and a binder capable of self-sustained combustion. *Combustion, explosion and Shock Waves*, 34(5):534–542, 1998.

[36] F. Dijkstra, P.A.O.G. Korting, and R.P. van der Berg. Ultrasonic Regression Rate Measurement in Solid Fuel Ramjets. AIAA Paper 90-1963, 1990.

[37] L.G. Dodge, J. Dusek, and M.F. Zabielski. Errors in the Reported Values for the Collisional Broadening Parameters for Nitric Oxide Gamma(0,0) Band. *Journal of Quantum Spectroscopy and Radiation Transfer*, 24:523–525, 1980.

[38] L.G. Dodge, J. Dusek, and M.F. Zabielski. Line Broadening and Oscillator Strength Measurements for the Nitric Oxide Gamma(0,0) Band. *Journal of Quantum Spectroscopy and Radiation Transfer*, 24:237–249, 1980.

[39] G. Doriath and B. d'Andrea. New Solid Propellants Formulations and Production Processes. 5th Internation Symposium Propulsion in Space Transportation, pp. 14.3-14.12, 1996.

[40] G. Dumas and R. Ben-Aim. Etude de la condition énergétique de propagation d'une flamme dans un propergol solide homogéne. Cahier de la Thermique **4**, Colloque sur la Combustion des Propergoles Solides, Poitiers, 1972.

[41] M. Dupuis, D. Spangler, and J.J. Wendoloski. Gamess. `http://www.msg.ameslab.gov/GAMESS/`, 1999.

[42] G. von Elbe, R. Friedman, J.B. Levy, and S.J. Adams. Research on combustion in solid rocket propellants: Hydrazine nitroform as a propellant ingredient. Technical Report DA-36-034-AMC-0091R, Atlantic Research Corporation, 1964.

[43] R. Engleman, P.E. Rouse, H.M. Peek, and V.D. Baiamonte. Beta and gamma band systems of nitric oxide. Technical Report LA-4364, Los Alamos National Laboratory, 1969.

[44] N.E. Ermolin and V.E. Zarko. Mechanism and kinetics of the thermal decomposition of cyclic nitramines. *Combustion Explosion and Shock Waves*, 33:251–269, 1997.

[45] J.C. Finlinson. Laser recoil combustion response of HNF oxidizer from 1 to 6 atmospheres. AIAA Paper 97-3342, 1997.

[46] J.C. Finlinson and A.I. Atwood. HNF burnrate, temperature sensitivity, and laser recoil response from 1 to 6 atm (sanitized). 34nd JANNAF Combustion Subcommittee Meeting, West Palm Beach, FL 27-31 Oct. 1997, 1997.

[47] J.E. Flanagan, M.B. Frankel, and D.O. Woolery. HMX Combustion Modification. Technical Report AFRPL-TR-84-044, Rockwell International / Air Force Rocket Propulsion Laboratory, 1984.

[48] M.B. Frankel, L.R. Grant, and J.E. Flanagan. Historical development of glycidyl azide polymer. *Journal of Propulsion and Power*, 8:560–563, 1992.

[49] G.M.H.J.L. Gadiot, J.M. Mul, J.J. Meulenbrugge, P.A.O.G. Korting, A.J. Schnorhk, and H.F.R. Schöyer. New solid propellants based on energetic binders and HNF. 43rd Congress of the International Astronautical Federation, PAPER IAF-92-0633, 1992.

[50] L. Galfetti, G. Riva, and C. Bruno. *Numerical Computations of Solid-Propellant Nonsteady Burning in Open or Confined Volumes, in: Nonsteady Burning and Combustion Stability of Solid Propellants, edited by L. Deluca, E.W. Price, and M. Summerfield*, volume 143 of *AIAA Progress in Astronautics and Aeronautics*. AIAA, Washington, 1992.

[51] L. Gero and R. Schmid. Dissociation Energy of the NO Molecule. *Proceedings of the Physical Society*, 60:35, 1948.

[52] R.L. Glick. Concurrent analysis of steady and nonsteady ballistic test data. AIAA Paper 99-2803, 1999.

[53] S. Gordon and B.J. McBride. Computer Code for Calculation of Complex Chemical Equilibrium Compositions, Rocket Performance, Incident and Reflected Shocks, and Chapman-Jouguet Detonations. Technical Report SP-273, interim revision, NASA, 1976.

[54] J. Gray. Low orbit is only half way. *Aerospace America*, 36:3, 1998.

[55] J.F. Grcar. The `TWOPNT` Program for Boundary Value Problems. Technical Report Report SAND91-8230, Sandia National Laboratories, 1992.

[56] D.M. Hanson-Parr and T.P. Parr. Spontaneous Raman Spectroscopy Applied to Nitramine Flames. 35th JANNAF Combustion Meeting, 1998.

[57] D.M. Hanson-Parr and T.P. Parr. Thermal properties measurements of solid rocket propellant oxidizers and binder material as a function of temperature. *Journal of Energetic Materials*, 17:1–47, 1999.

[58] A.E.D. van der Heijden. Review on stability, reactivity and curing of hnf. Technical Report NP HG ST 00 02 014 (2), Aerospace Propulsion Products, Hoogerheide, 1996. CONFIDENTIAL.

[59] C.A. Heller and A.S. Gordon. Structure of the Gas Phase Combustion Region of a Solid Double Base Propellant. *Journal of Physical Chemistry*, 59:773–777, 1955.

[60] T.K. Highsmith, C. McLeod, R.B. Wardle, R. Schmitt, J.Bottaro, P. Penwell, D. Bomberger, and J. Brough. ADN Manufacturing Technology. In *29th International Annual Conference of ICT, June 30-July 3, 1998, Karlsruhe*, pages 20–1 – 20–14, 1998.

[61] K. Hori and M. Kimura. Combustion mechanism of glycidyl azide polymer. *Propellants, Explosives and Pyrotechnics*, 21:160–165, 1996.

[62] M.M. Ibiricu and F.A. Williams. Influence of Externally Applied Thermal Radiation on the Burning Rates of Homogeneous Solid Propellants. *Combustion and Flame*, 24:185–198, 1975.

[63] S. Imanishi. Ultra-violet absorption and Raman effect for hydrazine. *Nature*, 127(3212):782, 1931.

[64] R.A. Isbell and M.Q. Brewster. Optical properties of energetic materials: RDX, HMX, AP, NC/NG, and HTPB. *Propellants, explosives and pyrotechnics*, 23:218–224, 1998.

[65] H. Jahanian. Hydrazinium nitroformate (HNF). The future solid propellant. Internship report: TNO Prins Maurits Laboratory / Delft University of Technology, 1999.

[66] R.J. Kee, J.F. Grcar, M.D. Smooke, and J.A. Miller. A Fortran Program for Modeling Steady Laminar One-Dimensional Premixed Flames. Technical Report SAND85-8240, Sandia National Laboratories, 1985.

[67] R.J. Kee, F.M. Rupley, and J.A. Miller. Chemkin-II: A fortran chemical kinetics package for the analysis of gas phase chemical kinetics. Technical Report SAND89-8009B, Sandia National Laboratories, 1991.

[68] A.B. Kiskin, V.N. Simonenko, V.E. Zarko, and A.G. Svit. Peculiarities of Sustaining Combustion of Nitramines at Atmospheric Pressure. Int. Workshop on Combustion Instability of Solid Propellants and Rocket Motors, Politecnico di Milano, 16-19 june, 1997.

[69] H.E. Kissinger. Reaction kinetics in differential thermal analysis. *Analytical Chemistry*, 29:1702–1706, 1957.

[70] K. Klager and G.A. Zimmerman. *Steady Burning Rate and Affecting Factors Experimental Results, in: Nonsteady Burning and Combustion Stability of Solid Propellants, edited by L. Deluca, E.W. Price, and M. Summerfield*, volume 143 of *AIAA Progress in Astronautics and Aeronautics*. AIAA, Washington, 1992.

[71] R. Klein, M. Mentser, G. Von Elbe, and B. Lewis. Determination of the Thermal Structure of a Combustion Wave by Fine Thermocouples. *Journal of Physical Chemistry*, 54:877–884, 1950.

[72] K. Knip. Gaten dichten in het 10-jarig ozon-protocol. NRC Handelsblad, 17 September, 1997.

[73] T.S. Konkova and Yu.N. Matyushin. Combined study of thermochemical properties of nitroform and its salts. *Russian Chemical Bulletin*, 47:2371–2374, 1998.

[74] V.A. Koroban, T.I. Smirnova, T.N. Bashirova, and B.S. Svetlov. Kinetics and mechanism of the thermal decomposition of hydrazine trinitromethane. *Tr.-Mosk. Khim.-Teknol. Inst. im D.I. Mendeleeva*, 104:38, 1979.

[75] O.P. Korobeinichev, L.V. Kuibida, A.A. Paletsky, and A.G. Shmakov. Molecular-Beam Mass-Spectrometry to Ammonium Dinitramide Combustion Chemistry Studies. *Journal of Propulsion and Power*, 14(6):991–1000, 1998.

[76] P.A.O.G. Korting, E.H. den Hertog, and H.F.R. Schöyer. Determination of the regression rate of solid fuels in solid fuel combustion chambers by means of the ultrasonic pulse-echo technique. part 1. the measurement technique. Technical Report Report LR-453, Report PML 1985-C-5, SFCC Publication No. 18, TNO Prins Maurits Laboratory / Delft University of Technology, 1985.

[77] P.A.O.G. Korting and H.F.R. Schöyer. Determination of the regression rate in solid fuel ramjets by means of the ultrasonic pulse echo method. In C.K. Law, Y. Jaluria, W.W. Yuen, and K. Miyasaka, editors, *Proceedings of Heat transfers in fire and combustion systems*, pages 347–353. HTD Vol 45, American Society of Mechanical Engineers, New York, 1985.

[78] E. Krabbendam-La Haye and W. de Klerk. Resultaten wrijving HNF tabletten. Technical report, TNO Prins Maurits Laboratory, 1998. COMPANY CONFIDENTIAL.

[79] H. Krause and A. Pfeil. FTIR-untersuchungen an pyrolyseprodukten von GAP. In *ICT Conference Proceedings*, pages 8–1, 1990.

[80] H. Krier, J.S. T'ien, W.A. Sirignano, and M. Summerfield. Nonsteady Burning Phenomena of Solid Propellants: Theory and Experiments. *AIAA Journal*, 6:278, 1968.

[81] N. Kubota. Combustion of energetic azide polymers. *Journal of Propulsion and Power*, 11:677, 1995.

[82] N. Kubota, T.J. Ohlemiller, L.H. Caveny, and M.Summerfield. An Experimental Study of the Site and Mode of Action of Platonizers in Double-Base Propellants. AIAA Paper 81-1555, 1981.

[83] N. Kubota, T.J. Ohlemiller, L.H. Caveny, and M. Summerfield. An Experimental Study of the Site and Mode of Action of Platonizers in Double-Base Propellants. AIAA Paper 74-124, 1974.

[84] N. Kubota and T. Sonobe. Combustion mechanism of azide polymer. *Propellants, Explosives, and Pyrotechnics*, 13:172–177, 1988.

[85] K.K. Kuo. *Principles of Combustion.* John Wiley & Sons New York, 1986.

[86] T. Kuwahara and N. Kubota. Role of boron in burning rate augmentation of AP composite propellants. *Propellants, explosives and pyrotechnics*, 14:43–46, 1989.

[87] A.J. Landman. Combustion Modeling of HNF/GAP propellants and sandwiches. Engineering thesis, Delft University of Technology, Fac. Applied Physics, 1999.

[88] J.C. Leahy and J.W. Jackson Jr. Improvements in the Measurement of Hybrid Rocket Fuel Regression Rate using Ultrasonic Transducers. AIAA Paper 97-3082, 1997.

[89] Y.J. Lee, C.J. Tang, G. Kudva, and T.A. Litzinger. Thermal Decomposition of 3,3-Bis-Azidomethyl-Oxetane. *Journal of Propulsion and Power*, 14:37–44, 1998.

[90] G. Lengellé. Thermal Degradation Kinetics and Surface Pyrolysis of Vinyl Polymers. *AIAA Journal*, 8:1989–1998, 1970.

[91] G. Lengellé. Recent Developments and Challenges in the Ignition and Combustion of Solid Propellants. In *Challenges in Propellants and Combustion, 100 Years after Nobel*, pages 515–548. Begell House Inc., New York, 1996.

[92] E. Lokke (RATEC). Study note on propellant ballistic and mechanical properties (wp0090). Technical Report Technical Report APP/1997016 NP HNF TN 00 00 026 (2), Aerospace Propulsion Products, 1997. COMPANY CONFIDENTIAL.

[93] P.S. Loner and M.Q. Brewster. Oscillatory Laser-Induced Combustion of HMX. 1997 JANNAF Combustion Meeting, CPIA, West Palm Beach, FL.,Oct, 1997.

[94] J. Louwers and G.M.H.J.L. Gadiot. Nonlinear Transient Burning of Composite Propellants: The Effect of Solid Phase Reactions. In *Challenges in Propellants and Combustion, 100 Years after Nobel*, pages 1146–1157. Begell House Inc., New York, 1996.

[95] J. Louwers and G.M.H.J.L. Gadiot. Model for the Transient Burning of Hydrazinium Nitroformate. Int. Workshop on Combustion Instability of Solid Propellants and Rocket Motors, Politecnico di Milano, 16-19 june, 1997.

[96] J. Louwers, G.M.H.J.L. Gadiot, M.Q. Brewster, and S.F. Son. Model for Steady-State HNF Combustion. Int. Workshop on Combustion Instability of Solid Propellants and Rocket Motors, Politecnico di Milano, 16-19 june, 1997.

[97] J. Louwers, G.M.H.J.L. Gadiot, A.J. Landman, T.W.J. Peeters, Th.H. van der Meer, and D. Roekaerts. Combustion and flame structure of HNF sandwiches and propellants. 35th AIAA/ASME/SAE/ASEE Joint Propulsion Conference and Exhibit, 20-24 June, Los Angeles, CA, Paper number AIAA 99-2359, 1999.

[98] J. Louwers, G.M.H.J.L. Gadiot, M. Versluis, A.J. Landman, Th. H. van der Meer, and D. Roekaerts. Combustion of hydrazinium nitroformate based compositions. 34th AIAA/ASME/SAE/ASEE Joint Propulsion Conference and Exhibit, 13-15 July, Cleveland, OH, Paper number AIAA 98-3385, 1998.

[99] J. Louwers, G.M.H.J.L. Gadiot, M. Versluis, A.J. Landman, Th.H. van der Meer, and D. Roekaerts. Measurement of Steady and Non-Steady Regression Rates of Hydrazinium Nitroformate with Ultrasound. Int. Workshop on Measurement of Thermophysical and Ballistic Properties of Energetic Materials, Politecnico di Milano, Milano, Italy, 22-24 June, 1998.

[100] J. Louwers and A.E.D. van der Heijden. Hydrazinium nitroformate. International Patent Application WO 99/58498, 1999.

[101] J. Louwers and A.E.D. van der Heijden. Hydrazinium nitroformate based high performance solid propellants. International Patent Application WO 99/59940, 1999.

[102] J. Louwers, T. Parr, and D. Hanson-Parr. Decomposition and flame structure of hydrazinium nitroformate. 37th AIAA Aerospace Sciences Meeting and Exhibit, January 11-14, Reno, NV, Paper number AIAA 99-1091, 1999.

[103] J. Louwers, T.P. Parr, and D.M. Hanson-Parr. HNF Combustion and Decomposition Experiments: UV-Absorptioin, Thermal Profile, PLIF. Technical Report PML-1997-C41, TNO Prins Maurits Laboratory, 1997. COMPANY CONFIDENTIAL.

[104] J. Louwers and M. Versluis. HNF spaart ozonlaag. *De Ingenieur*, 20:24–25, 1998.

[105] J.R. Lovett and N.J. Edison. Hydrazine nitroform and method of preparation. Technical Report 3,378,594, United States Patent, 1963.

[106] G.M. Low. Hydrazinium nitroformate propellant with saturated polymeric hydrocarbon binder. Technical Report 3,708,359, United States Patent, 1973.

[107] J. Luque and D.R. Crosley. LIFBASE 1.61. `http://www.sri.com/psd/lifbase/`, 1999.

[108] Y. Mantzaras and Th.H. van der Meer. Cars measurements of temperature fluctuations in turbulent natural gas-fuelled piloted jet diffusion flames. *Combustion and Flame*, 110:39–53, 1997.

[109] W.K. McGregor, J.D. Few, D.R. Keefer, H.S. Lowry III, and M.G. Davis. Note of Correction: Broadening of NO Band Lines. *Journal of Quantum Spectroscopy and Radiation Transfer*, 23:527–530, 1980.

[110] E.T. McHale and G. von Elbe. The deflagration of solid propellant oxidizers. *Combustion Science and Technology*, 2:227–237, 1970.

[111] C.F. Melius. Thermochemical Modeling: I. Application to Decomposition of Energetic materials. S.N. Bulusu (ed.), Chemistry and Physics of Energetic Materials, 1990.

[112] C.M. Milfeith, A.D. Baer, and N.W. Ryan. Propellant Combustion Instability as Measured by Combustion Recoil. *AIAA Journal*, 10:1280–1285, 1972.

[113] M.S. Miller. In Search of an Idealized Model of Homogeneous Solid Propellant Combustion. *Combustion and Flame*, 46:51–73, 1982.

[114] R. Millner. *Ultraschall-Technik: Grundlagen und Anwendungen.* Physik Verlag GmbH, Weinheim, 1987.

[115] L.M. Minier, K.R. Brower, and J.C. Oxley. Role of Intermolecular Reactions in Thermolysis of Aromatic Nitro Compounds in Supercritical Aromatic Solvents. *Journal of Organic Chemistry*, 56:3306–3314, 1991.

[116] J.M. Mul. Search for new storable high performance propellants. Technical Report PML 1988-C65, TNO Prins Maurits Laboratory, 1988. CONFIDENTIAL.

[117] J.M. Mul. Proof of concept of HNF/Al/GAP solid propellants. Technical Report PML 1990-C26, TNO Prins Maurits Laboratory, 1990. CONFIDENTIAL.

[118] J.M. Mul, P.A.O.G. Korting, H.F.R. Schöyer, and A.J.Schnorhk. Information note on HNF/Al/GAP solid propellant. Technical report, Aerospace Propulsion Products, ESA-ESTEC, TNO-PML, 1992.

[119] H. Östmark, N. Wingborg, and A. Langlet. ADN: A New High Performance Oxidizer for Solid Propellants. 16th International Symposium on Ballistics, San Francisco, CA, 23-28 September, 1996.

[120] Y. Oyumi. Thermal decomposition of azide polymers. *Propellants, Explosives, and Pyrotechnics*, 17:226–231, 1992.

[121] Y. Oyumi and T. Brill. Thermal decomposition of energetic materials 12. infrared spectral and rapid thermolysis studies of azide-containing monomers and polymers. *Combustion and Flame*, 55:203, 1986.

[122] T. Parr and D. Hanson-Parr. *Nonintrusive Diagnostic Techniques for Research on Nonsteady Burning of Solid Propellants, in: Nonsteady Burning and Combustion Stability of Solid Propellants, edited by L. Deluca, E.W. Price, and M. Summerfield*, volume 143 of *AIAA Progress in Astronautics and Aeronautics*. AIAA, Washington, 1992.

[123] T. Parr and D. Hanson-Parr. HNF: neat and diffusion flame structure. 32nd JANNAF Combustion Subcommittee Meeting, 1995.

[124] T. Parr and D. Hanson-Parr. Solid propellant flame structure. In T.B. Brill, T.P. Russell, W.C. Tao, and R.B. Wardle, editor, *Mat. Res. Soc. Symp. Proc. Vol. 418*, pages 207–219. Materials Research Society, Pittsburgh, Pennsylvania, 1995.

[125] T.W.J. Peeters. Numerical Modeling of Turbulent Natural-Gas Diffusion Flames. Ph.D. Thesis, Delft University of Technology, 1995.

[126] K. Prasad, R.A. Yetter, and M.D. Smooke. An eigenvalue method for computing the burning rates of RDX propellants. *Combustion, Science and Technology*, 124:35–82, 1997.

[127] E.W. Price. Review of sandwich burning. In *30th Jannaf Combustion Subcommittee Meeting Volume II*, pages 259–279, Naval Postgraduate School, Monterey, CA, 15-19 November 1993.

[128] Rocket Propulsion Laboratory, Solid Rocket Division. Development of high-energy solid propellants. final summary report. volume 1: Technical report. Technical Report RPL-TDR-64-10, Air Force Systems Command, Edwards, California, 1964.

[129] A.J. Sabadel, J. Wenograd, and M. Summerfield. Measurement of Temperature Profiles through Solid Propellant Flames using fine Thermocouples. *AIAA Journal*, 3:1580–1584, 1965.

[130] S.F. Sarner. *Propellant Chemistry.* Reinhold Publishing Corporation, New York, 1951.

[131] H. Scheingraber and C.R. Vidal. Measurement of the Honl-London Factors on 2(Sigma)-2(Pi) transitions in NO. *Journal of Chemical Physics*, 83:3873–3877, 1985.

[132] E.W. Schmidt. *Hydrazine and its derivatives.* John Wiley & Sons, New York, 1984.

[133] H.F.R. Schöyer and J.H. van Dijk. Analytic solution for premixed solid propellant flames. 20th AIAA/SAE/ASME Joint Propulsion Conference, June 11-13, Cincinnati, OH, AIAA Paper 84-1438, 1984.

[134] H.F.R. Schöyer, A.J. Schnorhk, P.A.O.G. Korting, and P.J. van Lit. First experimental results of an HNF/Al/GAP solid propellant. 33rd AIAA/ASME/SAE/ASEE Joint Propulsion Conference and Exhibit, July 6-9, Seattle, WA, AIAA Paper 97-3131, 1997.

[135] H.F.R. Schöyer, A.J. Schnorhk, P.A.O.G. Korting, P.J. van Lit, J.M. Mul, G.M.H.J.L. Gadiot, and J.J. Meulenbrugge. Development of hydrazinium nitroformate based solid propellants. 31st AIAA/ASME/SAE/ASEE Joint Propulsion Conference and Exhibit, July 10-12, San Diego, CA, AIAA Paper 95-2864, 1995.

[136] H.F.R. Schöyer, A.J. Schnorhk, P.A.O.G. Korting, P.J. van Lit, J.M. Mul, G.M.H.J.L. Gadiot, and J.J. Meulenbrugge. High Performance Propellants based on Hydrazinium Nitroformate. *Journal of Propulsion and Power*, 11:856, 1995.

[137] H.F.R. Schöyer, W.H.M. Veltmans, J. Louwers, A.E.D.M. van der Heijden, H.L.J. Keizers, and R.P. van den Berg. An overview of the development of HNF-based propellants. 36th AIAA/ASME/SAE/ASEE Joint Propulsion Conference and Exhibit, 16-19 July, Huntsville, AL, AIAA Paper 2000-3184, 2000.

[138] M.A. Schroeder. Possible chemical mechanisms for boron hydride acceleration of nitramine decomposition: Literature review. *Journal of Propulsion and Power*, 14(6):981–990, 1998.

[139] J.M. Seitzman and R.K. Hanson. *Planar Fluorescence Imaging in Gases, In: Instrumentation for Flows with Combustion, ed. by A.M.K.P. Taylor.* Academic Press Ltd., London, 1993.

[140] V.N. Simonenko and V.E. Zarko. Comparative studying the combustion behavior of composite propellants containing ultra fine aluminum. In *30th International Annual Conference of ICT*, pages 21–1 – 21–14, Karlsruhe, Federal Republic of Germany, June 29-July 2 1999.

[141] V.I. Slovetskii, S.A. Shevelev, A.A. Finzil'berg, and S.S. Novikov. Photospectroscopy of nitromethanes. *Mendeleeva*, 6:707–708, 1961.

[142] S.F. Son and M.Q. Brewster. Radiation-Augmented Combustion of Homogeneous Solids. *Combustion Science and Technology*, 107(1-3):127–154, 1995.

[143] R.G. Stacer and D.M. Husband. Molecular Structure of the Ideal Solid Propellant Binder. *Propellants, Explosives, Pyrotechnics*, 16:167, 1991.

[144] J.P. Stewart. MOPAC Manual (Seventh Edition). Technical report, U.S. Air Force Academy, Colorado Springs, 1993.

[145] R.C. Strittmater, H.E. Holmes, and L.A. Watermeier. Lead Loss Problem for a Thermocouple Imbedded in a Burning Propellant. *Journal of Spacecrafts and Rockets*, 3:1302–1303, 1966.

[146] P. Stroomer. Turbulence and OH Structures in Flames. Ph.D. Thesis, Delft University of Technology, 1995.

[147] G.P. Sutton. *Rocket Propulsion Elements: An Introduction to the Engineering of Rockets, sixth edition.* John Wiley & Sons, Inc. New York, 1992.

[148] J.R. Thornton. Salts of nitroform with hydrazines. Technical Report 3,297,747, United States Patent, 1967.

[149] H.D. Tietz. *Ultraschall-Messtechnik.* VEB Verlag Technik, Berlin, 1969.

[150] J.C. Traineau and P. Kuentzmann. Some Measurements of Solid Propellant Burning Rates in Nozzleless Motors. AIAA Paper 84-1469, 1984.

[151] A.G. Turner and L.P. Davis. Decomposition pathways leading to hono for nitroalkenes. *Journal of Energetic Materials*, 2:190–203, 1984.

[152] United Nations. Recommandations on the transport of dangerous goods: Manual of tests and criteria (second revised edition). UN, New York and Geneva, 1995.

[153] W.H.M. Veltmans. Preparation for industrialisation of HNF based advanced solid composite propellant, GSTP-1. Technical Report NP GE SR 00 01 028 (2), APP 1997-019, Aerospace Propulsion Products, 1997.

[154] W.H.M. Veltmans, M.J. Rodgers, A.E.D. van der Heijden, and R.M. Geertman. Improvement of Hydrazinium Nitroformate Product Characteristics. In *30th International Annual Conference of ICT*, pages 55–1 – 55–14, Karlsruhe, Federal Republic of Germany, June 29-July 2 1999.

[155] M. Versluis, A.J. Landman, T.W.J. Peeters, Th. H. van der Meer, D.J.E.M. Roekaerts, J. Louwers, and G.M.H.J.L. Gadiot. Decomposition and Combustion of Hydrazinium Nitroformate (HNF) and HNF-based propellants. Technical Report Progress meeting 3, Delft University of Technology, 17 November 1998. Reported to the Technology Foundation STW, CONFIDENTIAL.

[156] M. Versluis, A.J. Landman, Th. H. van der Meer, D.J.E.M. Roekaerts, J. Louwers, and G.M.H.J.L. Gadiot. Decomposition and Combustion of Hydrazinium Nitroformate (HNF) and HNF-based propellants. Technical Report Progress meeting 2, Delft University of Technology, 14 May 1998. Reported to the Technology Foundation STW, CONFIDENTIAL.

[157] M.J. Ward, S.F. Son, and M.Q. Brewster. Steady Deflagration of HMX with Simple Kinetics: A Gas Phase Chain Reaction Model. *Combustion and Flame*, 114:556–568, 1998.

[158] J. Warnsatz, U. Maas, and R.W. Dibble. *Combustion: Physical and Chemical Fundamentals, Modeling and Simulation, Experiments, Pollutant Formation, 2nd edition.* Springer Verlag, Berlin, 1999.

[159] V. Weiser, N. Eisenreich, A. Baier, and W. Eckl. Burning behavior of ADN formulations. *Propellants, Explosives, Pyrotechnics*, 24:163–167, 1999.

[160] F. Wierckx. HNF General Data Sheet. Technical Report APP 1995-015(4), Aerospace Propulsion Products, 1998.

[161] F.A. Williams. Quasi-Steady, Gas-Phase Flame Theory in Unsteady Burning of a Homogeneous Solid Propellant. *AIAA Journal*, 11:1328–1330, 1973.

[162] F.A. Williams. *Combustion Theory, 2nd edition.* The Benjamin/Cummings Publishing Company, Inc., Menlo Park, CA, 1985.

[163] G.K. Williams and T.B. Brill. Thermal Decomposition of Energetic Materials 67. Hydrazinium Nitroformate (HNF) Rates and Pathways under Combustionlike Conditions. *Combustion and Flame*, 102:418–426, 1995.

[164] Working group 27. Evaluation of Methods for Solid Propellant Burning Rate Measurement, Chapter 5: Non-Intrusive Measurement Techniques. Applied Vehicle Technology Panel, NATO-RTO, 1998.

[165] R.A. Yetter, F.L. Dryer, M.T. Allen, and J.L. Gato. Development of Gas-Phase Reaction Mechanisms for Nitramine Combustion. *Journal of Propulsion and Power*, 11:683–697, 1995.

[166] M.A Zebrowski and M.Q. Brewster. Theory of Unsteady Combustion of Solids: Investigation of Quasisteady Assumption. *Journal of Propulsion and Power*, 12:564–573, 1995.

[167] F.W.M. Zee, J.M. Mul, and A.C. Hordijk. Method of preparing hydrazine nitroform. Technical Report C06B47/08, C01B21/16, International Patent, 1994.

[168] Ya.B. Zeldovich. Chain Reactions in Hot Flames - an Approximate Theory of Flame Velocities. *Kinetika i Kataliz*, 2:305–318, 1961.

[169] M. van Zelst. Study note on improvement of HNF stability. Technical Report Technical Report APP/1999018 NP HNF TN 00 02 032 (1/0), Aerospace Propulsion Products, 1999. COMPANY CONFIDENTIAL.

[170] M. van Zelst and N. Wingborg. Comperative study of the properties of ADN and HNF. Technical Report Technical Report PML 1999-A79, TNO Prins Maurits Laboratory / Swedish Defence Research Establishment, 1999. COMPANY CONFIDENTIAL.

Appendix A

Solution of the PREMIX equations

This Appendix summarizes the solution method of the PREMIX equations of section 6.3.

Finite difference schemes

To solve the governing conservation equations, the equations are approximated by finite differences on a nonuniform grid. Let j denote the grid point, with $j = 1 \ldots J$, where $j = 1$ at the cold boundary, and $j = J$ at the hot boundary. The convective terms are approximated by forward differences, e.g.

$$\left(\dot{m}\frac{dT}{dx}\right)_j \simeq \dot{m}_j \frac{T_j - T_{j-1}}{x_j - x_{j-1}} \,. \tag{A.1}$$

In the energy Eq's. (6.25), (6.28) and (6.31), the first derivative is approximated by a central difference formula

$$\left(\frac{dT}{dx}\right)_j \simeq \left(\frac{h_{j-1}}{h_j(h_j + h_{j-1})}T_{j+1} + \frac{h_j - h_{j-1}}{h_j h_{j-1}}T_j - \frac{h_j}{h_{j-1}(h_j + h_{j-1})}T_{j-1}\right), \tag{A.2}$$

where $h_j = x_{j+1} - x_j$. The second derivative term in the energy equation is approximated by the following second order central difference formula

$$\begin{aligned}\frac{d}{dx}\left(\lambda A\frac{dT}{dx}\right)_j \simeq & \left(\frac{2}{x_{j+1} - x_{j-1}}\right) \times \\ & \left[\lambda A_{j+\frac{1}{2}}\frac{T_{j+1} - T_j}{x_{j+1} - x_j} - \lambda A_{j-\frac{1}{2}}\frac{T_j - T_{j-1}}{x_j - x_{j-1}}\right] ,\end{aligned} \tag{A.3}$$

For the finite difference approximation of the boundary conditions is referred to Ref.[66].

Solution method

Due to the wide variety of time and length scales associated with chemical reactions and transport processes, the set of differential equations is stiff, and needs careful numerical treatment. After discretization on a given mesh, a system of nonlinear algebraic equations

has to be solved. Similar to the PREMIX model, this is carried out by a damped Newton's method [66].

Assume that the (approximate) solution is given by the vector ϕ. When an arbitrary ϕ is substituted into the finite difference approximations of the conservation equations, there is generally a residual vector F. The solution of the problem is found when $F(\phi) = 0$. In the computer program ϕ is organized as follows

$$\phi = (T_1, Y_{1,1}, \ldots, Y_{1,K}, \dot{m}_1, \ldots\ldots, T_J, Y_{J,1}, \ldots, Y_{J,K}, \dot{m}_J)^T , \tag{A.4}$$

so ϕ has $(K+2)J$ elements.

Given the initial estimate ϕ^0 of the solution, Newton's method produces a sequence of solutions $\phi^1, \phi^2, \ldots, \phi^n, \phi^{n+1}, \ldots$, that converges to the solution ϕ. Newton's method is described by the following algorithm

$$\phi^{n+1} = \phi^n - F(\phi^n) \left(\frac{\partial F}{\partial \phi} \right)^{-1}_{\phi^n} . \tag{A.5}$$

Straightforward application of this method is impossible, as evaluation of the Jacobian matrices $\partial F / \partial \phi$ is time consuming, and a very good estimate ϕ^0 is necessary for convergence. At each iteration cycle, either the previous Jacobian matrix $\mathcal{J}^n = \mathcal{J}^{n-1}$ is used, or a new one is calculated $\mathcal{J}^n = (\partial F / \partial \phi)_{\phi^n}$. Furthermore, the solution is only partially adjusted by introducing the damping parameter λ^n $(0 < \lambda^n \leq 1)$

$$\phi^{n+1} = \phi^n - \lambda^n F(\phi^n) \, (\mathcal{J}^n)^{-1} . \tag{A.6}$$

For more information on the determination of λ^n and $\mathcal{J}^n$ is referred to Ref.[66].

If the initial estimates are not close to the actual solution, in many situations the Newton's method does not converge. By introducing the time derivatives into the conservation equations, it is possible to *time-step* from one estimated solution to another solution. Whenever it is impossible to obtain a following approximate solution ϕ^{n+1} by Newton's method, the program resorts to time-stepping to obtain an intermediate solution.

As the solid-liquid interface normally does not coincide with a mesh point and the precise location is changing during the iteration procedure, it is possible to accumulate energy between the grid points on both sides of this interface. So, during time-stepping the solid-liquid interface energy conservation equation (Eq.(6.37)), is modified by an energy accumulation term because it has a finite volume. For a control volume V with internal energy e this term is given by [85]

$$\frac{d}{dt} \iiint_V \rho e dv \simeq \frac{d}{dt} (\rho A H \Delta x) , \tag{A.7}$$

where Δx is the distance between the mesh points next to the phase transition surface. As the liquid-gas interface is always located *at* a mesh point, $\Delta x = 0$, hence the accumulation term is zero at the liquid-gas interface.

The solution of the equations is carried out by the TWOPNT computer program, which is an implementation of the hybrid numerical solution algorithm as discussed above [55].

Automatic grid refinement

The TWOPNT program is capable of automatic grid refinement. This grid refinement is carried out for two reasons:

1. To obtain a better approximation of the solution of the set of differential equations to be solved.

2. To improve solution efficiency. As the approximations improve from grid to grid, solving of the equations becomes easier.

TWOPNT uses two criterions to determine whether grid refinement is necessary. The first one is equidistribution of the *variation* of each variable between two grid points (x_{n-1} and x_n). Let X be one of the variables T or Y_k, then the maximum variation constraint is given by

$$\int_{x_{n-1}}^{x_n} \left| \frac{dX}{dx} \right| dx \;=\; \zeta \left| \max X^* - \min X^* \right| \;, \tag{A.8}$$

where $\max X^*$ and $\min X^*$ denote the maximum and the minimum value of X at the computational interval, based on the *previous* converged solution. The grid refinement is adjusted by selecting a proper value of ζ, $0 < \zeta < 1$. If the above constraint is not met at the interval (x_{n-1}, x_n), then a new grid point is introduced in the middle of this interval.

TWOPNT's second criterion is that of the maximum variation of dX/dx and is given by

$$\int_{x_{n-1}}^{x_n} \left| \frac{d^2X}{dx^2} \right| dx \;=\; \eta \left| \max \frac{dX^*}{dx} - \min \frac{dX^*}{dx} \right| \;, \tag{A.9}$$

where also $0 < \eta < 1$. Typical values for ζ and η are 0.2 and 0.5 respectively.

Appendix B

Flame chemistry

In this appendix the chemical mechanisms for the PREMIX and BIGMIX models is detailed. Section B.1 contains a modified version of Yetter's model for the combustion modeling of neat HNF [165]. Section B.2 contains the additional reactions (obtained from the GRI-mech [16]) that were used for HNF-mixtures and HNF-sandwiches.

B.1 HNF flame chemistry

Nr.	Reaction	A [s^{-1}]	n [$-$]	E [cal $mole^{-1}$]
1.	$H_2+M \rightleftharpoons H+H+M$	4.57E+19	-1.4	104000.0
	H_2 Enhanced by 2.500E+00			
	H_2O Enhanced by 1.200E+01			
	CO Enhanced by 1.900E+00			
	CO_2 Enhanced by 3.800E+00			
2.	$O+H_2O \rightleftharpoons OH+OH$	2.95E+06	2.0	13400.0
3.	$O+H_2 \rightleftharpoons H+OH$	5.08E+04	2.7	6290.0
4.	$O+O+M \rightleftharpoons O_2+M$	6.17E+15	0.5	0.0
	H_2 Enhanced by 2.500E+00			
	H_2O Enhanced by 1.200E+01			
	CO Enhanced by 1.900E+00			
	CO_2 Enhanced by 3.800E+00			
5.	$H+O_2 \rightleftharpoons O+OH$	3.52E+16	0.7	17070.0
6.	$H+O_2(+M) \rightleftharpoons HO_2(+M)$	4.52E+13	0.0	0.0
	Low pressure limit:	0.67500E-06	0.14200E-01	0.00000E+00
	H_2 Enhanced by 2.500E+00			
	H_2O Enhanced by 1.200E+01			
	CO Enhanced by 1.900E+00			
	CO_2 Enhanced by 3.800E+00			
7.	$H+O+M \rightleftharpoons OH+M$	4.72E+18	1.0	0.0
	H_2 Enhanced by 2.500E+00			
	H_2O Enhanced by 1.200E+01			

Nr.	Reaction	A [s^{-1}]	n [−]	E [cal $mole^{-1}$]
	CO Enhanced by 1.900E+00			
	CO_2 Enhanced by 3.800E+00			
8.	$OH+H_2 \rightleftharpoons H_2O+H$	2.16E+08	1.5	3430.0
9.	$OH+H+M \rightleftharpoons H_2O+M$	2.21E+22	2.0	0.0
	H_2 Enhanced by 2.500E+00			
	H_2O Enhanced by 1.200E+01			
	CO Enhanced by 1.900E+00			
	CO_2 Enhanced by 3.800E+00			
10.	$HO_2+O \rightleftharpoons O_2+OH$	1.75E+13	0.0	-397.0
11.	$HO_2+H \rightleftharpoons H_2+O_2$	6.62E+13	0.0	2130.0
12.	$HO_2+H \rightleftharpoons OH+OH$	1.69E+14	0.0	874.0
13.	$HO_2+OH \rightleftharpoons H_2O+O_2$	1.90E+16	1.0	0.0
14.	$HO_2+HO_2 \rightleftharpoons H_2O_2+O_2$	4.20E+14	0.0	11980.0
15.	$H_2O_2(+M) \rightleftharpoons OH+OH(+M)$	3.00E+14	0.0	48460.0
	Low pressure limit:	0.25000E-02	0.00000E00	0.29600E+04
16.	$H_2O_2+O \rightleftharpoons OH+HO_2$	9.64E+06	2.0	3970.0
17.	$H_2O_2+H \rightleftharpoons H_2O+OH$	1.00E+13	0.0	3590.0
18.	$H_2O_2+H \rightleftharpoons HO_2+H_2$	4.82E+13	0.0	7950.0
19.	$H_2O_2+OH \rightleftharpoons H_2O+HO_2$	5.80E+14	0.0	9557.0
20.	$CH_2O+M \rightleftharpoons HCO+H+M$	1.63E+33	4.1	92550.0
21.	$CH_2O+M \rightleftharpoons H_2+CO+M$	8.25E+15	0.0	69540.0
22.	$CH_2O+O_2 \rightleftharpoons HCO+HO_2$	2.05E+13	0.0	38920.0
23.	$CH_2O+O \rightleftharpoons HCO+OH$	1.81E+13	0.0	3078.0
24.	$CH_2O+H \rightleftharpoons HCO+H_2$	7.94E+07	1.7	2000.0
25.	$CH_2O+OH \rightleftharpoons HCO+H_2O$	3.43E+09	1.2	-447.0
26.	$CH_2O+HO_2 \rightleftharpoons HCO+H_2O_2$	1.99E+12	0.0	11660.0
27.	$HCO+M \rightleftharpoons H+CO+M$	1.86E+17	1.0	17000.0
	H_2 Enhanced by 1.890E+00			
	H_2O Enhanced by 1.200E+01			
	CO Enhanced by 1.900E+00			
	CO_2 Enhanced by 3.800E+00			
28.	$HCO+O_2 \rightleftharpoons CO+HO_2$	7.58E+12	0.0	410.0
29.	$HCO+O \rightleftharpoons CO+OH$	3.00E+13	0.0	0.0
30.	$HCO+O \rightleftharpoons CO_2+H$	3.00E+13	0.0	0.0
31.	$HCO+H \rightleftharpoons CO+H_2$	7.23E+13	0.0	0.0
32.	$HCO+OH \rightleftharpoons CO+H_2O$	3.00E+13	0.0	0.0
33.	$HCO+HO_2 \rightleftharpoons CO_2+OH+H$	3.00E+13	0.0	0.0
34.	$CO+O+M \rightleftharpoons CO_2+M$	2.51E+13	0.0	-4540.0
	H_2 Enhanced by 2.500E+00			
	H_2O Enhanced by 1.200E+01			
	CO Enhanced by 1.900E+00			
	CO_2 Enhanced by 3.800E+00			
35.	$CO+O_2 \rightleftharpoons CO_2+O$	2.53E+12	0.0	47700.0
36.	$CO+OH \rightleftharpoons CO_2+H$	1.50E+07	1.3	-765.0

Nr.	Reaction	A [s^{-1}]	n [−]	E [cal $mole^{-1}$]
37.	$CO+HO_2 \rightleftharpoons CO_2+OH$	6.03E+13	0.0	23000.0
38.	$N+H_2 \rightleftharpoons H+NH$	1.60E+14	0.0	25140.0
39.	$N+O_2 \rightleftharpoons NO+O$	6.40E+09	1.0	6280.0
40.	$N+OH \rightleftharpoons NO+H$	3.80E+13	0.0	0.0
41.	$N+HO_2 \rightleftharpoons NH+O_2$	1.00E+13	0.0	2000.0
42.	$N+HO_2 \rightleftharpoons NO+OH$	1.00E+13	0.0	2000.0
43.	$N+CO_2 \rightleftharpoons NO+CO$	1.90E+11	0.0	3400.0
44.	$N+NO \rightleftharpoons N_2+O$	3.27E+12	0.3	0.0
45.	$N+NO_2 \rightleftharpoons NO+NO$	4.00E+12	0.0	0.0
46.	$N+NO_2 \rightleftharpoons N_2O+O$	5.00E+12	0.0	0.0
47.	$N+NO_2 \rightleftharpoons N_2+O_2$	1.00E+12	0.0	0.0
48.	$N+HNO \rightleftharpoons NH+NO$	1.00E+13	0.0	2000.0
49.	$N+HNO \rightleftharpoons N_2O+H$	5.00E+10	0.5	3000.0
50.	$N+N_2O \rightleftharpoons N_2+NO$	1.00E+13	0.0	19870.0
51.	$NO+M \rightleftharpoons N+O+M$	9.64E+14	0.0	148400.0
	N_2 Enhanced by 1.500E+00			
	CO_2 Enhanced by 1.000E+01			
52.	$NO+H_2 \rightleftharpoons HNO+H$	1.39E+13	0.0	56530.0
53.	$NO+O(+M) \rightleftharpoons NO_2(+M)$	1.30E+15	0.8	0.0
	Low pressure limit:	0.27500E-09	0.21200E+01	-0.15510E+04
54.	$NO+H(+M) \rightleftharpoons HNO(+M)$	1.52E+15	0.4	0.0
	Low pressure limit:	0.17000E-04	0.91000E+00	-0.73520E+03
55.	$NO+OH(+M) \rightleftharpoons HONO(+M)$	1.99E+12	0.1	-721.0
	Low pressure limit:	0.39200E-11	0.24600E+01	-0.65300E+03
	H_2O Enhanced by 5.000E+00			
56.	$NO+HCO \rightleftharpoons HNO+CO$	1.40E+13	0.0	0.0
57.	$NO_2+O \rightleftharpoons O_2+NO$	1.00E+13	0.0	600.0
58.	$NO_2+O(+M) \rightleftharpoons NO3(+M)$	1.33E+13	0.0	0.0
	Low pressure limit:	0.89300E-15	0.40800E+01	-0.24670E+04
59.	$NO_2+H \rightleftharpoons NO+OH$	1.32E+14	0.0	361.6
60.	$NO_2+OH(+M) \rightleftharpoons HNO3(+M)$	2.41E+13	0.0	0.0
	Low pressure limit:	0.37500E-19	0.54900E+01	-0.23500E+04
61.	$HO_2+NO \rightleftharpoons NO_2+OH$	2.11E+12	0.0	-479.0
62.	$NO_2+CH_2O \rightleftharpoons HONO+HCO$	7.83E+02	2.8	13730.0
63.	$NO_2+HCO \rightleftharpoons CO+HONO$	1.24E+23	3.3	2354.0
64.	$NO_2+HCO \rightleftharpoons H+CO_2+NO$	8.39E+15	0.8	1927.0
65.	$NO_2+CO \rightleftharpoons CO_2+NO$	9.03E+13	0.0	33780.0
66.	$NO_2+NO_2 \rightleftharpoons NO3+NO$	9.64E+09	0.7	20920.0
67.	$NO_2+NO_2 \rightleftharpoons 2NO+O_2$	1.63E+12	0.0	26120.0
68.	$NH+M \rightleftharpoons N+H+M$	2.65E+14	0.0	75510.0
69.	$NH+O_2 \rightleftharpoons HNO+O$	3.89E+13	0.0	17890.0
70.	$NH+O_2 \rightleftharpoons NO+OH$	7.60E+10	0.0	1530.0
71.	$NH+O \rightleftharpoons NO+H$	5.50E+13	0.0	0.0
72.	$NH+O \rightleftharpoons N+OH$	3.72E+13	0.0	0.0

Nr.	Reaction	A [s^{-1}]	n [−]	E [cal $mole^{-1}$]
73.	NH+OH⇌HNO+H	2.00E+13	0.0	0.0
74.	NH+OH⇌N+H_2O	5.00E+11	0.5	2000.0
75.	NH+N⇌N_2+H	3.00E+13	0.0	0.0
76.	NH+NO⇌N_2O+H	2.94E+14	-0.4	0.0
77.	NH+NO⇌N_2+OH	2.16E+13	-0.2	0.0
78.	NH+NO_2⇌NO+HNO	1.00E+11	0.5	4000.0
79.	NH+NO_2⇌N_2O+OH	1.00E+13	0.0	0.0
80.	NH+NH⇌N_2+H+H	5.10E+13	0.0	0.0
81.	NH_2+O_2⇌HNO+OH	1.78E+12	0.0	14900.0
82.	NH_2+O⇌HNO+H	6.63E+14	-0.5	0.0
83.	NH_2+O⇌NH+OH	6.75E+12	0.0	0.0
84.	NH_2+H⇌NH+H_2	6.92E+13	0.0	3650.0
85.	NH_2+OH⇌NH+H_2O	4.00E+06	2.0	1000.0
86.	NH_2+N⇌N_2+2H	7.20E+13	0.0	0.0
87.	NH_2+NO⇌NNH+OH	2.80E+13	-0.6	0.0
88.	NH_2+NO⇌N_2+H_2O	8.82E+15	-1.3	0.0
89.	NH_2+NO⇌N_2O+H_2	5.00E+13	0.0	24640.0
90.	NH_2+NO⇌HNO+NH	1.00E+13	0.0	40000.0
91.	NH_2+NO_2⇌N_2O+H_2O	3.28E+18	-2.2	0.0
92.	NH_3+M⇌NH_2+H+M	2.20E+16	0.0	93470.0
93.	NH_3+O⇌NH_2+OH	9.40E+06	1.9	6460.0
94.	NH_3+H⇌NH_2+H_2	6.40E+05	2.4	10170.0
95.	NH_3+OH⇌NH_2+H_2O	2.04E+06	2.0	566.0
96.	NH_3+HO_2⇌NH_2+H_2O_2	3.00E+11	0.0	22000.0
97.	NH_2+HO_2⇌NH_3+O_2	1.00E+13	0.0	0.0
98.	NH_2+NH_2⇌NH_3+NH	5.00E+13	0.0	10000.0
99.	NNH+M⇌N_2+H+M	1.00E+14	0.0	3000.0
100.	NNH+H⇌N_2+H_2	1.00E+14	0.0	0.0
101.	NNH+NO⇌N_2+HNO	5.00E+13	0.0	0.0
102.	NNH+O⇌N_2O+H	1.00E+14	0.0	0.0
103.	NNH+OH⇌N_2+H_2O	5.00E+13	0.0	0.0
104.	NNH+NH⇌N_2+NH_2	5.00E+13	0.0	0.0
105.	NNH+NH_2⇌N_2+NH_3	5.00E+13	0.0	0.0
106.	HNO+O⇌OH+NO	1.81E+13	0.0	0.0
107.	HNO+OH⇌H_2O+NO	1.00E+13	0.0	993.5
108.	HNO+HCO⇌CH_2O+NO	6.02E+11	0.0	1987.0
109.	HNO+NO⇌N_2O+OH	2.00E+12	0.0	26000.0
110.	HNO+NO_2⇌HONO+NO	6.02E+11	0.0	1987.0
111.	HNO+HNO⇌H_2O+N_2O	8.51E+08	0.0	3080.0
112.	HNO+O_2⇌NO+HO_2	1.00E+13	0.0	25000.0
113.	HNO+NH_2⇌NO+NH_3	2.00E+13	0.0	1000.0
114.	HONO+O⇌OH+NO_2	1.20E+13	0.0	5961.0
115.	HONO+H⇌H_2+NO_2	1.20E+13	0.0	7352.0
116.	HONO+OH⇌H_2O+NO_2	1.26E+10	1.0	135.1

Nr.	Reaction	A [s^{-1}]	n [−]	E [cal mole^{-1}]
117.	HCN(+M)⇌H+CN(+M)	8.30E+17	-0.9	123800.0
	Low pressure limit:	0.23200E-08	0.16700E+01	-0.11000E+04
118.	HCN+O⇌CN+OH	2.70E+09	1.6	29200.0
119.	HCN+O⇌NH+CO	3.45E+03	2.6	4980.0
120.	HCN+O⇌NCO+H	1.38E+04	2.6	4980.0
121.	HCN+OH⇌H_2O+CN	3.90E+06	1.8	10290.0
122.	HCN+OH⇌H+HOCN	5.85E+04	2.4	12500.0
123.	HCN+OH⇌H+HNCO	1.98E-03	4.0	1000.0
124.	HCN+OH⇌NH_2+CO	7.83E-04	4.0	4000.0
125.	HCN⇌HNC	2.06E+14	-1.1	43710.0
126.	HNC+O⇌NH+CO	2.89E+12	0.0	0.0
127.	HNC+O⇌H+NCO	1.60E+01	3.1	-224.0
128.	HNC+OH⇌HNCO+H	2.80E+13	0.0	3700.0
129.	HNC+OH⇌CN+H_2O	1.50E+12	0.0	7680.0
130.	HNC+NO_2⇌HNCO+NO	1.00E+12	0.0	32000.0
131.	HNC+CN⇌C_2N_2+H	1.00E+13	0.0	0.0
132.	N_2O(+M)⇌N_2+O(+M)	7.91E+10	0.0	56040.0
	Low pressure limit:	0.90000E-04	0.00000E+00	-0.15100E+04
	H_2O Enhanced by 7.500E+00			
	NO Enhanced by 2.000E+00			
	CO Enhanced by 2.000E+00			
	CO_2 Enhanced by 3.000E+00			
	HCN Enhanced by 3.000E+00			
133.	N_2O+O⇌O_2+N_2	1.00E+14	0.0	28000.0
134.	N_2O+O⇌2NO	1.00E+14	0.0	28000.0
135.	N_2O+H⇌N_2+OH	2.23E+14	0.0	16750.0
136.	N_2O+OH⇌HO_2+N_2	2.00E+12	0.0	40000.0
137.	N_2O+CO⇌N_2+CO_2	3.19E+11	0.0	20330.0
138.	CN+H_2⇌H+HCN	5.50E+02	3.2	-223.0
139.	CN+O_2⇌NCO+O	7.50E+12	0.0	-389.0
140.	CN+O⇌CO+N	1.80E+13	0.0	0.0
141.	CN+OH⇌NCO+H	4.00E+13	0.0	0.0
142.	CN+OH⇌NH+CO	0.00E+00	0.0	0.0
143.	CN+OH⇌HNCO	0.00E+00	0.0	0.0
144.	CN+CH_2O⇌HCN+HCO	4.22E+13	0.0	0.0
145.	CN+HCO⇌HCN+CO	6.02E+13	0.0	0.0
146.	CN+NO⇌NCO+N	9.64E+13	0.0	42120.0
147.	CN+CO_2⇌CO+NCO	3.67E+06	2.2	26900.0
148.	CN+NO_2⇌NCO+NO	1.59E+13	0.0	-1133.0
149.	CN+HNO⇌HCN+NO	1.81E+13	0.0	0.0
150.	CN+HONO⇌HCN+NO_2	1.20E+13	0.0	0.0
151.	CN+HCN⇌H+C_2N_2	1.21E+07	1.7	1530.0
152.	CN+N_2O⇌NCN+NO	3.85E+03	2.6	3696.0
153.	CN+CN(+M)⇌C_2N_2(+M)	5.66E+12	0.0	0.0

Nr.	Reaction	A [s^{-1}]	n [−]	E [cal $mole^{-1}$]
	Low pressure limit:	0.16500E-12	0.26100E+01	0.00000E+00
154.	C_2N_2+O⇌NCO+CN	4.57E+12	0.0	8880.0
155.	C_2N_2+OH⇌HOCN+CN	1.86E+11	0.0	2900.0
156.	NCN+H⇌HCN+N	1.00E+14	0.0	0.0
157.	NCN+O⇌CN+NO	1.00E+14	0.0	0.0
158.	NCN+OH⇌HCN+NO	5.00E+13	0.0	0.0
159.	NCN+O_2⇌NO+NCO	1.00E+14	0.0	0.0
160.	NCO+M⇌N+CO+M	3.10E+16	-0.5	48300.0
	N_2 Enhanced by 1.500E+00			
161.	NCO+H_2⇌HNCO+H	7.60E+02	3.0	4000.0
162.	NCO+O⇌CO+NO	2.00E+13	0.0	0.0
163.	NCO+H⇌NH+CO	5.00E+13	0.0	0.0
164.	NCO+OH⇌NO+CO+H	1.00E+13	0.0	0.0
165.	NCO+OH⇌NO+HCO	5.00E+12	0.0	15000.0
166.	NCO+O_2⇌NO+CO_2	2.00E+12	0.0	20000.0
167.	NCO+CH_2O⇌HNCO+HCO	6.02E+12	0.0	0.0
168.	NCO+HCO⇌HNCO+CO	3.61E+13	0.0	0.0
169.	NCO+NO⇌N_2O+CO	6.20E+17	-1.7	763.0
170.	NCO+NO⇌CO_2+N_2	7.80E+17	-1.7	763.0
171.	NCO+NO_2⇌CO+2NO	1.39E+13	0.0	0.0
172.	NCO+NO_2⇌CO_2+N_2O	4.17E+12	0.0	0.0
173.	NCO+HNO⇌HNCO+NO	1.81E+13	0.0	0.0
174.	NCO+HONO⇌HNCO+NO_2	3.61E+12	0.0	0.0
175.	NCO+N_2O⇌N_2+NO+CO	9.03E+13	0.0	27820.0
176.	NCO+CN⇌NCN+CO	1.81E+13	0.0	0.0
177.	NCO+NCO⇌N_2+2CO	1.00E+13	0.0	0.0
178.	NCO+N⇌N_2+CO	2.00E+13	0.0	0.0
179.	CNO+O⇌CO+NO	1.00E+13	0.0	0.0
180.	CNO+NO_2⇌CO+2NO	1.00E+13	0.0	0.0
181.	CNO+N_2O⇌N_2+CO+NO	1.00E+12	0.0	15000.0
182.	HNCO(+M)⇌NH+CO(+M)	6.00E+13	0.0	99800.0
	Low pressure limit:	0.27600E-14	0.31000E+01	-0.21000E+04
183.	HNCO+O⇌CO_2+NH	9.64E+07	1.4	8524.0
184.	HNCO+O⇌OH+NCO	6.67E-04	4.5	1780.0
185.	HNCO+O⇌HNO+CO	1.58E+08	1.6	44300.0
186.	HNCO+H⇌NH_2+CO	2.20E+07	1.7	3800.0
187.	HNCO+OH⇌H_2O+NCO	6.38E+05	2.0	2563.0
188.	HNCO+CN⇌HCN+NCO	1.51E+13	0.0	0.0
189.	HNCO+HO_2⇌NCO+H_2O_2	3.00E+11	0.0	29000.0
190.	HNCO+O_2⇌HNO+CO_2	1.00E+12	0.0	35000.0
191.	HNCO+NH_2⇌NH_3+NCO	5.00E+12	0.0	6200.0
192.	HNCO+NH⇌NH_2+NCO	3.00E+13	0.0	23700.0
193.	HCNO+O⇌HCO+NO	1.00E+12	0.0	9000.0
194.	HCNO+OH⇌HCO+HNO	1.00E+13	0.0	5000.0

Nr.	Reaction	A [s^{-1}]	n [−]	E [cal $mole^{-1}$]
195.	HCNO+OH⇌CNO+H_2O	1.00E+12	0.0	2000.0
196.	HCNO+CN⇌HCN+CNO	1.00E+12	0.0	2000.0
197.	HOCN+H⇌HNCO+H	2.00E+07	2.0	2000.0
198.	HOCN+OH⇌NCO+H_2O	6.40E+05	2.0	2560.0
199.	HOCN+O⇌NCO+OH	1.50E+04	2.6	4000.0
200.	H_2CN+M⇌HCN+H+M	1.00E+17	0.0	30000.0
201.	H_2CN+NO⇌HCN+HNO	1.00E+11	0.0	3000.0
202.	H_2CN+NO_2⇌HCN+HONO	1.00E+11	0.0	1000.0
203.	N_2H_4⇌NH_2+NH_2	8.00E+13	0.0	55040.0
204.	2NYF⇌4NO_2+H_2O+N_2+CO+CO_2	1.00E+25	0.0	40000.0
205.	2HYNF⇌4NO+2CO+4H_2O+2N_2O+N_2+H_2	3.00E+13	0.0	35000.0
206.	2HYNF⇌4NO+2CO_2+4H_2O+3N_2+H_2	1.50E+15	0.0	45000.0
207.	N_2H_4+2NO_2 ⇌H_2O+NO+N_2	1.35E+16	0.0	26700.0
1.L	HYNF⇌N_2H_4+HONO+N_2O+O_2+CO	1.00E+12	0.0	25000.0
2.L	N_2H_4 ⇌NH_2+NH_2	8.00E+13	0.0	55040.0
3.L	N_2H_4+2NO_2 ⇌H_2O+NO+N_2	1.35E+16	0.0	26700.0

B.2 GRI-mech flame chemistry

Nr.	Reaction	A [s^{-1}]	n [−]	E [cal $mole^{-1}$]
208.	O+CH⇌H+CO	5.70E+13	0.0	0.0
209.	O+CH_2⇌H+HCO	8.00E+13	0.0	0.0
210.	O+CH_2(S)⇌H_2+CO	1.50E+13	0.0	0.0
211.	O+CH_2(S)⇌H+HCO	1.50E+13	0.0	0.0
212.	O+CH_3⇌H+CH_2O	8.43E+13	0.0	0.0
213.	O+CH_4⇌OH+CH_3	1.02E+09	1.5	8600.0
214.	O+CH_2OH⇌OH+CH_2O	1.00E+13	0.0	0.0
215.	O+CH_3O⇌OH+CH_2O	1.00E+13	0.0	0.0
216.	O+CH_3OH⇌OH+CH_2OH	3.88E+05	2.5	3100.0
217.	O+CH_3OH⇌OH+CH_3O	1.30E+05	2.5	5000.0
218.	O+C_2H⇌CH+CO	5.00E+13	0.0	0.0
219.	O+C_2H_2⇌H+HCCO	1.02E+07	2.0	1900.0
220.	O+C_2H_2⇌OH+C_2H	4.60E+19	-1.4	28950.0
221.	O+C_2H_2⇌CO+CH_2	1.02E+07	2.0	1900.0
222.	O+C_2H_3⇌H+CH_2CO	3.00E+13	0.0	0.0
223.	O+C_2H_4⇌CH_3+HCO	1.92E+07	1.8	220.0
224.	O+C_2H_5⇌CH_3+CH_2O	1.32E+14	0.0	0.0
225.	O+C_2H_6⇌OH+C_2H_5	8.98E+07	1.9	5690.0
226.	O+HCCO⇌H+2CO	1.00E+14	0.0	0.0
227.	O+CH_2CO⇌OH+HCCO	1.00E+13	0.0	8000.0

Nr.	Reaction	A [s^{-1}]	n [−]	E [cal $mole^{-1}$]
228.	$O+CH_2CO \rightleftharpoons CH_2+CO_2$	1.75E+12	0.0	1350.0
229.	$H+2O_2 \rightleftharpoons HO_2+O_2$	3.00E+20	-1.7	0.0
230.	$H+O_2+H_2O \rightleftharpoons HO_2+H_2O$	9.38E+18	-0.8	0.0
231.	$H+O_2+N2 \rightleftharpoons HO_2+N_2$	3.75E+20	-1.7	0.0
232.	$2H+H_2 \rightleftharpoons 2H_2$	9.00E+16	-0.6	0.0
233.	$2H+H_2O \rightleftharpoons H_2+H_2O$	6.00E+19	-1.2	0.0
234.	$2H+CO_2 \rightleftharpoons H_2+CO_2$	5.50E+20	-2.0	0.0
235.	$H+HO_2 \rightleftharpoons O+H_2O$	3.97E+12	0.0	671.0
236.	$H+CH \rightleftharpoons C+H_2$	1.10E+14	0.0	0.0
237.	$H+CH_2(+M) \rightleftharpoons CH_3(+M)$	2.50E+16	-0.8	0.0
	Low pressure limit:	0.32000E+28	-0.31400E+01	0.12300E+04
	H_2 Enhanced by 2.000E+00			
	H_2O Enhanced by 6.000E+00			
	CH_4 Enhanced by 2.000E+00			
	CO Enhanced by 1.500E+00			
	CO_2 Enhanced by 2.000E+00			
	C_2H_6 Enhanced by 3.000E+00			
238.	$H+CH_2(S) \rightleftharpoons CH+H_2$	3.00E+13	0.0	0.0
239.	$H+CH_3(+M) \rightleftharpoons CH_4(+M)$	1.27E+16	-0.6	383.0
	Low pressure limit:	0.24770E+34	-0.47600E+01	0.24400E+04
	H_2 Enhanced by 2.000E+00			
	H_2O Enhanced by 6.000E+00			
	CH_4 Enhanced by 2.000E+00			
	CO Enhanced by 1.500E+00			
	CO_2 Enhanced by 2.000E+00			
	C_2H_6 Enhanced by 3.000E+00			
240.	$H+CH_4 \rightleftharpoons CH_3+H_2$	6.60E+08	1.6	10840.0
241.	$H+HCO(+M) \rightleftharpoons CH_2O(+M)$	1.09E+12	0.5	-260.0
	Low pressure limit:	0.13500E+25	-0.25700E+01	0.14250E+04
	H_2 Enhanced by 2.000E+00			
	H_2O Enhanced by 6.000E+00			
	CH_4 Enhanced by 2.000E+00			
	CO Enhanced by 1.500E+00			
	CO_2 Enhanced by 2.000E+00			
	C_2H_6 Enhanced by 3.000E+00			
242.	$H+CH_2O(+M) \rightleftharpoons CH_2OH(+M)$	5.40E+11	0.5	3600.0
	Low pressure limit:	0.12700E+33	-0.48200E+01	0.65300E+04
	H_2 Enhanced by 2.000E+00			
	H_2O Enhanced by 6.000E+00			
	CH_4 Enhanced by 2.000E+00			
	CO Enhanced by 1.500E+00			
	CO_2 Enhanced by 2.000E+00			
	C_2H_6 Enhanced by 3.000E+00			
243.	$H+CH_2O(+M) \rightleftharpoons CH_3O(+M)$	5.40E+11	0.5	2600.0

Nr.	Reaction	A [s^{-1}]	n [−]	E [cal $mole^{-1}$]
	Low pressure limit:	0.22000E+31	-0.48000E+01	0.55600E+04
	H_2 Enhanced by 2.000E+00			
	H_2O Enhanced by 6.000E+00			
	CH_4 Enhanced by 2.000E+00			
	CO Enhanced by 1.500E+00			
	CO_2 Enhanced by 2.000E+00			
	C_2H_6 Enhanced by 3.000E+00			
244.	$H+CH_2OH(+M)\rightleftharpoons CH_3OH(+M)$	1.80E+13	0.0	0.0
	Low pressure limit:	0.30000E+32	-0.48000E+01	0.33000E+04
	H_2 Enhanced by 2.000E+00			
	H_2O Enhanced by 6.000E+00			
	CH_4 Enhanced by 2.000E+00			
	CO Enhanced by 1.500E+00			
	CO_2 Enhanced by 2.000E+00			
	C_2H_6 Enhanced by 3.000E+00			
245.	$H+CH_2OH\rightleftharpoons H_2+CH_2O$	2.00E+13	0.0	0.0
246.	$H+CH_2OH\rightleftharpoons OH+CH_3$	1.20E+13	0.0	0.0
247.	$H+CH_2OH\rightleftharpoons CH_2(S)+H_2O$	6.00E+12	0.0	0.0
248.	$H+CH_3O(+M)\rightleftharpoons CH_3OH(+M)$	5.00E+13	0.0	0.0
	Low pressure limit:	0.86000E+29	-0.40000E+01	0.30250E+04
	H_2 Enhanced by 2.000E+00			
	H_2O Enhanced by 6.000E+00			
	CH_4 Enhanced by 2.000E+00			
	CO Enhanced by 1.500E+00			
	CO_2 Enhanced by 2.000E+00			
	C_2H_6 Enhanced by 3.000E+00			
249.	$H+CH_3O\rightleftharpoons H+CH_2OH$	3.40E+06	1.6	0.0
250.	$H+CH_3O\rightleftharpoons H_2+CH_2O$	2.00E+13	0.0	0.0
251.	$H+CH_3O\rightleftharpoons OH+CH_3$	3.20E+13	0.0	0.0
252.	$H+CH_3O\rightleftharpoons CH_2(S)+H_2O$	1.60E+13	0.0	0.0
253.	$H+CH_3OH\rightleftharpoons CH_2OH+H_2$	1.70E+07	2.1	4870.0
254.	$H+CH_3OH\rightleftharpoons CH_3O+H_2$	4.20E+06	2.1	4870.0
255.	$H+C_2H(+M)\rightleftharpoons C_2H_2(+M)$	1.00E+17	-1.0	0.0
	Low pressure limit:	0.37500E+34	-0.48000E+01	0.19000E+04
	H_2 Enhanced by 2.000E+00			
	H_2O Enhanced by 6.000E+00			
	CH_4 Enhanced by 2.000E+00			
	CO Enhanced by 1.500E+00			
	CO_2 Enhanced by 2.000E+00			
	C_2H_6 Enhanced by 3.000E+00			
256.	$H+C_2H_2(+M)\rightleftharpoons C_2H_3(+M)$	5.60E+12	0.0	2400.0
	Low pressure limit:	0.38000E+41	-0.72700E+01	0.72200E+04
	H_2 Enhanced by 2.000E+00			
	H_2O Enhanced by 6.000E+00			

Nr.	Reaction	A [s^{-1}]	n [$-$]	E [cal mole^{-1}]
	CH_4 Enhanced by 2.000E+00			
	CO Enhanced by 1.500E+00			
	CO_2 Enhanced by 2.000E+00			
	C_2H_6 Enhanced by 3.000E+00			
257.	$H+C_2H_3(+M)\rightleftharpoons C_2H_4(+M)$	6.08E+12	0.3	280.0
	Low pressure limit:	0.14000E+31	-0.38600E+01	0.33200E+04
	H_2 Enhanced by 2.000E+00			
	H_2O Enhanced by 6.000E+00			
	CH_4 Enhanced by 2.000E+00			
	CO Enhanced by 1.500E+00			
	CO_2 Enhanced by 2.000E+00			
	C_2H_6 Enhanced by 3.000E+00			
258.	$H+C_2H_3\rightleftharpoons H_2+C_2H_2$	3.00E+13	0.0	0.0
259.	$H+C_2H_4(+M)\rightleftharpoons C_2H_5(+M)$	1.08E+12	0.5	1820.0
	Low pressure limit:	0.12000E+43	-0.76200E+01	0.69700E+04
	H_2 Enhanced by 2.000E+00			
	H_2O Enhanced by 6.000E+00			
	CH_4 Enhanced by 2.000E+00			
	CO Enhanced by 1.500E+00			
	CO_2 Enhanced by 2.000E+00			
	C_2H_6 Enhanced by 3.000E+00			
260.	$H+C_2H_4\rightleftharpoons C_2H_3+H_2$	1.32E+06	2.5	12240.0
261.	$H+C_2H_5(+M)\rightleftharpoons C_2H_6(+M)$	5.21E+17	-1.0	1580.0
	Low pressure limit:	0.19900E+42	-0.70800E+01	0.66850E+04
	H_2 Enhanced by 2.000E+00			
	H_2O Enhanced by 6.000E+00			
	CH_4 Enhanced by 2.000E+00			
	CO Enhanced by 1.500E+00			
	CO_2 Enhanced by 2.000E+00			
	C_2H_6 Enhanced by 3.000E+00			
262.	$H+C_2H_5\rightleftharpoons H_2+C_2H_4$	2.00E+12	0.0	0.0
263.	$H+C_2H_6\rightleftharpoons C_2H_5+H_2$	1.15E+08	1.9	7530.0
264.	$H+HCCO\rightleftharpoons CH_2(S)+CO$	1.00E+14	0.0	0.0
265.	$H+CH_2CO\rightleftharpoons HCCO+H_2$	5.00E+13	0.0	8000.0
266.	$H+CH_2CO\rightleftharpoons CH_3+CO$	1.13E+13	0.0	3428.0
267.	$H+HCCOH\rightleftharpoons H+CH_2CO$	1.00E+13	0.0	0.0
268.	$H_2+CO(+M)\rightleftharpoons CH_2O(+M)$	4.30E+07	1.5	79600.0
	Low pressure limit:	0.50700E+28	-0.34200E+01	0.84350E+05
	H_2 Enhanced by 2.000E+00			
	H_2O Enhanced by 6.000E+00			
	CH_4 Enhanced by 2.000E+00			
	CO Enhanced by 1.500E+00			
	CO_2 Enhanced by 2.000E+00			
	C_2H_6 Enhanced by 3.000E+00			

Nr.	Reaction	A [s^{-1}]	n [$-$]	E [cal $mole^{-1}$]
269.	OH+C⇌H+CO	5.00E+13	0.0	0.0
270.	OH+CH⇌H+HCO	3.00E+13	0.0	0.0
271.	OH+CH_2⇌H+CH_2O	2.00E+13	0.0	0.0
272.	OH+CH_2⇌CH+H_2O	1.13E+07	2.0	3000.0
273.	OH+CH_2(S)⇌H+CH_2O	3.00E+13	0.0	0.0
274.	OH+CH_3(+M)⇌CH_3OH(+M)	6.30E+13	0.0	0.0
	Low pressure limit:	0.27000E+39	-0.63000E+01	0.31000E+04
	H_2 Enhanced by 2.000E+00			
	H_2O Enhanced by 6.000E+00			
	CH_4 Enhanced by 2.000E+00			
	CO Enhanced by 1.500E+00			
	CO_2 Enhanced by 2.000E+00			
	C_2H_6 Enhanced by 3.000E+00			
275.	OH+CH_3⇌CH_2+H_2O	5.60E+07	1.6	5420.0
276.	OH+CH_3⇌CH_2(S)+H_2O	2.50E+13	0.0	0.0
277.	OH+CH_4⇌CH_3+H_2O	1.00E+08	1.6	3120.0
278.	OH+CH_2OH⇌H_2O+CH_2O	5.00E+12	0.0	0.0
279.	OH+CH_3O⇌H_2O+CH_2O	5.00E+12	0.0	0.0
280.	OH+CH_3OH⇌CH_2OH+H_2O	1.44E+06	2.0	-840.0
281.	OH+CH_3OH⇌CH_3O+H_2O	6.30E+06	2.0	1500.0
282.	OH+C_2H⇌H+HCCO	2.00E+13	0.0	0.0
283.	OH+C_2H_2⇌H+CH_2CO	2.18E-04	4.5	-1000.0
284.	OH+C_2H_2⇌H+HCCOH	5.04E+05	2.3	13500.0
285.	OH+C_2H_2⇌C_2H+H_2O	3.37E+07	2.0	14000.0
286.	OH+C_2H_2⇌CH_3+CO	4.83E-04	4.0	-2000.0
287.	OH+C_2H_3⇌H_2O+C_2H_2	5.00E+12	0.0	0.0
288.	OH+C_2H_4⇌C_2H_3+H_2O	3.60E+06	2.0	2500.0
289.	OH+C_2H_6⇌C_2H_5+H_2O	3.54E+06	2.1	870.0
290.	OH+CH_2CO⇌HCCO+H_2O	7.50E+12	0.0	2000.0
291.	HO_2+CH_2⇌OH+CH_2O	2.00E+13	0.0	0.0
292.	HO_2+CH_3⇌O_2+CH_4	1.00E+12	0.0	0.0
293.	HO_2+CH_3⇌OH+CH_3O	2.00E+13	0.0	0.0
294.	C+O_2⇌O+CO	5.80E+13	0.0	576.0
295.	C+CH_2⇌H+C_2H	5.00E+13	0.0	0.0
296.	C+CH_3⇌H+C_2H_2	5.00E+13	0.0	0.0
297.	CH+O_2⇌O+HCO	3.30E+13	0.0	0.0
298.	CH+H_2⇌H+CH_2	1.11E+08	1.8	1670.0
299.	CH+H_2O⇌H+CH_2O	1.71E+13	0.0	-755.0
300.	CH+CH_2⇌H+C_2H_2	4.00E+13	0.0	0.0
301.	CH+CH_3⇌H+C_2H_3	3.00E+13	0.0	0.0
302.	CH+CH_4⇌H+C_2H_4	6.00E+13	0.0	0.0
303.	CH+CO(+M)⇌HCCO(+M)	5.00E+13	0.0	0.0
	Low pressure limit:	0.26900E+29	-0.37400E+01	0.19360E+04
	H_2 Enhanced by 2.000E+00			

Nr.	Reaction	A [s^{-1}]	n [−]	E [cal $mole^{-1}$]
	H_2O Enhanced by 6.000E+00			
	CH_4 Enhanced by 2.000E+00			
	CO Enhanced by 1.500E+00			
	CO_2 Enhanced by 2.000E+00			
	C_2H_6 Enhanced by 3.000E+00			
304.	$CH+CO_2 \rightleftharpoons HCO+CO$	3.40E+12	0.0	690.0
305.	$CH+CH_2O \rightleftharpoons H+CH_2CO$	9.46E+13	0.0	-515.0
306.	$CH+HCCO \rightleftharpoons CO+C_2H_2$	5.00E+13	0.0	0.0
307.	$CH_2+O_2 \rightleftharpoons OH+HCO$	1.32E+13	0.0	1500.0
308.	$CH_2+H_2 \rightleftharpoons H+CH_3$	5.00E+05	2.0	7230.0
309.	$2CH_2 \rightleftharpoons H_2+C_2H_2$	3.20E+13	0.0	0.0
310.	$CH_2+CH_3 \rightleftharpoons H+C_2H_4$	4.00E+13	0.0	0.0
311.	$CH_2+CH_4 \rightleftharpoons 2CH_3$	2.46E+06	2.0	8270.0
312.	$CH_2+CO(+M) \rightleftharpoons CH_2CO(+M)$	8.10E+11	0.5	4510.0
	Low pressure limit:	0.26900E+34	-0.51100E+01	0.70950E+04
	H_2 Enhanced by 2.000E+00			
	H_2O Enhanced by 6.000E+00			
	CH_4 Enhanced by 2.000E+00			
	CO Enhanced by 1.500E+00			
	CO_2 Enhanced by 2.000E+00			
	C_2H_6 Enhanced by 3.000E+00			
313.	$CH_2+HCCO \rightleftharpoons C_2H_3+CO$	3.00E+13	0.0	0.0
314.	$CH_2(S)+N_2 \rightleftharpoons CH_2+N_2$	1.50E+13	0.0	600.0
315.	$CH_2(S)+O_2 \rightleftharpoons H+OH+CO$	2.80E+13	0.0	0.0
316.	$CH_2(S)+O_2 \rightleftharpoons CO+H_2O$	1.20E+13	0.0	0.0
317.	$CH_2(S)+H_2 \rightleftharpoons CH_3+H$	7.00E+13	0.0	0.0
318.	$CH_2(S)+H_2O(+M) \rightleftharpoons CH_3OH(+M)$	2.00E+13	0.0	0.0
	Low pressure limit:	0.27000E+39	-0.63000E+01	0.31000E+04
	H_2 Enhanced by 2.000E+00			
	H_2O Enhanced by 6.000E+00			
	CH_4 Enhanced by 2.000E+00			
	CO Enhanced by 1.500E+00			
	CO_2 Enhanced by 2.000E+00			
	C_2H_6 Enhanced by 3.000E+00			
319.	$CH_2(S)+H_2O \rightleftharpoons CH_2+H_2O$	3.00E+13	0.0	0.0
320.	$CH_2(S)+CH_3 \rightleftharpoons H+C_2H_4$	1.20E+13	0.0	-570.0
321.	$CH_2(S)+CH_4 \rightleftharpoons 2CH_3$	1.60E+13	0.0	-570.0
322.	$CH_2(S)+CO \rightleftharpoons CH_2+CO$	9.00E+12	0.0	0.0
323.	$CH_2(S)+CO_2 \rightleftharpoons CH_2+CO_2$	7.00E+12	0.0	0.0
324.	$CH_2(S)+CO_2 \rightleftharpoons CO+CH_2O$	1.40E+13	0.0	0.0
325.	$CH_2(S)+C_2H_6 \rightleftharpoons CH_3+C_2H_5$	4.00E+13	0.0	-550.0
326.	$CH_3+O_2 \rightleftharpoons O+CH_3O$	2.68E+13	0.0	28800.0
327.	$CH_3+O_2 \rightleftharpoons OH+CH_2O$	3.60E+10	0.0	8940.0
328.	$CH_3+H_2O_2 \rightleftharpoons HO_2+CH_4$	2.45E+04	2.5	5180.0

Nr.	Reaction	A [s^{-1}]	n [−]	E [cal $mole^{-1}$]
329.	$2CH_3(+M) \rightleftharpoons C_2H_6(+M)$	2.12E+16	-1.0	620.0
	Low pressure limit:	0.17700E+51	-0.96700E+01	0.62200E+04
	H_2 Enhanced by 2.000E+00			
	H_2O Enhanced by 6.000E+00			
	CH_4 Enhanced by 2.000E+00			
	CO Enhanced by 1.500E+00			
	CO_2 Enhanced by 2.000E+00			
	C_2H_6 Enhanced by 3.000E+00			
330.	$2CH_3 \rightleftharpoons H+C_2H_5$	4.99E+12	0.1	10600.0
331.	$CH_3+HCO \rightleftharpoons CH_4+CO$	2.65E+13	0.0	0.0
332.	$CH_3+CH_2O \rightleftharpoons HCO+CH_4$	3.32E+03	2.8	5860.0
333.	$CH_3+CH_3OH \rightleftharpoons CH_2OH+CH_4$	3.00E+07	1.5	9940.0
334.	$CH_3+CH_3OH \rightleftharpoons CH_3O+CH_4$	1.00E+07	1.5	9940.0
335.	$CH_3+C_2H_4 \rightleftharpoons C_2H_3+CH_4$	2.27E+05	2.0	9200.0
336.	$CH_3+C_2H_6 \rightleftharpoons C_2H_5+CH_4$	6.14E+06	1.7	10450.0
337.	$HCO+H_2O \rightleftharpoons H+CO+H_2O$	2.24E+18	-1.0	17000.0
338.	$CH_2OH+O_2 \rightleftharpoons HO_2+CH_2O$	1.80E+13	0.0	900.0
339.	$CH_3O+O_2 \rightleftharpoons HO_2+CH_2O$	4.28E-13	7.6	-3530.0
340.	$C_2H+O_2 \rightleftharpoons HCO+CO$	5.00E+13	0.0	1500.0
341.	$C_2H+H_2 \rightleftharpoons H+C_2H_2$	4.07E+05	2.4	200.0
342.	$C_2H_3+O_2 \rightleftharpoons HCO+CH_2O$	3.98E+12	0.0	-240.0
343.	$C_2H_4(+M) \rightleftharpoons H_2+C_2H_2(+M)$	8.00E+12	0.4	88770.0
	Low pressure limit:	0.70000E+51	-0.93100E+01	0.99860E+05
	H_2 Enhanced by 2.000E+00			
	H_2O Enhanced by 6.000E+00			
	CH_4 Enhanced by 2.000E+00			
	CO Enhanced by 1.500E+00			
	CO_2 Enhanced by 2.000E+00			
	C_2H_6 Enhanced by 3.000E+00			
344.	$C_2H_5+O_2 \rightleftharpoons HO_2+C_2H_4$	8.40E+11	0.0	3875.0
345.	$HCCO+O_2 \rightleftharpoons OH+2CO$	1.60E+12	0.0	854.0
346.	$2HCCO \rightleftharpoons 2CO+C_2H_2$	1.00E+13	0.0	0.0
347.	$NNH \rightleftharpoons N_2+H$	3.30E+08	0.0	0.0
348.	$NNH+O_2 \rightleftharpoons HO_2+N_2$	5.00E+12	0.0	0.0
349.	$NNH+O \rightleftharpoons OH+N_2$	2.50E+13	0.0	0.0
350.	$NNH+O \rightleftharpoons NH+NO$	7.00E+13	0.0	0.0
351.	$NNH+CH_3 \rightleftharpoons CH_4+N_2$	2.50E+13	0.0	0.0
352.	$H_2CN+N \rightleftharpoons N_2+CH_2$	6.00E+13	0.0	400.0
353.	$C+N_2 \rightleftharpoons CN+N$	6.30E+13	0.0	46020.0
354.	$CH+N_2 \rightleftharpoons HCN+N$	2.86E+08	1.1	20400.0
355.	$CH+N_2(+M) \rightleftharpoons HCNN(+M)$	3.10E+12	0.1	0.0
	Low pressure limit:	0.13000E+26	-0.31600E+01	0.74000E+03
	H_2 Enhanced by 2.000E+00			
	H_2O Enhanced by 6.000E+00			

Nr.	Reaction	A [s^{-1}]	n [$-$]	E [cal $mole^{-1}$]
	CH_4 Enhanced by 2.000E+00			
	CO Enhanced by 1.500E+00			
	CO_2 Enhanced by 2.000E+00			
	C_2H_6 Enhanced by 3.000E+00			
356.	$CH_2+N_2 \rightleftharpoons HCN+NH$	1.00E+13	0.0	74000.0
357.	$CH_2(S)+N_2 \rightleftharpoons NH+HCN$	1.00E+11	0.0	65000.0
358.	$C+NO \rightleftharpoons CN+O$	1.90E+13	0.0	0.0
359.	$C+NO \rightleftharpoons CO+N$	2.90E+13	0.0	0.0
360.	$CH+NO \rightleftharpoons HCN+O$	5.00E+13	0.0	0.0
361.	$CH+NO \rightleftharpoons H+NCO$	2.00E+13	0.0	0.0
362.	$CH+NO \rightleftharpoons N+HCO$	3.00E+13	0.0	0.0
363.	$CH_2+NO \rightleftharpoons H+HNCO$	3.10E+17	-1.4	1270.0
364.	$CH_2+NO \rightleftharpoons OH+HCN$	2.90E+14	-0.7	760.0
365.	$CH_2+NO \rightleftharpoons H+HCNO$	3.80E+13	-0.4	580.0
366.	$CH_2(S)+NO \rightleftharpoons H+HNCO$	3.10E+17	-1.4	1270.0
367.	$CH_2(S)+NO \rightleftharpoons OH+HCN$	2.90E+14	-0.7	760.0
368.	$CH_2(S)+NO \rightleftharpoons H+HCNO$	3.80E+13	-0.4	580.0
369.	$CH_3+NO \rightleftharpoons HCN+H_2O$	9.60E+13	0.0	28800.0
370.	$CH_3+NO \rightleftharpoons H_2CN+OH$	1.00E+12	0.0	21750.0
371.	$HCNN+O \rightleftharpoons CO+H+N_2$	2.20E+13	0.0	0.0
372.	$HCNN+O \rightleftharpoons HCN+NO$	2.00E+12	0.0	0.0
373.	$HCNN+O_2 \rightleftharpoons O+HCO+N_2$	1.20E+13	0.0	0.0
374.	$HCNN+OH \rightleftharpoons H+HCO+N_2$	1.20E+13	0.0	0.0
375.	$HCNN+H \rightleftharpoons CH_2+N_2$	1.00E+14	0.0	0.0
376.	$HNCO+OH \rightleftharpoons NH_2+CO_2$	1.55E+12	0.0	6850.0
377.	$HCNO+H \rightleftharpoons H+HNCO$	2.10E+15	-0.7	2850.0
378.	$HCNO+H \rightleftharpoons OH+HCN$	2.70E+11	0.2	2120.0
379.	$HCNO+H \rightleftharpoons NH_2+CO$	1.70E+14	-0.8	2890.0
380.	$HCCO+NO \rightleftharpoons HCNO+CO$	2.35E+13	0.0	0.0
381.	$CH_3+N \rightleftharpoons H_2CN+H$	6.10E+14	-0.3	290.0
382.	$CH_3+N \rightleftharpoons HCN+H_2$	3.70E+12	0.1	-90.0

Appendix C

Glossary

C.1 Glossary of terms

- **Binder:** The binder provides the structure or matrix in which solid granular ingredients (like oxidizer crystals) are held together in a composite propellant. The plastic-like or rubbery organic binder materials are also fuels for the propellant, and are oxidized by the oxidizer decomposition products. Curing agents or cross-linkers are used to form longer chains of the prepolymer binder molecules. The curing agent is the ingredient that causes the binder to solidify and become hard. Often a plasticizer is added to improve the mechanical properties of the final propellant (higher elongation). A plasticizer is a low-viscosity liquid ingredient that also yields a lower casting viscosity.

- **Differential scanning calorimetry (DSC):** The differential scanning calorimetry technique allows to measure endothermic and exothermic heat flows to and from a sample, while it is subjected to a programmed temperature envelope (e.g. linearly increasing with temperature). The heat flow is measured as a difference with respect to that of a sample with known properties. DSC allows to determine e.g. exothermic decomposition, and latent heat of phase transitions.

- **Friction sensitivity:** The friction sensitivity of a material is a measure of the sensitiveness of a material to frictional stimuli. The material to be tested is placed on a moving porcelain plate ($25 \times 25 \times 25$ mm^3). A fixed porcelain pin (10 mm diameter, 15 mm length) is pressed to the porcelain plate with the material in between. The loads on the peg can be set by the friction apparatus. The limiting load is defined as the lowest load at which an "explosion" is observed at least one out of at least six trials. For more information see Ref. [152].

- **Impact sensitivity:** The impact sensitivity of a material is a measure of the sensitiveness of solids and liquids to drop-weight impact. The material to be tested is subjected to the impact of a fallhammer with a certain weight from a specific height. The impact sensitivity is expressed in Joules (the product of the fallhammer weight and fall height). The limiting impact energy is defined as the lowest impact energy which results in an "explosion" in at least one out of at least six trials. For more information see Ref. [152].

- **Solid load:** A composite propellant is formed of a heterogeneous mixture of the liquid prepolymer and solid materials like the oxidizer and metal fuel ingredients. The solid load is defined as the total amount (weight percentage) of solid material present in the composite propellant. For most propellants the maximum performance is obtained for solid loads higher than 80%. To achieve these solid loads, mixtures of several particle sizes are used (multi-modal propellants).

- **Specific impulse:** The specific impulse, I_s, is the total impulse per unit weight of propellant. For a rocket motor with thrust envelope $F(t)$ and total propellant weight m_p it is calculated by

$$I_s = \frac{\int F(t)dt}{m_p} . \tag{C.1}$$

The specific impulse can also be expressed as a function of the combustion gas properties (γ, T and M) and ratio of expansion pressure and combustion pressure (p_e/p_c)

$$I_s = \sqrt{\frac{2\gamma}{\gamma - 1}\frac{RT}{M}\left[1 - \left(\frac{p_e}{p_c}\right)^{(\gamma-1)/\gamma}\right]} . \tag{C.2}$$

The vacuum specific impulse, I_{vac}, is the specific impulse for a rocket motor with nozzle expanding to vacuum conditions. This defines the maximum specific impulse for a given propellant.

C.2 Symbols

A	Area	m^2
	Frequency factor	1/s
	Absorption	-
B_g	Prefactor	m^3/kgK^2s
c	Specific heat capacity	J/kgK
	Ultrasound velocity	m/s
D	Diffusion coefficient	m^2/s
d	Thickness	m
E	Activation energy	J/mole
e	Internal energy	J/kg
F	Residual vector	Several
	Thrust	N
f	Reaction rates	1/s
	Focal length	m
	Frequency	Hz
f_r	Fraction of Q_r absorbed below the surface reaction zone $= exp(-K_a x_R)$	-
H	Enthalpy	J/kg
h_k	Specific enthalpy of the kth species	J/mole
I	Number of reactions	-

	Intensity	-
I_s	Specific impulse	m/s
I_{vac}	Specific impulse (expansion to vacuum)	m/s
i	Reaction number	-
J	Total number of grid points	-
$\mathcal{J}$	Jacobian	Several
j	Grid point number	-
K	Number of species	-
K_a	Absorption coefficient	1/m
K_c	Equilibrium constant	-
k	Species index	-
ld_{50}	Lethal dose	kg/kg
M	Molecular weight	kg/kmole
$\dot{m}$	Mass flow	kg/s
n	Pressure exponent	-
	Solution number	-
P	Sound pressure	Pa
p	Pressure	Pa
Q	Specific energy	J/kg
Q_r	Radiative energy	W/m^2
q	Rate-of-progress variable	$mole/m^3s$
R	Universal gas constant	J/moleK
	Response function	-
	Reflected fraction	-
r	Reflectivity	-
r_b	Burn rate	m/s
S	Entropy	J/moleK
T	Temperature	K
	Transmitted fraction	-
T_f	Adiabatic flame temperature	K
t^*	Characteristic time	s
V_k	Diffusion velocity of the kth species	m/s
v	Velocity	m/s
W	Molecular weight	g/mole
X	Variable quantity, e.g. T or Y	Several
x	Space coordinate	m
x_R	Reaction zone thickness = $(k_c/(\rho_c c_c))/(E_c/(2RT_s))$	m
Y_k	Mass fraction of the kth species	-
Z	Acoustic impedance	kg/ms
α	Efficiency factor	-
	Thermal diffusivity	m^2/s
	Solid load	-
α_{us}	Ultrasound attenuation coefficient	1/m
β	Temperature exponent	-
ΔH_f^0	Heat of formation	J/mole

ΔH^c	Heat of combustion	J/mole
ΔH_{sol}	Heat of solution	J/mole
Δt	Ultrasound pulse-echo time	s
Δt_{ox}	Oxidizer ignition delay	s
δ	Kronecker delta	-
	Reaction order	-
Φ	Soundwave amplitude	Pa
ϕ	Solution vector	Several
λ	Thermal conductivity	W/mK
	Wavelength	m
λ^n	Dampening parameter for nth solution	-
η	Curvature grid refinement parameter	-
ρ	Density	kg/m^3
σ_p	Burn rate temperature sensitivity	1/K
ν	Stoichiometric coefficient	-
ω	Angular frequency	rad/s
$\dot{\omega}$	Molar rate of production by chemical reaction	mole/m^{3}s
χ_k	Chemical symbol of the kth species	-
ξ	Volumetric fraction	-
ξ^*	Nondimensional flame standoff distance	-
ζ	Gradient grid refinement parameter	-

Subscripts, superscripts, notations

a	Activation
b	Boiling
$binder$	Binder
c	Condensed phase
evap	Vaporization
f	Forward
g	Gas phase
i	ith reaction
k	kth species
l	Liquid phase
m	Melting / Melt layer
ox	Oxidizer
p	Pressure coupled
q	Laser coupled
r	Reverse
s	Surface
subl	Sublimation
tot	Total
$\Delta \ldots$	Difference of quantity ...
$\overline{\ldots}$	Average of ...
(c)	Condensed phase

(g)	Gas phase
(l)	Liquid phase
$[\ldots]$	Molar concentration of ...
$\ldots^*$	Last converged solution of ...

C.3 Acronyms

AN	Ammonium nitrate
ANF	Ammonium nitroformate
AP	Ammonium perchlorate
APP	Aerospace propulsion products
BAMO	3,3-Bis-azidomethyl-oxetane
BDP	Beckstead-Derr-Price
DB	Double base
DNC	Dinitrocarbene
DSC	Differential scanning calorimetry
DTA	Differential thermal analysis
DUT	Delft university of technology
DBW	Denison-Baum-Williams
ESA	European space agency
FT-IR	Fourier transform infra-red
FWHM	Full width at half maximum
GAP	Glycidyl azide polymer
GSTP	General science and technology program
HGU	HNF-GAP-urethane
HHU	HNF-HTPB-urethane
HPU	HNF-polyNIMMO-urethane
HMX	Cyclotetramethylenetrinitramine
HNF	Hydrazinium nitroformate
HNIW	Hexanitrohexaza isowurtzitane
HTPB	Hydroxyl terminated polybutadiene
LIF	Laser-induced fluorescence
NIVR	Netherlands agency for aerospace programmes
PECH	Polyepichlorohydrin
PLIF	Planar laser-induced fluorescence
PML	Prins Maurits laboratory
PMMA	Polymethyl methacrylate
PMT	Photo Multiplier Tube
polyNIMMO	Poly-3-nitratomethyl-3-methyloxetane
PPG	Polypropylene glycol
PTP	Peak-to-peak
QSHOD	Quasi-steady gas phase, homogeneous one dimensional
RDX	Cyclotrimethylenetrinitramine
T-Jump	Temperature jump

TG	Thermo gravimetry
TMD	Theoretical maximum density
TNO	Netherlands organization for applied scientific research
URRA	Ultrasonic Regression Rate Analyzer
UV/Vis	Ultra-violet/visible
VTS	Vacuum thermal stability
WSB	Ward-Son-Brewster

Appendix D

Publications

- J. Louwers and G.M.H.J.L. Gadiot, *Model for the Nonlinear Transient Burning of Hydrazinium Nitroformate*, Int. Workshop on Combustion Instability of Solid Propellants and Rocket Motors, Politecnico di Milano, Italy, 16-19 June 1997, also published in Journal of Propulsion and Power, Vol. 5, No. 5, pp. 778-782, November-December 1999.

- J. Louwers, G.M.H.J.L. Gadiot, M.Q. Brewster, S.F. Son, T. Parr and D. Hanson-Parr, *Model for Steady-State HNF Combustion*, Int. Workshop on Combustion Instability of Solid Propellants and Rocket Motors, Politecnico di Milano, Italy, 16-19 June 1997, also published in Journal of Propulsion and Power, Vol. 5, No. 5, pp. 772-777, November-December 1999.

- J. Louwers, *Hydrazinium Nitroformate: A High Performance Next Generation Oxidizer*, Journal of Pyrotechnics, Vol. 6, pp. 36-42, 1997.

- J. Louwers, G.M.H.J.L. Gadiot, M. Versluis, A.J. Landman, Th.H. van der Meer and D.J.E.M. Roekaerts, *Measurement of Steady and Non-Steady Regression Rates of Hydrazinium Nitroformate with Ultrasound*, Int. Workshop on Measurement of Thermophysical and Ballistic Properties of Energetic Materials, Politecnico di Milano, Milano, Italy, 22-24 June 1998. Submitted to Journal of Propulsion and Power.

- J. Louwers, G.M.H.J.L. Gadiot, M. Versluis, A.J. Landman, Th.H. van der Meer and D.J.E.M. Roekaerts, *Combustion of Hydrazinium Nitroformate Based Compositions*, 34th AIAA/ASME/SAE/ASEE Joint Propulsion Conference and Exhibit, 13-15 July, Cleveland, OH, Paper number AIAA 98-3385, 1998.

- M. Versluis, Th. van der Meer, D.J.E.M. Roekaerts, J. Louwers and G.M.H.J.L. Gadiot, *Decomposition and Combustion of Hydrazinium Nitroformate, Poster presented at the 27th Symposium (International) on Combustion Institute*, The Combustion Institute, University of Colorado, Boulder, USA, 2-7 August 1998.

- J. Louwers and M. Versluis, *HNF spaart ozonlaag*, De Ingenieur nr. 20, 24-25, 2 December 1998.

- J. Louwers, T. Parr and D. Hanson-Parr, *Decomposition and Flame Structure of Hydrazinium Nitroformate*, 37th AIAA Aerospace Sciences Meeting and Exhibit, January 11-14, Reno, NV, Paper number AIAA 99-1091, 1999.

- J. Louwers, G.M.H.J.L. Gadiot, A.J. Landman, T.W.J. Peeters, Th.H. van der Meer and D.J.E.M. Roekaerts, *Combustion and Flame Structure of HNF Sandwiches and Propellants*, 35th AIAA/ASME/SAE/ASEE Joint Propulsion Conference and Exhibit, 20-24 June, Los Angeles, CA, Paper number AIAA 99-2359, 1999.

- G.G.M. Stoffels, D.J.E.M. Roekaerts, J. Louwers and G.M.H.J.L. Gadiot, *Diffusion Flame Structure of HNF Sandwiches*, 5-ISICP, Fifth International Symposium on Special Topics in Chemical Propulsion: Combustion of Energetic Materials, Stresa, Italy, 18-21 June, 2000.

- H.F.R. Schöyer, W.H.M. Veltmans, J. Louwers, A.E.D.M. van der Heijden, H.L.J. Keizers, and R.P. van den Berg, *An Overview of the Development of HNF-based Propellants*, 36th AIAA/ASME/SAE/ASEE Joint Propulsion Conference and Exhibit, 16-19 July, Huntsville, AL, Paper number AIAA 2000-3184, 2000.

- J. Louwers and A.E.D.M. van der Heijden, *Hydrazinium Nitroformate*, International Patent Application, WO 99/58498, 18 November, 1999.

- J. Louwers and A.E.D.M. van der Heijden, *Hydrazinium Nitroformate based High Performance Solid Propellants*, International Patent Application, WO 99/59940, 25 November, 1999.

Acknowledgments

There is nothing nicer than being able to do what you like to do. For several years rocketry has been my big hobby. By doing the work described in this thesis a dream came true: to be able to work on solid rocket propulsion. Now that the writing is finished, I would like to take this opportunity to thank some people and organizations who contributed to this dissertation.

First of all I would like to thank my promoter Dirk Roekaerts. Thank your for your help and guidance during this project. I would like to thank Guy Gadiot for his daily guidance. His comments and suggestions have been very helpful for this work.

I would like to thank Paul Korting from the TNO Prins Maurits Laboratory for making it possible to carry out this work. His enthusiasm really inspired me while doing this work. I would like to thank my colleges of the rocket technology research group (RT) of TNO. In particular I would like to thank Pieter Elands for having me in the group and helping me with all issues that came across including the lending of the equipment for my experiments. Ronald van den Berg helped by being an infinite source of online information. From the test group, I would like to thank Jaap Varkevisser, Monique Janssens, Jos van de Brand and Arjen Klein. Your help with my experiments greatly contributed to this work. Many times I was late with my samples, but because of your flexibility things could always be arranged. Maaike Rotteveel for her help with the strand burner measurements, and her critical questions. I could have written down the other group members here as well, because all of you have contributed to this thesis. I really enjoyed working within RT and consider it a privilege to have worked with you all.

I spent a great deal of my time preparing samples at the pyrotechnics and energetic materials (PE) group of TNO at Ypenburg. I would like to thank Jos Mul for his t(h)rust, and allowing me to use the pressing and mixing facilities. During all this work, I learned a lot of Arnold Leeuwenburgh. His experience in the lab in working with all kinds of energetic materials is certainly to be respected. Thank you for showing me all your tricks (including how to weigh a micro-droplet of cure catalyst). Other people of PE also contributed significantly to this work: John Koman and Rudy Krämer thank you for your help with obtaining access, the needed materials and paperwork for transportation of my samples. 'Mr. HNF' Antoine van der Heijden for the many discussions about possible reaction pathways, new formulations and exotic ideas. His extensive knowledge about HNF and propellants added greatly to this work. In that respect I would also like to thank Aat Hordijk for his help in formulating compositions. Then I come to 'Young-Pyro': Ernst-Jan van Hout, Rutger Webb, Michel van Zelst and myself. Many times, we discussed exotic propellant combinations, new management ideas and future plans. I hope we will continue this in the future! I really enjoyed working at Ypenburg. The surroundings significantly changed during this project, but luckily the people did not. The trips to Ypenburg always gave a welcome variation to the everyday routine.

And then there is my third group of colleagues at Delft University. Theo van der Meer, now at University of Twente, contributed tremendously by writing the joint STW-proposal and being the initial project leader, later succeeded by Dirk Roekaerts. Michel Versluis learned me a lot about optical diagnostics. Your input was indispensable for this project, especially during the construction of the experimental setup. Many of the PLIF images

that are presented in this thesis were obtained by Genie Stoffels. Thank you for your help and interest in this project. I think that the cooperation was very fruitful, and that we learned a lot from each other. I would also like to thank Anke Jannie Landman for the modeling efforts. Her work contributed significantly to this dissertation. The help of Tim Peeters for adapting the BIGMIX model for laminar sandwich combustion is acknowledged. Then there is 'Mr. disaster-scenario' Bart Hoek. Because of his sharp eye for details his designs approach perfection. His contributions are greatly valued. Of course I should not forget to mention all other people working at Delft University for their help during this project.

At the beginning of the project, I got the opportunity to learn more about solid propellant diagnostics at NAWC, China Lake. Tim Parr and Donna Hanson-Parr introduced me to many of the aspects, and showed many tricks. Their interest and support largely contributed to this work. I would also like to thank Jerry Finlinson from NAWC for providing experimental data and the helpful discussions about his laser-recoil experiments. I would like to thank Steve Son and Quinn Brewster for their suggestions and help with the WSB-model.

This work would not have been possible without the support of The Dutch Technology Foundation, STW. STW did not only contribute financially to this work, but also in terms of project guidance. The feedback during the progress meetings is greatly acknowledged. I would like to thank all people that took place in the steering committee: Marijke de Jong from STW, Harry Förster from the Netherlands Agency for Aerospace Programmes NIVR, Jim Kok from Twente University of Technology, Hans ter Meulen from Nijmegen University, Philip de Goey from Eindhoven University of Technology, Herman Schöyer from the European Space Agency, and Paul Korting from Aerospace Propulsion Products.

It would have been impossible to carry out experiments without HNF. Aerospace Propulsion Products contributed by providing the HNF for this work. Their contribution is gratefully acknowledged. Furthermore I would like to thank Willianne Veltmans and Frank Wierikx for answering all my questions about HNF and their production facility.

Despite the busy schedule, my hobbies were a welcome change to the laboratory work during the week. First, there was always the NERO. During the last few years we flew several rockets, and burned more AP, N_2O and HTPB than ever before. Martijn, René, Bob, Dirk, Wilfred, John, Leo, Bernard, Maarten, Laurens, Frank and Bert and all others, thank you all for your friendship. Now this thesis is finished, I hope there will be some more time for new challenges.

Traveling became one of my hobbies. Our trip to Africa with my brother Dirk and Jolande is an experience that I will not easily forget. This trip learned me that we carefully have to protect and respect our remaining nature. My special thanks go to our guide who took us on a game walk in the Okavango delta. I still remember his instructions before we left: "If you see elephant you must run zig-zag, if we see lion there is nothing we can do....".

Finally I would like to thank my parents for their continuous support. Without their help this thesis would never have been finished. Thank you.

Stellingen

1. De ontleding van hydrazine nitroformaat (HNF) begint met de overdracht van een proton van het hydrazine-ion naar een nitro-groep van het nitroformaat.
(*Hoofdstuk 2 van dit proefschrift.*)

2. Door een gecontroleerd persproces kan de lengte-diameter verhouding van HNF-kristallen worden verminderd.
(*Hoofdstuk 3 van dit proefschrift.*)

3. Tijdens de verbranding van HNF ontstaan als gevolg van thermische expansie scheuren evenwijdig aan het brandoppervlak. Ter plaatse van een dergelijke scheur neemt de thermische weerstand toe, met als gevolg een scherpe knik in het temperatuurprofiel.
(*Hoofdstuk 4 van dit proefschrift.*)

4. De HNF deeltjesgrootte heeft slechts een klein effect op de afbrandsnelheid van een HNF/GAP stuwstof.
(*Hoofdstuk 5 van dit proefschrift.*)

5. Resultaten van het BDP-model aangepast voor de verbranding van stuwstoffen bestaande uit HNF en GAP laten zien dat de HNF vlam de bepalende warmtebron is aan het verbrandingsoppervlak. De bijdrage van de oxydator-binder diffusie vlam is verwaarloosbaar in vergelijking met de HNF vlam.
(*Hoofdstuk 6 van dit proefschrift.*)

6. In geval van instabiele verbranding kan de instantane afbrandsnelheid met de ultrasoon puls-echo techniek alleen worden bepaald wanneer er voor de temperatuurafhankelijkheid van de ultrasoonsnelheid wordt gecompenseerd.
(*Hoofdstuk 7 van dit proefschrift.*)

7. In geen enkel proefschrift zou een index mogen ontbreken.

8. De melding "ontsteek uw lichten" bij het inrijden van een tunnel kan minimaal op twee manieren worden geïnterpreteerd.

9. Files op het internet worden veroorzaakt door grote files.

10. De tijdwinst die velen proberen te behalen door met hoge snelheid naar het werk te rijden, staat in vele gevallen in geen verhouding tot de tijd die vervolgens bij de koffieautomaat wordt doorgebracht.

11. Het hebben van een elfde stelling getuigt van inspiratie.

12. Niets is zo flexibel als een planning.

13. Door de invoering van de determinatieklas dreigt de brugpieper te verdwijnen.

14. Stellingen doen afbraak aan een proefschrift, omdat ze beter worden gelezen dan het proefschrift zelf.

15. Het ontsteken van een raket werkt aanstekelijk.

Curriculum vitae

Personal

Name	Jeroen Louwers
Date of birth	18 February 1972
Place of birth	Waalre, The Netherlands
Nationality	Dutch
Hobbies	Amateur rocketry, electronics, travelling, photography

Education

1995-1999	**Ph.D. research** TNO Prins Maurits Laboratory, Rijswijk, The Netherlands
1990-1995	**Student** Eindhoven University of Technology, Faculty of Applied Physics
1984-1990	**Secondary school** VWO Anton van Duinkerkencollege, Veldhoven, The Netherlands
1978-1984	**Primary school** De Wilderen, Waalre, The Netherlands

Work

2000-	**System architect** Philips Optical Storage, Eindhoven, The Netherlands

Index

ab-initio calculations, 23
absorption coefficient, 66, 100, 108, 149, 160
absorption spectroscopy, 57
aci-nitroform, 25
acknowledgments, 217
acronyms, 213
activation energy
    apparent, 81
activation energy asymptotics, AEA, 101
ADN, 49
Aerospace Propulsion Products, APP, 10
Alex, 68, 170
    PLIF images, 69
aluminum, 3, 67, 171
ammonium dinitramide, ADN, 3
ammonium nitroformate, ANF, 15
ammonium perchlorate, AP, 2
Ariane 5, 2

BDP, 126, 136
Beckstead-Derr-Price, *see* BDP
beryllium, 170
BIGMIX, 132
    comparison with experimental results, 136
    model input, 132
    results, 134
binder, 3, 75, 209
binning, 62
Bunsen burner, 60

carboxy-terminated polybutadiene, CTPB, 170
Clausius-Clapeyron, 12
CO_2-laser, 43, 108
Coherent Anti-Stokes Raman Spectroscopy, CARS, 65
collisional coefficients, 38
composite propellant, 2
    binder, 209
    combustion, 5
conclusions, 173
condensate, 19, 53
cross-linker, 209
curing agent, 209
curriculum vitae, 220

de-radiative extinguishment, 53
Denison-Baum-Williams, DBW, 99
Differential scanning calorimetry, DSC, 209
dinitrocarbene, DNC, 23
double base, 2
double bond, 9
DSC, 15, 56
ducted rocket, 4
dye laser, 43

Einstein coefficients, 38
electric conduction, 17
emission, 50
emission spectroscopy, 56
epichlorohydrin, ECH, 76
equivalence principle, 66
error
    burn rate, 45
    burn rate parameters, 79
    zone width, 85
European Space Agency, ESA, 3
excimer laser, 43

flame sheet, 169
frequency doubling, 60
friction sensitivity, 209
FT-IR, 15
FWHM, 51

GAMESS, 25
GAP, 75

decomposition, 79
monopropellant combustion, 76
properties, 76
GAP-A, 76, 92
glossary of terms, 209
glycidyl azide polymer, *see* GAP
graphite, 71, 121
GRI-Mechanism, 132
grid
BIGMIX, 132
PREMIX, 118
refinement, 193
GSTP-1, 6
GSTP-2, 6, 15

hazard properties, 33
heat of combustion, 11
heat of formation, 11
heat of solution, 11
heat of vaporization, 12
high-pressure bomb, 42
HMX, 49
HNF, 3, 9
absorption spectra, 12
adiabatic composition, 48
adiabatic flame temperature, 48
burn rate, 47, 52, 158
cool crystallization process, 10
crystals, 10
decomposition, 15
DSC trace, 15
evaporation process, 10
friction sensitivity, 10, 13, 33
grades, 10
heat of combustion, 11
heat of formation, 11
heat of solution, 11
heat of sublimation, 12, 24
heat of vaporization, 12
impact sensitivity, 10, 13, 33
improved morphology, 34
international programs, 6
lethal dose, 13
melting heat, 12
melting point, 10
monopropellant, 5, 47
pellets, 29
pressing, 30
production, 9
properties, 10
recrystallization, 10
reflection, 67
sandwich, 82
solvent/non-solvent, 10
sub-atmospheric combustion, 52
surface temperature, 54, 107, 115, 149
temperature profile, 65, 118
temperature sensitivity, 49
thermal properties, 11
ultrasound properties, 146
HNF-GAP
performance, 4
propellant, 90, 127
sandwich, 82
HNIW, 170
hot cell, 17
hot plate, 17
HTPB, 2, 4, 81, 168
propellant, 92
sandwich, 83
hydrazine, 5, 9, 25
hydrazinium nitroformate, *see* HNF
hydrochloric acid, HCl, 4
hydroxyl terminated polybutadiene, *see* HTPB

impact sensitivity, 10, 209

KTSS-flame, 149

L/D ratio, 10
LabVIEW, 44
laser
CO_2, 43, 108
dye, 43, 60
excimer, 43
power, 60
laser saturated fluorescence, 40
laser-assisted combustion, 49
laser-induced fluorescence, *see* LIF
laser-recoil, 49, 151, 154
Lewis number, 100
LIF, 38
saturated, 40

Stern-Vollmer factor, 39
LIFbase, 60

mass flux, 115
mean mixture fraction, 136
melting heat, 12
microscope, electron, 31
microscope, light, 30
microwave technique, 143
MOPAC, 23
multi-component diffusion, 132

NAWC, 15, 30, 52, 57
Netherlands Agency for Aerospace Programmes, NIVR, 3
nitroform, 9
nomenclature, 210

objectives, 6
OH-PLIF, 60
oscillations, 158
oxidizers
flame temperature, 47
oxygen/acetylene flame, 62

paraffin, 72, 121
pellets, 29
hazard properties, 33
structure, 30
vacuum pressing, 31
pilot scale, 10
planar laser-induced fluorescence, *see* PLIF
plasticizer, 76, 90, 92, 209
PLIF, 40, 51, 85
CN in neat HNF, 61
CN in sandwiches, 86
OH in HNF sandwiches, 85
OH in neat HNF, 60
OH in sandwiches, 85
sheet optics, 61
PLIF-temperature, 51
PM3 hamiltonian, 23
polyepichlorohydrin, PECH, 76
polyNIMMO, 3, 92, 168, 170
PREMIX, 71, 97, 112, 171
conclusions, 122
model, 112
program, 118
pressing, 29, 30
pressure exponent, 52, 68, 91, 104, 128, 167
proof of concept, 6
propellant
composite, 2
double base, 2
propositions, 219
publications, 215

QSHOD-model, 149
quantum chemical calculations
ab initio, 25
semi-empirical, 23
quenching, 38

radiation imprisonment, 38
ramjet, 4
RDX, 49
reaction order, 100, 169
reaction rates, 115
efficiency factor, 116
HNF mechanism, 194
recrystallization, 10
reflection coefficient, 66, 109, 149, 151
response function, 151, 161
rocket motor
hybrid, 2
liquid, 2
solid, 2

samenvatting, vii
sandwich, 82
diffusion flame, 136
emission imaging, 82
preparation, 36
selfdeflagration, 47
sensitivity
friction, 33, 209
impact, 33, 209
sodium azide, 76
sodium chloride, 54, 56
solid load, 210
Space Shuttle, 2, 3
specific impulse, 1, 3, 210
HNF propellants, 4

vacuum, 210
stellingen, 219
sublimation heat, 12, 24
summary, viii
symbols, 210

T-jump, 15
temperature sensitivity, 49
theoretical maximum density, TMD, 30
thermocouple, 41
systematic errors, 42
thermophysical properties, 11
titration, 10
TMD, 30, 47
transition state, 24
transmission, 66
Trouton's rule, 12
TWOPNT, 192

ultrasonic regression rate analyzer, *see* URRA
ultrasound, 143, 144
attenuation, 145
coupling, 155
data reduction, 156
propagation, 144
pulse-echo technique, 145
reflection, 145
scattering, 145
setup, 153
technique, 143
waves, 144
unsaturated binder, 9
unsteady combustion, 143
URRA, 144, 154

vacuum pressing, 32
vacuum thermal stability, VTS, 10

Ward-Son-Brewster, WSB, 99

zinc selenide, ZnSe, 43